Aerodynamic and Aeroacoustic Interaction Effects for Tip-Mounted Propellers

An Experimental Study

Sinnige, Tomas

DOI
10.4233/uuid:214e1e9a-c53e-47c7-a12c-b1eb3ec8293b

Publication date
2018

Document Version
Final published version

Citation (APA)
Sinnige, T. (2018). *Aerodynamic and Aeroacoustic Interaction Effects for Tip-Mounted Propellers: An Experimental Study*. [Dissertation (TU Delft), Delft University of Technology].
https://doi.org/10.4233/uuid:214e1e9a-c53e-47c7-a12c-b1eb3ec8293b

Important note
To cite this publication, please use the final published version (if applicable).
Please check the document version above.

Aerodynamic and Aeroacoustic Interaction Effects for Tip-Mounted Propellers

An Experimental Study

Aerodynamic and Aeroacoustic Interaction Effects for Tip-Mounted Propellers

An Experimental Study

Dissertation

for the purpose of obtaining the degree of doctor
at Delft University of Technology,
by the authority of the Rector Magnificus prof. dr. ir. T.H.J.J. van der Hagen
chair of the Board for Doctorates,
to be defended publicly on
Tuesday 25 September 2018 at 12:30 o'clock

by

Tomas Sinnige

Master of Science in Aerospace Engineering, Delft University of Technology, the Netherlands
born in Amsterdam, the Netherlands

This dissertation has been approved by the promotors.

Composition of the doctoral committee:

Rector Magnificus	chairperson
Prof. dr. ir. L. L. M. Veldhuis	Delft University of Technology, *promotor*
Prof. Dr.-Ing. G. Eitelberg	Delft University of Technology, *promotor*
Independent members:	
Prof. dr. G. J. W. van Bussel	Delft University of Technology
Prof. dr. P. Liu	Beihang University, China
Prof. Dr.-Ing. R. Radespiel	Technische Universität Braunschweig, Germany
Dr. L. G. Trapp	Embraer, Brazil
Prof. dr. ir. P. Colonna	Delft University of Technology, reserve member
Other member:	
Dr. D. Ragni	Delft University of Technology

Parts of this research were funded by the European Union's 7th Framework Programme for Research and Technological Development (FP7-INFRASTRUCTURE-2008-1) under grant agreement n° 227816, and the European Union's Horizon 2020 Framework Programme for Research and Innovation under grant agreement n° CS2-LPA-GAM-2014-2015-01.

Keywords: Propeller–airframe interactions, propeller aeroacoustics, propeller aerodynamics, propeller slipstream characteristics, tip-mounted propellers, wind-tunnel testing

Printed by: Gildeprint

Front & Back: Tip-mounted propeller setup installed in the Low-Turbulence Tunnel at Delft University of Technology (image digitally enhanced).

ISBN 978-94-9301-446-6

An electronic version of this dissertation is available at
`http://repository.tudelft.nl/`.

SUMMARY

Propellers can enable a significant reduction in energy use of future aircraft by offering a higher propulsive efficiency than turbofan engines. However, the integration of propellers with the airframe is complicated by aerodynamic and aeroacoustic interactions, which can lead to performance and noise penalties. Yet, by optimally integrating the propellers with the airframe, these installation penalties can be minimized or even converted into significant performance benefits. Recent interest in hybrid-electric and fully-electric propulsion has made propeller–airframe integration even more relevant because of the close coupling between multiple propellers and the airframe typical of aircraft with such propulsion technologies. A key example of a potentially beneficial integration approach is the tip-mounted propeller. Wingtip-mounted configurations provide efficiency benefits due to tip-vortex attenuation, while pylon-mounted and horizontal-tailplane-mounted configurations avoid issues such as cabin noise and ground clearance. This thesis provides an experimental analysis of the aerodynamic and aeroacoustic interactions and potential performance-enhancement strategies for tip-mounted propellers, focusing on the wingtip-mounted and pylon-mounted configurations.

An experimental approach was taken to allow for rapid analysis of the interaction effects and their sensitivity to several dominant variables, and to generate data sets which can be used to validate future numerical simulations. Measurements were taken with three test setups in open-jet and closed-section low-speed wind tunnels, featuring two single-rotating propeller models installed in close proximity to different wing and pylon models. Various measurement techniques were applied to quantify the impact of the interaction effects on the flowfield, the propeller performance and noise emissions, and the wing or pylon loading. Compared to typical cruise flight conditions of propeller aircraft, the experiments were performed at relatively low Mach and Reynolds numbers. Even though this may have led to offsets in a number of quantitative conclusions, all dominant physical phenomena will have been captured in the experiments.

The performance of propulsion systems with tip-mounted propellers is strongly affected by the interaction between the propellers and the tip vortex of their support, both for tractor-propeller and pusher-propeller configurations. Detailed measurements for the tractor configuration showed that wingtip-mounted propellers with inboard-up rotation decrease wing induced drag by attenuating the wingtip vortex by the swirl in the propeller slipstream. In a direct comparison with a conventional propeller–wing layout, the wingtip-mounted configuration showed a drag benefit of around 15% at a thrust coefficient of 0.12 and a wing lift coefficient of 0.5. This aerodynamic benefit increased upon increasing the propeller thrust setting and the wing lift coefficient. For pusher propellers, the circumferential velocity components induced by the tip vortex modify the effective advance ratio of the propeller. Preliminary measurements with a pylon model at nonzero angle of attack showed that this improves the propeller performance when the sense of rotation of the propeller is opposite to that of the tip vortex.

The tip-vortex interaction causes asymmetric aerodynamic loading for vehicles with co-rotating tractor propellers. In such case, swirl-recovery vanes (SRVs) can be applied to recover the propeller-induced swirl before it interacts with the wing, thereby mitigating the potential performance penalty. Measurements with an isolated propeller–SRV combination confirmed the potential of SRVs to reduce the swirl in the propeller slipstream. However, the propulsive performance of these SRVs was limited by stall on the inboard part of the vanes. Preliminary investigations with an installed tip-mounted tractor propeller showed that the reduction in swirl in the slipstream can decrease the difference in aerodynamic loading for the cases with inboard-up and outboard-up propeller rotation. This confirms that SRVs can be applied to alleviate the asymmetric loading in case of a co-rotating propeller configuration. In addition to the effects on the time-averaged performance, the unsteady interactions between the propeller and the SRVs introduce additional noise sources due to unsteady propeller-blade and SRV loading. The resulting increase in tonal noise was manifested mostly by a significant amplification of the levels of the higher harmonics. This especially affected the system noise emissions at low propeller thrust setting, with a noise penalty of up to 7 dB. At higher thrust settings, the tonal noise penalty was lower at 3 – 5 dB.

For tractor-propeller configurations, harmonic loading occurs on the downstream aerodynamic surface due to the unsteady interaction with the propeller slipstream. This may result in vibrations which are transmitted to the fuselage, and can be perceived inside the cabin as structure-borne noise. The measurements showed that the pressure fluctuations on the downstream aerodynamic surface are dominated by the propeller-blade tip vortices, which cause a periodic pressure response with strong harmonics. The amplitude of the pressure fluctuations increases with increasing thrust setting, while the unsteady lift coefficient features a nonmonotonic dependency on the thrust setting. The lowest integrated unsteady loads were obtained for cases with approximately integer ratios between the surface's chord length and the wavelength of the perturbation associated with the propeller-blade tip vortices. This implies that structure-borne noise may be reduced by matching the downstream chord length with an integer multiple of the axial separation between the propeller tip vortices.

A flow-permeable leading edge provides an alternative, passive means to alleviate the unsteady loading. Experiments were performed to quantify the potential benefits of such an approach compared to the solid baseline configuration. The geometry of the considered flow-permeable leading edges was not optimized; instead, the designs were based on previous work available in the literature. Measurements with particle-image velocimetry showed that the flow through the flow-permeable leading edge increases the boundary-layer thickness on the suction side of the pylon. This caused higher drag due to viscous dissipation, and reduced lift at angles of attack above 6 deg. The increased boundary-layer thickness and flow through the cavity enhanced the viscous interaction with the cores of the propeller tip vortices, reducing the velocity fluctuations near the pylon surface by up to 35%. Consequently, lower tonal noise emissions from the pylon were measured in the far field, suggesting the desired reduction in surface pressure fluctuations by application of the flow-permeable leading edge.

Pusher propellers suffer from a dominant interaction between the blades and the wake of the upstream wing or pylon. An analysis of the pylon-mounted configuration showed that the wake encounter leads to periodic impulsive blade-loading fluctuations. These cause unsteady-loading noise, resulting in a measured tonal noise penalty of up to 24 dB. The unsteady-loading noise peaked in the upstream direction and became increasingly relevant with decreasing propeller thrust setting because of the associated reduction of the steady blade loads. In contrast, the integrated propeller performance was not significantly altered by the pylon-wake encounter.

Pylon-blowing systems can be applied as active control technique to minimize the noise penalty caused by the wake encounter. Particle-image-velocimetry measurements between a pylon and a propeller confirmed the efficacy of a trailing-edge blowing system to reduce the momentum deficit in the pylon wake. Consequently, the application of the blowing system alleviated the pylon-installation effects at the source. At an intermediate thrust setting, the root mean square of the blade-loading fluctuations due to the wake encounter was reduced by up to 60%, resulting in noise emissions approximately equal to those recorded for the isolated propeller. At a lower thrust setting, on the other hand, a noise penalty remained due to the velocity deficit which persisted on both sides of the blowing jet. This can be solved by using a chordwise blowing system, which provides higher wake uniformity than the trailing-edge blowing system, while also enabling effective wake filling at nonzero angle of attack.

The results presented in this thesis emphasize the sensitivity of the aerodynamic and aeroacoustic performance of installed tip-mounted propeller propulsion systems to interactions between the propeller and the airframe. It is shown that significant integration benefits can be obtained by exploiting the beneficial interactions, while both active and passive control techniques are available to mitigate the adverse interactions. The knowledge gained from the research study discussed in this thesis can be used to advantage in the design of future highly efficient aircraft.

SAMENVATTING

Het hogere voortstuwingsrendement van propellers ten opzichte van turbofans maakt het mogelijk om het energieverbruik van toekomstige vliegtuigen significant te verminderen. Echter, de integratie van propellers met de rest van het vliegtuig wordt gecompliceerd door aerodynamische en aero-akoestische interacties, welke tot prestatie- en geluidsproblemen kunnen leiden. Door de propellers optimaal te integreren met de rest van het vliegtuig kunnen deze negatieve installatie-effecten geminimaliseerd worden, of zelfs omgezet worden in een aanzienlijke verbetering van de prestaties. De recente interesse in hybride en volledig elektrische voortstuwing heeft de integratie van propellers nog relevanter gemaakt vanwege de nauwe koppeling tussen de propellers en de rest van het vliegtuig die typisch is bij toepassing van dergelijke voortstuwingstechnieken. Een belangrijk voorbeeld van een potentiële voordelige integratieaanpak is het installeren van de propeller aan de tip van de vleugel, een pylon, of het horizontale staartvlak. Vleugeltip-geïnstalleerde configuraties bieden efficiëntievoordelen door de gunstige interactie tussen de slipstroom van de propeller en de tipwervel van de vleugel, terwijl configuraties met de propellers geïnstalleerd aan een pylon of het horizontale staartvlak problemen vermijden ten aanzien van cabinegeluid en bodemvrijheid. Dit proefschrift presenteert een experimentele analyse van de belangrijkste interacties en mogelijke strategieën voor prestatieverbeteringen voor propellers geïnstalleerd aan de tip van een pylon of de vleugel.

Het werk is gebaseerd op windtunnel experimenten, omdat deze snelle analyses mogelijk maken van de interacties en hun gevoeligheid ten aanzien van verschillende dominante variabelen, en tevens gegevenssets opleveren die gebruikt kunnen worden om toekomstige numerieke analyses te valideren. De metingen werden gedaan met drie verschillende opstellingen in open-straal en gesloten lage-snelheids windtunnels, waarbij gebruik werd gemaakt van twee propellermodellen geïnstalleerd in de nabijheid van verschillende vleugel- en pylonmodellen. Diverse meettechnieken werden toegepast om de invloed van de interacties op het stromingsveld, de prestaties en geluidsemissies van de propeller, en de belasting van de vleugel of pylon te kwantificeren. Ten opzichte van typische vliegcondities tijdens de kruisvlucht van propellervliegtuigen werden de experimenten uitgevoerd bij relatief lage Mach- en Reynoldsgetallen. Hoewel dit tot afwijkingen geleid zou kunnen hebben in een aantal kwantitatieve conclusies, zullen alle overheersende fysische verschijnselen in het experiment opgetreden zijn.

De prestatie van voortstuwingssystemen met aan de tip geïnstalleerde propellers wordt sterk beïnvloed door de interactie tussen de propeller en de tipwervel van zijn ophanging, zowel voor trek- als duwconfiguraties. Uitvoerige metingen gericht op de trekconfiguratie toonden aan dat aan de vleugeltip geïnstalleerde propellers de geïnduceerde weerstand van de vleugel verminderen doordat de tipwervel verzwakt wordt door de draaiing in de slipstroom van de propeller. In een direct vergelijk met een conventionele propeller–vleugel configuratie vertoonde de aan de vleugeltip geïnstalleerde pro-

peller een weerstandsvermindering van ongeveer 15% bij een voortstuwingscoëfficiënt van 0.12 en een liftcoëfficiënt van de vleugel van 0.5. Dit aerodynamische voordeel nam toe met toenames van de voortstuwingscoëfficiënt van de propeller en de liftcoëfficiënt van de vleugel. Voor propellers in duwconfiguratie veranderen de snelheidscomponenten in de omtrekrichting, geïnduceerd door de tipwervel, de effectieve voortgangscoëfficiënt van de propeller. Initiële metingen met een pylonmodel onder invalshoek toonden aan dat dit de propellerprestaties verbetert indien de draairichting van de propeller tegenovergesteld is aan die van de tipwervel.

De tipwervelinteractie leidt tot een asymmetrische aerodynamische belasting voor vliegtuigen met co-roterende propellers in trekconfiguratie. In zulke gevallen kunnen 'swirl-recovery vanes' (SRV's) toegepast worden om de draaiing in de slipstroom te verminderen voordat deze een interactie kan aangaan met de vleugel. Op deze wijze kan de mogelijke verstoring van de prestaties voorkomen worden. Metingen met een geïsoleerde propeller–SRV combinatie bevestigden het potentieel van SRV's om de draaiing in de propellerslipstroom te verminderen. Echter, de voortstuwingsprestaties van deze SRV's werden beperkt door overtrek op hun binnenste gedeelte. Een initiële studie met een aan de tip van een pylon geïnstalleerde propeller in trekconfiguratie bevestigde het potentieel van SRV's om het verschil in aerodynamische belasting tussen de gevallen met 'inboard-up' en 'outboard-up' rotatie van de propeller te verkleinen en derhalve de asymmetrie in krachten in het geval van een vliegtuig met co-roterende propellers te verminderen. Naast de effecten op de tijdgemiddelde prestaties introduceren de tijdafhankelijke interacties tussen de propeller en de SRV's geluidsbronnen ten gevolge van de tijdafhankelijke belasting op de propellerbladen en de SRV's. De resulterende toename in tonaal geluid manifesteerde zich voornamelijk als een significante versterking van de niveaus van de hogere harmonischen. Dit beïnvloedde de geluidsemissies vooral bij een lage stuwkrachtinstelling van de propeller, waarvoor een geluidstoename van tot 7 dB gemeten werd. Bij hogere stuwkrachtinstellingen van de propeller was de toename in tonaal geluid kleiner met $3-5$ dB.

Voor propellers geïnstalleerd in een trekconfiguratie ontstaat een harmonische belasting op stroomafwaarts gelegen aerodynamische oppervlakten door de tijdafhankelijke interactie met de slipstroom van de propeller. Dit kan leiden tot vibraties, welke worden doorgevoerd naar de romp en als structuurgedragen geluid kunnen worden ervaren in de cabine. De metingen hebben bevestigd dat de drukfluctuaties op in de slipstroom gelegen oppervlakten overheerst worden door de tipwervels van de propellerbladen, die zorgen voor een periodieke drukrespons met sterke harmonischen. De amplitude van de drukfluctuaties neemt toe met toenemende stuwkrachtinstelling, terwijl de tijdafhankelijke liftcoëfficiënt een niet-monotoon verband vertoont met de stuwkrachtinstelling van de propeller. De kleinste tijdafhankelijke integrale belastingen werden gemeten in gevallen waarvoor de verhouding tussen de koordelengte en de golflengte van de verstoring door de tipwervels van de propeller gelijk was aan een geheel getal. Dit houdt in dat verminderingen van structuurgedragen geluid behaald zouden kunnen worden door het afstemmen van de stroomafwaarts gelegen koordelengte op een geheel veelvoud van de afstand in stromingsrichting tussen de tipwervels van de propeller.

Een alternatieve passieve manier om de tijdafhankelijke belasting te verminderen is door de vleugel of pylon uit te rusten met een voorrand die de stroming deels doorlaat.

Experimenten werden uitgevoerd om de voordelen van een dergelijke aanpak te kwantificeren ten opzichte van een niet-doorlaatbare referentieconfiguratie. De geometrie van de permeabele voorranden was niet geoptimaliseerd; in plaats daarvan waren de ontwerpen gebaseerd op eerder werk beschreven in de literatuur. Metingen met 'particle-image velocimetry' toonden aan dat de stroming door de permeabele voorrand de dikte van de grenslaag op de zuigzijde van de pylon vergrootte. Dit resulteerde in een hogere weerstand door viskeuze dissipatie en een lagere draagkracht bij invalshoeken groter dan 6 graden. De toegenomen grenslaagdikte en de stroming door de holte vergrootten de viskeuze interactie met de tipwervelkernen, waardoor de snelheidsfluctuaties in de nabijheid van het oppervlakte van de pylon afnamen met maximaal 35%. Dientengevolge werden lagere tonale geluidsemissies gemeten in het verre veld, hetgeen suggereert dat de toepassing van de permeabele voorrand de gewenste afname in drukfluctuaties op het oppervlakte opleverde.

Propellers in duwconfiguratie ondervinden een dominante interactie tussen de bladen en het zog van de stroomopwaarts gelegen vleugel of pylon, hetgeen resulteert in een niet-uniforme instroming naar de propeller. Een analyse van de pylon-geïnstalleerde configuratie toonde aan dat de zog-interactie tot een periodieke impulsieve belasting leidt, als gevolg waarvan een tonale geluidstoename van maximaal 24 dB gemeten werd. De geluidstoename was het sterkst in stroomopwaartse richting en werd in toenemende mate relevant met afnemende stuwkrachtinstelling van de propeller door de bijbehorende afname van de tijdgemiddelde bladbelasting. In tegenstelling hiertoe werden de geïntegreerde propellerprestaties niet significant veranderd door de zog-interactie.

Een aanblaassysteem in de pylon biedt een actieve controletechniek om de geluidstoename door de zog-interactie te minimaliseren. Metingen met 'particle-image velocimetry' tussen een pylon en een propeller toonden de effectiviteit aan van een in de achterrand geïntegreerd aanblaassysteem voor het verminderen van het impulsverlies in het zog van de pylon. De toepassing van het aanblaassysteem verminderde de effecten van de installatie van de pylon derhalve aan de bron. Bij een gematigde stuwkrachtinstelling van de propeller werd het kwadratisch gemiddelde van de bladbelastingfluctuaties ten gevolge van de zog-interactie verminderd met maximaal 60%, hetgeen resulteerde in geluidsemissies die ongeveer gelijk waren aan die van de geïsoleerde propeller. Bij een lagere stuwkrachtinstelling daarentegen restte een geluidstoename door het snelheidsdefect dat overbleef aan beide kanten van de geblazen straal. Dit kan opgelost worden door een aanblaassysteem te gebruiken met de uitstroomopeningen geïntegreerd langs de koorde van het profiel. Dit zal tot een hogere uniformiteit van het zog leiden dan met het in de achterrand geïntegreerde aanblaassysteem, terwijl het ook de mogelijkheid biedt om het zog effectief te vullen onder invalshoek.

De resultaten besproken in dit proefschrift benadrukken de gevoeligheid van de aerodynamische en aero-akoestische prestaties van aan de tip geïnstalleerde propellervoortstuwingssystemen voor interacties tussen de propeller en de rest van het vliegtuig. Significante integratievoordelen kunnen behaald worden door de gunstige interacties uit te buiten via een integraal ontwerpproces, terwijl zowel actieve als passieve technieken beschikbaar zijn om de invloed van nadelige interacties te beperken. De kennis vergaard tijdens het onderzoek besproken in dit proefschrift kan benut worden voor het ontwerp van toekomstige zeer efficiënte vliegtuigen.

CONTENTS

NOMENCLATURE

VARIABLES

a	=	speed of sound, m/s
A	=	integral wake velocity deficit (Eq. A.3)
A_{out}	=	outflow area of pylon blowing system, m^2
AR	=	b^2/S, aspect ratio
b	=	$2s$, span, m
b_{insert}	=	pylon span affected by flow-permeable insert, m
b_{w}	=	wake semiwidth, m
B	=	propeller blade count
BPF	=	nB, blade-passage frequency, Hz
c	=	chord length, m
c_d	=	$d/q_\infty c$, section drag coefficient
$c_{d_{\text{p}}}$	=	$d_{\text{p}}/q_\infty c$, section pressure-drag coefficient
c_l	=	$l/q_\infty c$, section lift coefficient
$c_{\dot{m}}$	=	$\dot{m}/(\rho_\infty V_\infty A_{\text{out}})$, blowing coefficient (Chapter 11)
c_n	=	$n/q_{\text{eff}} c$, section normal-force coefficient
$\overline{c_n}$	=	time-averaged section normal-force coefficient
c'_n	=	unsteady section normal-force coefficient
$c'_{n_{\text{SRV}}}$	=	unsteady SRV section normal-force coefficient
$c_{n_{\text{wake}}}$	=	section normal-force coefficient at maximum impact of wake encounter
c_q	=	$q/q_\infty c$, section torque coefficient
c_t	=	$t/q_\infty c$, section thrust coefficient
$c_{t_{\text{SRV}}}$	=	$t_{\text{SRV}}/\rho_\infty n^2 D^3$, sectional SRV thrust coefficient
C_D	=	$D/q_\infty S$, drag coefficient
$C_{D_{\text{min}}}$	=	minimum drag coefficient
C_L	=	$L/q_\infty S$, lift coefficient
C'_L	=	unsteady lift coefficient
$C_{L_{C_{D_{\text{min}}}}}$	=	lift coefficient at minimum drag coefficient
$C'_{L_{\text{rms}}}$	=	rms of unsteady lift coefficient (Eq. 7.2)
C_{L_α}	=	lift-curve slope, 1/deg
C_p	=	$(p - p_\infty)/q_\infty$, static-pressure coefficient
C'_p	=	p'/q_∞, unsteady pressure coefficient
$\tilde{C}'_p$	=	Fourier coefficients of unsteady pressure coefficient
$C'_{p_{\text{adv}}}$	=	unsteady pressure coefficient on advancing side of the pylon
$C'_{p_{\text{retr}}}$	=	unsteady pressure coefficient on retreating side of the pylon
$C'_{p_{\text{rms}}}$	=	rms of unsteady pressure coefficient

$\overline{C'_{p_{\mathrm{rms}}}}$	=	spatial average of rms of unsteady pressure coefficient (Eq. 7.1)
$C_{p_{\mathrm{t}}}$	=	$(p_{\mathrm{t}} - p_\infty)/q_\infty$, total-pressure coefficient
C_P	=	$P/\rho_\infty n^3 D^5$, propeller power coefficient
C_Q	=	$Q/\rho_\infty n^2 D^5$, propeller torque coefficient
C_T	=	$T/\rho_\infty n^2 D^4$, propeller thrust coefficient
$C_{T_{\mathrm{SRV}}}$	=	$T_{\mathrm{SRV}}/\rho_\infty n^2 D^4$, SRV thrust coefficient
C_μ	=	$2h_{\mathrm{slot}} V_{\mathrm{j}}^2/cV_\infty^2$, blowing coefficient (Appendix A)
C_μ^*	=	optimal blowing coefficient (Appendix A)
d	=	drag force per unit span, N/m
d_{p}	=	pressure-drag force per unit span, N/m
$\mathrm{d}A$	=	infinitesimal area element, m^2
$\mathrm{d}\Gamma$	=	shed circulation due to spanwise lift gradient, m^2/s
D	=	drag force, N
	=	propeller diameter, m
D_{a}	=	effective diameter of microphone array, m
D_{hole}	=	hole diameter in flow-permeable surface, m
e	=	span-efficiency parameter
f	=	frequency, Hz
F_{SRV}	=	resultant force on SRV, N
h_{slot}	=	slot height, m
J	=	V_∞/nD, propeller advance ratio
k	=	wave number
l	=	lift force per unit span, N/m
L	=	lift force, N
$\dot{m}$	=	mass flow, kg/s
M	=	V/a, Mach number
n	=	normal force per unit span, N/m
	=	propeller rotational speed, Hz
n_{BPF}	=	number of tones used to compute cumulative tonal noise level
p	=	acoustic pressure, Pa
	=	static pressure, Pa
∇p	=	pressure gradient, Pa/m
p'	=	unsteady pressure, Pa
p_{atm}	=	atmospheric pressure, Pa
$p_{i\cdot BPF}$	=	acoustic pressure of tone at i times the blade-passage frequency, Pa
p_{t}	=	$p + q$, total pressure, Pa
P	=	propeller power, W
q	=	$\rho V^2/2$, dynamic pressure, Pa
	=	torque contribution per unit span, N/m
Q	=	propeller torque, Nm
r	=	radial coordinate, m
r_{mic}	=	distance from propeller center to microphone, m
R	=	propeller radius, m
R_{hub}	=	hub radius, m
R_{nac}	=	nacelle radius, m

R_{SRV}	=	SRV radius, m
Re_c	=	Vc/ν, Reynolds number based on chord length
Re_D	=	$V_\infty D/\nu$, Reynolds number based on propeller diameter
s	=	wing semispan, m
S	=	Sears function (Eq. 2.7)
	=	wing reference area, m^2
SO	=	f/n, shaft order
SPL	=	sound-pressure level, dB
t	=	thrust contribution per unit span, N/m
	=	time, s
t_{cavity}	=	cavity depth underneath flow-permeable surface, m
t_{SRV}	=	sectional SRV thrust, N/m
T	=	thrust, N
T_{SRV}	=	SRV thrust, N
V	=	velocity, m/s
$\lvert\mathbf{V}\rvert$	=	velocity magnitude, m/s
V_{a}	=	axial velocity, m/s
V_{disk}	=	effective velocity at propeller disk (from actuator-disk theory), m/s
V_{j}	=	jet velocity, m/s
V_{n}	=	normal velocity, m/s
V_{t}	=	tangential velocity, m/s
w_k	=	Fourier component of periodic upwash velocity, m/s
W	=	W-criterion (Eq. A.2)
W^*	=	W-criterion at best available blowing parameters
x	=	chordwise coordinate, m
X, Y, Z	=	streamwise, spanwise, vertical coordinate, m
X_{slot}	=	chordwise location of blowing slot, m
X^*_{slot}	=	best available chordwise location of blowing slot, m
y^+	=	normal spacing at first cell adjacent to airfoil surface
Y_{n}	=	wall-normal coordinate, m
Z_{max}	=	spanwise coordinate of upper integration limit in Eqs. 7.1 and 7.2, m
Z_{min}	=	spanwise coordinate of lower integration limit in Eqs. 7.1 and 7.2, m
α	=	angle of attack, deg
β	=	angle of sideslip, deg
	=	blade pitch angle, deg
Γ	=	circulation strength, m^2/s
δ	=	boundary-layer thickness, m
δ_{f}	=	flap deflection angle, deg
Δc_{l_k}	=	$2\pi w_k S/V_{\text{eff}}$, Fourier component of unsteady lift coefficient
ΔC_D	=	$(C_{D_{\text{P}xx\text{C}y}} - C_{D_{\text{s}}})/C_{D_{\text{s}}}$, relative drag increase due to application of flow-permeable insert PxxCy
$\Delta C_{D_{\text{t}}}$	=	$C_{D_{\text{t}}} - C_{D_{\text{c}}}$, difference in drag coefficient due to tip-mounted configuration
$\Delta C'_p$	=	difference between unsteady pressure coefficients on retreating and advancing sides of the pylon

ΔC_{p_t}	=	$C_{p_t}^{\text{P-on}} - C_{p_t}^{\text{P-off}}$, rise in total-pressure coefficient due to propeller
$\overline{\Delta C_{p_t}}$	=	circumferentially averaged rise in total-pressure coefficient due to propeller
$\Delta \dot{E}_{k_{rot}}$	=	change in rotational kinetic energy flow due to the propulsion system, J/s (Eq. 9.1)
$\Delta \dot{E}_{k_{tot}}$	=	change in total kinetic energy flow due to the propulsion system, J/s (Eq. 9.2)
ΔJ_α	=	change in effective advance ratio due to interaction with pylon tip vortex
ΔR	=	microphone-array resolution, m (Eq. 4.2)
ΔSPL	=	$SPL_s - SPL_{\text{P}xx\text{C}y}$, reduction in sound pressure level due to application of flow-permeable insert PxxCy, dB
ΔT	=	propeller thrust modification, N
ΔV	=	change in velocity with respect to baseline, m/s
$\lvert\Delta\mathbf{V}\rvert$	=	magnitude of propeller-induced velocity, m/s
$\Delta\lvert\mathbf{V}\rvert$	=	$\lvert\mathbf{V}\rvert_{\text{P}xx\text{C}y} - \lvert\mathbf{V}\rvert_s$, change in velocity magnitude due to flow-permeable insert PxxCy, m/s
ΔV_a	=	induced axial velocity, m/s
ΔV_t	=	induced tangential velocity, m/s
ΔX_p	=	distance from propeller plane to wing/pylon leading edge, m
ΔX_{pyl}	=	distance from pylon trailing edge, m
$\Delta\alpha$	=	angle-of-attack perturbation, deg
$\Delta\eta$	=	$\eta_{\text{SRVs-on}} - \eta_{\text{SRVs-off}}$, change in propulsive efficiency due to SRVs
ε_V	=	uncertainty velocity component from PIV, m/s
η	=	JC_T/C_P, propeller efficiency
η_p	=	$2/(2+\Delta V/V_\infty)$, propulsive efficiency
$\eta_{\text{SRVs-off}}$	=	propulsive efficiency without swirl-recovery vanes installed
$\eta_{\text{SRVs-on}}$	=	propulsive efficiency with swirl-recovery vanes installed
θ	=	advance angle of blade section, deg
	=	axial (geometric) directivity angle, deg
	=	$\tan^{-1}(V_t/V_a)$, swirl angle, deg
θ_e	=	axial emission angle, deg
λ	=	wavelength, m
ν	=	kinematic viscosity, m^2/s
ρ	=	air density, kg/m^3
σ	=	$k\pi nc/V_{\text{eff}}$, reduced frequency
σ_p	=	porosity factor
$\sigma_{SPL}^{i\cdot BPF}$	=	standard deviation of measured sound-pressure levels at i times the blade-passage frequency, dB
ΣSPL	=	cumulative tonal noise level, dB (Eq. 9.3)
ϕ	=	blade angular position, deg
	=	circumferential directivity angle, deg
ϕ'	=	blade angular position at approximate time of impingement of tip vortex on pylon leading edge, deg
ϕ_{SRV}	=	circumferential position of SRV, deg

ϕ_{vortex}	=	vortex swirl angle, deg
ω_{t}	=	vorticity in tangential direction, 1/s
ω_Z	=	Z-component of vorticity, 1/s
ω_Z^*	=	$\omega_Z D/V_{\text{disk}}$, Z-component of normalized vorticity
Ω	=	propeller rotational speed, rad/s

SUB- AND SUPERSCRIPTS

∞	=	freestream
$0.7R$	=	related to radial station at $r/R = 0.7$
b	=	blade
	=	bound
c	=	conventional configuration
e	=	at wake edge
eff	=	based on effective velocity in rotational frame
insert	=	related to leading-edge insert
IU	=	inboard-up propeller-rotation case
l	=	lower surface
LE	=	leading edge
max	=	maximum
no wake	=	outside of wake
OU	=	outboard-up propeller-rotation case
p	=	porosity
pres	=	pressure side
prop	=	propeller
pyl	=	pylon
P-off	=	propeller-off
P-on	=	propeller-on
Pylon-off	=	pylon-off
Pylon-on	=	pylon-on
PxxCy	=	related to flow-permeable insert PxxCy
$r/R \approx 0.65$	=	related to radial station at $r/R \approx 0.65$
s	=	related to solid pylon (*PROWIM-US* setup)
	=	sleeve (*PROWIM-US* setup)
	=	symmetric configuration (*PROWIM-T* setup)
suc	=	suction side
t	=	tip-mounted configuration
tip	=	at the tip of the propeller blade
u	=	upper surface
w	=	wake
wake	=	inside of wake
X	=	in axial direction

I

BACKGROUND

1

INTRODUCTION

WHEN Orville Wright took off in 1903, he relied on propellers to generate the thrust required for the first ever successful powered, heavier-than-air, controlled flight. In the decades following this historic moment, all powered aircraft were equipped with propeller propulsion systems. The propellers were driven by piston engines, which limited the airplane performance in terms of service ceiling and flight velocity. It was only at the end of World War II that a radically new aircraft propulsion system was introduced to overcome these drawbacks: the jet engine. Providing the opportunity to reach higher flight velocities than with propellers, the jet engine has been the propulsion type of choice for most passenger aircraft ever since. This is reflected in modern airliners, which are predominantly equipped with turbofan engines.

Following the introduction of the jet engine, the development of propellers slowed down for several decades, until NASA resumed propeller research activities in the 1970s. Driven by the 1973 oil crisis and the resulting imminent need for more fuel-efficient aircraft, the Advanced Turboprop Project (ATP) [1] was started to explore the potential benefits of advanced propellers for passenger-transport aircraft. The very high effective bypass ratio of propellers promised a significant propulsive-efficiency gain compared to turbofan engines. This can be understood from the combination of Eqs. 1.1 and 1.2, which describe the system thrust T (ignoring the potential contribution due to pressure) and propulsive efficiency η_p as a function of mass flow $\dot{m}$ and velocity increment ΔV:

$$T = \dot{m}\Delta V, \tag{1.1}$$

$$\eta_\mathrm{p} = \frac{2}{2 + \Delta V / V_\infty}. \tag{1.2}$$

By increasing the bypass ratio, the mass flow can be increased, and thus the same thrust can be obtained with a smaller velocity increment (Eq. 1.1). This directly leads to a higher propulsive efficiency (Eq. 1.2), an inherent benefit of propeller propulsion systems.

The advanced-propeller concept proposed by NASA and partners, named *propfan*, was unveiled in 1975 [2], one year before the official start of ATP. Extensive research

was then performed on the aerodynamics and aeroacoustics of both single-rotating and contra-rotating propeller designs, ultimately leading to full-scale flight tests with contra-rotating open rotors (CRORs) on McDonnell Douglas and Boeing aircraft (Fig. 1.1) [3]. However, despite promising test results [4], the decrease in fuel prices toward the end of the 1980s reduced the commercial appeal of the propfan, and the ATP was terminated in 1987 [5]. In parallel with the activities by NASA, propeller-related research had started in Europe at Airbus in the early 1980s [6]. This continued throughout the 1990s, with as most notable activities the EU-funded research projects SNAAP, GEMINI, GEMINI II, and APIAN, focusing especially on propeller–airframe interactions for wing-mounted propeller configurations.

Figure 1.1: Boeing 727 testbed equipped with contra-rotating open rotor (GE-36 unducted fan) developed during NASA's Advanced Turboprop Project.*

Concerns about the growing impact of air travel on global warming and an increasing pressure on airlines' profit margins have once more revived interest in propeller technology since the mid-2000s. Efficient propulsion systems are required to achieve a step change in the performance of future aircraft designs, which will have to address both of the above concerns. Advanced propellers provide a potential solution to this challenge by offering a higher propulsive efficiency than turbofan engines, as discussed before. However, the use of propellers also has several disadvantages. Historically, the two main drawbacks have been the limitation of the aircraft's cruise speed and the relatively high noise emissions, while additional challenges arise due to aspects like ground clearance, certification issues related to blade failure, and the need for a complex and heavy blade pitch-control system [2, 6, 7].

Improved blade designs and manufacturing processes have lifted the constraint on the maximum attainable flight velocity with propellers, which used to be a significant drawback for applications on larger transport aircraft [2]. An example of an aircraft featuring the resulting advanced, highly swept blades is the Airbus A400M (Fig. 1.2), a military airlifter capable of reaching a cruise Mach number of 0.72. By allowing higher disk

*© Boeing, licensed use

loadings with minimal swirl losses, contra-rotating propeller systems can be used to further increase attainable flight speeds to Mach numbers around 0.8 [8]. However, this benefit comes at the cost of adverse aerodynamic and aeroacoustic interaction effects and increased complexity.

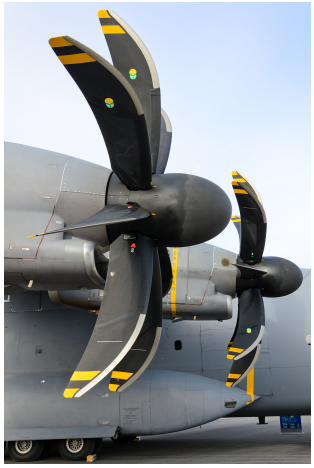

Figure 1.2: Advanced propellers installed on the Airbus A400M.

The noise problem of isolated propellers has been addressed by extensive research studies in the United States [3, 8, 9] and Europe [10, 11], especially focusing on CRORs. Improved computer hardware and simulation techniques have enabled simultaneous consideration of aerodynamic and aeroacoustic performance during the blade design process [10]. As a result, the CROR's high propulsive efficiency can nowadays be achieved while maintaining margins to noise certification standards [8, 9]. This was confirmed by analyses at airplane design level [12, 13]. When compared to an equivalent-technology-level geared turbofan, estimated fuel-burn reductions of approximately $10-20\%$ were computed, with sufficient noise margin relative to current certification standards.

The main challenge that remains to be overcome for propellers to make a widespread comeback on passenger aircraft is the optimal integration of the propellers with the airframe [3]. Propeller–airframe interactions modify the aircraft performance and noise emissions, which so far has not been sufficiently taken into account in the design process. For tractor propellers, aerodynamic surfaces immersed in the propeller slipstream experience unsteady loading, which may lead to vibrations and associated cabin noise. For pusher propellers, the inflow to the propeller is perturbed by the wake of the upstream support, leading to unsteady blade loads and increased noise emissions. Following previous work on semi-installed configurations (e.g. Refs. [14–17]), recent experiments have considered the aerodynamic and aeroacoustic performance of both pusher and tractor propellers on model-scale aircraft [18, 19]. Although such experiments have provided increased insight into the impact of airframe-installation effects on propeller performance and noise emissions, detailed investigations of the physical mechanisms behind several of the interaction phenomena are still missing.

1

Previous studies have identified tip-mounted propellers as a potential way to minimize the airframe-integration problems. Two types of aft-mounted propeller configurations have been proposed, with the propellers installed at the tip of either dedicated support pylons or the horizontal tailplane [6, 20, 21]. The advantages of such layouts are the 'clean' wing, potentially increased ground clearance, and reduced cabin-noise levels due to the larger distance from the propellers to the passenger seats compared to conventional wing-mounted propeller configurations. Despite several successful test flights with concepts featuring pylon-mounted propellers (Figs. 1.1 and 1.3), until now such aircraft configurations have not been commercialized. At present, research on the tailplane-mounted layout is ongoing through the EU-funded Clean Sky 2 Regional Aircraft Innovative Aircraft Demonstrator Platform, again focusing on the aerodynamic and aeroacoustic integration challenges.

a) NAL Saras PT1N[†] b) Cessna ATPTB[‡] c) Embraer CBA-123 Vector[§]

Figure 1.3: Examples of experimental aircraft with pylon-mounted propellers.

Recent interest in hybrid-electric [22] and fully-electric [23] propulsion has made propeller–airframe integration even more relevant because of the close coupling between multiple propellers and the airframe typical of aircraft featuring these propulsion technologies. The use of electric motors increases design flexibility by practically eliminating potential penalties of downscaling the motors [23]. This enables novel configurations involving for example distributed propellers, for which successful propulsion–airframe integration is crucial.

The increased design freedom offered by electrification of the propulsion system also allows to revisit an abandoned concept: the wingtip-mounted propeller. For such a configuration, the system efficiency can be enhanced significantly due to a favorable interaction between the propeller slipstream and the wingtip vortex [24–26]. This was already known in the 1940s, when the Vought V-173 (Fig. 1.4a) and subsequently Vought XF5U were developed and flight tested as part of a U.S. Navy fighter aircraft program started during World War II. However, development was canceled in 1947 because of the introduction of the jet engine. Ever since, the use of wingtip-mounted propellers has been prevented by aeroelastic problems, high wing mass imposed by inertia loads, and insufficient control power to overcome a one-engine-inoperative condition. The wingtip-mounted propeller configuration also occurs for tiltrotor aircraft in cruise mode [27]. However, the relatively low disk loadings typical of such vehicles combined with the complicated, multi-objective rotor design reduces the potential aerodynamic benefits.

[†]Credits: National Aerospace Laboratories (NAL)
[‡]Credits: http://cessnateur.blogspot.com/
[§]© Bill Blanchard, used with permission

The emergence of electric propulsion makes the wingtip-mounted propeller a feasible design option for future aircraft. By downscaling the motors and propellers, the major drawbacks of the wingtip-mounted configuration can be overcome. The NASA X-57 Maxwell [28, 29] (Fig. 1.4b), currently under development, is a prime example of a modern vehicle with wingtip-mounted propellers. In order to maximize the performance benefits offered by wingtip-mounted propellers, the aerodynamic and aeroacoustic interactions between the propellers and the airframe need to be understood in detail.

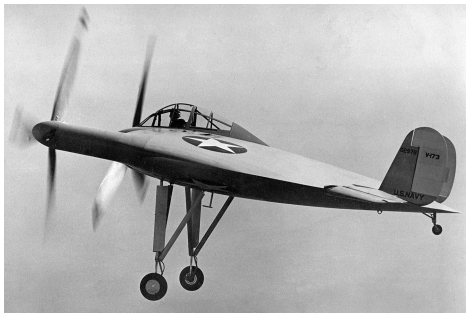

a) Vought V-173.[¶]

b) Artist impression of NASA's X57 Maxwell.[‖]

Figure 1.4: Examples of experimental aircraft with wingtip-mounted propellers.

1.1. THESIS OBJECTIVE

Existing research on propeller–airframe interactions has mostly considered the conventional layout with the propellers installed on the inboard part of the wing, while the interactions specific to the tip-mounted configuration have not received sufficient attention. A detailed understanding of the relevant interaction effects is crucial to identify performance-enhancement strategies, which could be applied to maximize the installed performance of tip-mounted propellers. In addition, comprehensive experimental data are needed to validate both low-order and high-order computational tools, which are necessary for future design and analysis of tip-mounted propellers. The objective of this thesis is to supply this crucial missing information, as summarized in the central research question:

> *What are the key aerodynamic and aeroacoustic interaction effects for tip-mounted propeller configurations, and how can the performance of such configurations be enhanced?*

To answer the first part of this research question, in-depth investigations are presented to explain and quantify three dominant interaction effects, focusing on the following subquestions:

1. What is the physical mechanism driving the efficiency increase observed for wingtip-mounted propellers in tractor configuration, and how does it relate to the propeller and wing operating conditions?

[¶]Credits: U.S. Navy

[‖]Credits: NASA Graphic / NASA Langley / Advanced Concepts Lab, AMA, Inc.

2. What is the physical mechanism driving the unsteady loading on a surface immersed in the slipstream of a tractor propeller, and how does it relate to the propeller operating conditions and the spacing between propeller and downstream surface?

3. What is the physical mechanism driving the noise penalty for propellers in pusher configuration, and how does it relate to the propeller operating conditions?

Having discussed the physical mechanisms behind the interaction effects, the potential of three performance-enhancement strategies is discussed based on the following subquestions:

4. To what extent can swirl-recovery vanes increase the efficiency of an isolated propeller without prohibitive noise penalty, and can these vanes be used to eliminate the asymmetry in aerodynamic loading for a vehicle configuration with corotating propellers in tractor configuration?

5. To what extent can a flow-permeable leading edge alleviate the unsteady loading caused by slipstream impingement for propellers in tractor configuration, and what is the associated impact on the lift and drag performance?

6. To what extent can pylon trailing-edge blowing alleviate the noise penalty due to the wake encounter for propellers in pusher configuration?

1.2. THESIS APPROACH

In order to answer the questions defined in Section 1.1, experiments were performed using typical wingtip-mounted and pylon-mounted propeller configurations. The results also apply to horizontal-tailplane-mounted propellers, although in that case additional effects may occur due to interactions with control surfaces; these are not considered in this thesis.

Three key interaction effects were studied:

1. Wingtip-vortex attenuation and swirl recovery
2. Propeller-slipstream impingement (on a pylon)
3. Pylon-wake encounter (by a propeller)

For each of these interaction effects, a suitable performance-enhancement strategy was investigated through the application of:

1. Swirl-recovery vanes
2. Flow-permeability at the pylon leading edge
3. Pylon trailing-edge blowing

Throughout the thesis, both the tractor-propeller and pusher-propeller configurations are considered. No attempt was made to directly compare the two, since such a comparison would only be fair if an optimized setup were devised for both configurations. This was outside of the scope of work; instead, the tractor and pusher configurations were studied separately. The resulting insight into the interaction effects and performance-enhancement strategies relevant to both configurations can be used by others to make an informed decision on the use of either configuration.

An experimental approach was taken for two reasons. First, it allows for rapid parameter sweeps, making it possible to study the sensitivity of the interaction effects to several key variables. If a numerical approach had been selected, such sensitivity analyses would have been prohibited by the large computational cost of simulating the inherently unsteady interaction phenomena investigated in this thesis. Second, insufficient reference data were available in the literature to properly validate a fully computational effort without performing in-house experiments. Therefore, the decision was made to focus on these experiments instead. The resulting data sets can be used to validate future high-order and low-order numerical methods, which are useful for obtaining additional insight into physical phenomena and for performing design studies.

1.3. THESIS LIMITATIONS

Because the experiments were performed at model scale in low-speed unpressurized wind tunnels, the Mach and Reynolds numbers were relatively low when compared to those representative of typical cruise flight conditions of propeller aircraft. As a result, the data will have been affected by for example laminar-flow effects (partly mitigated by applying trip strips), relatively large boundary-layer thicknesses, and an absence of compressibility effects. Since several of the key propeller–airframe interactions are a direct result of viscous effects (interaction of a wingtip vortex with a propeller slipstream, impingement of blade wakes and tip vortices on a downstream surface, encounter of a pylon wake by a downstream propeller), the low Reynolds number may have led to offsets in a quantitative sense. However, in most cases the change in propeller or airframe response due to the interactions can be considered primarily as a potential-flow effect, induced by the changes in velocity and pressure in the vortical regions which cause the interaction effects. Therefore, the dominant physical phenomena caused by the interactions will be present also at the lower Reynolds numbers typical of the experiments. Moreover, for the viscous interactions the low Reynolds number condition is somewhat mitigated by the low Mach number, since the ratio of pressure and viscous forces scales with Re/M^2.

For typical propeller aircraft, significant compressibility effects are mostly confined to the propeller blade-tip region and surfaces washed by the propeller slipstream. In such regions, supersonic conditions may exist, leading to the formation of shock waves and associated aerodynamic and aeroacoustic effects. Since the experiments discussed in this thesis were performed at low Mach numbers only ($M_\infty < 0.2$, $M_{\text{tip}} < 0.6$), these effects could not be simulated. Therefore, in terms of compressibility effects, the analyses are mostly representative of the takeoff and approach phases of the flight, for which the freestream Mach number is relatively low.

To focus the research scope and align the project with available experimental apparatus, only single-rotating propellers were considered. Considering the interest in contra-rotating systems for high-speed propeller applications, this limitation might seem to reduce the applicability of the work performed. However, the physical background of the propeller–airframe interactions is comparable for single-rotating and contra-rotating propellers. Increased understanding of the effects for single-rotating propellers can thus also be applied in the analysis and design of contra-rotating propellers.

1

1.4. THESIS OUTLINE

This thesis consist of six parts, as illustrated in Fig. 1.5. In **Part I**, the background of the problem is discussed. Following the present introduction, **Chapter 2** summarizes the most relevant aerodynamic and aeroacoustic propeller–wing interaction effects, with a special focus on tip-mounted configurations. The discussion will be based on existing studies published in the literature, and will confirm the knowledge gaps identified above.

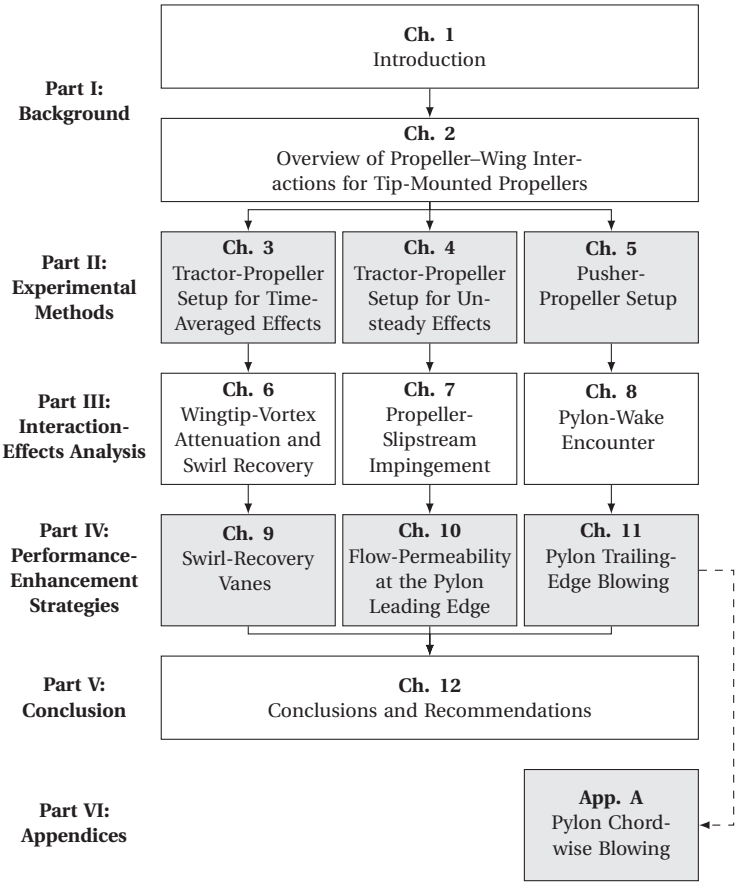

Figure 1.5: Thesis outline.

Part II then describes the experimental methods applied to obtain the results discussed in the thesis. The setup used to study the time-averaged interaction effects for tractor propellers is introduced in **Chapter 3**, followed by a description of the setup used to measure the unsteady interaction effects for tractor propellers in **Chapter 4**. Subsequently, the pusher-propeller setup is treated in **Chapter 5**. Along with a description of the models, the wind-tunnel facilities and measurement techniques used with each of the setups are also detailed.

Having defined the methods, **Part III** analyzes three key interaction effects for tip-mounted propellers. **Chapter 6** treats the beneficial tip-vortex-attenuation and swirl-recovery mechanisms for the tractor-propeller configuration, while the unsteady effects of propeller-slipstream impingement are discussed in **Chapter 7**. Subsequently, **Chapter 8** describes the wake-encounter phenomena characteristic of pusher propellers.

For each of the interaction effects studied in Part III, a promising performance-enhancement strategy is considered in **Part IV**. **Chapter 9** investigates the aerodynamic benefits and aeroacoustic penalties of swirl-recovery vanes. Subsequently, **Chapter 10** treats the impact of a pylon with flow-permeable leading edge on the unsteady loading caused by propeller-slipstream impingement. Thereafter, the potential of pylon trailing-edge blowing to alleviate wake-encounter phenomena is assessed in **Chapter 11**.

Following the detailed discussions of the results, **Part V** presents the conclusions of the work in **Chapter 12**. Apart from the main observations drawn from the analysis of the interaction effects and potential performance-enhancement strategies, also recommendations for future work are given.

Finally, **Part VI** contains the appendices, of which the numerical investigation of pylon chordwise blowing provided in **Appendix A** is the most notable.

2

OVERVIEW OF PROPELLER–WING INTERACTIONS FOR TIP-MOUNTED PROPELLERS

Propeller–wing interactions have been a popular topic of research for almost a century now. This chapter provides background on the aerodynamic and aeroacoustic interaction effects for installed propellers, with a focus on tip-mounted configurations. First, Section 2.1 discusses the propulsive and acoustic performance of the isolated propeller. Then, typical propeller–wing interaction effects are treated in Section 2.2, including consideration of the pylon-mounted configuration. Finally, Section 2.3 discusses potential strategies to enhance the performance of installed tip-mounted propellers, either by exploiting the beneficial interactions between the propeller and wing or pylon, or by mitigating the adverse interaction effects that also occur. The chapter's analyses are based on the literature, and serve as starting point for the in-depth investigations of the key interaction effects and potential performance-enhancement strategies presented in Parts III and IV of this thesis.

2.1. ISOLATED PROPELLER PERFORMANCE

Before elaborating on the key propeller–wing interactions for tip-mounted propellers, first the characteristics of the isolated propeller are discussed. Extensive literature is available on both the propulsive [30] and acoustic [31] performance of the isolated propeller. Below, only a brief overview is provided of both topics.

2.1.1. PROPULSIVE PERFORMANCE

The propeller should provide the thrust required to fly the aircraft, ideally at the lowest possible input power, i.e. the lowest torque. Both thrust and torque are a result of the lift and drag forces acting on the blades. These forces are generated because of the angle of attack experienced by the blade sections, caused by the velocity components due to translation (V_a), rotation (V_t), and induced effects (ΔV_a, ΔV_t), as illustrated in Fig. 2.1.

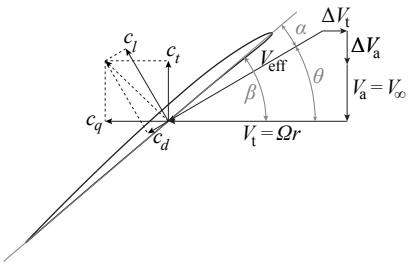

Figure 2.1: Velocity diagram and resulting force components of a propeller blade section at radial position r.

PERFORMANCE CHARACTERISTICS

The angle of attack of the blade sections is governed by the local blade pitch angle β and the ratio between the axial and rotational velocity components, commonly defined by the advance ratio J:

$$J = \frac{V_\infty}{nD}. \tag{2.1}$$

At a given blade pitch setting, the advance ratio can be used as an independent variable to define the propeller performance characteristics. These are often expressed by the combination of three nondimensionalized parameters: the thrust coefficient C_T, the power coefficient C_P (or torque coefficient C_Q), and the propeller efficiency η:

$$C_T = \frac{T}{\rho_\infty n^2 D^4}, \tag{2.2}$$

$$C_P = \frac{P}{\rho_\infty n^3 D^5} (= 2\pi C_Q), \tag{2.3}$$

$$\eta = J\frac{C_T}{C_P}. \tag{2.4}$$

Figure 2.2 depicts typical propeller performance data as a function of the advance ratio, as measured with the 6-bladed propeller model described in Ref. [32] and the rotating-shaft-balance discussed in Ref. [33]. In this case, the advance ratio was varied by changing the propeller's rotational speed at a constant freestream velocity, and the blade pitch angle was fixed. As shown in Fig. 2.2a, the propeller loading increases with decreasing advance ratio, with a maximum efficiency occurring at a unique advance-ratio setting. At high loading conditions, boundary-layer growth on the blades and eventually separation cause a flattening of the thrust and power response.

Together with the radial loading distribution, the similarity parameters described by Eqs. 2.2 through 2.4 define the propeller response. Therefore, similarity is obtained between experiments at model scale and full-scale conditions in flight if these parameters are matched. However, this is challenging since the propeller performance is sensitive to the Reynolds number [34, 35], especially in the case of small models at relatively low freestream velocities. This is illustrated by Fig. 2.2b for the propeller efficiency. With increasing Reynolds number, blade lift increases and blade drag decreases due to the associated reduction in boundary-layer thickness. As a result, the thrust increases more

rapidly than the torque, and the propeller efficiency goes up with increasing Reynolds number. For this propeller model, the performance is especially sensitive to the Reynolds number for approximately $Re_c^{0.7R} < 1.5 \cdot 10^5$. Note that this is less than the typically considered critical value of $Re_c^{0.7R} < 5 \cdot 10^5$ [34].

Even though the Reynolds-number effects may modify the absolute propeller loading, the general characteristics of the propeller response remain the same, and thus the phenomena related to interactions between the wing and the propeller slipstream will not change. The same conclusion holds for compressibility effects related to the effective Mach number of the blades, up to conditions at which shock waves start to form. For the low-speed experiments discussed in this thesis, such conditions will not have occurred.

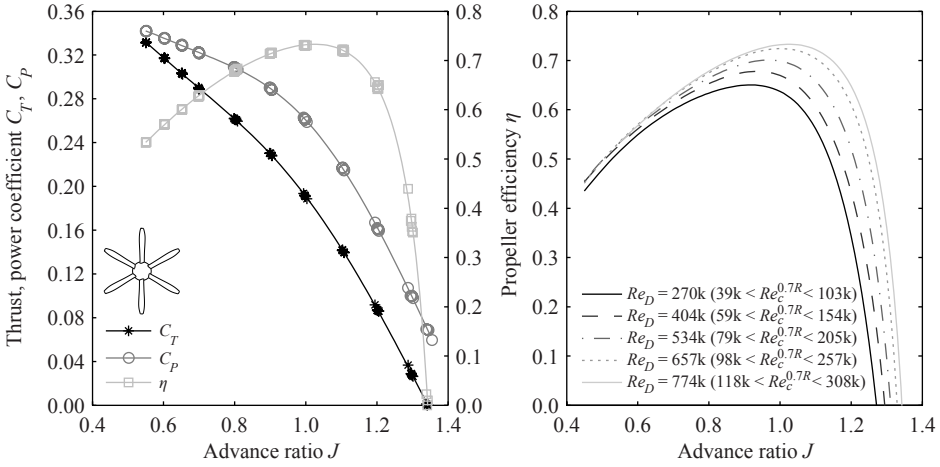

a) Propeller performance at $Re_D = 774{,}000$

b) Effect of Reynolds number on propeller efficiency

Figure 2.2: Example performance results measured with the six-bladed propeller described in Ref. [32] at $\beta_{0.7R} = 30$ deg ($Re_D = V_\infty D/\nu$, $Re_c^{0.7R} = V_{\text{eff}}^{0.7R} c^{0.7R}/\nu$).

When operating at a nonzero angle of incidence to the incoming flow, the propeller response is modified due to the variation in effective rotational velocity experienced by the blades throughout the rotation. At positive angle of attack, for example, the effective rotational velocity increases for the downgoing blade and decreases for the upgoing blade [36]. As a result, a circumferential variation occurs in blade angle of attack and effective velocity, leading to a cyclic variation in blade loading. Apart from modifying the propeller thrust and torque, this also leads to in-plane forces [37], which may affect the stability and trim characteristics of the aircraft. The loading on each blade will display a sinusoidal-like variation, with a frequency equal to the rotational speed of the propeller. This is illustrated by Fig. 2.3, which displays the effect of incidence angle on the blade normal force at 65% of the radius for the propeller model discussed in Chapter 5. For this uninstalled case, the results at positive and negative incidence angle are equivalent, only shifted by a phase offset of 180 deg. Furthermore, since in this case the measurement setup was mounted vertically, the incidence angle was set by yawing the setup. At positive incidence angle, the blade loading increased in the upper part of the disk

($\phi \approx 0$ deg) due to the local increase in effective rotational velocity, while the opposite occurred at negative incidence angle. The measurements taken under symmetric inflow conditions also showed a slight one-per-revolution oscillation. This was an artifact of the test setup, attributed to a flow perturbation introduced by in-flow measurement infrastructure which led to an inflow angularity of approximately 0.2 deg. The change in dynamic pressure and angle of attack experienced by the blades is slightly asymmetric between the two sides of the disk. As a result, the time-averaged propeller forces are also affected. At high incidence angles and low propeller thrust settings, an increase in propeller thrust can occur (see for example Section 6.1).

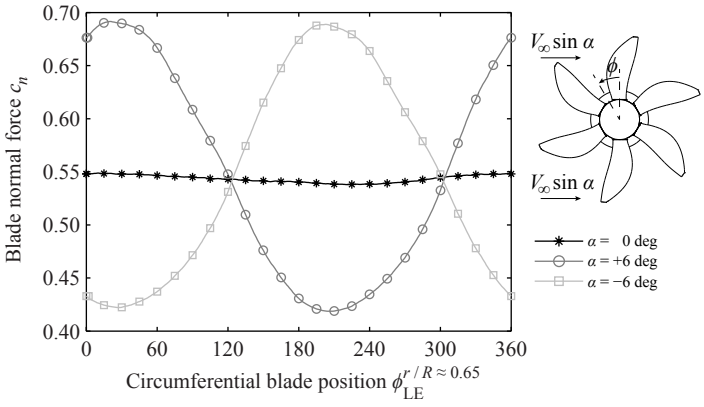

Figure 2.3: Nonuniform blade loading due to asymmetric inflow, as measured with the setup described in Chapter 5 ($C_T = 0.51$).

SLIPSTREAM CHARACTERISTICS

The thrust and torque produced by the propeller are associated with an increase in axial and tangential velocity in the propeller slipstream compared to freestream conditions. Furthermore, each blade sheds a vortical wake, making the slipstream unsteady in the stationary frame. Both effects are illustrated in Fig. 2.4 (obtained from measurements), and can have a strong impact on the loading distribution of downstream aerodynamic surfaces for installed tractor-propeller configurations, as discussed in Section 2.2.1 and Chapters 6 and 7. A comprehensive discussion of propeller slipstream characteristics has been provided in Ref. [36]; here, only a few important features are treated.

When considering a time average, the slipstream of the isolated propeller at zero angle of incidence is axisymmetric, hence constant in the circumferential direction. The propeller-induced velocities vary in the radial and axial (streamwise) directions though, as shown in Fig. 2.5. At a given streamwise location, the axial velocity displays a peak around the radial station at 75% of the propeller radius, corresponding to the spanwise location of maximum loading on the blades. On the inboard part of the blade, the loading is less and thus the downstream axial velocity is lower, while at the slipstream edge the induced velocity quickly tends to zero. For the example data shown in Fig. 2.5, separation occurred on the most inboard part of the blade, causing a local reduction of the axial velocity compared to the freestream conditions. The axial velocity in the slipstream

develops in the downstream direction due to the increasing length of the vortex system which induces the velocity increment. Consequently, the distance between the propeller plane and a downstream surface will affect the interaction effects.

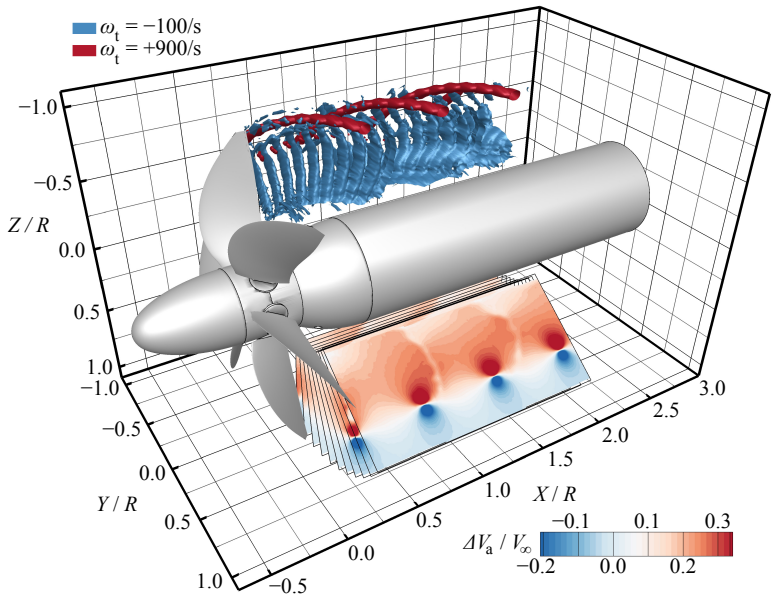

Figure 2.4: Flow topology in a propeller slipstream, as measured with the setup described in Chapter 5 ($C_T = 0.36$).

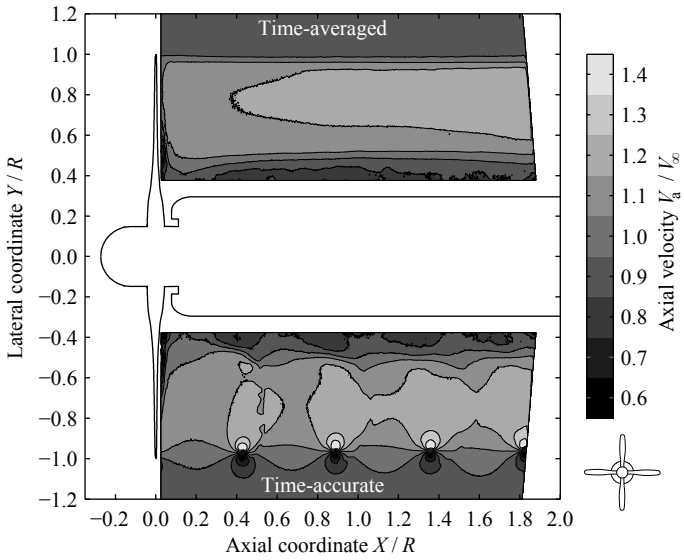

Figure 2.5: Propeller-induced velocities in the axial direction, as measured with the setup described in Chapter 4 ($C_T = 0.095$).

Because of the finite number of blades, the propeller slipstream is unsteady in the stationary frame, as can be seen in Fig. 2.4 and in the lower half of Fig. 2.5. The blade wakes and tip vortices introduce strong velocity and pressure gradients into the flowfield, which persist up to several times the propeller diameter downstream of the propeller. This has a dominant impact on the aerodynamic interactions for installed tractor-propeller configurations, as discussed in Section 2.2.1 and Chapter 7.

Apart from the increase in axial velocity, the propeller also induces a tangential velocity component, often referred to as swirl. Since the tangential velocity does not add to the axial momentum in the slipstream, its generation can be considered as a loss mechanism. Contra-rotating propeller configurations use a second blade row to recover the swirl introduced by the first blade row, thereby enhancing propulsive efficiency [38]. To quantify the amount of swirl in a propeller slipstream, the ratio of tangential to axial velocity in the slipstream is often expressed in terms of the swirl angle:

$$\theta = \tan^{-1}\left(\frac{V_t}{V_a}\right). \tag{2.5}$$

The characteristics of the slipstream depend uniquely on the similarity parameters defined by Eqs. 2.1 through 2.4, and the loading distribution on the propeller blades. Therefore, a slipstream representative of full-scale conditions can be produced in an experiment by selecting the right combination of thrust coefficient, power coefficient, advance ratio, and blade planform geometry.

2.1.2. ACOUSTIC PERFORMANCE

Unlike turbofan engines, propellers do not feature a casing around the blades which can attenuate noise through shielding and the application of acoustic liners. Furthermore, the large propeller diameters lead to relatively high tip speeds, causing an increase in amplitude of the sound emissions at the source. Therefore, it is important to understand the various noise sources associated with the propeller to minimize its sound emissions. Figure 2.6 provides a schematic overview of the most relevant noise sources for a propeller with two blade rows. Rotor-alone sources are indicated in the top half of the figure, while interaction sources are displayed in the bottom half. The case with two blade rows is considered here, since Chapter 9 discusses the acoustic performance of a propeller with a downstream row of swirl-recovery vanes. For a single-rotating propeller, only the rotor-alone sources are present. Figure 2.6 includes both tonal and broadband noise sources; the noise emissions of propellers are dominated by the tonal components, with broadband sources only becoming relevant at high frequency [39]. The various tonal and broadband noise sources are discussed in more detail below.

The noise of a conventional propeller propulsion system is not only due to the propeller(s), but also due to the turboshaft engine (compressor noise, turbine noise, jet noise); this thesis only considers the propeller-related sources. In the design study discussed in Ref. [12], jet noise was found practically negligible compared to the noise of the (contra-rotating) propellers, while compressor and turbine noise only contributed to the overall sound pressure level at low propeller thrust settings (approach conditions). For electric engines, the noise contribution due to the engine will be even smaller.

As for the aerodynamic performance of the propeller, the acoustic performance will exhibit scaling effects. A direct comparison between acoustic results for full-scale and

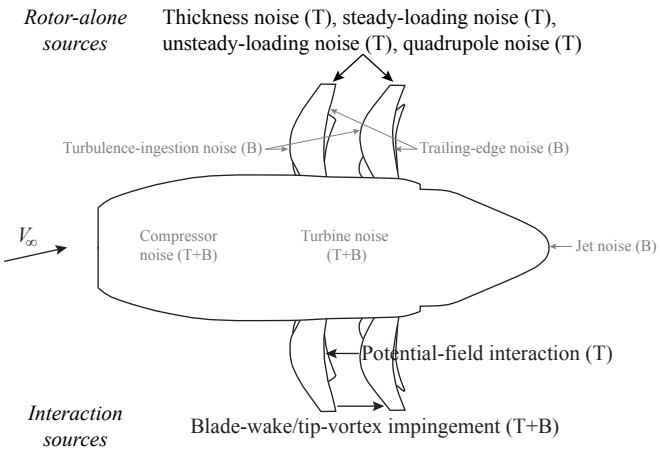

Figure 2.6: Overview of tonal (T) and broadband (B) noise sources for an isolated propeller with two blade rows, with the dominant tonal-noise sources by the blades indicated in black. For a single-rotating propeller, only the rotor-alone sources remain.

1/4-scale models of the same propeller geometry is provided in Ref. [40]. It was shown that good agreement can be reached between model-scale and full-scale results if the tip Mach number is matched.

TONAL NOISE SOURCES

The propeller's tonal noise emissions are due to rotor-alone and interaction sources. Rotor-alone sources are emitted from each blade row of the propeller system and therefore represent all noise sources for a single-rotating propeller, while interaction sources only arise for propeller configurations with a second blade row (rotating or stationary). The rotor-alone tones occur at multiples of the blade-passage frequency of the respective rotor, with the fundamental tone dominating the sound emissions. Four sources of rotor-alone noise can be distinguished [31]:

- **Thickness noise** is the result of the periodic displacement of air due to the volume of the propeller blades. The amplitude of this noise source scales with the blade volume, while it is especially relevant at higher tip speeds. Thin and swept blades should be used under such conditions to minimize thickness noise.

- **Steady-loading noise** is caused by the pressure disturbances introduced into the medium by the pressure fields associated with the loading on the propeller blades. This source is dominant at lower tip speeds, and its amplitude can be reduced by decreasing the blade loading, for example by increasing the number of blades or the propeller diameter.

- **Unsteady-loading noise** occurs at nonzero angle of incidence due to the associated circumferential variation of the blade loading (Section 2.1.1). This source leads to constructive and destructive interference with the steady-loading noise,

thereby introducing a circumferential variation into the sound emissions. For installed propellers, interactions with the airframe will lead to additional sources of unsteady blade loading, and thus increased unsteady-loading noise.

- **Quadrupole noise** sources account for possible transonic effects on the thickness and steady-loading noise. This is especially relevant for unswept blades operating at a high tip speed.

For propeller systems with two blade rows, interaction noise occurs next to the rotor-alone noise. The interaction tones occur at linear combinations of the blade-passage frequencies of the front and rear rotors, and are especially relevant at low-speed conditions when the rotor-alone noise sources are relatively weak. Compared to the rotor-alone tones, the interaction noise is caused by more impulsive pressure fluctuations, and thus features a richer spectral content. Two main interaction noise sources can be identified [31]:

- **Potential-flowfield interaction noise** is due to unsteady blade loading caused by the modification of the potential flowfield experienced by the front blade row, as a result of the blockage and upwash from the rear rotor. This source is most easily mitigated by increasing the spacing between the two blade rows.
- **Blade-wake and tip-vortex impingement noise** originates from the downstream blade row due to the periodic unsteady interaction with the passing blade wakes and tip vortices from the front blade row. A common approach to reduce the noise associated with the blade-vortex interaction is to crop the second blade row.

BROADBAND NOISE SOURCES

Broadband sources account for a secondary contribution to propeller noise. Since the tonal noise sources are known to be dominant [39], in this thesis only very limited attention is given to the broadband noise emissions. For completeness, the three possible broadband noise sources [31] are introduced here:

- **Turbulence-ingestion noise** is caused by inflow turbulence interacting with the leading edges of the blades. The resulting random blade-loading fluctuations are experienced as a broadband noise source, which only becomes relevant under conditions with high inflow turbulence.
- **Trailing-edge noise** is generated near the trailing edge of the blades due to scattering of the turbulent boundary layer.
- **Blade-wake and tip-vortex impingement noise** not only consists of a (dominant) tonal component, but also features a broadband contribution. The interaction between the rear blade row and the unsteady wakes and tip vortices of the first blade row also causes random load fluctuations, and thus broadband noise.

2.2. PROPELLER–WING INTERACTION EFFECTS

Already in 1921, Ludwig Prandtl published the results of a pioneering wind-tunnel experiment that highlighted the effect of the close coupling between propeller and wing

on the aerodynamic performance of both components [41]. Ever since, the interactions between propellers and the airframe have been a popular topic of research. This section provides an overview of the most relevant propeller–wing interaction effects, with a focus on tip-mounted propeller configurations. The discussion is based on the literature, and motivates the need for the detailed investigations presented in Part III of this thesis.

Figure 2.7 gives an overview of the dominant interaction effects for tip-mounted propellers from aerodynamic and aeroacoustic points of view. Sections 2.2.1 and 2.2.2 discuss these effects separately for the tractor and pusher configurations.

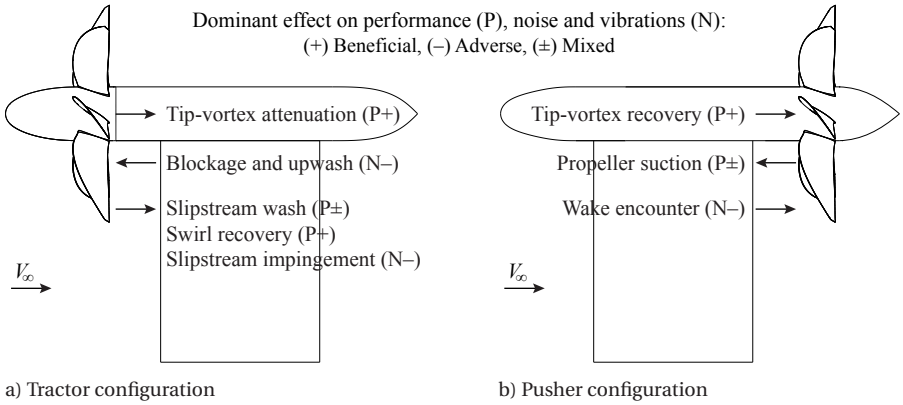

Figure 2.7: Overview of key interaction effects for tip-mounted propellers. Downstream-pointing arrows indicate downstream effect, upstream-pointing arrows indicate upstream effect.

2.2.1. TRACTOR-PROPELLER CONFIGURATION

In a tractor configuration, the propeller is positioned upstream of its support. Table 2.1 lists the main interaction effects for this configuration, together with their consequences and the resulting relevance for the aerodynamic and aeroacoustic vehicle performance. In the subsequent descriptions of the interaction effects, the wingtip-mounted configuration is taken as an example. The effects for pylon-mounted propellers are largely similar, with the exception of the tip-vortex-attenuation mechanism which for this case is less relevant due to the lower lift coefficient in the design condition.

Table 2.1: Overview of key interaction effects for tip-mounted propellers in tractor configuration.

Interaction effect	Consequence	Relevance
Slipstream wash	Lift augmentation	Performance increase
	Scrubbing drag	Performance decrease
	Separation delay (low Re)	Performance increase
Swirl recovery	Induced-drag reduction	Performance increase
Tip-vortex attenuation	Induced-drag reduction	Performance increase
Slipstream impingement	Unsteady wing loading	Vibrations
Blockage and upwash	Unsteady propeller loading	Noise increase

SLIPSTREAM WASH, SWIRL RECOVERY, AND TIP-VORTEX ATTENUATION

The increased dynamic pressure and swirl in the propeller slipstream modify the loading distribution on the downstream surface (wing, pylon, etc.). Figure 2.8 illustrates the change in local angle of attack and dynamic pressure experienced by a wing in a tip-mounted configuration due to the interaction with the incoming propeller slipstream. Note that the resulting effects for tip-mounted propellers are largely comparable to those occurring for conventional configurations with the propellers mounted on the inboard part of the wing; the conventional configuration has been discussed extensively in the literature [36, 42–44].

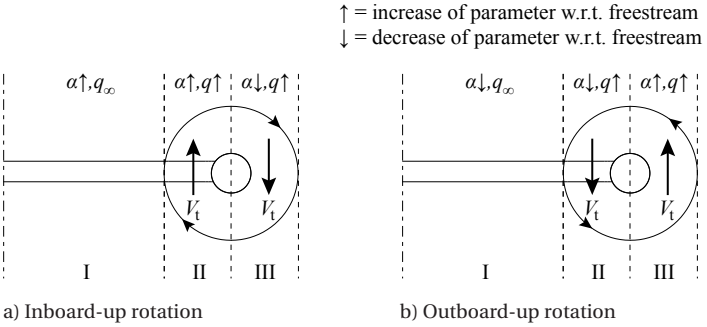

a) Inboard-up rotation b) Outboard-up rotation

Figure 2.8: Sketch of wing-inflow modification due to the propeller.

The increased dynamic pressure and swirl in the slipstream modify the lift and drag distributions over the entire wing, with the strongest effects occurring on the part of the wing immersed in the propeller slipstream. With inboard-up rotation, the wing experiences upwash and higher dynamic pressure in the spanwise part washed by the slipstream (region II in Fig. 2.8), thereby enhancing the lift compared to the propeller-off case. The resulting spanwise lift gradient near the slipstream edge causes vorticity to be shed, which leads to an upwash also on the inboard part of the wing (region I in Fig. 2.8). This is illustrated in Fig. 2.9a. For the case with outboard-up rotation, the direction of the propeller swirl is reversed, causing downwash on the wing. Therefore, for a vehicle configuration with co-rotating propellers (i.e. inboard-up on one side and outboard-up on the other), a loading asymmetry will occur. The performance penalty due to swirl with outboard-up rotation is partially offset by the increased dynamic pressure in the slipstream; the relative impact of both effects depends on the propeller design and operating conditions.

The shed vorticity associated with the spanwise lift gradient also introduces velocities in the spanwise direction (Fig. 2.9b and 2.9c), which distort the propeller slipstream during and after its interaction with the wing [36, 45, 46], resulting in a spanwise shearing of the slipstream. The slipstream moves away from the propeller axis on the advancing blade side, and toward the propeller axis on the retreating blade side. This occurs for both the cases with inboard-up and outboard-up rotation, matching the directions of the spanwise flow depicted in Fig. 2.9b and 2.9c. The spanwise shearing of the slipstream modifies the local wing performance near the slipstream edge. Although this especially affects the unsteady lift and drag response [45, 46], also the time-averaged wing loading is altered. This is discussed in more detail in Chapters 6 and 7.

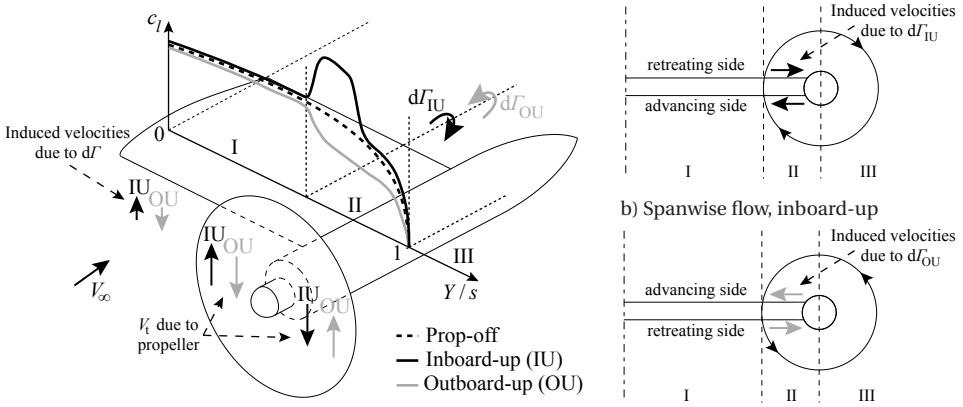

Figure 2.9: Sketch explaining the induced velocities due to the spanwise lift gradient at the slipstream edge caused by the propeller–wing interaction.

The increased dynamic pressure in the propeller slipstream not only augments the local lift, but also increases the viscous drag over the entire extent of the wing washed by the propeller slipstream (region II in Fig. 2.8). In case of operation at high freestream velocities, this drag penalty could be amplified by an increase in compressibility drag. The rise in local dynamic pressure also leads to an increase of the local Reynolds number, which can lead to a delay of separation. The latter effect is only relevant for applications operating at low Reynolds numbers, since in such case the interaction with the slipstream offers a relatively large increase in local Reynolds number.

Besides the modification of the lift vector's amplitude, also its orientation changes. With inboard-up rotation, the lift vector is tilted forward due to the propeller-induced upwash. This leads to decreased induced drag, a phenomenon known as swirl recovery [36]. With outboard-up rotation, on the other hand, the induced drag increases if the wing lift is positive. The effects are amplified with increasing propeller thrust setting due to the associated increase in propeller-induced swirl angle and dynamic-pressure rise.

The swirl-recovery mechanism discussed above is further amplified for tip-mounted tractor propellers due to tip-vortex attenuation. When the propeller rotation direction is opposite to that of the wingtip vortex, the propeller swirl partially cancels the tangential velocities associated with the wingtip vortex. Already in the 1960s, Snyder [24] showed that this leads to a decrease in wing drag and an increase in the wing's maximum lift coefficient and effective aspect ratio. The benefits of the tip-vortex-attenuation mechanism were later confirmed by both experimental [36] and numerical [25] studies.

At present, the literature lacks comprehensive analyses of the above-mentioned aerodynamic interaction effects for wingtip-mounted propellers. Although the potential for integration benefits has been proven in various independent studies [24, 25, 27, 36], thorough investigations of the effects on the local loading distributions and the flowfield are missing. Chapter 6 addresses this knowledge gap by providing a detailed aerodynamic analysis of the tip-mounted configuration, including measurements of integrated and

local forces and comprehensive flowfield evaluations. Furthermore, the aerodynamic performance of the wingtip-mounted configuration is compared to a conventional configuration, with the propeller mounted on the inboard part of the wing. The resulting data set provides insight into the interaction phenomena for conventionally-mounted and wingtip-mounted propellers, and the mechanisms leading to the performance benefits of wingtip-mounted propellers. The data are suited for code benchmarking because of the unique combination of local loading information on the wing and velocity and pressure data in the downstream wake, capturing the interaction between the propeller slipstream and the wingtip vortex.

PROPELLER-SLIPSTREAM IMPINGEMENT

Apart from the modification of the time-averaged wing loading due to the effects discussed above, the periodic impingement of the wakes and tip vortices of the propeller blades (Fig. 2.4) on the wing or pylon also results in a time-varying loading component. This loading is periodic at the blade-passage frequency and its harmonics, as shown by the experimental studies by Johnston and Sullivan [45] and Ljunggren et al. [47]. The locally increased turbulence levels in the slipstream [48] will also lead to periodic laminar-to-turbulent transition on the downstream element [49, 50], introducing additional load fluctuations. This secondary phenomenon is not considered in this thesis.

The unsteady loading caused by the impingement of the propeller slipstream on the wing or pylon results in structural vibrations, which are transmitted to the fuselage [51]. These vibrations may then be perceived as additional noise inside the cabin, reducing passenger comfort. This phenomenon is known as structure-borne noise, and is illustrated in Fig. 2.10. The structure-borne noise mechanism has been extensively investigated in the 1980s, both experimentally [52–56] and analytically [57–61]. Its relevance was first outlined by the study of Miller et al. [52], who identified the propeller blade tip vortices as dominant sources of pressure fluctuations on the wing. The amplitude of these hydrodynamic pressure fluctuations was found to be about 15 dB higher than the acoustic pressure measured at the wind-tunnel ceiling, representative of the fuselage sidewall location [52]. This shows that the unsteady pressures caused by the impingement of the propeller slipstream on the wing can be an important source of cabin noise. A secondary source of structure-borne noise can be caused by the unsteady loading on the propeller blades [51, 61]. However, the contribution due to the propeller-slipstream impingement on the wing or pylon is considered dominant [51, 53, 58].

The potential impact of the unsteady loads caused by propeller-slipstream impingement on passenger comfort motivates the need to understand the mechanism by which the unsteady loads are generated. However, so far limited information is available regarding the spatial distribution of the pressure fluctuations. Also, the sensitivity to operating conditions such as thrust setting, propeller–pylon spacing, and angle of attack has not been treated in detail. Chapter 7 of this thesis presents the results of an experimental study that combined unsteady surface-pressure measurements on a pylon with visualizations of the surrounding flowfield. In this way, the unsteady interaction effects caused by the impingement of the propeller slipstream on the pylon are explained and quantified for a typical pylon-mounted tractor-propeller configuration. The focus of the chapter is on the aerodynamic forcing function of the structure-borne noise; the structural response of the pylon to this forcing is not considered.

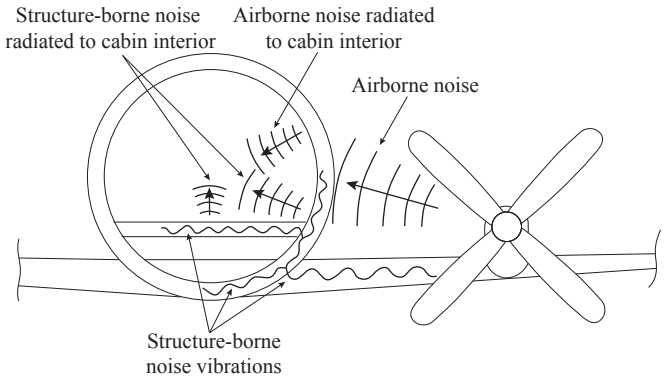

Figure 2.10: Sketch explaining the airborne and structure-borne noise paths [54].

BLOCKAGE AND DOWNWASH

The dominant upstream effect for tractor propellers is due to upwash and blockage by a downstream lifting surface. As a result, the propeller experiences a nonuniform inflow, which leads to cyclic load fluctuations and potentially an associated noise penalty. This would especially be relevant for a wingtip-mounted configuration with a relatively small spacing between the wing and the propeller. Both mechanisms are illustrated in Fig. 2.11. The effect of blockage is to reduce the axial inflow velocity to the propeller in the region upstream of the wing, resulting in a localized increase in blade loading. The effect of upwash, on the other hand, is more gradual and is comparable to operation of an isolated propeller at nonzero angle of attack [62]. It will be shown in Chapter 6 that for typical propeller–wing spacings and moderate wing loadings, the upstream effect on the propeller performance is small.

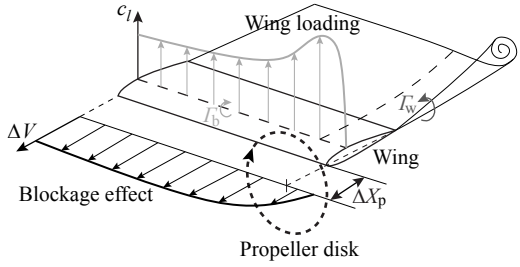

a) Wing loading and blockage characteristics

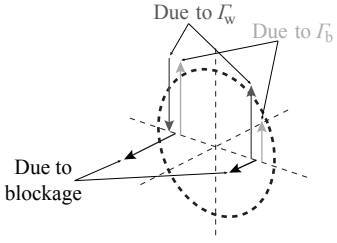

b) Resulting induced velocities at propeller plane

Figure 2.11: Sketch of blockage and downwash effects on the propeller.

2.2.2. PUSHER-PROPELLER CONFIGURATION

For the pusher configuration, the propeller is positioned downstream of its support (Fig. 1.3). In this case, the key interaction effects are the result of modifications to the propeller inflow. Table 2.2 lists the dominant interaction effects for the pusher configuration, together with their main consequences and the relevance for the aerodynamic and aeroacoustic performance of the vehicle.

Table 2.2: Overview of key interaction effects for tip-mounted propellers in pusher configuration.

Interaction effect	Consequence	Relevance
Wake impingement	Unsteady propeller loading	Noise increase
Tip-vortex recovery	Propeller power reduction	Performance increase
Propeller suction	Unsteady pylon loading	Vibrations
	Separation delay	Performance increase
	Drag penalty (high-speed)	Performance decrease

WAKE IMPINGEMENT

Since a pusher propeller is positioned downstream of its support, severe unsteady blade loading occurs [63]. This is due to the cyclic passage of the blades through the momentum deficit in the wake, illustrated in Fig. 2.12. Figure 2.13 shows that the sudden reduction in inflow velocity during the wake encounter causes an increase in angle of attack and a decrease in local dynamic pressure experienced by the blade sections. The resulting periodic change in the pressure field is a source of unsteady-loading noise.

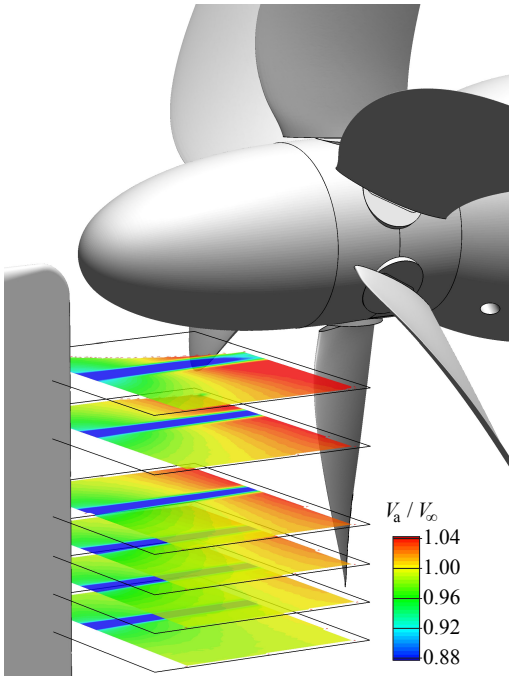

Figure 2.12: Velocity deficit in pylon wake upstream of the propeller, as measured with the setup described in Chapter 5 ($C_T = 0.36$).

Previous experimental work [16, 17, 64–67] has focused on the aeroacoustic impact of wake impingement for semi-installed pusher propellers. More recently, acoustic investigations were reported that extended the scope to complete aircraft configurations [18, 68]. In all cases, significant tonal noise penalties were measured compared to the

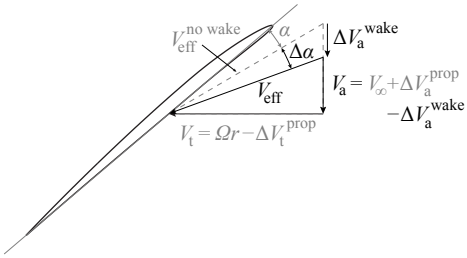

Figure 2.13: Effect of wake encounter on the velocity diagram at a propeller blade section. Properties in undisturbed inflow (Fig. 2.1) indicated in gray.

isolated propeller test case. Such noise penalties have been observed for both single-rotating and contra-rotating propellers; for the latter, the phenomenon is dominated by the tones emitted by the first blade row [16, 17].

The additional noise due to the wake encounter is a function of the propeller operating conditions. Block and Gentry [64] showed that the magnitude of the tonal noise penalty decreases with increasing tip Mach number and disk loading. Magliozzi [66] observed that the noise penalty was larger at zero angle of attack than at nonzero angle of attack. This was attributed to a flow-straightening effect of the installed pylon. Apart from the increased amplitude of the noise emissions, the installation of the pylon also introduces a shift in harmonic content and a change in directivity of the propeller noise [14]. The interaction noise penalty is especially pronounced away from the propeller plane, where the noise emissions of the isolated propeller are relatively low [14, 64].

Despite the main source of noise being known, the relation between the pylon-wake interaction and the propeller performance is still controversial. Amongst the few existing studies on the topic, Gentry et al. [69] observed a favorable installation effect on the thrust of a propeller with an upstream pylon and nacelle. This was, however, attributed to the presence of the nacelle wake, while the effect of the pylon wake was considered negligible. No blade-loading information was available to support this conclusion. Such data were available in the work of Farokhi et al. [63, 70], which showed that the pylon-wake impingement is experienced by the blades as a periodic, impulsive increase in blade loading.

Numerical work [71] confirmed previous findings regarding the pylon-wake impact on the propeller noise emissions, while additionally discussing the effects of the unsteady blade loads during the wake encounter. Moreover, a combined experimental–analytical study [72] identified the wake-impingement effect on the propeller noise signatures. Consequently, it is understood that the pylon-wake encounter causes unsteady blade loads and an increase in noise. However, no experimental study is available that discusses both simultaneously. Chapter 8 provides such a comprehensive analysis of the aerodynamic and aeroacoustic interaction effects for pylon-mounted pusher propellers, based on experimental data measured in a large-scale industrial wind-tunnel facility. Following a characterization of the nonuniform inflow to the propeller due to the pylon wake, the resulting unsteady aerodynamic response of the blades is discussed. The impact of the pylon-wake encounter on the propeller thrust and torque is then substantiated, after which the aeroacoustic interaction effects are assessed.

TIP-VORTEX RECOVERY

As discussed in Section 2.2.1, tip-mounted tractor propellers feature enhanced performance due to the favorable interaction of the propeller slipstream with the tip vortex of the wing or pylon. For pusher configurations, the opposite situation occurs, with the propeller performance being modified by the tip vortex. By positioning the propeller in the vortex field, part of the vortex energy can be recovered, as illustrated by Fig. 2.14. Experimental work by Patterson and Bartlett [26, 73] has shown that power reductions of around 25% can be achieved in this way at operating conditions representative of cruise. At the same time, a 30% reduction in wing induced drag was obtained due to the favorable modification of the downstream vortex field. The unsteady propeller blade loads were not considered, hence a complete understanding of the vortex recovery mechanism, including the effects on the propeller noise emissions, remains unavailable. A preliminary study of the tip-vortex recovery mechanism was performed with the pylon-mounted setup designed to study the wake-impingement phenomenon explained above. The results are discussed as part of Chapter 8.

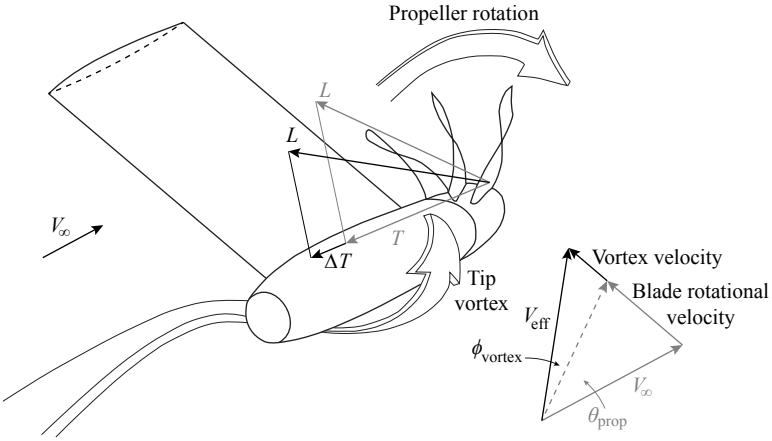

Figure 2.14: Sketch explaining the tip-vortex recovery mechanism for tip-mounted pusher propellers [26].

PROPELLER SUCTION

For pusher configurations, the upstream interaction effect is due to the suction by the propeller, which affects the loading on the upstream surface. Numerical simulations of a pylon-mounted CROR in pusher configuration [11] showed that this not only increases the mean loads, but also results in unsteady loading over the entire surface of the pylon. The unsteady loads were dominated by a component at the blade-passage frequency of the front rotor, while the influence of the aft rotor was only marginal. The modification of the pylon loading due to the suction by the propeller affects the pylon-wake characteristics, and thus the pylon wake-impingement phenomenon. This is briefly discussed in Chapter 8. The favorable pressure gradient imposed by the propeller also delays separation on the upstream element at higher angles of attack [74]. Furthermore, an increase in compressibility drag could occur under high-speed conditions.

2.3. POTENTIAL PERFORMANCE-ENHANCEMENT STRATEGIES

The interaction effects discussed above modify the propulsive and acoustic performance of the aircraft. Based on the literature, performance-enhancement strategies were identified which have the potential to mitigate the adverse interactions and maximize the beneficial ones. A subset of the these performance-enhancement strategies was selected for further investigations, as described in Part IV of this thesis.

2.3.1. TRACTOR-PROPELLER CONFIGURATION

Table 2.3 provides an overview of potential performance-enhancement strategies for each of the interaction effects identified in Section 2.2.1. Each of these strategies is described below, with a special focus on the two strategies investigated in detail in this thesis: swirl-recovery vanes and leading-edge treatment with a flow-permeable skin.

Table 2.3: Overview of the potential performance-enhancement strategies for tip-mounted propellers in tractor configuration.

Interaction effect	Enhancement strategy	Objective
Slipstream wash	Design optimization	Increase system efficiency
Swirl recovery & tip-vortex attenuation	Design optimization	Increase system efficiency
	Swirl-recovery vanes	Decrease loading asymmetry Increase propeller efficiency
Slipstream impingement	Leading-edge treatment	Decrease unsteady loading
	Propeller blowing	Decrease tip-vortex strength
	Design optimization	Decrease unsteady loading
Blockage and upwash	Propeller–wing spacing increase	Decrease unsteady loading

DESIGN OPTIMIZATION

The beneficial effects due to slipstream wash, swirl recovery, and tip-vortex attenuation can be maximized by design optimization. This is typically achieved by changing the wing's chord and twist distributions, with the objective to minimize the induced drag. Such an approach has been taken by multiple researchers for the conventional configuration [36, 75, 76]. In Ref. [76], induced-drag reductions were reported in the order of 10%. Considering the strong impact of the propeller slipstream on the wing performance for tip-mounted propellers, it is expected that the potential for shape optimization of the wing (with nacelle) would be even higher for such a configuration. Ideally, the propeller design would be optimized simultaneously with the wing design to arrive at the optimal vehicle performance.

Preliminary investigations were started during the research project discussed in this thesis to optimize the wing planform of a wingtip-mounted propeller configuration, for a given propeller design. However, additional work is required to improve the (low-order) analysis methods necessary to perform such an optimization, especially in terms of modeling the influence of the tip-mounted nacelle on the overall lift distribution. Therefore, the results are not included in this thesis, and the potential of wing-design optimization to improve the performance of tip-mounted propellers is not discussed.

Apart from maximizing the time-averaged system performance, wing-design optimization could also be useful to reduce the unsteady loading caused by the impingement of the propeller slipstream. The results of Chapter 7 indicate that unsteady-load reductions may be obtained by tailoring the local chord to the axial spacing between the propeller tip vortices. Dedicated follow-up experiments are required to verify this preliminary conclusion. Therefore, the opportunity to reduce unsteady loading by modifying the wing design is not discussed in Part IV of this thesis.

SWIRL-RECOVERY VANES

For wingtip-mounted tractor propellers, the effects due to swirl recovery and tip-vortex attenuation can enhance vehicle performance in case of inboard-up rotation, as discussed in Section 2.2.1. For pylon-mounted (or horizontal-tailplane-mounted) configurations, on the other hand, the potential benefits due to this favorable interaction are smaller due to the lower loading on the aerodynamic surface compared to the wing. Therefore, for such configurations the increased cost of employing counter-rotating propellers (inboard-up on both sides of the vehicle) might not be justified, and a co-rotating configuration may be adopted. This will lead to asymmetric loading, causing rolling and yawing moments that need to be trimmed, thereby increasing drag. To alleviate this effect, the swirl in the propeller slipstream needs to be reduced. This can be achieved by installing a second blade row, rotating in the opposite direction of the front rotor. This contra-rotating configuration has been studied extensively in the literature [10, 77, 78]. Alternatively, stationary swirl-recovery vanes (SRVs) can be used, functioning similarly to stator vanes in turbomachinery. The benefit of SRVs is that their installation adds less complexity to the propulsion system when compared to the contra-rotating solution. Figure 2.15 displays a set of SRVs installed downstream of an isolated propeller model.

Figure 2.15: APIAN propeller model with downstream swirl-recovery vanes, installed in the test setup described in Chapter 5.

Besides their potential to reduce the loading asymmetry on vehicle configurations with co-rotating propellers, SRVs have an additional benefit. Since the swirl induced by the propeller does not add to the thrust, its generation constitutes a loss mechanism. By recovering the swirl, the SRVs generate thrust, thereby enhancing the efficiency of the propulsion system. To maximize this benefit, the integration of the SRVs with the propulsion system is critical. Previous research by NASA confirmed the potential of SRVs to enhance the propulsive efficiency, with measured efficiency gains of about 2% in cruise conditions [79]. Numerical analyses using an Euler solver, on the other hand, predicted a propulsive efficiency increase of approximately 5% for the same configuration and operating conditions [80]. This indicates that viscous drag needs to be taken into account during both analysis and design of the SRVs. A more recent CFD analysis using a RANS solver showed increased thrust levels due to application of SRVs [81]. However, in the same study it was found that the total system efficiency was reduced, stressing the importance of proper SRV design and integration. This was addressed by follow-up work of the same research groups [32], focusing on the development, application, and experimental validation of a low-fidelity tool for SRV design. In this work, a measured 2.6% increase in thrust was reported at the design condition for high propeller thrust at low flight velocity and low Reynolds number. Additional design studies [82] highlighted the sensitivity of SRV performance to the selection of the vane count, the design point, and airframe installation effects. Detailed flowfield information of the propeller–SRV configuration has not been published in literature though, and the existing numerical studies do not contain thorough validations with experimental data.

Apart from the modification of the time-averaged propulsive performance, the installation of the SRVs introduces two unsteady interactions. First, the propeller blade loading becomes unsteady due to the periodic disturbance experienced by the blades when passing by in front of the SRVs. Second, the SRV loading is unsteady due to the periodic fluctuations induced by the impinging propeller blade wakes and tip vortices. Both effects have been confirmed by transient simulations using a profile transformation method, hence simulating a single blade passage only [83]. The aerodynamic interaction mechanisms for the propeller–SRV configuration are largely similar to rotor–stator interactions occurring in turbomachinery, as discussed in for example Refs. [84] and [85]. However, for the propeller–SRV configuration the reduced frequency of the interaction mechanism is lower, and the axial spacing between the rotating and stationary rows is larger than for conventional turbomachinery configurations. The unsteady loading on the propeller and SRVs causes two additional noise sources. However, so far the only acoustic measurements published for a configuration with SRVs showed a small noise reduction in the cruise condition when compared to the isolated propeller [86]. This was attributed to unloading of the propeller, which decreased the steady-loading noise. Apparently, in this case the reduction in steady-loading noise was sufficient to offset the interaction noise caused by the unsteady loading on the propeller blades and the SRVs.

The existing evaluations of the performance of SRVs have only focused on integral aerodynamic parameters, such as thrust and torque. Moreover, the aeroacoustic impact of the SRVs has only been assessed for high-speed cases, with relatively little detail. As such, a detailed understanding of the effect of the SRVs on the flowfield, the resulting unsteady interactions, and the aeroacoustic behavior is still missing. Such understand-

ing is of crucial importance for the successful design of SRVs which are to deliver the maximum performance benefit compared to an isolated single-rotating propeller. Furthermore, the installed configuration with SRVs integrated with a tip-mounted propeller has not been considered. The study discussed in Chapter 9 addresses these concerns by providing a detailed analysis of the propeller-slipstream flowfield, the propulsive performance, and the noise emissions of an isolated propeller with and without SRVs installed. Subsequently, a preliminary investigation is presented of the aerodynamic performance of an installed configuration, with a propeller with SRVs mounted at the tip of a pylon.

LEADING-EDGE TREATMENT

The potential structure-borne-noise penalty due to propeller-slipstream impingement can be mitigated by either modifying the transmission path of the vibrations through the aircraft structure [55], or directly at the source by decreasing the amplitude of the unsteady aerodynamic loads. The latter could be achieved by using a wing or pylon with a flow-permeable leading edge, also referred to as passive porosity. Such an approach has been studied numerically for unsteady stator loading due to the interaction between rotor and stator in turbomachinery [87–89], and blade–vortex interaction noise for helicopter applications [90]. The work by Tinetti et al. [87–89] predicted reductions in unsteady loading of up to 21% by application of passive porosity at the leading edge of the stator. It was shown that mass flow going in and out of the porous medium changed the effective aerodynamic shape of the outer surface, thereby modifying the pressure distribution. In a similar way, treating the leading edge of a rotor blade with passive porosity reduced the amplitude of blade–vortex interaction noise by 30%, as shown by Lee [90]. An example layout of a flow-permeable surface is shown in Fig. 2.16, which also illustrates the throughflow mechanism which occurs when the surface is exposed to an external pressure gradient.

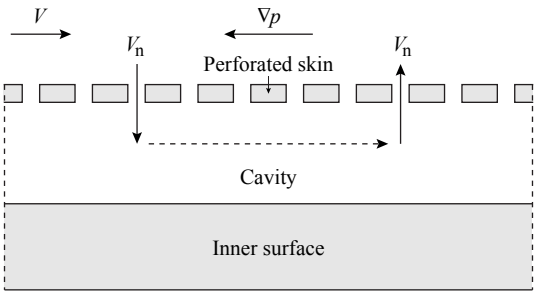

Figure 2.16: Notional drawing of the mechanism behind the flow through a permeable surface.

More recently, a combined experimental–analytical study [91] discussed measurements of the potential of porous material for tonal source attenuation in rotor–stator interactions, with the experimental setup designed to match the reduced frequencies typical of rotor–rotor interactions for contra-rotating open rotors. Tonal noise reductions of up to 5 dB were achieved for a stator vane with NACA 0012 airfoil and perforated leading edge featuring a porosity distribution similar to that considered in the work of Tinetti et al. [87–89] No measurements were taken of the impact of the perforated leading

edge on the aerodynamic performance of the vane. Other research on porous materials has mostly focused on the mitigation of shock-wave–boundary-layer interactions [92], leading-edge noise in turbulent inflow [93], flap side-edge noise [94], and trailing-edge noise [95, 96].

The results presented in Refs. [87–91] confirm that passive porosity can alleviate the unsteady loads due to rotor–stator and blade–vortex interactions. However, so far no study exists of the potential of passive porosity to alleviate unsteady loading caused by the impingement of a propeller slipstream on a downstream surface, for which wake-impingement and vortex-impingement phenomena occur simultaneously. Chapter 10 analyzes the time-averaged and unsteady performance of a pylon with a flow-permeable leading edge, aimed at alleviating unsteady loading due to propeller-slipstream impingement. The design of the flow-permeable leading edges was based on the optimal configuration identified by Tinetti et al. [87–89] for rotor-wake impingement on stator vanes. The effects of the flow-permeable leading edges on the time-averaged and unsteady aerodynamic performance of the pylon were quantified by flowfield measurements, lift and drag evaluations, and far-field noise acquisitions. The resulting data set provides unique experimental evidence of the potential of a flow-permeable leading edge to alleviate unsteady loading due to both wake impingement and tip-vortex impingement.

PROPELLER BLOWING

An alternative approach to reducing the unsteady loads generated by the impingement of the propeller slipstream on a downstream element would be to modify the characteristics of the tip vortices of the propeller blades. By accelerating the diffusion of the tip vortices, their effect on the unsteady loading on the downstream element can be decreased. This can be achieved by injecting turbulence into the vortex core [97] or by spanwise blowing into the vortex core [98–103]. Experiments by Han [100] showed that a passive blowing system integrated into a rotor blade could lead to a 60% reduction in the peak swirl-velocity component in the tip vortex compared to the unblown configuration. The associated aerodynamic performance penalty was relatively minor, with an increase in rotor input power of about 3% with blowing enabled. Similar results have been reported in Ref. [103] for a propeller blade, with in this case a 33% reduction in the maximum swirl velocity and a performance penalty of 2%.

The decay of the propeller tip vortex promised by passive blowing should be an effective performance-enhancement strategy to mitigate unsteady loading on a downstream element immersed in the propeller slipstream. Time constraints prevented an experiment in which this hypothesis was tested. Therefore, propeller blowing is not further discussed in this thesis.

PROPELLER–WING SPACING INCREASE

The distortion of the propeller inflow due to blockage and upwash associated with the downstream wing or pylon is a direct function of the distance from the wing or pylon to the propeller plane. Therefore, a trivial solution to reduce this effect is to increase the spacing between the propeller and the wing. Considering the results of Chapter 6, which show that the upstream effect of the wing on the propeller performance was small for a typical propeller–wing spacing, the sensitivity of this upstream effect to the propeller–wing spacing is not further discussed in this thesis.

2.3.2. PUSHER-PROPELLER CONFIGURATION

Table 2.4 lists potential performance-enhancement strategies for each of the interaction effects for tip-mounted pusher propellers discussed in Section 2.2.2. The identified strategies are described below, with a special focus on the strategy investigated in detail in this thesis: wake filling by blowing.

Table 2.4: Overview of the potential performance-enhancement strategies for tip-mounted propellers in pusher configuration.

Interaction effect	Enhancement strategy	Objective
Wake impingement	Wake filling by blowing	Minimize noise penalty
	Propeller design optimization	Minimize noise penalty
Tip-vortex recovery	Propeller design optimization	Maximize prop. performance
Propeller suction	Propeller-spacing increase	Decrease upstream effect

WAKE FILLING BY BLOWING

As discussed in Section 2.2.2, pusher propellers feature unsteady loading and an associated noise penalty due to the periodic passage of the blades through the momentum deficit in the wake of the upstream pylon or wing. Active wake filling by blowing can be applied to eliminate the momentum deficit in the incoming wake, thereby removing the physical mechanism driving the adverse installation effects. Figure 2.17 illustrates two possible blowing approaches: trailing-edge blowing and chordwise blowing. The trailing-edge blowing approach employs a single outlet in the trailing edge, whereas the chordwise blowing approach relies on a blowing slot positioned along the chord on both sides of the pylon or wing. This thesis focuses on the application of blowing to the pylon-mounted configuration. The results also apply to the wing-mounted configuration, although in that case the energy required by the blowing system would be higher due to the larger viscous losses on the wing compared to the unloaded pylon.

a) Trailing-edge blowing

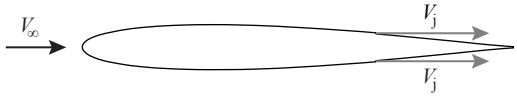

b) Chordwise blowing

Figure 2.17: Sketch comparing the trailing-edge and chordwise blowing approaches.

Depending on the layout of the blowing system and the operating conditions, the velocity profile in the blown wake will have different characteristics. Five generic types of velocity profiles can be identified, as shown in Fig. 2.18.

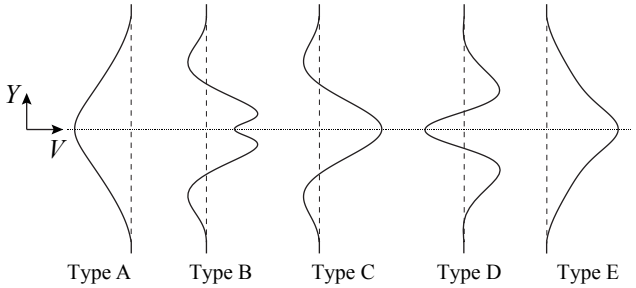

Figure 2.18: Overview of the different types of velocity profiles in the blown pylon wake [104].

- **Type A:** this velocity profile is characteristic of the unblown case, and is also obtained at low blowing momentum coefficients.
- **Type B:** at increased blowing coefficients, the blown jets in a chordwise blowing system start to re-energize the boundary layer. Two velocity overshoots appear around the wake center. The central velocity deficit is due to the momentum deficit in the boundary layers developing downstream of the blowing slots. Additionally, two minima occur near the wake edges due to insufficient mixing between the boundary layer upstream of the blowing slot and the blown jets.
- **Type C:** by moving the blowing slots downstream, the central velocity deficit is eliminated because of reduced boundary-layer growth downstream of the slots. The remaining minima near the wake edges indicate that a longer distance is required to accelerate the boundary layers developed upstream of the blowing slot. This type of velocity profile is typical for the trailing-edge blowing approach.
- **Type D:** an increased distance available for mixing can be provided by moving the blowing slots upstream. In this way, the velocity minima near the wake edges can be eliminated. However, the increased distance from the blowing slots to the trailing edge introduces an increased deficit on the wake centerline if the blowing rate is insufficiently high.
- **Type E:** increasing the blowing rate compared to the type-D profile, the central velocity deficit is turned into a velocity overshoot.

Numerical simulations [105] and several experiments [16–18, 106] have confirmed the effectiveness of blowing to reduce the unsteady blade loading and resulting noise penalty for pylon-mounted pusher propellers. However, previous literature has not discussed direct measurements of the reduction of the installation penalty at the source: the fluctuating propeller blade loads. As such, a complete analysis of the physical working principles of pylon blowing based on experimental data is still missing. Chapter 11 focuses on the relation between the modification of the propeller inflow by blowing and the resulting propeller response, for the trailing-edge blowing approach. Following a characterization of the pylon-wake flowfields with and without blowing, the effects of pylon trailing-edge blowing are quantified in terms of the suppression of the unsteady

propeller blade loads. Subsequently, the corresponding changes to the propeller noise emissions are evaluated, and related to the changes in the flowfield resulting from the application of pylon blowing. In this way, a thorough description is provided of the aerodynamic and aeroacoustic impact of pylon trailing-edge blowing on the installation effects occurring for pylon-mounted pusher propellers.

In terms of wake uniformity, the chordwise blowing approach offers performance superior to that of the trailing-edge blowing approach [107]. For the latter, the shorter distance between the pylon trailing edge and the propeller leads to wake profiles characterized by a velocity overshoot at the wake centerline with velocity deficits on both sides (velocity profile type C in Fig. 2.18). The chordwise blowing approach, on the other hand, provides increased length for mixing, and thinner boundary layers at the blowing slots. Consequently, the wake can be made more uniform (velocity profile types B and D in Fig. 2.18), as confirmed by experiments [106]. Recent work by Bury et al. [108] successfully attempted to further improve upon the uniformity of the blown pylon wake by combining chordwise blowing with an upstream boundary-layer scooping system. In this way, the pylon wake was made even more uniform, at the cost of additional complexity.

Although previous investigations have confirmed the potential for significant improvements in wake uniformity using the chordwise blowing approach, so far no consideration has been given to the optimal positioning of the blowing slots. Also, the performance of pylon blowing has only been evaluated under symmetric inflow conditions, whereas during takeoff and landing, for example, the pylon–propeller combination will operate at a nonzero angle of attack. The numerical study discussed in Appendix A addresses these concerns. The results are focused on the chordwise blowing approach, while the trailing-edge blowing layout is considered for comparison purposes only. By analyzing the downstream wake uniformity for a range of blowing slot parameters, the sensitivity of the pylon wake to the design of the blowing system is illustrated. Moreover, the robustness of the chordwise blowing approach under asymmetric inflow conditions is discussed, and a method is presented to estimate the required blowing rates for asymmetric cases based on reference values obtained for the case with symmetric inflow.

PROPELLER-DESIGN OPTIMIZATION

The disadvantage of the blowing approach discussed above is that it is an active control technique, which requires energy for operation. An alternative strategy could be to optimize the propeller design. This could be done with a low-order analysis tool based on analytical methods. The periodic velocity perturbation experienced by the blades can be modeled as a combination of sinusoidal gusts in the direction normal to the airfoil. Following a Fourier decomposition of the periodic gusts, the frequency-domain response of a blade section can then be modeled using the Sears function S [109–111]:

$$\Delta c_{l_k} = 2\pi \frac{w_k}{V_{\text{eff}}} S, \tag{2.6}$$

with w_k the Fourier coefficients of the harmonic gusts and V_{eff} the effective velocity experienced by the blade section (Fig. 2.13). The incompressible Sears function S is defined by [112, 113]:

$$S(\sigma) = \frac{J_0(\sigma) K_1(\mathrm{i}\sigma) + \mathrm{i} J_1(\sigma) K_0(\mathrm{i}\sigma)}{K_0(\mathrm{i}\sigma) + K_1(\mathrm{i}\sigma)}, \tag{2.7}$$

with J_0 and J_1 the zeroth- and first-order Bessel functions of the first kind, K_0 and K_1 the modified zeroth- and first-order Bessel functions of the second kind, and σ the reduced frequency:

$$\sigma = k\frac{\pi nc}{V_{\text{eff}}}, \tag{2.8}$$

with c the local blade chord and n the rotational frequency of the propeller. Figure 2.19 plots the real and imaginary parts of the Sears function versus reduced frequency. Due to the rotation of the propeller, the local effective Mach number at the outboard sections typically attains values for which compressibility effects can no longer be ignored. Therefore, a (low-frequency) compressibility correction can be applied to Eq. 2.7, as discussed in Ref. [114]. Following a strip-theory approach, Eqs. 2.6 through 2.8 can be evaluated for each blade section separately, after which the results can be converted into the time domain using an inverse Fourier transformation.

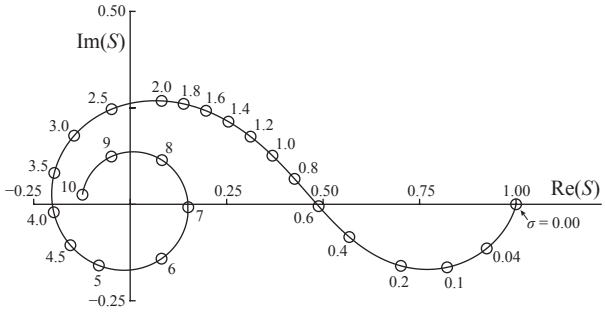

Figure 2.19: Real and imaginary parts of the Sears function (Eq. 2.7) versus reduced frequency [112].

Equation 2.6 shows that the unsteady lift is dominated by two factors: the amplitude of the gust, which is defined by the wake characteristics, and the amplitude of the Sears function. From Fig. 2.19 it can be seen that the amplitude of the Sears function decreases with increasing reduced frequency. Therefore, it can be expected from Eq. 2.8 that an increase of the chord length would be a propeller-design modification which could aid in reducing the unsteady loads caused by the wake-impingement phenomenon. This could further be enhanced by exploiting phase lag effects due to blade sweep. Unfortunately, this hypothesis could not be tested within the time frame of this thesis, and therefore is not further discussed.

Besides optimizing the propeller design for minimum sensitivity to inflow perturbations, the blade geometry could also be modified to maximize the tip-vortex recovery mechanism. In this way, this beneficial aerodynamic interaction can be exploited to obtain the maximum aerodynamic benefit. A simple optimization could already be performed by coupling a computed tip-vortex flowfield to a low-order tool for propeller analysis, such as a blade element method.

PROPELLER-SPACING INCREASE

Similarly as for the tractor configuration, the upstream interaction effect for pusher propellers can be mitigated by increasing the spacing between the propeller and the pylon or wing. This approach is not investigated in this thesis.

II

Experimental Methods

3

TRACTOR-PROPELLER SETUP FOR TIME-AVERAGED EFFECTS

Chapter 2 identified the aerodynamic and aeroacoustic interaction mechanisms and associated performance-enhancement strategies for installed propellers in tractor and pusher configurations. Specific experimental setups were used to study both configurations. The current chapter details the setup used to analyze the time-averaged interaction effects for tractor propellers. The model setup was based on the propeller–wing interference model (PROWIM) discussed in Ref. [36], converted into a tip-mounted configuration. Therefore, the setup is referred to as PROWIM-T in the remainder of the thesis. Section 3.1 first gives an overview of the test setup. Subsequently, the wind-tunnel facility is outlined in Section 3.2, followed by a description of the models in Section 3.3. Then, the measurement techniques are described in Section 3.4, after which Section 3.5 discusses the test conditions. The PROWIM-T setup was used to acquire results presented in Chapters 6 and 9.

3.1. OVERVIEW OF THE TEST SETUP

The *PROWIM-T* setup was used to analyze the time-averaged aerodynamic interactions for tip-mounted tractor propellers. Semi-installed propeller–wing configurations were simulated by connecting an existing tractor propeller model with nacelle to two different wing models. A low-aspect-ratio symmetric wing with integrated flap and pressure taps (Model I) was used for a detailed investigation of the wingtip-vortex-attenuation and swirl-recovery phenomena occurring for the wingtip-mounted configuration. The advantage of this existing wing model, adapted from the one used before by Veldhuis [36], is that it is equipped with a large number of pressure taps. These enabled local measurements of the wing loading. Furthermore, the flap allowed to simulate cases with inboard-up and outboard-up propeller rotation, by using opposite flap deflections with the same existing propeller model. In the configuration without flap deflection, the wing

Parts of this chapter have been adapted from Refs. [46] and [115], which provide CAD models of the experimental setup.

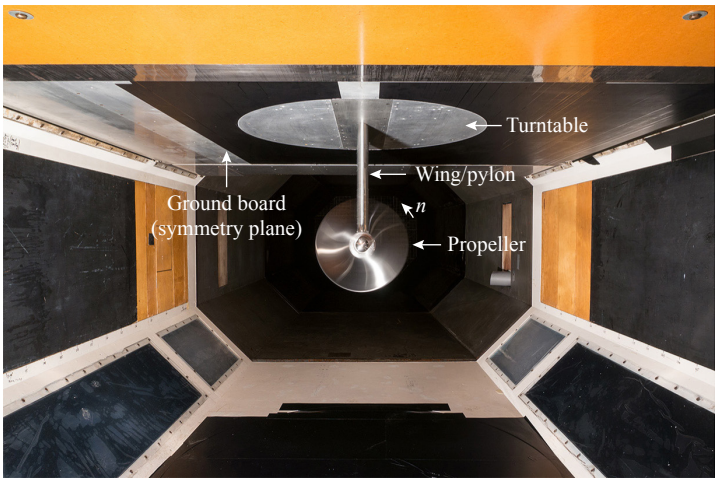

Figure 3.1: Front view of the *PROWIM-T* setup with the short-span symmetric wing model (Model I) installed in Delft University of Technology's Low-Turbulence Tunnel.

represented a typical pylon, which was tested with and without swirl-recovery vanes installed. Figure 3.1 provides a photograph of the *PROWIM-T* setup with the symmetric wing model installed in the wind tunnel.

Apart from the symmetric wing (Model I), also a new modular wing with camber was tested (Model II). This model with higher aspect ratio was used to compare the aerodynamic performance of the wingtip-mounted configuration and the conventional configuration, for which the propeller was mounted on the inboard part of the wing.

3.2. WIND-TUNNEL FACILITY

The experiments were performed in the Low-Turbulence Tunnel at Delft University of Technology. This low-speed closed-return wind tunnel features a closed-wall test section (Fig. 3.1) with a cross-section of 1.80 × 1.25 m. At the selected freestream velocity of 40 m/s, the turbulence level is below 0.1% (bandpass filtered between 2 and 5000 Hz). The models were attached to a 2.055-m long ground board suspended from the test section's ceiling, spanning the entire width of the test section. This ground board represents the symmetry plane for the experimental arrangement, and reduced the height of the test section to 0.995 m. The flow on the ground board was made turbulent by a transition strip, applied at 0.140 m from the board's leading edge. A turntable was integrated into the ground board to allow for measurements at nonzero angle of attack.

3.3. MODELS

3.3.1. PROPELLER

The propeller had a diameter of 0.237 m and its four blades were set to a blade pitch angle (defined between the local chord line and the propeller plane) of 23.9 deg at 75% of the radius. Considering the small scale of the propeller, it was decided not to apply

a means to force transition on the blades, since it was expected that the nonzero thickness of a tripping device would have posed too large a disturbance to the local blade performance. Technical drawings of the propeller geometry and blade cross-sections at 8 radial stations are given in Figs. 3.2 and 3.3. Additionally, Fig. 3.4 provides the radial distributions of the blade chord and pitch angle. The propeller was driven by a 5.5 kW three-phase induction motor housed inside an axisymmetric nacelle with a diameter of 0.070 m. The nacelle was connected directly to the wing models described later. Compared to modern designs, the propeller has a low blade count, a low solidity, and no sweep. Still, its slipstream introduced the aerodynamic phenomena to the flowfield relevant to the propeller–wing interaction (see Sections 2.1.1 and 2.2.1). Therefore, the model was considered adequate for the current investigation. The same propeller was also used in previous work by Veldhuis [36] and Ragni [116].

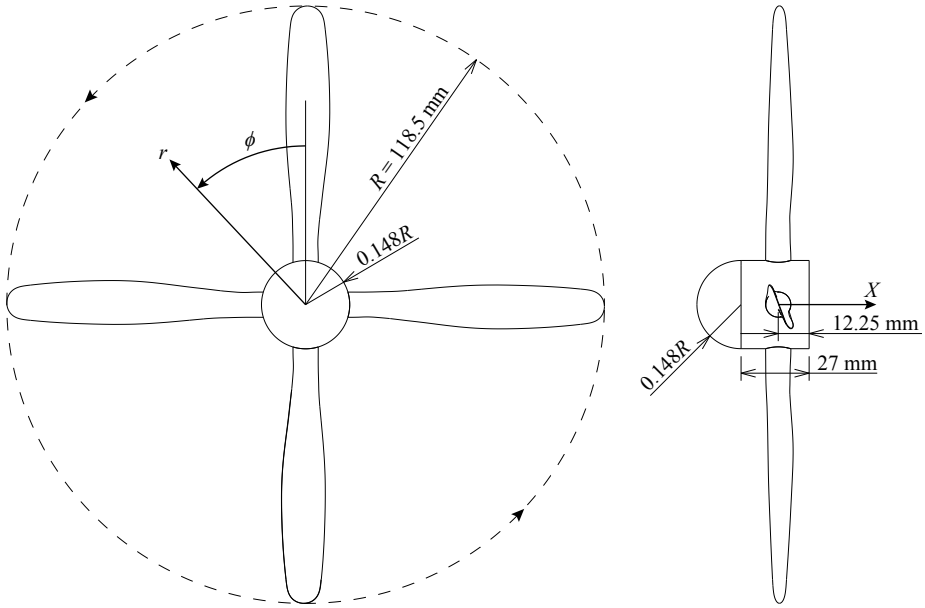

a) Front view b) Side view

Figure 3.2: Technical drawing of the propeller.

Since the propeller was not instrumented, reference measurements of the isolated propeller performance were taken with a sting-mounted configuration, as shown in Fig. 3.5. The sting was connected directly to an external balance (discussed in Section 3.4.2), with the height of the sting selected such that the propeller was positioned in the middle of the wind tunnel. A test section without ground board had to be used, which was considered acceptable since in this case the balance measurements did not include the forces acting on the turntable. A separately supported streamlined sleeve, not connected to the external balance, was installed around the sting to eliminate measurement error due to the interaction of the model support with the propeller slipstream. The forces on the nacelle were included in the thrust measurements. Tare runs were taken with

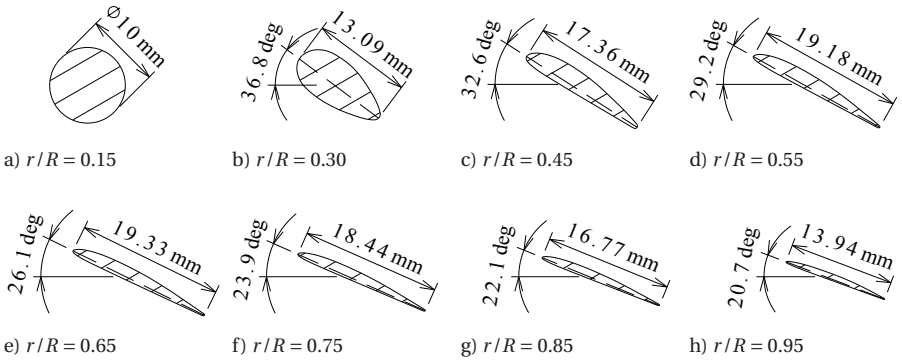

a) $r/R = 0.15$ b) $r/R = 0.30$ c) $r/R = 0.45$ d) $r/R = 0.55$

e) $r/R = 0.65$ f) $r/R = 0.75$ g) $r/R = 0.85$ h) $r/R = 0.95$

Figure 3.3: Technical drawing of the propeller blade cross-sections.

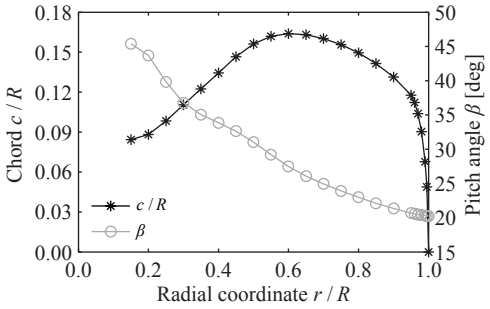

Figure 3.4: Radial distributions of the propeller blade chord and pitch angle.

a dummy spinner (blades off) and subtracted from the propeller-on data to isolate the blade forces, neglecting the nacelle interference-drag component caused by the interaction with the propeller slipstream. The axial spacing between the sleeve's leading edge and the propeller plane (1.5 times the propeller diameter) was sufficient to prevent an upstream effect on the propeller performance.

3.3.2. WINGS

MODEL I: SYMMETRIC WING WITH INTEGRATED FLAP

Figure 3.6 provides a photograph of the model configuration with the symmetric wing (referred to as Model I) installed in the test section, while Figs. 3.7 and 3.8 display the corresponding technical drawings. The nacelle was connected to a straight, untapered wing with a chord length of 0.240 m, a span of 0.292 m, a symmetric NACA 64_2A015 profile, and an integrated 25%-chord plain flap with a flap gap of 1 mm. This low-aspect-ratio wing with a high ratio of propeller diameter to wingspan was chosen to obtain a relatively strong interaction between the propeller slipstream and the wing, which aided in the interpretation of the aerodynamic interaction mechanisms. Transition was forced using strips with silicon-carbide particles, positioned at $X/c = 0.12$ on both the upper and lower sides of the wing. Chordwise rows of static-pressure taps were available at

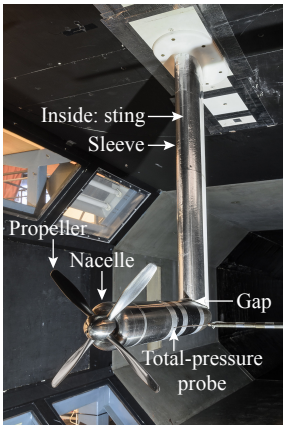

Figure 3.5: Photograph of sting-mounted setup, representing the isolated propeller case.

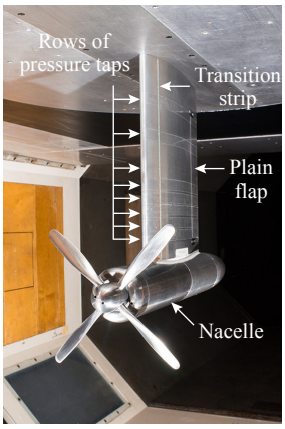

Figure 3.6: Photograph of Model I (symmetric wing with flap).

8 spanwise locations, as discussed in Section 3.4.3. The spacing between the propeller plane and the wing leading edge was fixed at 44% of the propeller diameter.

The flap was used to simulate the cases with the propeller slipstream rotating in the same and opposite directions of the wingtip vortex (outboard-up and inboard-up propeller rotation) with a single propeller model. This was achieved by running the tests at positive and negative flap deflection angles (±10 deg). The results obtained at the negative flap deflection angle were inverted during postprocessing by changing the sign of the angle of attack and the lift coefficient to represent the outboard-up rotating case:

$$\begin{aligned} \alpha_{\mathrm{OU}} &= -\alpha_{\mathrm{IU}}, \\ C_{L_{\mathrm{OU}}} &= -C_{L_{\mathrm{IU}}}, \\ C_{D_{\mathrm{OU}}}(C_{L_{\mathrm{OU}}}) &= C_{D_{\mathrm{IU}}}(-C_{L_{\mathrm{IU}}}). \end{aligned} \tag{3.1}$$

Additionally, the case with zero flap deflection represented a typical pylon configuration.

Since the flap only covered the spanwise extent from $Y/s_{\mathrm{s}} = 0.163$ to $Y/s_{\mathrm{s}} = 0.729$, the lift distribution will have differed somewhat from that on a wing with equal planform but having a cambered airfoil profile. The vorticity shed from the flap side edges causes a reduction in circulation of the wingtip vortex for the case with flap deflection. This may have slightly reduced the magnitude of the interaction effects compared to a more representative cambered wing without flap. However, comparisons with a short-span version of the modular cambered wing model discussed below showed that the general trends for the inboard-up rotation case were the same as measured with the model with flap, at all considered propeller operating conditions. Therefore, it was concluded that the model with flap was adequate to study the aerodynamic phenomena relevant to the wingtip-mounted propeller configuration.

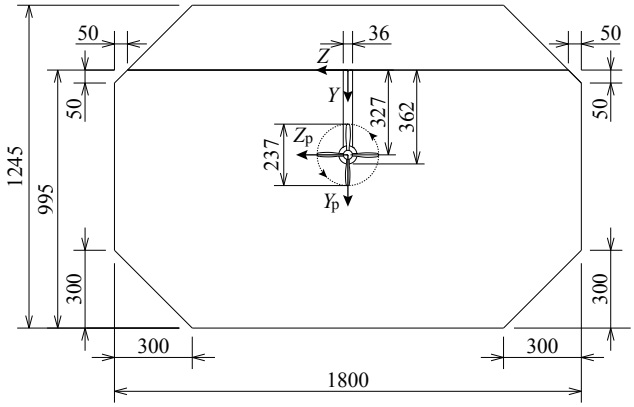

Figure 3.7: Overview technical drawing of Model I (symmetric wing with flap) installed in the wind tunnel. Dimensions in millimeters.

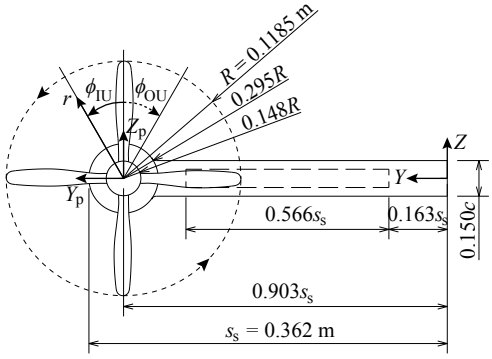

a) Front view

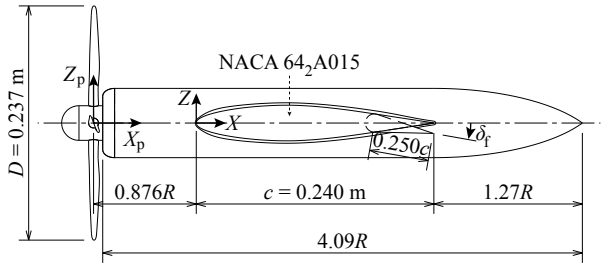

b) Section view

Figure 3.8: Detailed technical drawings of Model I (symmetric wing with flap).

MODEL II: MODULAR CAMBERED WING

Figure 3.9 displays photographs of the modular cambered wing (referred to as Model II) in the conventional and wingtip-mounted configurations, of which technical drawings are provided in Figs. 3.10 and 3.11. The straight and untapered wing consisted of two spanwise segments, which could be installed such that the nacelle was positioned in between both segments (conventional configuration) or at the tip of the two segments combined (wingtip-mounted configuration). The wing chord length was the same as for Model I (0.240 m), while a modified NACA 64_2A615 profile was chosen to achieve a lift coefficient of around $C_L = 0.3$ at $\alpha = 0$ deg. For manufacturing reasons, the trailing-edge thickness was increased to $8.3 \cdot 10^{-4}$ times the chord. This resulted in a slight bulge in the aft part of the profile (around $X/c = 0.9$), which may have promoted separation. Transition was fixed using strips with the same silicon-carbide particles as applied for Model I, in this case installed at $X/c = 0.08$ on both the upper and lower sides of the wing. The spacing between the propeller plane and the wing leading edge was fixed at 43% of the propeller diameter (approximately the same as for Model I), while the wing was oriented such that the propeller–wing combination featured inboard-up rotation.

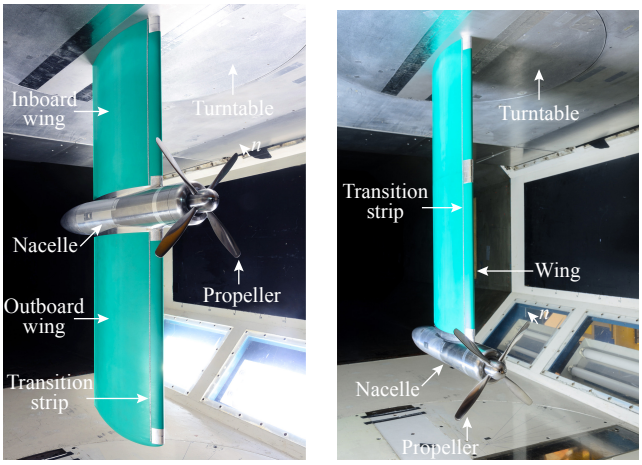

a) Conventional configuration b) Wingtip-mounted configuration

Figure 3.9: Photographs of Model II (modular cambered wing).

The conventional configuration had a rounded tip and a semispan of 0.748 m ($AR = 6.2$), leading to a ratio of propeller diameter to wing semispan of 0.32, a typical value according to the twin-engine propeller-aircraft database provided in Ref. [36]. The span of the inboard wing segment was approximately equal to the total span of Model I. As a result, the propeller axis was positioned at $Y/s_c = 0.444$, which is somewhat more outboard than the typical value of $Y/s = 0.30$ [36]. This was considered acceptable for the present study, since the spanwise loading gradient on the inboard part of the wing is relatively small. Therefore, the sensitivity of the propeller–wing interaction effects to the spanwise location of the propeller will be small as well on this part of the wing. The semispan of the wingtip-mounted configuration was 0.730 m up to the outboard edge

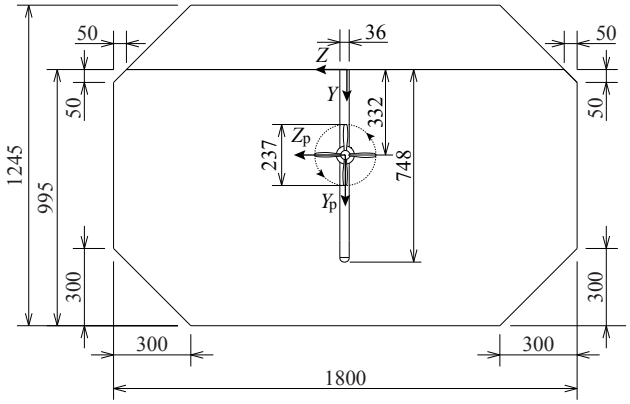

a) Conventional configuration

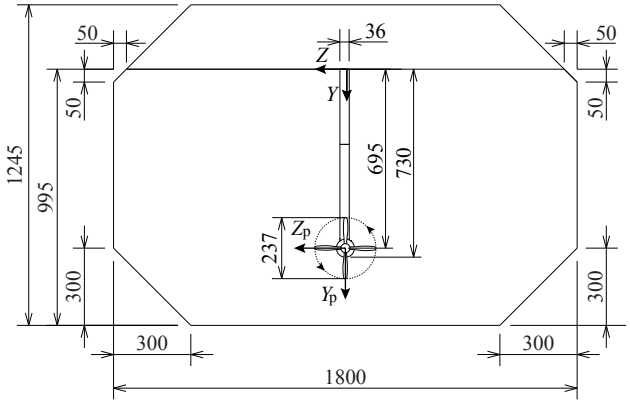

b) Wingtip-mounted configuration

Figure 3.10: Overview technical drawings of Model II (modular cambered wing) installed in the wind tunnel. Dimensions in millimeters.

of the nacelle ($AR = 6.1$), with a spanwise propeller position of $Y/s_t = 0.952$. Although the location of the propeller with respect to the wind-tunnel walls differed between the conventional and wingtip-mounted configurations, it was assumed that the propeller performance was the same for both cases. This is supported by previous work focusing on propeller aerodynamics in close ground proximity [117], which showed that propeller performance remains unaffected by wall spacing for spacing values above 1.5 times the propeller radius.

3.3.3. SWIRL-RECOVERY VANES

In case of a vehicle configuration with co-rotating propellers, i.e. inboard-up propeller rotation on one side of the aircraft and outboard-up on the other, the aerodynamic interaction effects for tip-mounted propellers in tractor configuration (see Section 2.2.1 and Chapter 6) would cause a strong asymmetry in the aerodynamic loading. Measurements

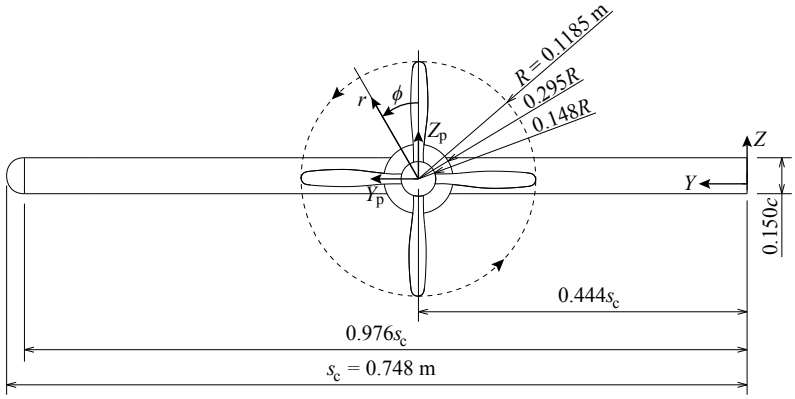

a) Conventional configuration

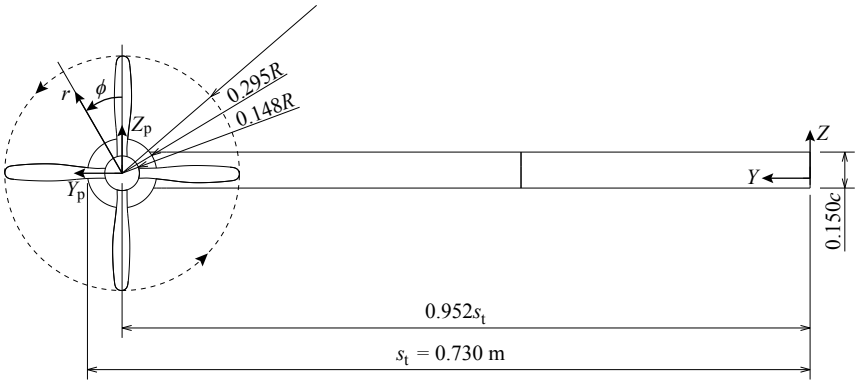

b) Wingtip-mounted configuration

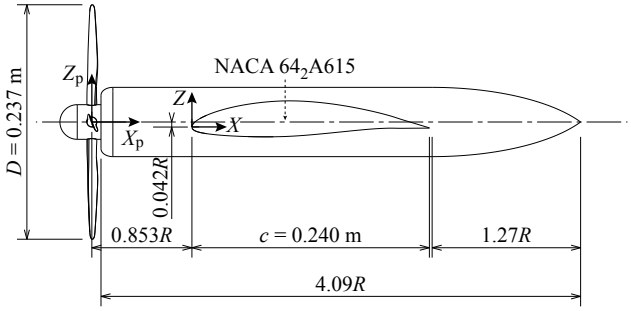

c) Section view

Figure 3.11: Detailed technical drawings of Model II (modular cambered wing).

were taken with swirl-recovery vanes installed between the propeller and Model I (symmetric wing model) to reduce the swirl in the slipstream and assess the resulting impact on the asymmetric loading for the cases with inboard-up and outboard-up propeller rotation. The SRVs were designed for maximum thrust in the isolated configuration (without wing), following the design method outlined in Ref. [32]. A design advance ratio of $J = 0.7$ was chosen, corresponding to a propeller thrust coefficient of around $C_T = 0.12$. To maximize the aerodynamic impact of the SRVs, it was decided not to apply cropping; hence, the radius was equal to that of the propeller.

The SRVs were positioned approximately half-way the propeller and the wing leading edge. The spacing from the propeller to the SRVs should be sufficiently large to prevent a large noise penalty due to the interaction noise sources discussed in Section 2.1.2. A spacing between propeller center and SRV quarter-chord line of 0.47 times the propeller radius was selected based on the recommendations for contra-rotating open rotors given in Ref. [10]. Figure 3.12 provides a technical drawing of the SRVs and their position with respect to the propeller and the wing. The SRVs were mounted on the nacelle through 3-mm thick interfaces, which increased the local nacelle radius to 38 mm ($0.321R$).

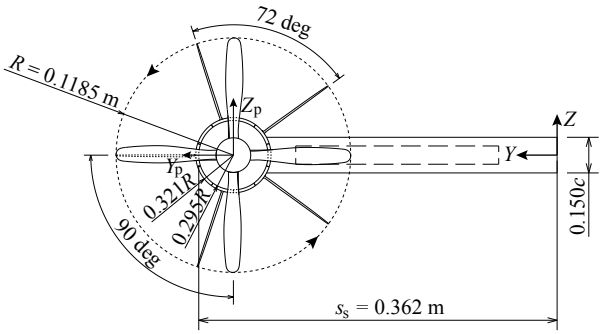

a) Front view

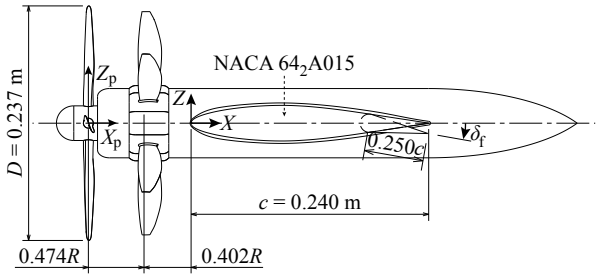

b) Section view

Figure 3.12: Technical drawings of Model I (symmetric wing) with swirl-recovery vanes installed.

3.4. MEASUREMENT TECHNIQUES

Table 3.1 provides an overview of the measurement techniques applied for the tests with Models I and II. Since the experimental data were also intended for the validation of CFD simulations in which the wind-tunnel walls were modeled, no corrections were performed for wind-tunnel wall effects and buoyancy effects.

Table 3.1: Overview of measurement techniques used for Model I (symmetric wing with flap) and Model II (modular cambered wing).

Measurement aim	Measurement technique	Model I	Model II
Flowfield information	Particle-image velocimetry	Yes	No
	Wake rake	Yes	Yes
Integrated loading	External balance	Yes	Yes
Sectional wing loading	Pressure taps	Yes	No
Local propeller loading	Total-pressure probe	Yes	No
Surface-flow features	Oil-flow visualization	No	Yes

3.4.1. QUANTITATIVE FLOWFIELD EVALUATIONS

PARTICLE-IMAGE VELOCIMETRY

Flowfield measurements were taken in the wake of Model I using stereoscopic particle-image velocimetry (PIV). Table 3.2 provides an overview of the measurement and post-processing characteristics of the PIV setup, while Fig. 3.13 illustrates the position of the PIV plane with respect to the model. The laser and cameras were traversed simultaneously in the vertical direction to allow for measurements in three different planes, oriented perpendicularly to the freestream flow direction at $1.5c$ downstream of the wing trailing edge ($X/c = 2.5$). The results from the three measurement planes were combined in postprocessing to obtain a final field of view with dimensions of 360×485 mm, which covered the entire wake of the propeller–wing model. Both phase-uncorrelated and phase-locked measurements were taken. Phase-locking was achieved using a one-per-revolution trigger signal integrated into the motor driving the propeller. Six blade phase angles were considered with a 15 deg spacing between consecutive angles. This thesis only considers the phase-uncorrelated data. Postprocessing was performed with an iterative multi-grid approach [118], with a final window size of 24×24 pixel and 50% overlap. The resulting vector spacing of 0.9 mm was appropriate to identify the dominant flow structures in the wing wake and the propeller slipstream. The uncertainty of the instantaneous velocity components was computed with the method by Wieneke [119]. The statistical uncertainty of the mean velocity components was obtained from the variations between uncorrelated samples at each vector location and the local number of samples available for averaging. Table 3.2 lists the uncertainty values averaged over the field of view; the uncertainty of the velocity components near the slipstream edge was up to 3 times larger due to the local effect of the propeller blade tip vortices. Besides the contribution due to uncertainty of the instantaneous velocity fields, the statistical uncertainty of the mean also contains a contribution due to turbulence.

Table 3.2: Measurement and postprocessing characteristics of the stereoscopic PIV setup.

Parameter	Value
Laser	Nd:YAG 200 mJ
Cameras	2× 16 Mpixel CCD sensor
Objective	200 mm $f/4$
Field-of-view size	360 × 485 mm
Field-of-view position (X/c)	2.5
Pulse separation	40 μs
Max. particle displacement	25 pixel
Image pairs	300[a], 1000[b]
Final interrogation window size	24 × 24 pixel
Window overlap factor	50%
Vector spacing	0.9 mm
Uncertainty instantaneous velocity magnitude	$0.018V_\infty$
Uncertainty mean velocity magnitude	$0.002V_\infty$[a], $0.001V_\infty$[b]

[a] phase-locked measurements, [b] phase-uncorrelated measurements

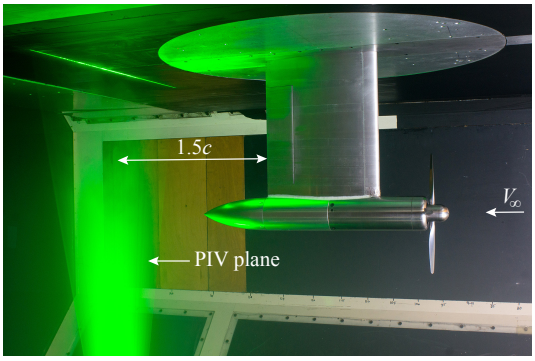

Figure 3.13: Illustration of the position of the PIV plane with respect to the model.

WAKE RAKE

A traversable wake rake was used to map the total-pressure distribution in the wake of the models at the same axial position as the PIV plane ($X/c = 2.5$). For Model II, only total-pressure measurements were taken, with a resolution of 3 mm in the lateral and vertical directions. For Model I, the spatial resolution was increased to 2 mm, while static-pressure measurements were done with a resolution of 4 mm. The traversing range was selected such that the wing and nacelle wakes and the propeller slipstream were positioned entirely inside the field of view. The pressures at all probe locations were recorded simultaneously with the same electronic pressure scanner as used for the surface-pressure measurements with pressure taps (Section 3.4.3). Since the maximum swirl angle in the wake of the models was approximately 12 deg, a maximum error of about 2% occurred due to local misalignment of the probes [120]. The wake rake was removed from the test section during all other measurements to prevent an unwanted upstream effect on the wing and propeller performance.

3.4.2. INTEGRATED LOADING

The total forces and moments generated by the propeller–wing combinations were obtained with an external six-component balance. Measurements were taken both with and without the propeller blades installed to allow for an assessment of the aerodynamic interaction effects caused by the propeller slipstream. A simple bookkeeping procedure was followed to separate the forces and moments generated by the wing with nacelle and the propeller. To this end, the isolated propeller's performance data were used, as measured with the sting-mounted configuration. In this process, the upstream effect of the wing on the propeller performance was neglected. Apart from the forces acting on the models, the balance data also included the forces and moments on the turntable in the wind-tunnel ceiling (see Figs. 3.1 and 3.9), mostly dominated by skin-friction drag. Tare measurements were taken with the models removed from the test section to correct for this effect. This approach cannot account for the interference drag associated with the junction flow at the interface between the wing and the turntable. The uncertainty of the balance measurements was estimated from repeated measurements at equal operating conditions. The standard deviation of the lift data was 0.04 lift counts, while the standard deviation of the drag data was 3 drag counts.

3.4.3. WING LOADING

The symmetric wing model contained a total of 408 pressure taps, providing local measurements of the pressure distribution at 8 spanwise locations: $Y/s_s = 0.171, 0.308, 0.445, 0.500, 0.555, 0.611, 0.666, 0.721$. The pressure taps were cross-connected in the spanwise direction at each chordwise position. Therefore, the measurements were taken per chordwise pressure row, with all other rows closed by tape. The pressures from each chordwise row were simultaneously recorded at a sampling rate of 5 Hz using an electronic pressure scanner, and averaged over time to obtain the final results per data point. The pressure data were integrated to obtain the section lift and pressure-drag coefficients on the wing. In this process, the local geometry of the wing profile was accounted for.

3.4.4. PROPELLER LOADING

A circular, square-ended total-pressure probe with a diameter of 1.5 mm was used to measure the total-pressure rise induced by the propeller. Measurements were taken both for the sting-mounted propeller and Model I (symmetric wing with flap) to study the upstream effect of the wing on the propeller loading. The probe was designed such that it could provide measurements of the propeller loading distribution in the region upstream of the wing, with the tip of the probe positioned at $0.15R$ downstream of the propeller center. The maximum swirl angle in the propeller slipstream at the measurement location was about 8 deg, leading to a maximum error of less than 0.5% due to local misalignment of the probe [120]. The probe and its support infrastructure were removed from the test section during all other measurements. Data were acquired over the entire propeller disk by traversing the probe in the radial and circumferential directions, with a radial resolution of 3 mm ($0.025R$) and a circumferential resolution of 10 deg. This full measurement grid was only considered for the wing-installed configuration at $J = 0.8$. At the other advance ratios, the full radial range was measured only at $\phi = [0, 90, 180, 270]$ deg, while the full circumferential range was only covered

at $r/R = 0.76$. Considering the expected axisymmetry of the sting-mounted propeller, for this configuration only circumferential angles in the range of $90 \leq \phi \leq 270$ deg were evaluated.

3.4.5. SURFACE-FLOW FEATURES

Surface-flow visualizations were performed using a fluorescent oil technique [121] on the upper surface of Model II (modular cambered wing). Following each data point, the tunnel was stopped and the oil was redistributed over the model. The visualizations were performed to identify the flow-separation pattern over the wing and nacelle, with and without the propeller running. Furthermore, the effectiveness of the transition strips could be verified.

3.5. TEST CONDITIONS

The majority of the measurements taken with the *PROWIM-T* setup were acquired at a freestream velocity of $V_\infty = 40$ m/s. This velocity provided the best compromise between achievable Reynolds number and the operating range of the propeller, which was constrained by the output power of the electric motor. The resulting Reynolds number based on the wing chord was about $Re_c = 650{,}000$, while the Reynolds number based on the propeller diameter was $Re_D = 640{,}000$. The propeller was operated at four thrust settings, corresponding to advance ratios J of 0.7, 0.8, 0.9, and 1.0. The associated thrust coefficients C_T were equal to 0.123, 0.095, 0.053, and 0.014, respectively, while the Reynolds number at $r/R = 0.7$ was in the range of 130,000−180,000 (for $J = 1.0$ down to $J = 0.7$). For Model II, additional measurements were taken at $V_\infty = 28$ m/s to achieve higher thrust coefficients. At this velocity, the propeller was also operated at advance ratios of 0.5 and 0.6, resulting in thrust coefficients of 0.168 and 0.144, respectively. The corresponding Reynolds numbers were 455,000 based on the wing chord, 450,000 based on the propeller diameter, and 90,000−170,000 based on the effective velocity and chord at $r/R = 0.7$ (for $J = 1.0$ down to $J = 0.5$). The sting-mounted propeller data were acquired at Reynolds numbers of $Re_D = 620{,}000$ and $Re_D = 470{,}000$. The difference in Reynolds number of at most 4% between the sting-mounted and wing-installed measurements is ignored in the evaluations discussed in this thesis. For all configurations, tare measurements were taken with the blades removed to obtain a baseline to which the propeller-on data could be compared. The test cases are particularly representative of smaller vehicles with low-speed propellers; compared to high-speed propellers with high disk loading, the considered thrust coefficients are relatively low. Considering that the wingtip-mounted propeller is especially feasible for aircraft with (distributed) electric propulsion, this was considered acceptable.

The aerodynamic performance measurements with the external balance and surface-pressure taps were taken over a range of angles of attack α, at zero sideslip angle. For Model I, the angle of attack was varied over the range $-20 \leq \alpha \leq 20$ deg. For Model II, the angle-of-attack range was $-8 \leq \alpha \leq +15$ deg for the wingtip-mounted configuration and $-8 \leq \alpha \leq +10$ deg for the conventional configuration. For the latter case, the maximum angle of attack was limited because of the weaker connection between the nacelle and the outboard wing segment. The wake-rake, PIV, and propeller-slipstream evaluations

with Model I were intended to be performed at $\alpha = 0$ deg, but due to a small misalignment of the setup the actual angle of attack was $\alpha = -0.2$ deg for the inboard-up case and $\alpha = +0.2$ deg for the outboard-up case. For Model II, the wake-rake data were acquired at $\alpha = 0$ deg and at a constant lift coefficient of $C_L = 0.5$. The misalignment of Model I was resolved before performing the pressure and balance measurements discussed in this thesis. The sting-mounted propeller was evaluated before the misalignment was resolved, and thus the propeller performance data also suffered from a -0.2-deg misalignment. Interpolation was performed to obtain the propeller performance at the same angles of attack as the balance data acquired with Models I and II.

4

TRACTOR-PROPELLER SETUP FOR UNSTEADY EFFECTS

Whereas the setup discussed in the previous chapter could only be used to investigate the time-averaged interaction effects for tractor propellers, the setup described in the current chapter was devised to study the unsteady effects occurring for such a configuration. This setup is referred to as PROWIM-US in the remainder of the thesis, and was built around the same propeller model as used in the PROWIM-T setup. The test setup is introduced in Section 4.1, after which Section 4.2 briefly discusses the wind-tunnel facility. Thereafter, the models are described in Section 4.3 and the measurement techniques are detailed in Section 4.4. Finally, Section 4.5 provides the test conditions. The PROWIM-US setup was used to acquire results presented in Chapters 7 and 10.

4.1. OVERVIEW OF THE TEST SETUP

A typical pylon-mounted tractor-propeller configuration was simulated by positioning a generic pylon model downstream of a sting-mounted propeller. To achieve commonality with the propeller slipstream characteristics obtained in the tests focusing on time-averaged effects, the propeller model was the same as for the *PROWIM-T* setup (Chapter 3). Also, its relative position with respect to the pylon was approximately the same. A photograph of the *PROWIM-US* test setup is given in Fig. 4.1.

4.2. WIND-TUNNEL FACILITY

All measurements with the *PROWIM-US* setup were taken in the Low-Turbulence Tunnel at Delft University of Technology, as already described in Section 3.2. In this case, no ground board was installed in the top of the test section, resulting in a cross-section of 1.80 × 1.25 m. The propeller model was supported by a sting, while the pylon model was mounted to the floor of the test section.

The contents of this chapter have been adapted from Refs. [46] and [122], which provide CAD models of the experimental setup.

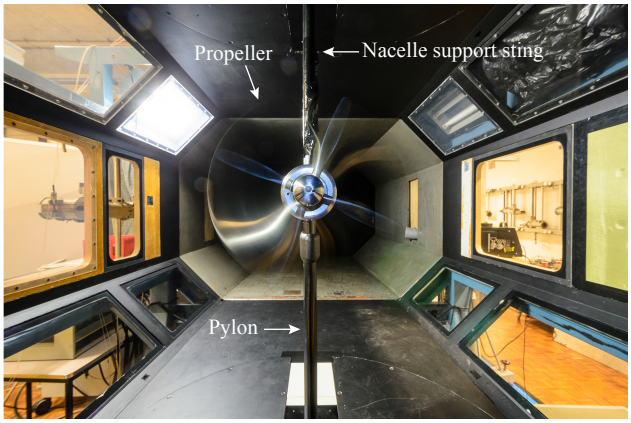

Figure 4.1: Front view of the *PROWIM-US* setup installed in Delft University of Technology's Low-Turbulence Tunnel.

4.3. MODELS

4.3.1. PROPELLER

The propeller model was the same as used with the *PROWIM-T* setup, and was already described in detail in Section 3.3.1. In this case, the nacelle was supported by an integrated sting, connected to an external balance through the wind-tunnel ceiling. Unlike with the *PROWIM-T* setup, no sleeve was installed around the sting. The pitch angle was again set to 23.9 deg at $r/R = 0.75$.

4.3.2. PYLONS

The propeller was positioned upstream of a pylon to allow for measurements of the unsteady loading caused by the periodic impingement of the slipstream on a downstream aerodynamic surface, and to attempt to alleviate this unsteady loading with a flow-permeable leading edge. Separate pylon models were used to achieve these goals: a pylon with grooves and sleeve, and a pylon with a replaceable leading-edge insert. Both models featured a straight, untapered planform with NACA 0012 cross-section. The chord length c was equal to 0.200 m, with a span of 0.592 m. In this way, the propeller could be positioned in the center of the test section with the pylon mounted to the floor of the wind tunnel. A gap of 1 mm was left between the nacelle and the pylon, which allowed for external balance measurements of the propeller forces with and without pylon installed, and prevented the transmission of potential vibrations caused by the propeller to the pylon. The leading edge of the pylon was positioned at 0.100 m from the propeller center, corresponding to an axial spacing of 0.42 times the propeller diameter.

PYLON WITH GROOVES AND SLEEVE

The pylon with grooves and sleeve was used to measure the unsteady pressures on the surface caused by the periodic impingement of the propeller slipstream. It was equipped with a sleeve containing 16 microphones aligned in the streamwise direction, as discussed in more detail in Section 4.4.2. The sleeve had a width of 0.045 m and a thickness

of 0.005 m, while the shape was designed as an offset from the pylon's baseline NACA 0012 profile, resulting in a chord of $c_s = 0.210$ m. Quantitative flowfield measurements using PIV showed that the presence of the sleeve did not significantly alter the flowfield compared to that around a two-dimensional pylon with the cross-section of the sleeve. The sleeve was traversed in the vertical direction (pylon spanwise direction) through two grooves on each side of the pylon, centered at $X_{pyl}/c = 0.23$ and $X_{pyl}/c = 0.60$ from the leading edge. Figure 4.2 displays a technical drawing of the pylon model with grooves and sleeve installed in the test setup.

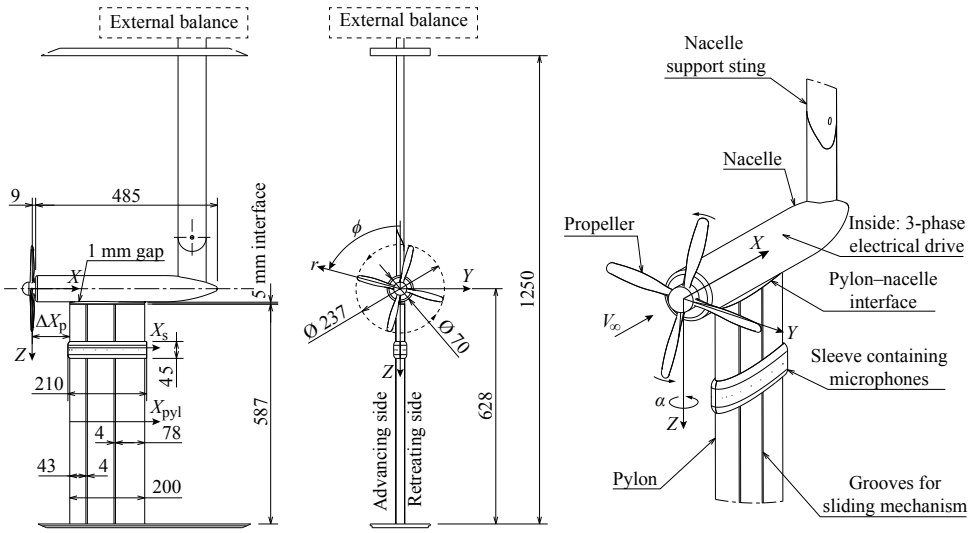

a) Side view b) Front view c) Isometric view

Figure 4.2: Technical drawing of the test setup with the pylon with grooves and sleeve. Dimensions in millimeters.

PYLON WITH REPLACEABLE LEADING-EDGE INSERT

A pylon featuring a replaceable leading-edge insert with a chord of 0.060 m (0.3c) was used to study the potential of a flow-permeable leading edge to alleviate the unsteady loading on the pylon caused by the impingement of the propeller slipstream. The replaceable insert was integrated into the leading-edge region of the top part of the pylon, allowing for different treatments at the pylon leading edge. The span of the insert was 0.100 m, meaning that it extended up to 19% of the propeller radius below the tip of the propeller. Figure 4.3 depicts a technical drawing of the test setup with the pylon with replaceable leading-edge insert.

An aluminum solid insert was used as baseline configuration to which the performance of four different flow-permeable leading edges was compared. The flow-permeable inserts were designed with a perforated skin covering an empty cavity underneath, as sketched in Fig. 4.4, and manufactured from polyamide by selective laser sintering. No optimizations were performed to define the characteristics of the flow-permeable inserts. Instead, the porosity distribution was taken from the work of Tinetti et al. [87–89] as the one which provided the best compromise between unsteady-load reductions and

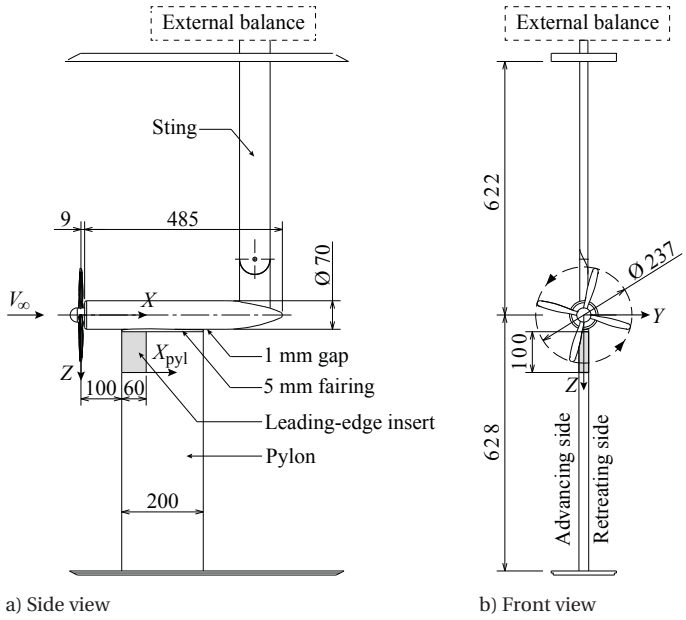

a) Side view b) Front view

Figure 4.3: Technical drawing of the test setup with the pylon with replaceable leading-edge insert. Dimensions in millimeters.

time-averaged airfoil performance for rotor–stator interactions. This meant a constant permeability of $\sigma_p^{max} = 0.22$ for $0 \leq X_{pyl}/c \leq 0.05$, after which the porosity decreased elliptically down to $\sigma_p = 0.10$ over the range $0.05 < X_{pyl}/c \leq 0.10$ [87–89]. The porosity factor σ_p is defined here as the ratio between open and closed surface area. No barriers were placed in the cavity to allow for communication between the pressure and suction sides of the airfoil, again following the work of Tinetti et al. [87–89]

Different hole diameters D_{hole} and cavity depths t_{cavity} were considered to study the sensitivity of the performance of the flow-permeable inserts to their design. Two hole diameters were used, equal to 0.5 and 1.0 mm, respectively, with a skin thickness of 1 mm. The default cavity depth was 3 mm (measured perpendicularly to the surface), while for the model with holes of 0.5 mm also depths of 1 and 5 mm were tested. An overview of the characteristics of the leading-edge inserts is provided in Table 4.1. The flow-permeable configurations are referred to as PxxCy, with xx the hole diameter in millimeters multiplied by ten, and y the cavity depth in millimeters. Figure 4.5 depicts a photograph of the P10C3 insert installed in the pylon downstream of the propeller.

Apart from modifying the unsteady pylon loads, the installation of a flow-permeable leading edge also affects the time-averaged aerodynamic performance of the pylon. This was quantified by measuring the lift and drag of an extended pylon model spanning the height of the test section (minus 2-mm gaps on both sides). The extended pylon featured the same profile and chord length as used for the pylon–propeller interaction measurements, while the replaceable inserts were positioned around the center of the wind tunnel. During these measurements, the propeller setup was removed, including the nacelle and support sting. The resulting test setup is shown in Fig. 4.6.

Table 4.1: Geometry characteristics of the leading-edge inserts.

Configuration	D_{hole}, mm	t_{cavity}, mm
Solid	N/A	N/A
P05C1	0.5	1
P05C3	0.5	3
P05C5	0.5	5
P10C3	1.0	3

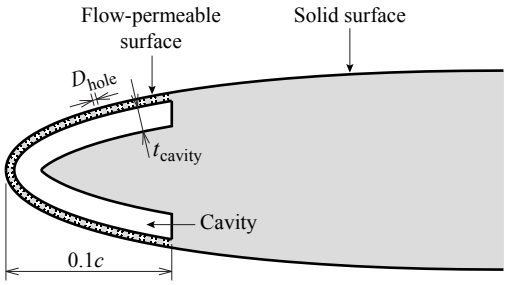

Figure 4.4: Geometry of the flow-permeable leading-edge inserts.

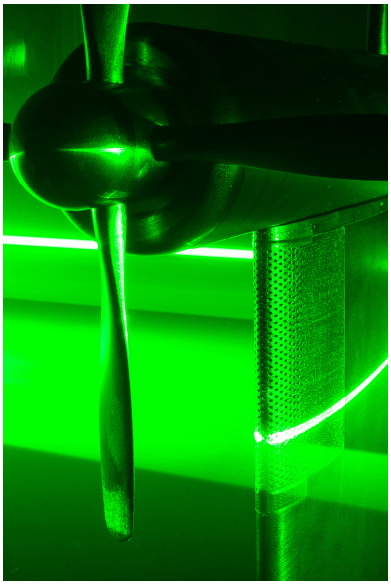

Figure 4.5: Photograph of the test setup with P10C3 flow-permeable leading-edge insert during particle-image-velocimetry measurements.

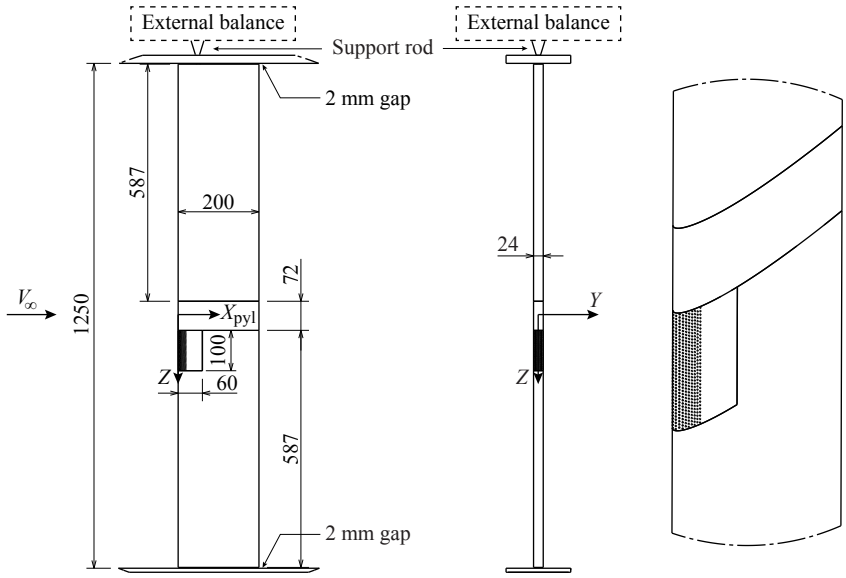

a) Side view b) Front view c) Isometric view

Figure 4.6: Experimental setup for the aerodynamic-performance measurements of the pylon without propeller. Dimensions in millimeters.

4.4. MEASUREMENT TECHNIQUES

4.4.1. QUANTITATIVE FLOWFIELD EVALUATIONS

Flowfield measurements were taken with PIV. Four different setups were used to characterize the flowfield in the slipstream of the isolated propeller (SSFOV), the propeller-slipstream distortion caused by the pylon (WFOV), the flowfield around the entire pylon (CWFOV), and the slipstream-impingement process at the pylon leading edge (LEFOV). The corresponding measurement setups are illustrated in Fig. 4.7. Tables 4.2 and 4.3 provide detailed measurement and postprocessing characteristics for the different setups. The same processing techniques were used as for the data measured with the *PROWIM-T* setup, as discussed in Section 3.4.1.

ISOLATED PROPELLER SLIPSTREAM (SSFOV)

The flowfield downstream of the isolated propeller (without pylon) was measured using stereoscopic PIV (SSFOV setup, Fig. 4.7a). Ignoring the influence of the support sting, which was placed sufficiently far downstream of the propeller plane to have a negligible effect on the propeller loading, the isolated propeller case is axisymmetric. Therefore, the complete slipstream could be mapped using measurements in a single plane positioned at the vertical position of the propeller axis ($Z/R = 0$). To clearly identify the characteristics of the blade wakes and tip vortices, the measurements were taken phase-locked with the propeller blade position. This was achieved using an optical one-per-revolution trigger signal integrated into the motor driving the propeller. Moreover, phase-uncorrelated measurements were performed to obtain a representation of the time-averaged flowfield in the propeller slipstream.

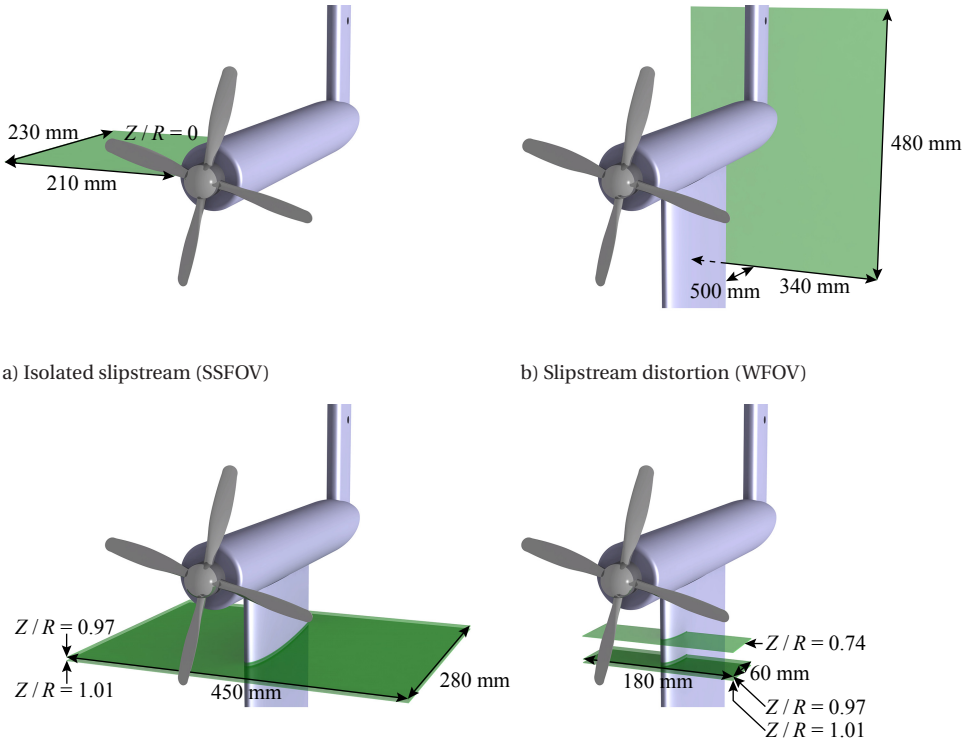

a) Isolated slipstream (SSFOV)

b) Slipstream distortion (WFOV)

c) Flowfield around pylon (CWFOV)

d) Slipstream impingement (LEFOV)

Figure 4.7: Illustration of the PIV setups.

PROPELLER-SLIPSTREAM DISTORTION CAUSED BY THE PYLON (WFOV)

The distortion of the propeller slipstream due to the interaction with the pylon was evaluated to better understand the spatial distribution of the unsteady surface pressures measured with the microphones (Section 4.4.2). A stereoscopic PIV setup was used with the field of view positioned at 2.5 times the chord length downstream of the pylon trailing edge (WFOV setup, Fig. 4.7b). Two measurement planes were used, after which the data were combined in postprocessing to obtain the final results. Measurements were taken both with and without the pylon, while only phase-uncorrelated acquisitions were performed. The microphone sleeve was not present during these measurements, and the pylon model without grooves was used.

FLOWFIELD AROUND ENTIRE PYLON (CWFOV)

A stereoscopic PIV setup, referred to as CWFOV, was employed to characterize the flowfield in a field of view surrounding the entire pylon without grooves (Fig. 4.7c). The CWFOV measurements were only taken for the solid and P10C3 configurations, since the largest differences were expected to occur between these two cases. Four cameras were installed in two separate stereoscopic layouts, synchronously acquiring the flowfields on each side of the pylon, after which the resulting vector fields were combined

Table 4.2: Measurement and postprocessing characteristics of the three stereoscopic PIV setups.

	SSFOV	WFOV	CWFOV
Laser		Nd:YAG 200 mJ	
Cameras		16 Mpixel CCD sensor	
Number of cameras	2	2	4
Objective		200mm $f/4$	
Field-of-view size	210×230 mm	340×480 mm	450×280 mm
Field-of-view position	$Z/R = 0.0$	$X_{\text{pyl}} = 3.5c$	$Z/R = 0.97, 1.01$
Pulse separation	20 μs	40 μs	19 μs
Max. particle displacement	14 pixel	13 pixel	12 pixel
Image pairs	250^a, 500^b	N/A^a, 500^b	250^a, 500^b
Final interrogation window size	12×12 pixel	32×32 pixel	48×48 pixel
Window overlap factor	75%	50%	50%
Vector spacing	0.2 mm	2.0 mm	2.0 mm
Uncertainty instant. velocity	$0.027V_\infty$	$0.018V_\infty$	$0.039V_\infty$
Uncertainty mean velocity	$0.002V_\infty{}^a$, $0.003V_\infty{}^b$	N/A^a, $0.003V_\infty{}^b$	$0.002V_\infty{}^a$, $0.005V_\infty{}^b$

^{a} phase-locked measurements, ^{b} phase-uncorrelated measurements

Table 4.3: Measurement and postprocessing characteristics of the planar PIV setup.

	LEFOV
Laser	2× Nd:YAG 200 mJ
Cameras	16 Mpixel CCD sensor
Number of cameras	2
Objective	200mm $f/4$
Field-of-view size	180×60 mm
Field-of-view position	$Z/R = 0.74, 0.97, 1.01$
Pulse separation	5 μs
Max. particle displacement	10 pixel
Image pairs	300^a, 500^b
Final interrogation window size	24×24 pixel
Window overlap factor	50%
Vector spacing	0.2 mm
Uncertainty instantaneous velocity	$0.018V_\infty$
Uncertainty mean velocity	$0.002V_\infty{}^a$, $0.003V_\infty{}^b$

^{a} phase-locked measurements, ^{b} phase-uncorrelated measurements

in postprocessing. A single laser was used to create light sheets on both sides of the pylon by splitting the laser beam, similarly to the setup described in Ref. [123]. Only the tip-vortex impingement region was considered, with measurement planes at $Z/R = 0.97$ and $Z/R = 1.01$. Phase-locked acquisitions were performed for a total of 17 phase angles to achieve high temporal resolution, while also uncorrelated measurements were taken.

PROPELLER-SLIPSTREAM IMPINGEMENT AT THE PYLON LEADING EDGE (LEFOV)
The effects of the slipstream on the flowfield near the pylon leading edge were quantified with a planar PIV setup (Fig. 4.7d), referred to as LEFOV. The fields of view surrounded the leading-edge region of the pylon, extending up to approximately $X_{\text{pyl}}/c = 0.20$. Two cameras were used to synchronously capture the flowfield on each side of the pylon, after which the resulting vector fields were combined in postprocessing. Illumination was provided by two lasers, one on each side of the test section. Cameras and lasers were traversed simultaneously to obtain measurements at three vertical positions, characteristic of the wake impingement region ($Z/R = 0.74$) and the tip-vortex impingement region ($Z/R = 0.97$ and $Z/R = 1.01$). The locations of the two planes in the tip-vortex impingement region were chosen to match the spanwise positions of maximum pressure fluctuations on the retreating and advancing blade sides of the pylon, respectively, as measured with the microphone sleeve (Section 4.4.2). Both uncorrelated and phase-locked acquisitions were performed. Phase-locking was again achieved using an optical one-per-revolution trigger signal installed in the electric motor driving the propeller. Six different phase angles were considered, corresponding to time instances before, during, and after impingement of the tip vortex on the leading edge of the pylon. The phase angle at the approximate time of impingement was defined as $\phi' = 0$ deg, while the remaining measurements were taken at −17.5, −2.5, 5, 27.5, and 52.5 deg. Again, the microphone sleeve was removed for these measurements, and the pylon model without grooves was used.

The phase-uncorrelated velocity fields were used to compute the pressure field at $Z/R = 0.97$ by solving the Poisson equation for the pressure, obtained from the incompressible Navier–Stokes equations. An extensive review of this technique is provided in Ref. [124]. Three-point central schemes were applied to compute the in-plane spatial derivatives. The Poisson equation, including the viscous terms, was then solved by means of the second-order scheme developed by Ragni, van Oudheusden, and Scarano [125]. Neumann conditions were specified on the inflow and outflow boundaries and on the airfoil contour, while Dirichlet boundary conditions were used to prescribe the total pressure on the lateral sides of the domain, where the flow was isentropic. Since the LEFOV setup only allowed for planar PIV measurements, the out-of-plane velocity component was unavailable. However, previous work for similar configurations has shown that this component has a negligible impact on the results [125]. This was confirmed by analysis of time-averaged pressure fields computed from the stereoscopic velocity data measured with the CWFOV setup.

The stochastic uncertainty of the pressure data was evaluated by propagating the statistical uncertainty of the PIV data through the routine used for the pressure computation. This was done following a Monte Carlo approach, in which the pressure was computed repeatedly from the time-averaged velocity field with superimposed random noise. The noise was obtained from a normal distribution with zero mean and standard deviation equal to the 0.3% uncertainty of the mean (phase-uncorrelated) velocity data from PIV. A total of 10,000 iterations were performed, resulting in a converged standard deviation of the pressure coefficient of 0.04. Note that this error estimate does not include the propagation of potential bias error in the PIV data.

4.4.2. PYLON LOADING

TIME-AVERAGED PYLON LOADING WITHOUT PROPELLER

The time-averaged lift and drag of the pylon with the different leading-edge inserts were quantified using a wake rake, wall-pressure taps, and an external six-component balance. For these measurements, the extended pylon configuration was used (Fig. 4.6).

Pylon Lift The lift generated by the pylon was measured with pressure taps distributed over four longitudinal strips installed in the walls of the test section. The pressure taps extended approximately $5c$ on both sides of the model along the tunnel walls. A lift correction factor of 1.13 was applied to the measured lift values to account for the effect of the finite axial extent of the pressure taps, following the method outlined in Ref. [126].

The section lift coefficient of the flow-permeable inserts was derived from the wall-pressure-tap data by scaling with the spanwise part of the pylon affected by the insert. This spanwise extent was determined from the wake-rake data (see below) as the spanwise range over which the measured drag coefficient of the pylon with flow-permeable insert was different from that obtained for the solid pylon. This is sketched in Fig. 4.8. The lift on the remainder of the pylon was considered the same for all configurations:

$$C_L = c_l^{\mathrm{s}} \left(\frac{b - b_{\mathrm{insert}}}{b} \right) + c_l^{\mathrm{insert}} \frac{b_{\mathrm{insert}}}{b}, \tag{4.1}$$

with b the span of the extended pylon model (Fig. 4.6), b_{insert} the spanwise extent of the pylon affected by the flow-permeable insert (Fig. 4.8), C_L the lift coefficient of the entire pylon (measured), c_l^{insert} the section lift coefficient of the flow-permeable insert (unknown), and c_l^{s} the section lift coefficient of the solid pylon (known from measurements with the solid pylon).

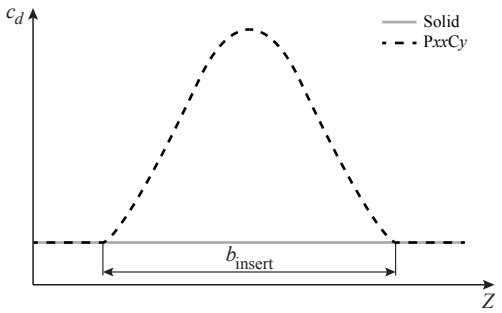

Figure 4.8: Determination of spanwise extent of the pylon affected by the flow-permeable insert, based on the sectional drag data.

Pylon Drag The sectional drag of the pylon was measured with a wake rake positioned at $2.6c$ downstream of the pylon trailing edge. At this position, the static pressure was verified to be recovered to the freestream value. The width of the rake equaled 0.504 m, over which 67 total-pressure probes and 16 static-pressure probes were distributed in two separate rows, offset in the vertical direction. The total-pressure probes were spaced nonequidistantly to achieve a maximum resolution of 3 mm in the center part of the rake.

The lateral position of the rake was changed for each data point to achieve this maximum spatial resolution over the entire pylon wake. All pressures were acquired simultaneously with an electronic pressure scanner recording at a rate of 5 Hz. The wake rake was traversed in the vertical direction to acquire the sectional drag distribution along the span of the pylon over a range of 1.5 times the chord (0.300 m). Starting at $Z = c$, the rake was moved upward at a constant velocity of 2.5 mm/s while the pressure data were acquired.

As sketched in Fig. 4.8, the spanwise drag distributions for the configurations with flow-permeable leading-edge insert showed a maximum near the center of the insert. The drag coefficient decreased toward the edges of the insert, eventually reaching the value obtained for the solid pylon. This was because only part of the pylon span was covered by the leading-edge insert. The maximum value measured over the span of the insert was taken here as a representative section drag coefficient of the insert. In this way, effects related to the finite span of the flow-permeable inserts were minimized.

UNSTEADY LOADING WITH PROPELLER

The unsteady loading on the pylon was quantified using flush-mounted microphones integrated into a sleeve, which was traversed in the spanwise direction as discussed in Section 4.3.2. On each side of the sleeve, 8 Sonion 8010T microphones were installed at (linear) distances from the leading edge of the sleeve of 0.02, 0.05, 0.10, 0.20, 0.35, 0.50, 0.70, and 0.90 times the sleeve chord (Fig. 4.9a). The microphones were placed recessed from the surface in individual cavities (Fig. 4.9b) with a resonance frequency of approximately 16.8 kHz. No protection grid was installed between the diaphragm of the microphones and the outer flow. The microphones measured in the frequency range of 10 Hz – 11.5 kHz, with a maximum input level of 112 dB at 1 kHz and a noise floor of 28 dBA. Since the maximum blade-passage frequency of the propeller was only 242 Hz during the unsteady pressure measurements, the frequency range of the microphones was sufficient to acquire the fundamental tone and up to 46 harmonics. A sampling rate of 25.6 kHz was used, with 30 s of acquisition time per data point. Considering the importance of a frequency-dependent calibration [47], such a calibration was performed using an external reference microphone with known frequency response. Phase-locking was applied during postprocessing to extract the periodic signal related to the propeller-slipstream impingement phenomena. The measurement data were divided into individual rotations using a simultaneously recorded optical one-per-revolution trigger signal, and subsequently averaged per phase angle. In this way, the parts of the signal that were not related to the periodic slipstream-impingement phenomena were eliminated.

4.4.3. PROPELLER LOADING

The thrust of the propeller was measured using an external six-component balance. Both the configurations with and without the pylon installed were considered. In this way, the impact of the installation of the pylon on the propeller performance could be assessed. Tare measurements were taken with the blades removed to subtract the drag contributions of the nacelle and support sting. The change in drag of the nacelle and support sting due to the increased dynamic pressure and swirl in the propeller slipstream was not corrected for. Evaluations of the results from repeated measurements showed that the thrust data were reproducible to within approximately 2%.

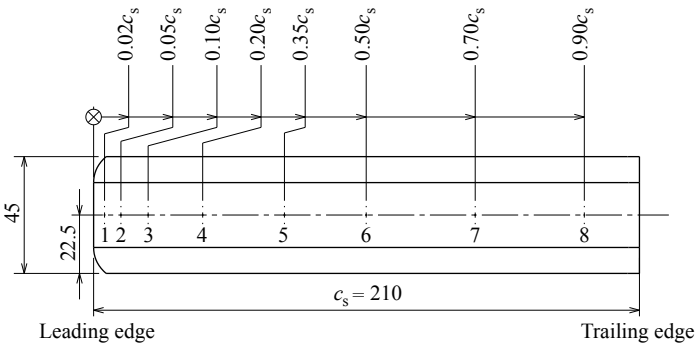

a) Side view

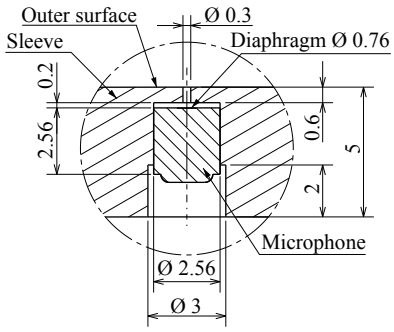

b) Cross-sectional view at microphone location

Figure 4.9: Technical drawing of the microphone sleeve; dimensional numbers in millimeters.

4.4.4. PROPELLER AND PYLON NOISE EMISSIONS

An acoustic array was used to measure the sound generated by the propeller and the leading-edge region of the pylon. The resulting far-field noise data served as indication of the source strength of the pressure fluctuations at the pylon surface. The array was integrated into the wall of the test section (retreating blade side), at a sideline distance of 0.9 m from the propeller center. Since the measurements were taken in the reverberant environment of a hard-walled test section, the array data may have been influenced by acoustic reflections. However, the data were used to compare relative differences between configurations at the same frequency. In such case, the effect of acoustic reflections is identical for all configurations, and thus will not affect the measured deltas.

The microphone array contained 64 PUI Audio POM-2735P-R microphones, with a sensitivity of -35 ± 2 dB (ref. 1 V/Pa) over a frequency range of $0.02 - 25$ kHz. Each microphone was installed recessed in a cavity covered by Kevlar fabric to reduce flow-induced noise stemming from the hydrodynamic pressure fluctuations in the boundary layer on the wind-tunnel wall. The microphone array had an approximately elliptical shape with a major axis in the flow direction of 0.93 m and a minor axis in the vertical direction of 0.48 m. Figure 4.10 displays the microphone locations with respect to the position of the models.

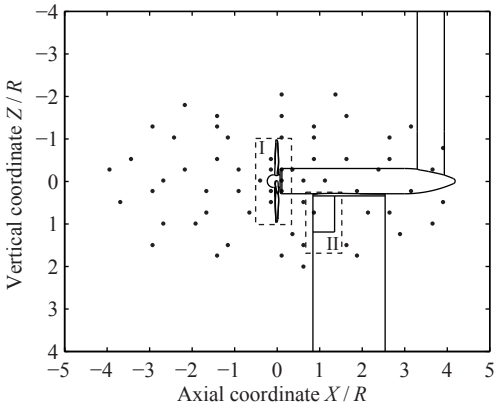

Figure 4.10: Microphone locations with respect to the position of the models. Dashed boxes indicate the propeller (I) and pylon (II) integration sectors used for source power integration.

The microphone-array data were acquired at a sampling rate of 50 kHz and with a recording time of 120 s. The acoustic data were averaged with time blocks of 4096 samples for each Fourier transform and windowed using a Hann function with 50% data overlap. With these parameters, the frequency resolution is 12.2 Hz and the expected error in the cross-spectrum estimate [127] is 1.9%. Conventional frequency-domain beamforming [128] was applied to obtain the source maps, which were computed for a grid with 1 mm spacing. The convection of sound waves was accounted for in the formulation of the steering vectors [129]. Furthermore, the main diagonal of the cross-spectral matrix was removed to suppress the effect of incoherent noise (mostly due to remaining pressure fluctuations caused by the boundary layer on the wind-tunnel wall) and improve the beamforming results [129].

The processed array data were used to synthesize the sound spectra emitted from the propeller and the leading-edge inserts by the technique of source power integration [129]. The two integration sectors used for this purpose are shown in Fig. 4.10. In each sector, the integrated beamforming results (per frequency) were normalized by the integral of a simulated unitary point source at the center of that integration sector, evaluated within the same spatial domain [130]. According to the Rayleigh criterion, the spatial resolution ΔR at the position of the scan plane and at the blade-passage frequency ($f = BPF = 848$ Hz) equals approximately [129, 131]:

$$\Delta R = Y \tan\left(\frac{1.22a}{D_\mathrm{a} f}\right) = 0.52 \text{ m}. \tag{4.2}$$

The effective diameter of the array D_a was taken here as the length of the array in the streamwise direction (0.93 m), since in this case the separation of sources in the flow direction is of interest. The result of Eq. 4.2 implies that the sources due to the propeller and pylon could not be separated at the lowest frequencies, because of the limited spatial resolution of the array. However, the array data could still be used to assess the relative change in the acoustic signature of the different pylon models with respect to the baseline solid configuration. This is discussed in more detail in Section 10.2.4.

4.5. TEST CONDITIONS

The propeller performance measurements and flowfield visualizations using PIV were done at a freestream velocity of 40 m/s, corresponding to Re_c = 530,000 and Re_D = 628,000. All microphone measurements, on the other hand, were taken at V_∞ = 10 m/s to maximize the dynamic range of the microphone data, leading to Re_c = 132,000 and Re_D = 157,000. Analysis of a number of PIV measurements taken at 10 m/s showed that the difference in freestream velocity and thus Reynolds number between the PIV and microphone measurements did not appreciably affect the dominant flow phenomena.

The effects of propeller thrust setting, propeller–pylon spacing, and angular inflow on the unsteady surface pressures were investigated by performing measurements with the pylon with grooves and sleeve for a range of propeller advance ratios, axial separations between propeller and pylon, and angles of attack. A baseline advance ratio of J = 0.8 was selected, at which the blades were significantly loaded, while preventing separated flow on the blade sections. The corresponding value of the thrust coefficient C_T was 0.095. In addition, advance ratios of 0.7, 0.9, and 1.0 were considered to assess the sensitivity of the unsteady pylon loads to the thrust setting. The propeller–pylon spacing ΔX was varied from 0.21 up to 0.84 times the propeller diameter, at a baseline spacing of $0.42D$. Finally, the angle of attack was changed from 0 up to 12 deg at 6 deg intervals, while measurements were also taken at −6 deg to obtain insight into the effect of the propeller rotation direction on the unsteady loads.

The measurements with the pylon with flow-permeable leading edge were mostly taken under symmetric inflow conditions, and at J = 0.8 only. The two-dimensional aerodynamic performance of the pylon without propeller, however, was also evaluated for the extended-span configuration at nonzero incidence angles ranging from −6 up to +12 deg. The test results were not corrected for wind-tunnel wall effects.

5

PUSHER-PROPELLER SETUP

Following the description of the experimental setups used for the tractor-propeller configuration in Chapters 3 and 4, the present chapter discusses the setup applied to study the pusher-propeller configuration, which was used to obtain results discussed in Chapters 8, 9, and 11. The setup was built around the instrumented propeller model designed and tested previously in the EU-funded Advanced Propulsion Integration Aerodynamics and Noise (APIAN) project. Since this propeller was now operated in nonuniform flow, the setup was denoted APIAN-INF. First, Section 5.1 gives an overview of the test setup, after which the wind-tunnel facility is introduced in Section 5.2. Then, the models are discussed in Section 5.3, followed by a description of the measurement techniques in Section 5.4. Finally, Section 5.5 provides an overview of the test conditions considered in the experiment.

5.1. OVERVIEW OF THE TEST SETUP

The *APIAN-INF* setup was used to study the aerodynamic and aeroacoustic performance of a semi-installed, single-rotating pusher propeller. For this purpose, measurements were taken of the propeller performance and noise emissions for configurations with and without an upstream pylon installed. The setup was also used to study the interaction effects caused by the installation of swirl-recovery vanes downstream of an isolated propeller. Since the key interaction effect for pusher propellers, the wake encounter, is directly related to the propeller blade loading (Section 2.2.2), a model was required with instrumented blades. The APIAN propeller [135–137] was selected since it was available, featured the required instrumentation, and represents a high-speed propeller design typical of the advanced propellers proposed for application in pylon-mounted pusher configurations.

The measurements were taken in the German–Dutch Wind Tunnels' (DNW) Large Low-Speed Facility, a large-scale industrial wind tunnel with semi-anechoic test section. In this way, also the acoustic performance of the propeller could be assessed. Figure 5.1 shows an overview of the test setup, while a definition of the Cartesian and polar

The contents of this chapter have been adapted from Refs. [132], [133], and [134].

coordinate systems is provided in Fig. 5.2. The origin of both coordinate systems is defined at the intersection of the propeller axis and the pitch change axis of the blades.

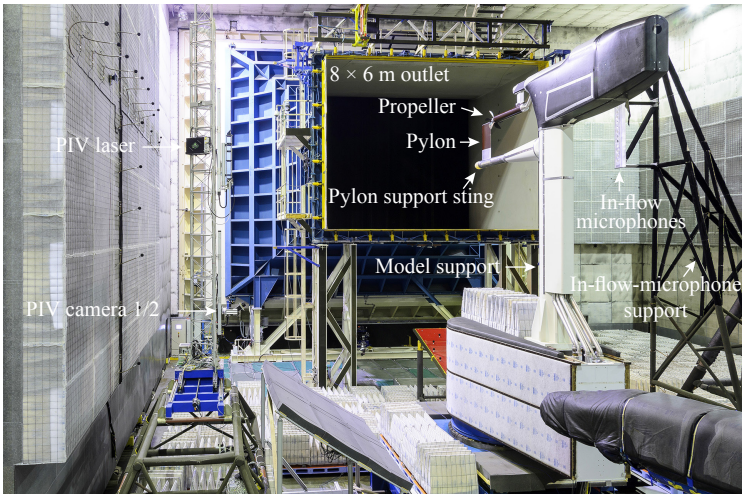

Figure 5.1: Overview of the *APIAN-INF* setup installed in the German–Dutch Wind Tunnel's Large Low-Speed Facility.

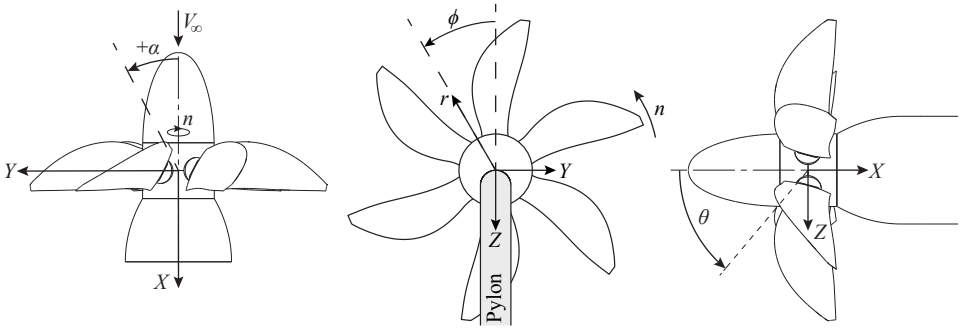

a) Top view b) Front view c) Side view

Figure 5.2: Definition of reference systems used for the *APIAN-INF* setup.

5.2. WIND-TUNNEL FACILITY

The experiments were performed at the Large Low-Speed Facility of the German–Dutch wind tunnels (DNW–LLF). This closed-circuit low-speed wind tunnel was operated in the open-jet configuration, with an 8 × 6 m outlet. At the selected freestream velocity (60 m/s), the turbulence intensity is 0.24% in the longitudinal direction and 0.13% in the lateral direction. The test hall is treated with acoustic liners to achieve a semi-anechoic environment.

5.3. MODELS

5.3.1. PROPELLER

The APIAN propeller has a diameter of 0.508 m and six highly swept blades. The propeller was driven by a pneumatic motor, housed inside a nacelle with a radius of $0.35R$. Toward the propeller, this radius gradually decreased to the hub radius of $0.24R$. The blade pitch angle at $r/R = 0.75$ was set to 40.4 deg with respect to the local chord line. The pitch angle is defined here such that the blade section is aligned with the rotational direction for a pitch angle of 0 deg. Photographs of the propeller model are shown in Fig. 5.3. The radial distributions of the chord length and blade pitch angle are provided in Fig. 5.4. The propeller was mounted on a fixed support (Fig. 5.1), which could be rotated around its vertical axis to perform tests at nonzero incidence angle. The system allowed operation at angles of attack of +6 deg and −6 deg, defined positive as in Fig. 5.2a.

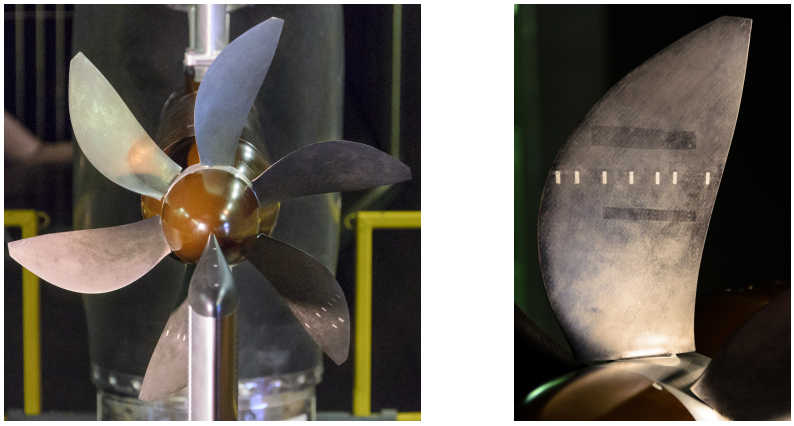

a) Front view of propeller installed downstream of pylon

b) Surface-pressure transducers integrated into blade

Figure 5.3: Photographs of the APIAN propeller.

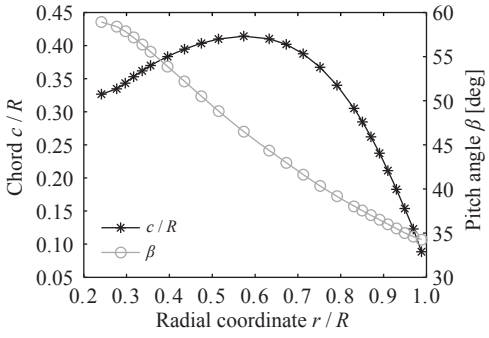

Figure 5.4: Radial distributions of the chord and pitch angle of the APIAN propeller blades.

5.3.2. PYLON

The pylon featured a straight, untapered planform of 0.489 m chord and 0.9 m span and a modified NACA 0010 profile. This simple design was selected to introduce the typical interaction effects occurring for a propeller–pylon combination, without attempting to address all design considerations relevant for an actual pylon applied on a high-speed airliner. This also simplified the integration of the trailing-edge blowing system discussed below. The fixed spacing between the pylon trailing edge and propeller leading edge was approximately 30% of the propeller diameter. A photograph of the pylon–propeller combination is provided in Fig. 5.5, while a technical drawing is provided in Fig. 5.6. The pylon was mounted on a fixed sting, which was connected to the support structure holding the propeller (Fig. 5.1). For the measurements taken with the isolated propeller, the pylon support sting was not removed.

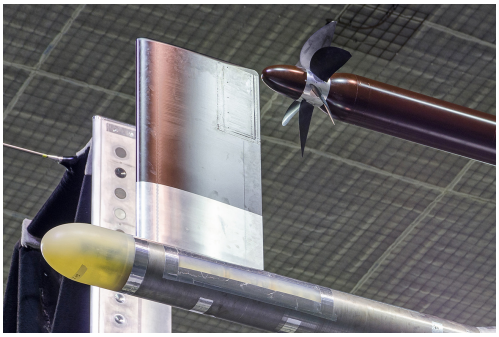

Figure 5.5: Photograph of the pylon model installed upstream of the propeller.

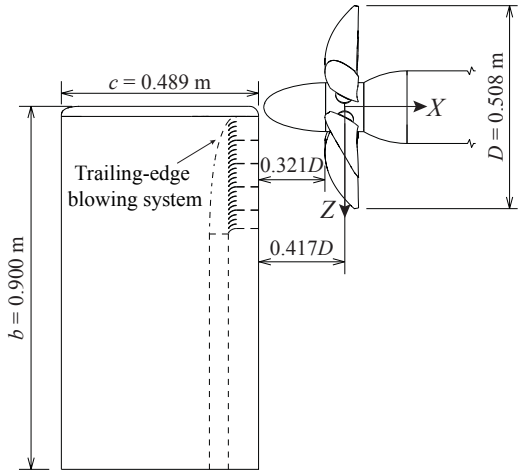

Figure 5.6: Technical drawing of the pylon–propeller combination, also displaying the internal geometry of the trailing-edge blowing system.

A pylon-blowing system was installed in the aft part of the pylon, with the outlet integrated into the trailing edge. This required an increase in trailing-edge thickness of the pylon to 0.8% of the chord, blended into the profile geometry from 60% of the chord onward. The blowing system was designed to provide uniform outflow along the spanwise part of the pylon positioned upstream of the propeller. The final design of the blowing system is indicated in Fig. 5.6 by the dashed lines. Figure 5.7 depicts the typical outflow profile of the blowing system for the range of blowing rates considered. The outflow velocities were measured in static conditions ($V_\infty = 0$ m/s), using a total-pressure probe that was traversed along the spanwise direction of the pylon. The spacing between the probe and the pylon trailing edge ΔX_{pyl} equaled 10% of the propeller diameter. The measured velocities were nondimensionalized with the maximum outflow velocity acquired along the span of the blowing system. A uniform velocity distribution was achieved upstream of the outboard part of the propeller blades ($0.6 \leq Z/R \leq 1.0$), with variations in outflow velocity of less than 5%. The four dips in the velocity away from the pylon tip are due to the struts in the outflow channel, positioned at the vertical locations indicated by the dashed lines in Fig. 5.7.

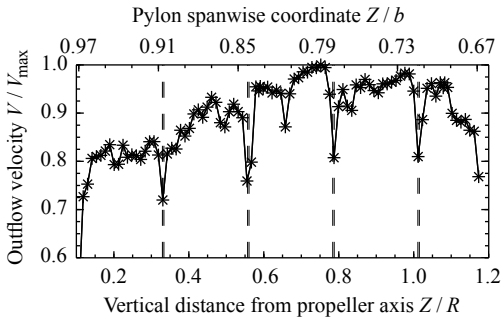

Figure 5.7: Pylon-blowing system outflow-velocity profile; $\Delta X_{\text{pyl}}/D = 0.1$, $V_\infty = 0$ m/s.

5.3.3. SWIRL-RECOVERY VANES

The *APIAN-INF* setup was also used to test the effect of swirl-recovery vanes on the aerodynamic and aeroacoustic performance of the configuration without pylon. A technical drawing of the propeller–SRV configuration is provided in Fig. 5.8.

The SRVs were designed to achieve a positive efficiency increase for advance ratios up to $J = 1.75$. Although not optimized for maximum aerodynamic or aeroacoustic performance, the used SRV geometry introduced all flow phenomena relevant to a typical propeller–SRV configuration, and therefore is considered adequate for the purpose of this thesis. The radial distributions of the chord and pitch of the SRV satisfying the design objective were defined using an in-house developed, low-fidelity design method based on the propeller analysis and design program XROTOR [138]. In this process, the number of SRVs, the SRV radius, and the propeller–SRV spacing were fixed. A total of five vanes was chosen to limit interaction noise by reducing the number of both total and concurrent interactions compared to an axisymmetric propeller–SRV configuration with six SRVs. The SRVs were distributed around the nacelle at circumferential angles

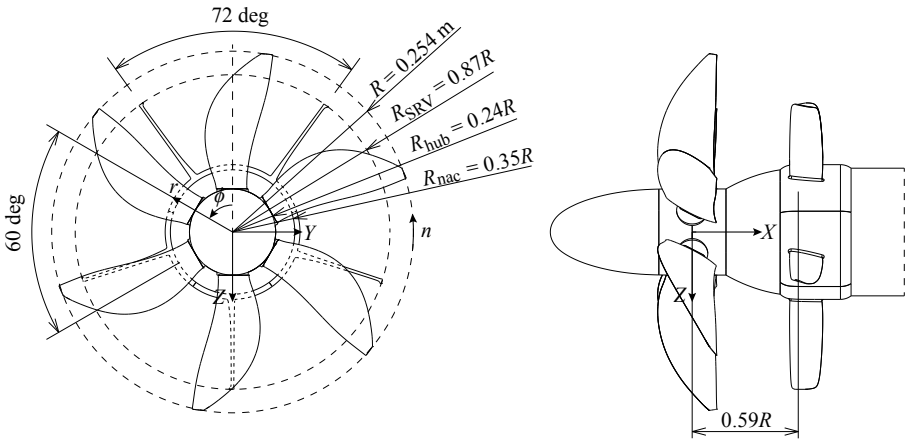

a) Front view b) Side view

Figure 5.8: Technical drawing of the propeller–SRV configuration.

of $\phi_{SRV} = 36, 108, 180, 252, 324$ deg. To minimize additional noise due to the interaction between the tip vortices of the propeller blades and the SRVs, the radius of the SRVs was set to 90% of the local contracted slipstream radius, resulting in an SRV radius of 87% of that of the propeller. The spacing between the propeller and the SRVs was equal to approximately 60% of the propeller radius. The selected distributions of the SRV chord and pitch angle are shown in Fig. 5.9. The pitch angle β_{SRV} is defined here in the same way as used for the propeller blade. A symmetrical airfoil was selected for the entire vane; manufacturing constraints on the minimum thickness led to the selection of an NACA 0009 profile. Later studies [32, 82], performed after the work with the current setup had been completed, showed that cambered airfoils typically provide better performance.

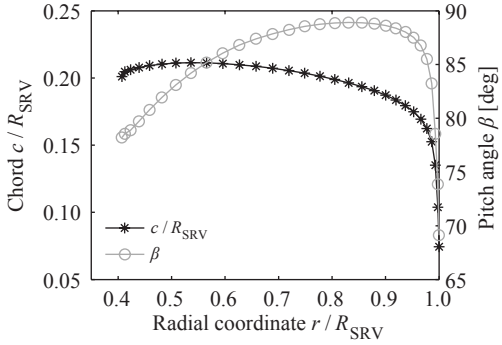

Figure 5.9: Radial distributions of the chord and pitch angle of the swirl-recovery vanes.

5.4. MEASUREMENT TECHNIQUES

5.4.1. QUANTITATIVE FLOWFIELD EVALUATIONS

Stereoscopic PIV was used to measure the flowfields in the pylon wake and propeller slipstream. This technique allowed for a characterization of the phase-locked velocity fields around the models in relatively large field of views with a limited measurement time. Furthermore, it enabled measurements of the pylon-wake characteristics with the propeller running, which would not have been possible with an intrusive technique such as a wake rake. To quantify the nonuniformity of the pylon wake, horizontal measurement planes were positioned between the pylon trailing edge and the propeller. The effects of the SRVs on the flowfield in the propeller slipstream were quantified using longitudinally adjacent planes downstream of the propeller, located slightly below the propeller axis at a vertical position of $Z/R = 0.03$ due to a small misalignment of the setup. The data extracted from the separate planes were combined in postprocessing to obtain a single representation of the propeller-slipstream flow. An illustration of the measurement-plane locations for the pylon-wake and propeller-slipstream measurements is provided in Fig. 5.10. Table 5.1 provides an overview of the most relevant measurement and processing characteristics. For both setups, the image pairs were acquired phase-locked with the blade position to obtain flowfield information for eleven different blade orientations. The time-averaged flowfields were approximated by averaging the results obtained at the individual phase angles. Postprocessing was performed using an iterative multi-grid method, and the uncertainty of the PIV data was estimated from the correlation statistics, following the method by Wieneke [119].

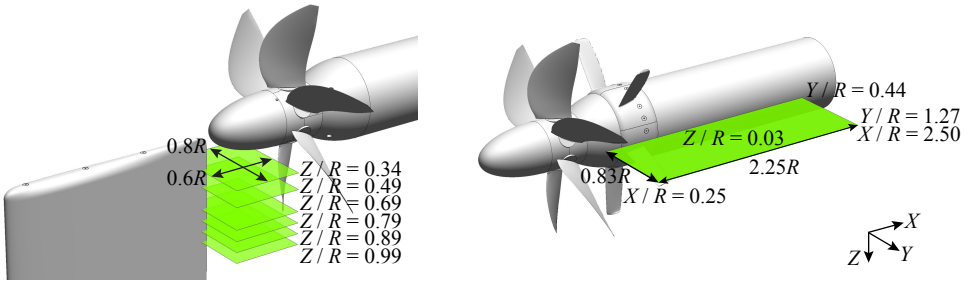

a) Pylon-wake flowfield

b) Propeller-slipstream flowfield

Figure 5.10: Illustration of the position of the PIV measurement planes.

5.4.2. PROPELLER LOADING

INTEGRATED LOADING

The propeller was connected to a three-spoke, six-component rotating shaft balance (RSB), shown in Fig. 5.11. The RSB provided measurements of the propeller thrust and torque during operation. These data were used to assess the effects of the wake encounter and tip-vortex recovery (Section 2.2.2) on the integrated propeller loading. Only the out-of-plane components (thrust and torque) were extracted from the RSB data, averaged over the measurement duration of 30 s per data point. For each configuration,

Table 5.1: Measurement and postprocessing characteristics of the stereoscopic PIV setups.

	Pylon Wake	Propeller slipstream
Laser	Nd:YAG 200 mJ	
Cameras	2× 1.3 Mpixel CCD sensor	
Objective	200mm $f/2.0$ + 2× teleconverter	
Field-of-view size	152 × 212 mm	572 × 212 mm
Field-of-view positions (Z/R)	0.34, 0.49, 0.69 0.79, 0.89, 0.99	0.03
Pulse separation	15 μs	15 μs
Max. particle displacement	5 – 7 pixel	5 – 7 pixel
Image pairs	330	550
Final interrogation window size	24 × 24 pixel	24 × 24 pixel
Window overlap factor	50%	50%
Vector spacing	2.0 mm	2.0 mm
Uncertainty instantaneous velocity	$0.036V_\infty$	$0.025V_\infty$

the final results were obtained by averaging over 24 – 39 repeated runs at constant operating conditions. The thrust data were corrected for the pressure acting on the back of the propeller hub by measuring the static pressure in the small gap between the hub and the front of the motor. The resulting force was subtracted from the raw RSB data to obtain the corrected propeller thrust. The design and operation of RSBs for propeller testing has recently been discussed in detail in Refs. [33, 139].

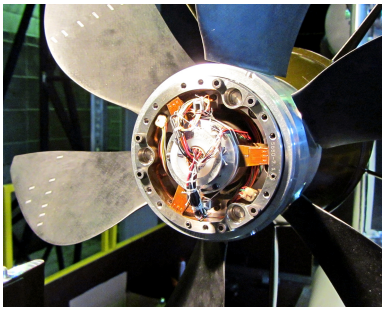

Figure 5.11: Rotating shaft balance integrated into the APIAN propeller model.

LOCAL BLADE LOADING

Miniature surface-pressure transducers were integrated into the propeller blades (Fig. 5.3b) to obtain phase-accurate pressure distributions. These were measured to quantify the unsteady blade loading caused by the wake encounter. At a radial station of $r/R \approx 0.65$, seven sensors were installed on both the suction side and the pressure side of a blade, providing data at chordwise locations of $x/c = 0.05, 0.15, 0.30, 0.45, 0.60, 0.70, 0.90$ on the suction side and $x/c = 0.05, 0.15, 0.30, 0.45, 0.60, 0.75, 0.90$ on the pressure side. The transducers measured pressure fluctuations in the frequency range of 0 – 10 kHz.

The measurements on the pressure and suction sides were taken on opposite blades. To obtain the correct phase-accurate pressure distributions, a constant 180-degree phase-offset was applied to the results from the pressure side. The measurement time per data point was 30 s, corresponding to approximately 2,000 − 3,500 propeller revolutions, depending on the rotational speed of the propeller. Calibration drifts were limited by correcting the output of each sensor with the barometric pressure measured during the zero run performed before and after each series of data points. Furthermore, the measurement data were averaged over 6 – 17 repeated runs per operating condition.

The raw measurement data were postprocessed by phase-locking with a one-per-revolution trigger signal. Subsequently, the measured pressure jump between the pressure and suction sides of the blade was integrated using the trapezoidal rule to obtain the local normal force (thus neglecting the contribution of the viscous forces). To account for the steep pressure gradient near the airfoil's leading edge, the pressure jump measured at the pressure transducer closest to the blade leading edge ($x/c = 0.05$) was prescribed up to the leading edge. Moreover, at the trailing edge a pressure difference of zero was prescribed. The validity of this approach was assessed by comparison with downsampled CFD data for the isolated propeller (Ref. [134]), which showed that the associated integration error was less than 1%. In addition to the time-accurate investigations, spectral analysis was performed on the raw data using Welch's method [140] with 94 blocks, no overlap, and Hann windows, resulting in frequency spectra with a frequency resolution of approximately 3 Hz.

5.4.3. PROPELLER NOISE EMISSIONS

The acoustic performance of the *APIAN-INF* setup was measured using microphones integrated into a wing-shaped structure [18] that was positioned in the flow at a sideline distance of 2.8 m from the propeller center. In-flow microphones were used to maximize signal amplitude and to avoid adverse effects due to refraction and scattering of sound when passing through the shear layer of the open-jet wind tunnel. A technical drawing of the aeroacoustic measurement setup is depicted in Fig. 5.12, while Fig. 5.13 provides a photograph of the microphone wing.

The microphone wing was equipped with 1/4-in pressure-field microphones, featuring a flat response (±1 dB) in the frequency range of 4 − 25,000 Hz, an electronic noise level below 40 dB, and a maximum input level of 168 dB. The microphones were installed recessed in the microphone wing, in individual cavities covered by wire meshes. By traversing the microphone wing through the test hall in the axial direction, a geometric axial directivity range was covered of $30 \leq \theta \leq 150$ deg. The corresponding circumferential directivity angles equaled $57 \leq \phi \leq 111$ deg. The definition of both directivity angles is included in Fig. 5.12. The data presented in this thesis were obtained using the microphone positioned at $\phi = 90$ deg, at a distance of $r_{\text{mic}} = 2.8$ m from the propeller center at $\theta = 90$ deg. All microphone acquisitions were performed for 30 s, at a sampling rate of 51.2 kHz. Spectral analysis and phase averaging of the data were performed using the same approach as taken for the pressure-transducer data (Section 5.4.2). To extract the purely harmonic content from the microphone data, bandpass filters were applied around the frequencies corresponding to the first ten multiples of the blade-passage frequency. In this way, the acoustic signatures were obtained associated with each of the individual propeller tones.

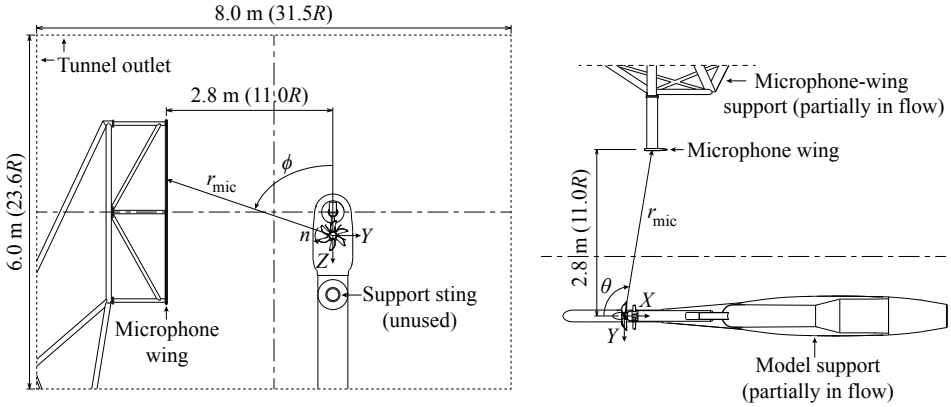

a) Front view b) Top view

Figure 5.12: Technical drawing of the aeroacoustic measurement setup.

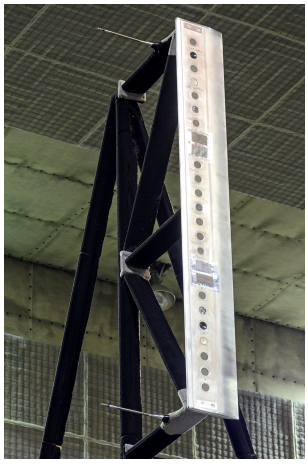

Figure 5.13: Microphone wing.

5.5. TEST CONDITIONS

All measurements with the *APIAN-INF* setup were taken at a freestream velocity of V_∞ = 60 m/s, which is the default setting for acoustic measurements at DNW–LLF. Three different propeller operating conditions were tested, corresponding to high, medium, and low thrust conditions. The associated advance ratios were J = 1.05, 1.40, and 1.75, leading to measured propeller thrust coefficients of C_T = 0.51, 0.36, and 0.18, respectively. The corresponding Reynolds number based on the diameter was Re_D = 2,000,000; the Reynolds number at a blade section of the propeller at $r/R \approx 0.65$ was in the range of 600,000−900,000. At the high thrust condition (J = 1.05), the propeller operated right at the onset of nonlinearities in the thrust response. Note that the thrust coefficients are significantly higher than for the tractor-propeller setups discussed in Chapters 3 and 4.

Whereas that propeller represented a low-speed design, typically operated at low disk loadings, the APIAN model is more typical of a high-speed propeller. Therefore, higher disk loadings were considered.

Symmetric inflow conditions were set for the largest part of the test program, while selected cases were also evaluated at angles of attack of $\alpha = \pm 6$ deg. The measurements at nonzero incidence angle were performed mostly at the low thrust setting, which was considered representative of an approach condition. The positive and negative incidence angles correspond to a positive angle of attack with inboard-up and outboard-up propeller rotation, respectively. Both cases are equally relevant for the pylon-mounted configuration, since an aircraft with pylon-mounted propellers would most likely feature a co-rotating propeller layout.

The pylon blowing system was operated at four different blowing rates to measure the development of the unsteady propeller blade loads and associated propeller noise levels with the injected mass flow. A zero-blowing configuration was used as the reference case to which the blown results could be compared. For the configurations with blowing enabled, an optimal rate was found that resulted in the largest reduction in propeller noise emissions. Additionally, blowing rates equal to 85% and 115% of this optimum were used. A blowing coefficient $c_{\dot{m}}$ was defined as the ratio between the blown mass flow and an equivalent freestream mass flow referenced to the outflow area of the blowing slit A_{out}:

$$c_{\dot{m}} = \frac{\dot{m}}{\rho_\infty V_\infty A_{\text{out}}} \tag{5.1}$$

At the selected freestream velocity of 60 m/s, the optimal blowing rate corresponded to $c_{\dot{m}} = 1.6$.

III

Interaction-Effects Analysis

6

WINGTIP-VORTEX ATTENUATION AND SWIRL RECOVERY

The key aerodynamic advantage of wingtip-mounted tractor propellers is a reduction of the wing induced drag. This chapter discusses the results of an experiment performed to investigate the working principle of the wingtip-vortex-attenuation and swirl-recovery mechanisms that are responsible for this aerodynamic advantage. The chapter focuses on the tractor-propeller configuration; swirl-recovery effects for pusher propellers are treated briefly in Chapter 8. The results provide the first thorough assessment of wingtip-vortex attenuation and swirl recovery for wingtip-mounted tractor propellers, despite the fact that the existence of these mechanisms has already been known for over 50 years. Following a characterization of the isolated propeller performance in Section 6.1, Section 6.2 presents a detailed aerodynamic analysis of the interaction effects, including measurements of integrated and sectional loading, and comprehensive flowfield evaluations. Subsequently, Section 6.3 compares the aerodynamic performance of the wingtip-mounted propeller configuration to that of a conventional configuration, with the propeller mounted on the inboard part of the wing. Finally, the key findings are summarized in Section 6.4. All data were acquired with the PROWIM-T setup treated in Chapter 3.

6.1. ISOLATED PROPELLER PERFORMANCE

The performance of the isolated propeller used in the *PROWIM-T* and *PROWIM-US* setups was determined as baseline for the wing-installed measurements discussed in the subsequent sections. The data were acquired with the sting-mounted configuration described in Section 3.3.1. Figure 6.1 provides the performance data and the radial distribution of the total-pressure rise downstream of the propeller as measured at $\alpha = -0.2$ deg and $Re_D = 620{,}000$. The performance data (Fig. 6.1a) feature markers at each individual data point recorded during the tests, together with curve fits through the thrust and power data. Third-order polynomials were used, since these resulted in the

The contents of this chapter have been adapted from Ref. [115], which provides all experimental data.

best fit through the data without introducing artifacts typical of higher-order fits. The fit through the propeller efficiency data was obtained by combining the polynomials computed for the thrust and power coefficients. The total-pressure data (Fig. 6.1b) were acquired at $\phi = 180$ deg.

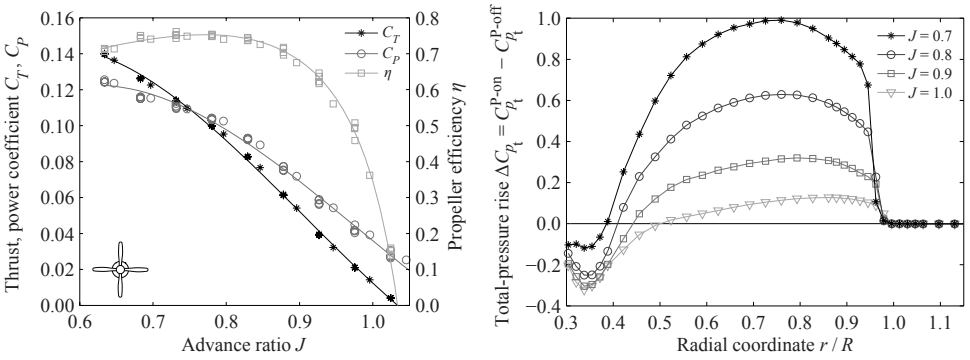

a) Performance map

b) Total-pressure rise at $0.15R$ downstream of propeller (nacelle edge located at $r/R = 0.295$)

Figure 6.1: Isolated propeller performance of the propeller used in the *PROWIM-T* and *PROWIM-US* setups; $\alpha = -0.2$ deg and $Re_D = 620{,}000$.

Figure 6.1a displays the expected quasi-linear behavior of the thrust and power coefficients at low propeller loading conditions. The maximum propeller efficiency is limited to about 0.75, occurring at $J = 0.77$. The total-pressure data depicted in Fig. 6.1b demonstrate that this relatively low efficiency can be attributed to a total-pressure loss on the inboard part of the blades. Previous numerical simulations [141] showed that this total-pressure loss was due to flow separation on the locally inefficient blade cross sections.

To extend the range of attainable thrust coefficients, measurements with the sting-mounted propeller were also taken at a lower Reynolds number of $Re_D = 470{,}000$. A third-order curve was again fit through the measurement data, as plotted in Fig. 6.2 together with the result obtained at $Re_D = 620{,}000$. The lowest advance ratio attainable at $Re_D = 470{,}000$ was equal to $J = 0.5$, at which a maximum thrust coefficient of $C_T = 0.168$ was achieved. At a given advance ratio, the reduction in Reynolds number of 25% led to a mean decrease in thrust coefficient of about 0.006 for the case at $Re_D = 470{,}000$ compared to the result at $Re_D = 620{,}000$.

When operating the propeller under asymmetric inflow conditions, the blade loading changes due to nonuniform inflow. For a positive angle of attack, the downgoing blade experiences an increase in loading, while the upgoing blade experiences a decrease in loading [36]. Figure 6.3 displays the effect of angle of attack on the time-averaged thrust coefficient, defined positive in the negative drag direction. At $J = 1.0$, the lowest thrust setting considered, the thrust coefficient increased by 0.027 when going from $\alpha = 0$ deg to $\alpha = 20$ deg. The sensitivity of the propeller thrust coefficient to the angle of attack decreases with increasing thrust setting because of the associated increase in rotational velocity of the blades. This decreases the angle-of-attack perturbation experienced by the blade sections at a given propeller angle of attack. At $J = 0.7$, the thrust was insen-

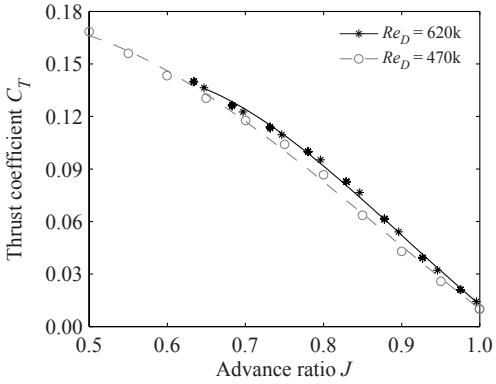

Figure 6.2: Effect of Reynolds number on the propeller thrust at $\alpha = -0.2$ deg.

sitive to the angle of attack over the entire range of inflow angles considered. The data shown in Fig. 6.3 are used in Section 6.3.3 to isolate the forces on the wing from the overall system forces (which include the propeller loading).

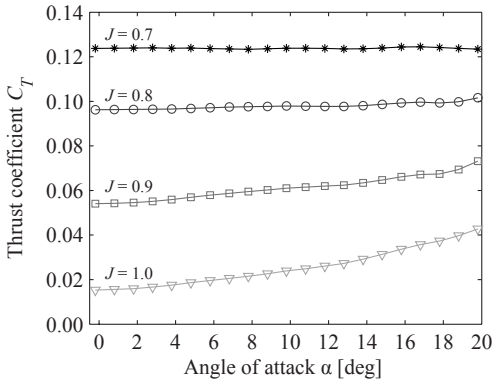

Figure 6.3: Effect of angle of attack on the propeller thrust at Re_D = 620,000.

6.2. AERODYNAMIC ANALYSIS OF INTERACTION EFFECTS

The mechanisms behind the attenuation of the wingtip vortex and the swirl recovery characteristic of the wingtip-mounted propeller (Section 2.2.1) were studied using Model I of the *PROWIM-T* setup (symmetric wing model with flap, see Figs. 3.6 through 3.8) at $Re_D = 640,000$. As discussed in Section 3.3.2, the inboard-up and outboard-up rotation cases were simulated with the same propeller model by deflecting the flap in the positive and negative directions, and inverting the data for the case with the negative flap deflection (Eq. 3.1). The data labeled as inboard-up and outboard-up with the propeller off represent the measurements taken with the positive and negative flap deflections without propeller installed. Considering the symmetry of the setup without propeller, the corresponding results should be the same.

6.2.1. WINGTIP-VORTEX ATTENUATION AND SWIRL RECOVERY

In the wingtip-mounted configuration, the propeller slipstream interacts with the flow around the wingtip. This strongly affects the lift and drag of the wing, as will be shown in Section 6.2.3. To assess the modification of the swirl due to the interaction between the propeller slipstream and the wingtip vortex, Fig. 6.4 provides contours of the swirl angle (Eq. 2.5) measured with PIV for the inboard-up and outboard-up rotation cases. The measurements were taken at $\alpha = -0.2$ deg for the inboard-up case and $\alpha = +0.2$ deg for the outboard-up case (due to a small misalignment), meaning that the lift coefficients differed between the considered propeller operating conditions. The absolute value of the swirl angle is shown in Fig. 6.4 to highlight the differences in magnitude of the swirl for both rotation directions. To compare the inboard-up and outboard-up rotation cases quantitatively, the mean swirl angle was computed over a circular domain enclosing the propeller slipstream:

$$\frac{1}{\pi(1.1R)^2}\int_0^{2\pi}\int_0^{1.1R}\theta r\,\mathrm{d}r\,\mathrm{d}\phi, \tag{6.1}$$

with the outer integration limit set to $1.1R$ to account for the slipstream distortion at the higher thrust settings. The corresponding results are listed in Table 6.1; note again that the lift coefficient varied between the different operating conditions considered.

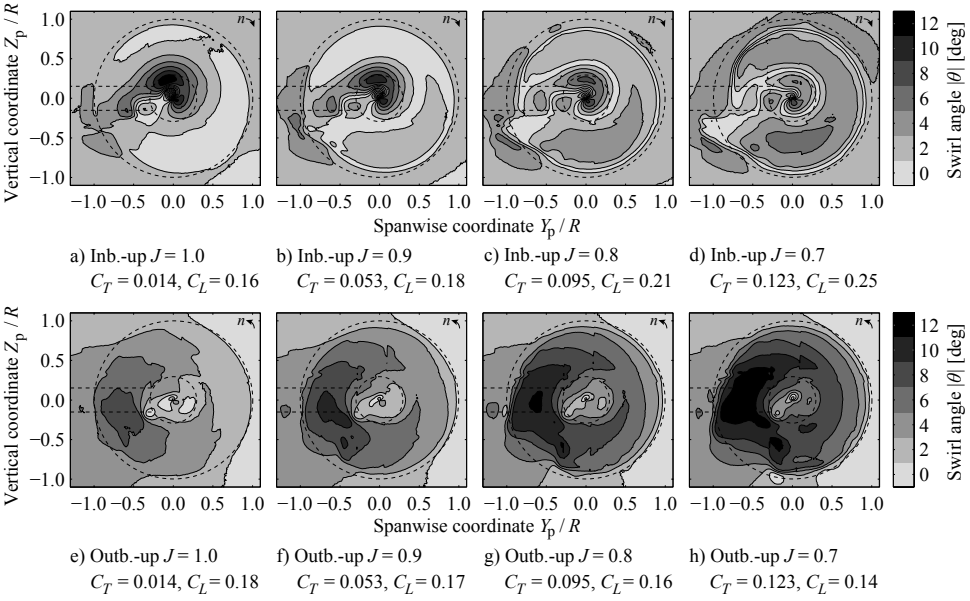

Figure 6.4: Absolute swirl angle at $1.5c$ downstream of the wing trailing edge at $\alpha = -0.2$ deg (inboard-up) and $\alpha = +0.2$ deg (outboard-up), $|\delta_f| = 10$ deg; rear view.

Figure 6.4 shows that, despite the higher lift coefficients, the remaining swirl in the wake of the models is considerably lower with inboard-up rotation than with outboard-up rotation, at all thrust settings. For the inboard-up rotation case, the swirl in the propeller slipstream partially cancels the swirl associated with the wingtip vortex, while with

Table 6.1: Mean swirl angle in the wake of the propeller–wing model at $\alpha = -0.2$ deg (inboard-up) and $\alpha = +0.2$ deg (outboard-up).

Operating point		C_L		$\frac{1}{\pi(1.1R)^2}\int_0^{2\pi}\int_0^{1.1R}\theta r\,dr\,d\phi$	
J	C_T	Inboard-up	Outboard-up	Inboard-up	Outboard-up
Prop-off	-	0.16	0.18	−2.9 deg	−3.0 deg
1.0	0.014	0.16	0.18	−2.0 deg	−3.5 deg
0.9	0.053	0.18	0.17	−1.0 deg	−4.5 deg
0.8	0.095	0.21	0.16	−0.1 deg	−5.4 deg
0.7	0.123	0.25	0.14	+0.7 deg	−6.3 deg

outboard-up rotation these two contributions are in the same direction and hence the total swirl is amplified. This is substantiated by Table 6.1, which highlights that with inboard-up rotation the negative swirl of the wingtip vortex is increasingly compensated for by the positive swirl contribution by the propeller when increasing the thrust setting. With outboard-up rotation, on the other hand, the swirl angle becomes increasingly negative with increasing thrust setting. Apart from the modification of the mean swirl, Fig. 6.4 also shows that the interaction between the propeller slipstream and the wingtip vortex changes the swirl in the vicinity of the wingtip-vortex core (near $Y_p/R = Z_p/R = 0$). With inboard-up rotation, the local maximum in swirl is decreased, confirming the existence of the wingtip-vortex-attenuation mechanism. For the case with outboard-up rotation, a strong maximum in swirl occurred near the flap edge due to the combined effects of the flap-edge vortex and the propeller-blades' tip vortices [142]. For a model without a flap, this local maximum in swirl would not occur; instead, the swirl would be more spread out over the entire disk.

6.2.2. SYSTEM PERFORMANCE

The difference in swirl downstream of the model with inboard-up and outboard-up rotation (Fig. 6.4, Table 6.1) can be expected to cause a strong offset in system performance between these two cases. This is confirmed by Fig. 6.5, which displays the lift and drag of the entire system, including propeller forces, with inboard-up and outboard-up rotation. The fact that the propeller-off results for the inboard-up and outboard-up cases (measured with $\delta_f = +10$ deg and $\delta_f = -10$ deg) overlap, confirms the symmetry of the setup between the positive and negative flap settings, except at the highest positive angles of attack at which the stall behavior was slightly different for the two cases. This is very likely due to an asymmetry in the model.

In terms of lift (Fig. 6.5a), the interaction between the propeller slipstream and the wing increases the system performance for the case with inboard-up rotation. With outboard-up propeller rotation, on the other hand, the lift decreases compared to the propeller-off case for angles of attack below approximately 4 deg, and the lift is lower than with inboard-up rotation over the entire angle-of-attack range, including the maximum lift coefficient. The propeller–wing interaction also affects the system drag (Fig. 6.5b). Again, a clear benefit can be seen for the case with inboard-up rotation. This benefit increases with increasing lift coefficient and thrust setting.

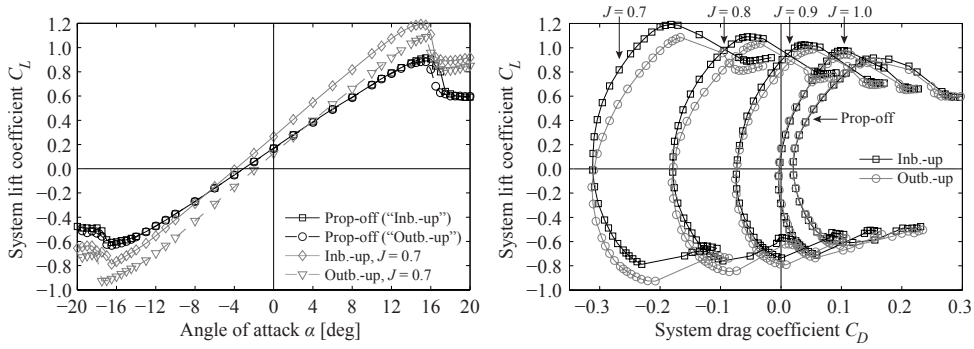

a) Lift polar b) Drag polar

Figure 6.5: System lift and drag polars (including propeller forces) with inboard-up and outboard-up rotation; $|\delta_f| = 10$ deg.

6.2.3. WING PERFORMANCE

The aerodynamic advantages observed in Fig. 6.5 for the case with inboard-up rotation are a direct result of the interaction between the propeller slipstream and the wing. To identify the sources of the dominant interaction mechanisms, the local pressure data on the wing were analyzed. In this way, the impact of the interaction effects on the wing performance and propeller performance could be separated. The pressure data were integrated to obtain the section lift and pressure-drag coefficients at 8 spanwise stations. Figure 6.6 presents the resulting lift distributions for the inboard-up and outboard-up rotation cases for all thrust settings considered, at $\alpha = 0$ deg. The wing loading decreased toward the root of the wing ($Y/s_s = 0$) because the flap did not cover the entire span of the wing. This will have modified the lift distribution somewhat when compared to a cambered wing without flap deflection.

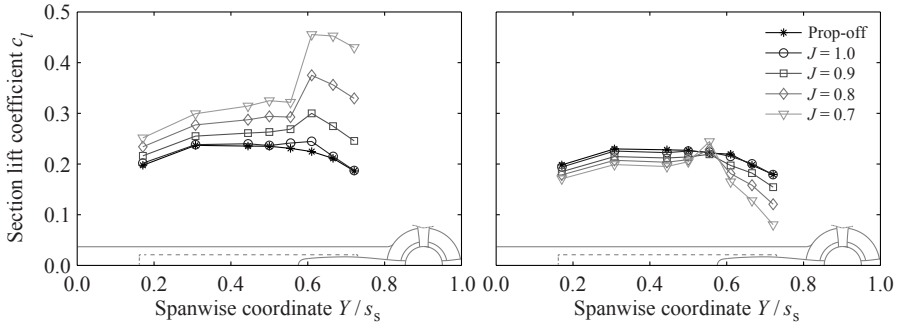

a) Inboard-up b) Outboard-up

Figure 6.6: Effect of propeller rotation direction and thrust setting on the spanwise lift distribution at $\alpha = 0$ deg; $|\delta_f| = 10$ deg.

Figure 6.6 confirms that the interaction with the propeller slipstream increases the wing lift with inboard-up rotation and decreases the wing lift with outboard-up rotation. This is due to the difference in upwash experienced by the wing for the two cases, as sketched in Fig. 2.8. With inboard-up rotation, the wing experiences upwash and higher dynamic pressure on the spanwise part washed by the slipstream, thereby enhancing the lift compared to the propeller-off case. For the outboard-up rotation case, the direction of the propeller swirl is reversed, causing a downwash contribution to the local wing inflow and a resulting reduction in lift compared to the propeller-off case. The interaction effects are amplified with increasing propeller thrust setting due to the associated increase in swirl and dynamic-pressure rise induced by the propeller.

With the propeller on, a steep lift gradient occurs around the slipstream boundary ($Y/s_s \approx 0.6$). This lift gradient causes vorticity to be shed, which modifies the inflow angle on the spanwise part of the wing not immersed in the propeller slipstream. As illustrated before in Fig. 2.9a, an upwash occurs with inboard-up rotation and a downwash with outboard-up rotation. Consequently, with inboard-up rotation the local lift increases compared to the propeller-off result also outside of the slipstream wash (Fig. 6.6a). The spanwise lift gradient becomes steeper with increasing thrust setting due to the associated increase in swirl and dynamic pressure in the slipstream region. For the case with outboard-up rotation, the situation is reversed. However, the spanwise lift gradient is smaller than for the inboard-up rotation case due to the opposing effects of the downwash and increased dynamic pressure in the slipstream (Fig. 2.8b). Therefore, the modification of the wing lift on the spanwise part of the wing away from the slipstream is smaller with outboard-up rotation than with inboard-up rotation.

The shedding of vorticity associated with the spanwise lift gradient also induces velocities in the spanwise direction (Fig. 2.9b and 2.9c), which distort the propeller slipstream during and after its interaction with the wing [36, 45, 143–145]. The resulting spanwise shearing of the slipstream is visualized in Fig. 6.7 by contours of the total-pressure coefficient measured downstream of the models, with inboard-up rotation ($\alpha = -0.2$ deg) and outboard-up rotation ($\alpha = +0.2$ deg). For reference, the propeller-off data are also included; these display the expected regions of total-pressure loss in the wing wake, wingtip vortex, and nacelle wake. Furthermore, the flap-edge vortices can be recognized, which will have led to a reduction in strength of the wingtip vortex.

The propeller-on data show that the slipstream moves away from the propeller axis on the advancing blade side, and toward the propeller axis on the retreating blade side. This occurs for both the cases with inboard-up and outboard-up rotation, matching the directions of the spanwise flow depicted in Fig. 2.9b and 2.9c. The slipstream distortion becomes stronger with increasing thrust setting due to the associated increase of the spanwise lift gradient (Fig. 6.6). The spanwise shearing of the slipstream modifies the local wing performance near the slipstream edge. This especially affects the unsteady lift and drag response, as discussed in Chapter 7 of this thesis. However, also the time-averaged wing loading is altered. This can be seen in Fig. 6.6b by the sudden increase in lift at $Y/s_s = 0.555$ for the case with outboard-up rotation at the highest thrust coefficient ($J = 0.7$, $C_T = 0.123$). The strong spanwise displacement of the slipstream at the high thrust setting (Fig. 6.7j) made that at this spanwise station part of the wing's suction side was washed by the slipstream, while the pressure side was not.

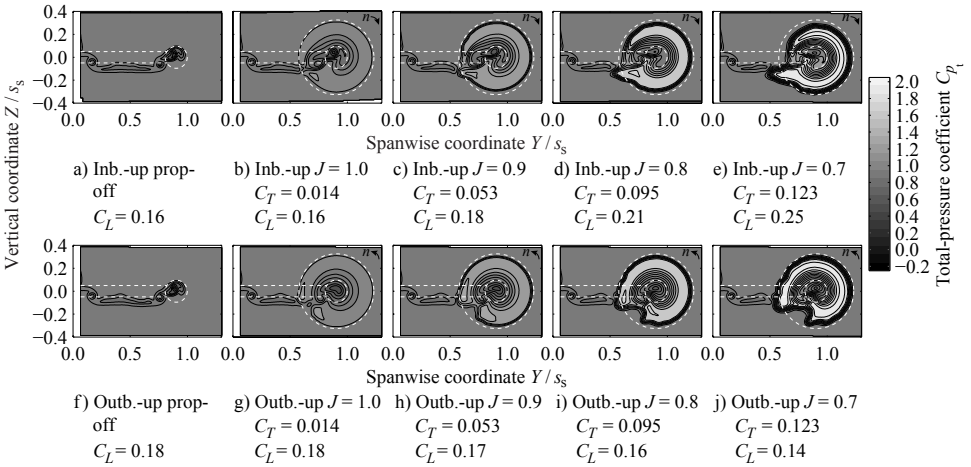

Figure 6.7: Effect of propeller rotation direction and thrust setting on the slipstream distortion at $\alpha = -0.2$ deg (inboard-up) and $\alpha = +0.2$ deg (outboard-up), $|\delta_f| = 10$ deg; rear view.

The rise in lift due to the slipstream interaction with inboard-up rotation (Fig. 6.6a) is mostly due to an increase in loading on the front part of the profile, which becomes more pronounced with increasing thrust setting. This is shown by the pressure distributions provided in Fig. 6.8, in which the results measured at $J = 1.0$ and $J = 0.8$ are omitted for clarity. The results are given for two spanwise stations: one inside the slipstream ($Y/s_s = 0.666$) and one outside the slipstream ($Y/s_s = 0.445$). Markers are displayed at the individual sampling locations, while the lines indicate the inter- and extrapolated results used as input for the integration procedure applied to compute the sectional lift and pressure drag on the wing. The local jump in the pressure distribution at $X/c = 0.75$ is due to the deflected flap. The effects for the outboard-up rotation case (not shown) were similar but opposite, with a decrease in front loading due to the downwash induced by the propeller.

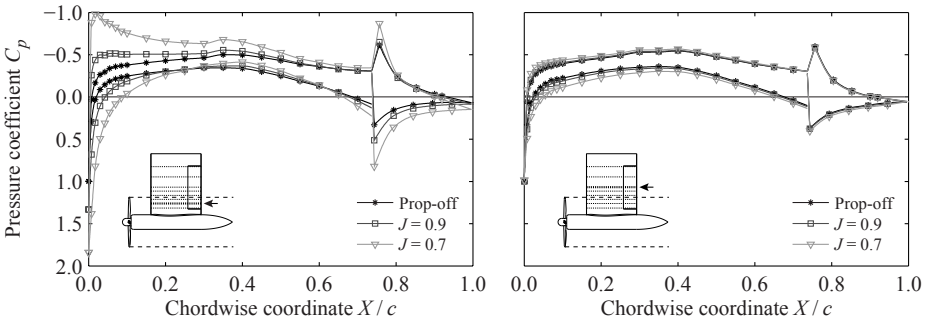

Figure 6.8: Effect of propeller thrust setting on the wing pressure distribution with inboard-up rotation at $\alpha = 0$ deg; $|\delta_f| = 10$ deg.

To assess the impact of the propeller on the wing lift under asymmetric inflow conditions, the pressure integration was performed for all considered angles of attack. Figure 6.9 presents the resulting lift polars at the same spanwise stations as considered in Fig. 6.8. Similarly as for the integral forces depicted in Fig. 6.5, both the inboard-up and outboard-up rotation cases are shown. Only the highest thrust setting $J = 0.7$ ($C_T = 0.123$) is considered here for clarity, together with the propeller-off results. The effects for the intermediate thrust settings were similar, albeit with smaller differences in amplitude compared to the propeller-off case.

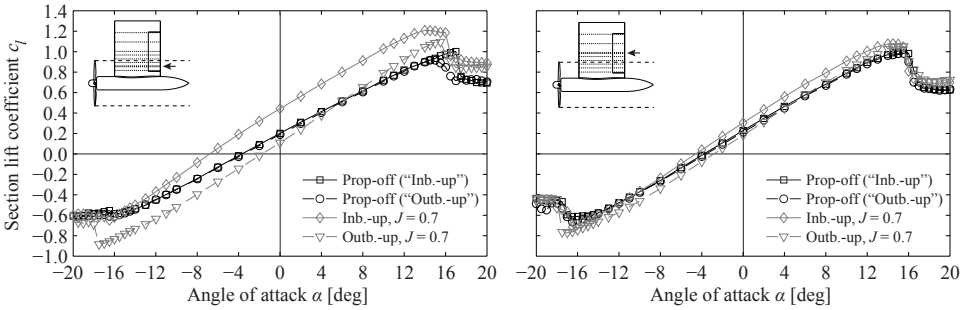

a) Inside slipstream ($Y/s_s = 0.666$) b) Outside slipstream ($Y/s_s = 0.445$)

Figure 6.9: Effect of propeller thrust setting on the wing's section lift polars; $|\delta_f| = 10$ deg.

The section lift polars plotted in Fig. 6.9 substantiate the mechanism sketched in Figs. 2.8 and 2.9. The upwash and increased dynamic pressure in the slipstream experienced with inboard-up rotation increase the sectional lift compared to the propeller-off case over the entire angle-of-attack range. The same effect, although with smaller magnitude, occurs outside of the slipstream due to the induced velocities associated with the spanwise lift gradient on the wing and the decrease in downwash due to wingtip-vortex attenuation. For the outboard-up rotation case, on the other hand, the propeller swirl is experienced as a downwash, resulting in a loss of lift which is only partially compensated for by the increased dynamic pressure in the slipstream. The effective downwash induced by the propeller leads to an increase of the stall angle with outboard-up rotation, while with inboard-up rotation the stall angle decreases compared to the propeller-off case. The behavior of the system lift with propeller on, shown before in Fig. 6.5, falls between the local lift polars measured inside and outside the slipstream. This confirms that the measured change in system lift was due to the local changes to the wing pressure distribution, which behaved according to the sketches provided in Figs. 2.8 and 2.9.

As shown in Fig. 6.5b, the modification of the up- and downwash experienced by the wing with the propeller on results in clear shifts in the system drag. To relate this to a modification of the wing drag, the pressure data were integrated to obtain polars of the pressure drag as a function of angle of attack, as shown in Fig. 6.10. Note that these polars do not include the viscous drag term, and therefore only represent part of the total drag acting on the wing. Furthermore, the integration of the pressure in the drag direction features a relatively high uncertainty, as illustrated by the difference between the propeller-off results obtained from the configurations with opposite flap deflections.

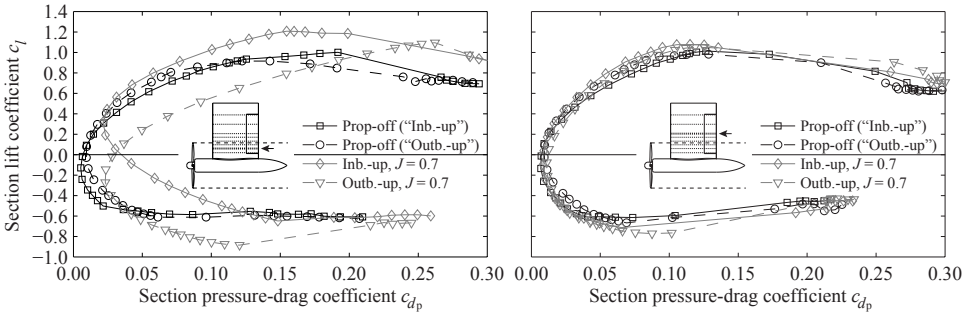

a) Inside slipstream ($Y/s_s = 0.666$) b) Outside slipstream ($Y/s_s = 0.445$)

Figure 6.10: Effect of propeller thrust setting on the wing's section pressure-drag polars; $|\delta_f| = 10$ deg.

The pressure-drag polars presented in Fig. 6.10 show that at positive lift coefficients, the wing performance improves with inboard-up rotation and worsens with outboard-up rotation compared to the case without propeller. Inside the slipstream, the propeller-induced swirl modifies the wing induced drag by tilting the lift vector. With inboard-up rotation, the propeller swirl is experienced as upwash. Therefore, at positive lift coefficients the lift vector is tilted forward and the induced drag decreases: swirl recovery [36]. Furthermore, the form drag decreases due to the lower angle of attack required to reach a given lift coefficient. With outboard-up rotation, the opposite situation occurs, and the pressure drag increases compared to the propeller-off case. The modification of the wingtip vortex due to the interaction with the propeller slipstream should enhance the swirl-recovery effect. The decrease in downwash occurring with inboard-up rotation reduces the induced drag, while with outboard-up rotation the downwash is amplified, thus the induced drag increased. At negative lift coefficients, for which the wingtip vortex rotates in the opposite direction, both the swirl-recovery and wingtip-vortex-attenuation mechanisms are reversed, and the case with outboard-up rotation displays best performance. The trends in the pressure-drag polars shown in Fig. 6.10 match with the behavior of the system drag presented in Fig. 6.5b. This confirms that the reduction in system drag with inboard-up rotation is directly related to the modification of the swirl by the interaction of the propeller slipstream with the wing.

Apart from the effects due to swirl, the wing drag is also affected by the modified dynamic pressure in the spanwise part of the wing washed by the propeller slipstream. The local increase in velocity causes an increase in pressure drag and viscous drag compared to the propeller-off case, with both propeller rotation directions. This is reflected in Fig. 6.10a by the lower pressure drag for the propeller-off case at small values of the wing lift coefficient ($-0.5 < c_l < 0.4$).

6.2.4. PROPELLER PERFORMANCE

So far, only the downstream interaction of the propeller slipstream with the wing has been discussed. The upstream effect of the wing on the propeller was quantified by total-pressure measurements taken at $0.15R$ downstream of the propeller plane for the wing-installed configuration. Figure 6.11 presents contours of the total-pressure rise due

to the propeller for the configurations with inboard-up and outboard-up rotation at an advance ratio of $J = 0.8$ ($C_T = 0.095$). The measurements were taken at $\alpha = -0.2$ deg for the inboard-up case and $\alpha = +0.2$ deg for the outboard-up case due to a small misalignment of the model. Combined with the change in slipstream interaction effects for the different rotation directions, this means that the wing lift coefficients were different for the inboard-up ($C_L = 0.21$) and outboard-up ($C_L = 0.16$) cases.

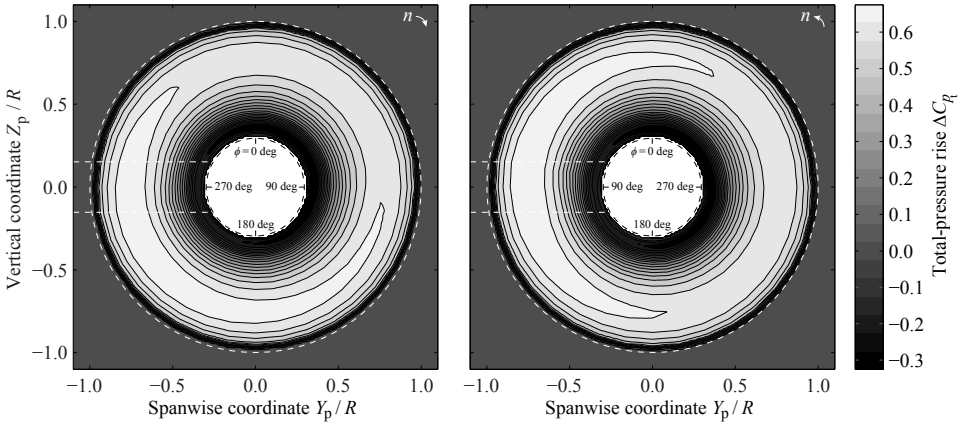

a) Inboard-up ($C_L = 0.21$) b) Outboard-up ($C_L = 0.16$)

Figure 6.11: Total-pressure rise at $0.15R$ downstream of the propeller at $J = 0.8$ ($C_T = 0.095$), $\alpha = -0.2$ deg (inboard-up) and $\alpha = +0.2$ deg (outboard-up), $|\delta_f| = 10$ deg; rear view.

As discussed in Section 2.2.1, the upstream perturbation of the propeller inflow by the wing is due to a combination of blockage and upwash. Independent of the propeller rotation direction, the blockage effect reduces the axial velocity at the propeller plane, thereby increasing the local blade loading. The upwash affects the effective tangential velocity experienced by the blades when passing by the wing: the tangential velocity decreases with inboard-up rotation and increases with outboard-up rotation. Therefore, the two effects partially cancel for the case with inboard-up rotation. Consequently, for this case the resulting upstream effect of the wing on the propeller loading is smaller than with outboard-up rotation, and peaks somewhat further away from the wing. This can be seen in Fig. 6.11 by the smaller increase in loading near the wing for the inboard-up rotation case. For both cases, however, the upstream effect of the wing on the blade loading was limited. Compared to the total-pressure rise measured for the isolated propeller (Fig. 6.1b), the circumferentially integrated loading increased by 1.7% with inboard-up rotation and 2.3% with outboard-up rotation. The maximum circumferential variations in blade loading were also small, as can be seen in Fig. 6.12a for both rotation directions. The data are provided for a radial station of $r/R = 0.76$, at which the blade loading was at a maximum, while the circumferential blade position ϕ is defined as in Figs. 3.8 and 6.11. With both rotation directions, the maximum perturbation of the blade loading was about 2% of the time-averaged result.

For the inboard-up rotation case, the sensitivity of the blade-loading variations to the propeller thrust setting was assessed by also taking measurements at the other advance

ratios. Figure 6.12b shows that the unsteady propeller loading features a nonmonotonic variation with the propeller thrust setting. On the one hand, an increase in propeller thrust amplifies the downstream wing loading (Fig. 6.6), which leads to a stronger perturbation of the propeller inflow due to increased upwash. On the other hand, the sensitivity of the propeller loading to inflow perturbations decreases with increasing thrust setting, as shown by the variation of the isolated propeller's thrust coefficient with angle of attack (Fig. 6.3). For the current configuration, the maximum unsteady blade loads occurred at $J = 0.9$ ($C_T = 0.053$), for which a maximum change in blade loading was measured of 3% of the time-averaged result. Therefore, it is concluded that at the considered angle of attack of around 0 deg, the upstream effect of the wing on the propeller was small.

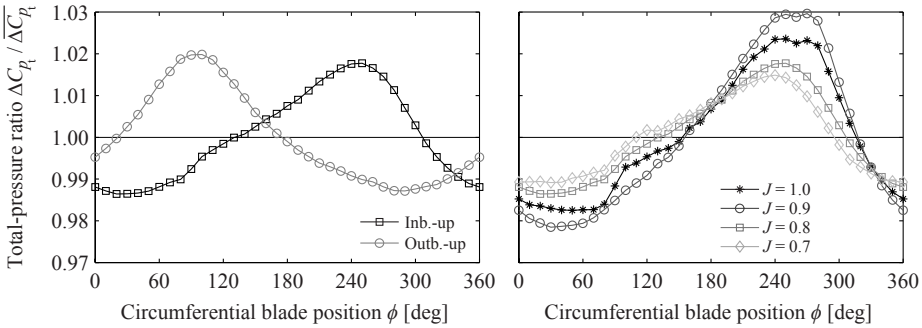

a) Effect of rotation direction ($J = 0.8$)

b) Effect of thrust setting (inboard-up)

Figure 6.12: Circumferential variation of the total-pressure rise at $r/R = 0.76$, $\alpha = -0.2$ deg (inboard-up) and $\alpha = +0.2$ deg (outboard-up); $|\delta_f| = 10$ deg.

No measurements were taken to study the upstream effect of the wing on the propeller loading at nonzero angle of attack (ignoring the 0.2 deg misalignment). However, previous numerical investigations [142] of the same setup operated at $J = 0.8$ ($C_T = 0.095$) showed that at $\alpha = +10$ deg, the relative impact of the upstream effect decreased over the largest part of the blade span when compared to the case at $\alpha = 0$ deg. For the latter, Ref. [142] predicted an increase in propeller loading of around 3% due to the presence of the wing, which is slightly more than measured in the experiments discussed in the present chapter.

6.3. COMPARISON WITH CONVENTIONAL CONFIGURATION

The aerodynamic interaction effects for wingtip-mounted propellers discussed in the previous section show the potential for significant performance benefits due to wingtip-vortex attenuation and swirl recovery. To illustrate the potential aerodynamic performance gain of the wingtip-mounted propeller, a direct comparison was made with the conventional configuration, with the propeller mounted on the inboard part of the wing. For this comparison, Model II was used (modular cambered wing, see Figs. 3.9 through 3.11). The traversable wake rake was employed first to highlight the differences in wake

and slipstream flowfield between the two configurations. Subsequently, the system and wing performance were evaluated based on measurements with the external balance. All data were acquired at $Re_D = 640{,}000$, unless noted otherwise, while the propeller rotation direction was always inboard-up.

6.3.1. WAKE AND SLIPSTREAM FLOWFIELD

The flowfield in the wake of the conventional and wingtip-mounted configurations was visualized by means of contours of the total pressure at 1.5 times the chord length downstream of the wing trailing edge. Figure 6.13 compares the results obtained without the propeller present. To allow for a fair comparison between the two configurations, the measurements were taken at a constant lift coefficient of $C_L = 0.5$, which was selected to be representative of a typical wing loading in cruise conditions. This lift coefficient was achieved at $\alpha = 2.8$ deg for the conventional configuration and $\alpha = 2.9$ deg for the wingtip-mounted configuration. The dashed lines indicate the projection of the model geometry onto the measurement plane (at $\alpha = 0$ deg).

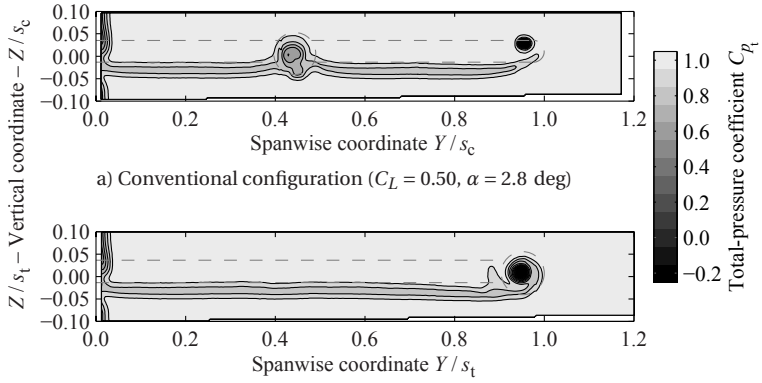

Figure 6.13: Wake flowfield without propeller, rear view.

For both configurations, the viscous wake of the wing can be recognized by the wide region of total-pressure loss below the projected chordline. The wake has displaced downward due to the downwash created by the lifting wing, and rolls up into a wingtip vortex, which features a strong total-pressure deficit due to the local viscous losses. The region of total-pressure loss at the wingtip is more spread out for the wingtip-mounted configuration due to the addition of the viscous losses associated with the nacelle. This is further strengthened by the complex flowfield in the wing–nacelle junction, which at this angle of attack seems to have led to flow separation inboard of the nacelle. Compared to the conventional configuration, the tip-vortex location for the wingtip-mounted configuration was positioned somewhat more inboard ($Y/s_t = 0.949$ versus $Y/s_c = 0.955$). This is a result of the slightly higher aspect ratio for the conventional configuration due to the addition of the rounded wingtip. For both configurations, the boundary layer on the ground board is visible near $Y/s = 0$, with a flow pattern typical of the junction flow at the interface of a wing and a flat plate [146, 147].

As shown before in Fig. 6.7, the operation of the propeller causes a strong modification of the wake flowfield. Figure 6.14 provides total-pressure contours for the conventional and wingtip-mounted configurations for the case with propeller running at $J = 0.7$ ($C_T = 0.123$). As for the propeller-off case shown in Fig. 6.13, the data were acquired at a constant lift coefficient of $C_L = 0.5$. The corresponding angles of attack were $\alpha = 2.0$ deg for the conventional configuration and $\alpha = 1.9$ deg for the wingtip-mounted configuration. Note that the scale of the contour levels is different from the one used in Fig. 6.13.

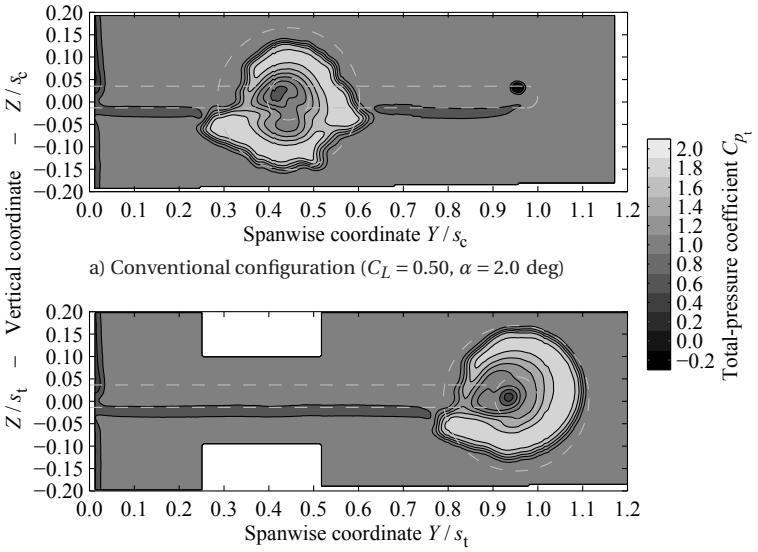

a) Conventional configuration ($C_L = 0.50$, $\alpha = 2.0$ deg)

b) Wingtip-mounted configuration ($C_L = 0.50$, $\alpha = 1.9$ deg)

Figure 6.14: Slipstream distortion at $J = 0.7$ ($C_T = 0.123$), rear view.

The total-pressure contours plotted in Fig. 6.14 display the expected spanwise shearing of the propeller slipstream due to its interaction with the wing. The spanwise velocities are as illustrated in Fig. 2.9, displacing the propeller slipstream away from the propeller axis on the advancing blade side, and toward the propeller axis on the retreating blade side. The slipstream distortion is most pronounced for the conventional configuration, since it occurs on both the inboard and outboard sides of the nacelle. For the wingtip-mounted configuration, the outboard part of the slipstream remains approximately circular, since it is away from the wing. The vertical position of the slipstream is about $0.15R$ higher for the wingtip-mounted configuration than for the conventional configuration. This is due to the lower downwash near the tip of the wing. In both cases, the flow topology around the nacelle and away from the propeller slipstream is similar to that observed for the propeller-off case in Fig. 6.13.

The slipstream distortion for the wingtip-mounted configuration (Fig. 6.14b) was less pronounced than that shown before for Model I at the same propeller thrust setting (Fig. 6.7e). This is because the diameter-to-span ratio was smaller for Model II than for Model I, leading to a smaller perturbation of the wing lift distribution by the propeller at a given thrust coefficient. As a result, the distortion of the slipstream was decreased,

following the mechanism sketched in Fig. 2.9. Moreover, the results for Model I may have featured an additional distortion of the slipstream near the flap edge, which did not occur with Model II.

6.3.2. SYSTEM PERFORMANCE

The external balance was used to quantify the aerodynamic performance of the conventional and wingtip-mounted configurations. In this section, the lift and drag of the entire system are considered, including propeller forces. Figure 6.15 compares the lift and drag polars measured for both configurations as a function of the propeller thrust setting.

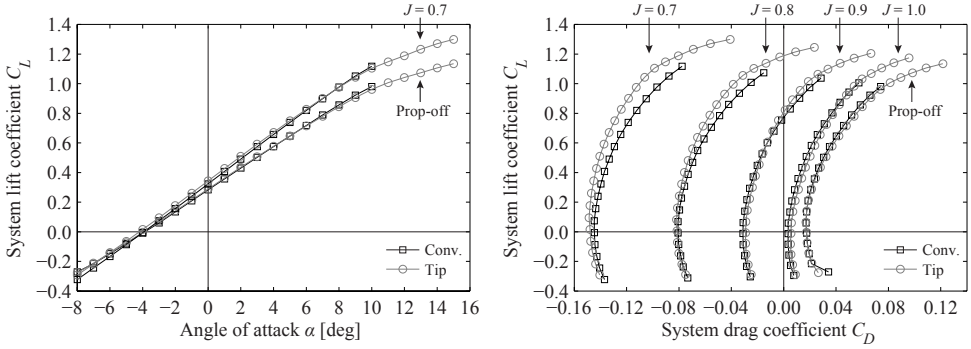

a) Lift polar

b) Drag polar

Figure 6.15: Lift and drag polars of the conventional (Conv.) and wingtip-mounted (Tip) configurations, including propeller forces.

The lift polars plotted in Fig. 6.15a show little difference between the lift performance of the conventional and wingtip-mounted configurations. At higher angles of attack, the conventional configuration provided slightly higher lift than the wingtip-mounted configuration. This may have been due to the local upwash introduced on both sides of the nacelle when it is subjected to a positive angle of attack. For the conventional configuration, this affects the wing lift on both sides of the nacelle, thus resulting in a larger lift increase than for the wingtip-mounted configuration, for which only the lift on the inboard side of the nacelle is impacted.

As discussed in Section 6.2.3, the effect of the propeller is to increase the lift for the wingtip-mounted configuration due to the local increase in dynamic pressure and inflow angle caused by the propeller slipstream. Similar effects occur for the conventional configuration [36, 42], as sketched in Fig. 6.16. With inboard-up rotation, the propeller-induced upwash increases the angle of attack and dynamic pressure on the inboard part of the wing immersed in the slipstream (region II). On the outboard part of the wing immersed in the slipstream (region III), on the other hand, the propeller causes a downwash which decreases the local angle of attack. This is partially offset by the local increase in dynamic pressure. The spanwise lift gradients at the edges of regions II and III cause induced velocities which also modify the local angle of attack on the parts of the wing not immersed in the propeller slipstream. On the inboard part (region I) the angle of attack increases, while on the outboard part (region IV) the angle of attack decreases.

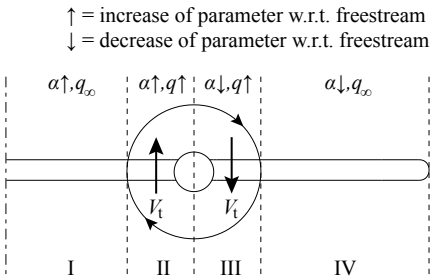

Figure 6.16: Sketch of wing-inflow modification due to the propeller for the conventional configuration with inboard-up rotation.

Whereas the conventional and wingtip-mounted configurations produced approximately equal lift, the system drag (Fig. 6.15b) reveals an increasing drag benefit for the wingtip-mounted configuration with increasing propeller thrust setting. Note that the thrust force, which is negative in the drag direction, is included in the plotted drag coefficient, and hence more negative values of the drag coefficient indicate better system performance at a given lift coefficient and propeller setting.

For the propeller-off condition at positive lift coefficients, the conventional configuration showed slightly lower drag than the wingtip-mounted configuration. This was an unexpected result, seeing that for the wingtip-mounted configuration the nacelle acts as a wingtip device which should lead to lower induced drag. However, this may have been offset by the slightly higher geometric aspect ratio of the conventional configuration. Furthermore, the upwash induced by the nacelle, discussed before, may have led to a reduction of the lift-induced drag for the conventional configuration. For both configurations, trailing-edge separation was present at all angles of attack above 0 deg, as indicated by the oil-flow images shown in Fig. 6.17. This was due to the modification of the trailing-edge geometry, discussed before in Section 3.3.2, which was required for manufacturing reasons. For the wingtip-mounted configuration, corner flow separation can be observed near the wing–nacelle junction, explaining the local total-pressure loss seen before in Fig. 6.13b. The images recorded at higher angles of attack (not shown here) displayed a particularly complex flow topology around the wing–nacelle junctions for the conventional configuration. Apparently this did not lead to a noticeable drag penalty compared to the wingtip-mounted configuration.

With the propeller running, clear shifts occurred in the drag polars. For the conventional configuration, the upwash and downwash on the inboard and outboard parts of the wing (Fig. 6.16) modified the wing induced drag by tilting the lift vector forward and backward. Furthermore, the lower effective angle of attack on the outboard segment of the wing immersed in the slipstream (region III in Fig. 6.16) eliminated or delayed the trailing-edge separation occurring without the propeller present, as shown by the oil-flow images depicted in Fig. 6.18. This was further amplified by the increased Reynolds number associated with the increased velocity in the slipstream, which also delayed the separation on the inboard side of the wing. On the other hand, the higher velocity experienced by the parts of the wing immersed in the propeller slipstream leads

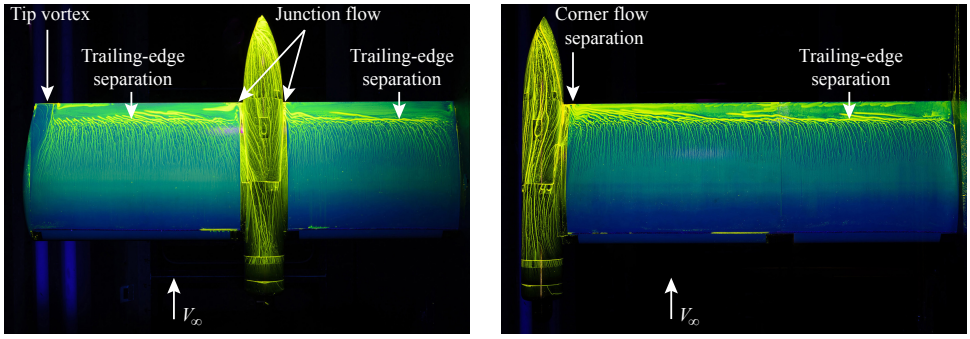

a) Conventional configuration b) Wingtip-mounted configuration

Figure 6.17: Oil-flow visualizations of the surface flow with propeller off at $C_L = 0.5$, top view.

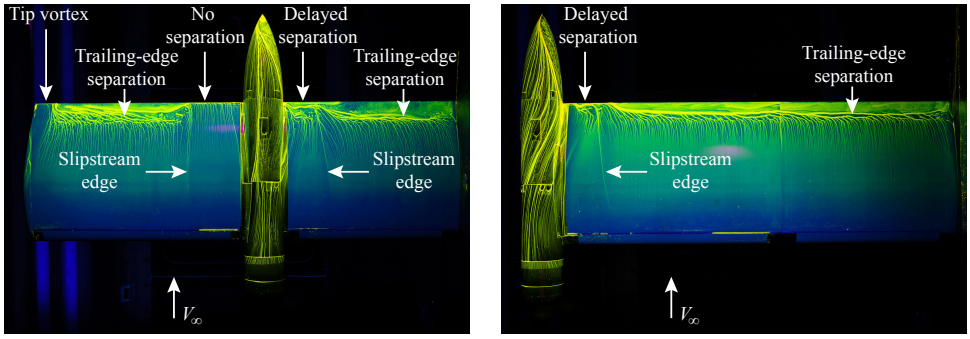

a) Conventional configuration b) Wingtip-mounted configuration

Figure 6.18: Oil-flow visualizations of the surface flow with propeller on ($J = 0.7$, $C_T = 0.12$)) at $C_L = 0.5$, top view.

to an increase in drag compared to the propeller-off case, as discussed in Section 6.2.3. The relative magnitude of the above-mentioned mechanisms depends on the propeller efficiency, propeller-diameter-to-span ratio, Reynolds number, wing zero-lift drag coefficient, and wing lift coefficient. The Reynolds-number effect would be less pronounced at full scale than in the wind tunnel, since at full scale the absolute value of the Reynolds number would be higher, and thus the local effect of the Reynolds-number increase by the propeller would be less relevant. For the wingtip-mounted configuration, the effects are as discussed in Section 6.2.3. The combination of wingtip-vortex attenuation and swirl recovery reduces the induced drag of the wing when the propeller is operated with inboard-up rotation.

Figure 6.15b shows that the drag reduction offered by the wingtip-mounted configuration becomes increasingly dominant with increasing propeller thrust setting. At $J = 0.8$ and $J = 0.7$, clear induced-drag benefits can be seen when compared to the conventional configuration. This is confirmed by Fig. 6.19, which displays the change in drag of the wingtip-mounted configuration compared to the conventional configuration as

a function of propeller thrust coefficient and system lift coefficient. Note that negative numbers for the drag delta ΔC_{D_t} indicate a drag benefit for the wingtip-mounted configuration. The data measured at Re_D = 450,000 are also included, thereby extending the range of thrust conditions to $C_T = 0.168$ (at $J = 0.5$). The data points at $C_T = 0$ were obtained with the blades removed, and thus are representative of the propeller-off case.

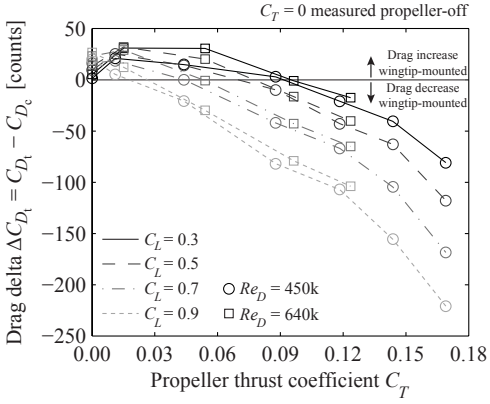

Figure 6.19: Drag benefit of wingtip-mounted configuration compared to conventional configuration.

Figure 6.19 highlights the sensitivity of the drag benefit of the wingtip-mounted configuration to the propeller thrust setting. As discussed before, for the propeller-off case the drag was higher for the wingtip-mounted configuration than for the conventional configuration, which is reflected in Fig. 6.19 by the positive values of ΔC_{D_t} at $C_T = 0$. For lift coefficients below around $C_L = 0.7$, this drag benefit of the conventional configuration initially increased at the lowest propeller thrust setting. This could be due to the elimination of flow separation on the outboard part of the wing washed by the slipstream, as discussed before, which may have also occurred at the lowest thrust setting. The drag penalty of the wingtip-mounted configuration then gradually turned into a drag reduction with increasing propeller thrust setting. For the tested geometry, drag reductions of 15 – 40 counts were achieved with the wingtip-mounted configuration compared to the conventional configuration at $C_L = 0.5$ and $0.09 < C_T < 0.13$ ($0.7 < J < 0.8$), corresponding to an overall drag reduction of 5 – 15%. The drag benefit of the wingtip-mounted configuration further increases upon increasing the system lift coefficient and propeller thrust setting. For thrust settings of $0.14 < C_T < 0.17$ ($0.5 < J < 0.6$) and a lift coefficient of $C_L = 0.7$, drag reductions were measured of 100 – 170 counts (25 – 50%). It should be noted that these values are specific to the tested configuration. Still, they confirm a strong potential for drag reductions by the wingtip-mounted configuration due to the wingtip-vortex-attenuation mechanism.

6.3.3. WING PERFORMANCE

The propeller forces discussed in Section 6.1 were removed from the system forces presented in Fig. 6.15 to study the effect of the propeller on the performance of the wing with nacelle. At each angle of attack, the propeller performance was subtracted as mea-

sured with the sting-mounted propeller setup at that same angle of attack. Therefore, the procedure accounts for the change in propeller normal force and thrust with angle of attack. However, the upstream effect of the wing on the propeller performance is neglected. This was considered acceptable based on the discussion of Section 6.2.4. The data with propeller forces subtracted were used to determine the wing's lift-curve slope C_{L_α} and span-efficiency parameter e for the conventional and wingtip-mounted configurations, as a function of the propeller thrust setting.

LIFT-CURVE SLOPE

The lift-curve slope was obtained by fitting a first-order polynomial through the $C_L - \alpha$ data for an angle-of-attack range of $-8 \leq \alpha \leq +8$ deg. An estimate of the error of the fitting procedure was made by statistical analysis. The procedure was repeated 5,000 times, each time with a random error superimposed on the lift data. This random error was based on a normal distribution with standard deviation equal to the known uncertainty of the balance data. The standard deviation of the 5,000 tests was then taken as the uncertainty of the determined lift-curve slope. Figure 6.20 displays the results as a function of the propeller thrust coefficient, for both the conventional and wingtip-mounted configurations. The data points at $C_T = 0$ again represent the propeller-off case, as measured without blades. The uncertainty (approximately $2 \cdot 10^{-5}$/deg) is indicated by error bars surrounding the individual data points.

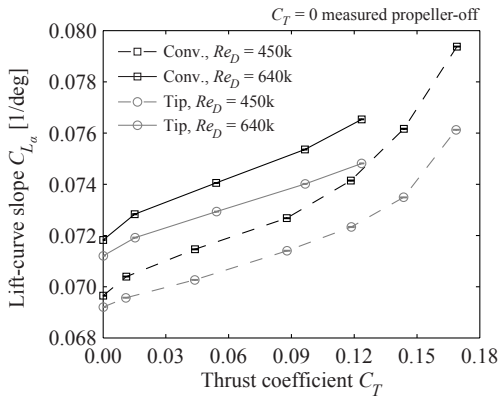

Figure 6.20: Effect of propeller thrust setting on the lift-curve slope of the wing with nacelle for the conventional and wingtip-mounted configurations.

Figure 6.20 shows that at the propeller-off condition, the lift-curve slope was higher for the conventional configuration than for the wingtip-mounted configuration. This may have been due to the upwash induced by the nacelle when operating at nonzero angle of attack, as discussed before in relation to Fig. 6.15. Decreasing the Reynolds number from Re_D = 640,000 to Re_D = 450,000 led to a reduction of the lift-curve slope. The increase in boundary-layer thickness with decrease in Reynolds number causes a stronger effective decambering of the wing profile, thus worsening the lift performance.

The lift-curve slope increased with increasing thrust coefficient for both the conventional and wingtip-mounted configurations due to the combination of the dynamic-

pressure rise and swirl in the slipstream, as discussed before. At the maximum thrust setting considered ($J = 0.5$, $C_T = 0.168$), the propeller effect increased the lift-curve slope by 14% for the conventional configuration and 10% for the wingtip-mounted configuration. At thrust settings more representative of cruise conditions for the tested configuration ($0.7 < J < 0.8$, $0.09 < C_T < 0.13$), this decreased to $4-7$% for the conventional configuration and $3-5$% for the wingtip-mounted configuration. The larger changes for the conventional configuration are because the increased dynamic pressure in the propeller slipstream affects a larger part of the wing than for the wingtip-mounted configuration (see Fig. 6.16 versus Fig. 2.8a), and acts on the inboard part of the wing where the section lift is higher than near the wingtip. Apparently this was sufficient to offset the higher span efficiency of the wing for the wingtip-mounted configuration shown below. The relative change of the lift-curve slope due to the propeller effect was approximately equal at the two Reynolds numbers considered.

SPAN-EFFICIENCY PARAMETER

The drag polars displayed in Fig. 6.15b already indicated that the wingtip-mounted configuration offered an induced-drag benefit compared to the conventional configuration. To verify the sensitivity of this induced-drag benefit to the propeller thrust coefficient, the span-efficiency parameter e of the wing with nacelle was derived from the drag data with propeller forces removed. To this end, a parabolic relation was assumed between the drag coefficient and the lift coefficient:

$$C_D = C_{D_{\min}} + \frac{1}{\pi AR e}\left(C_L - C_{L_{C_{D_{\min}}}}\right)^2. \tag{6.2}$$

To extract the value of the span-efficiency parameter e, the $C_L - C_D$ data were first interpolated. After subtracting the minimum drag coefficient, a linear curve was then fit to obtain the value of e from Eq. 6.2. The uncertainty was again obtained from a statistical analysis with 5,000 evaluations. The procedure was relatively sensitive to scatter in the input data, as indicated by the computed uncertainty of approximately $0.05-0.09$. Figure 6.21 presents the evolution of the span-efficiency parameter with the propeller thrust coefficient, for the conventional and wingtip-mounted configurations. The reference results obtained with the propeller blades removed are again indicated by the data points at $C_T = 0$.

Figure 6.21 shows that the span efficiency was higher for the conventional configuration than for the wingtip-mounted configuration for the case without the propeller. This matches with the induced-drag benefit observed for the conventional configuration in Fig. 6.15b. Despite the relatively high uncertainty, significant differences can be seen between the two configurations when the propeller was operated. For the conventional configuration, the beneficial effects due to swirl recovery (forward tilting of the wing lift vector) are countered by the decrease in span efficiency caused by the distorted wing lift distribution. As a result, a nonmonotonic behavior of the span-efficiency factor with thrust coefficient is observed. The span efficiency of the wing remained constant (within the uncertainty) for thrust coefficients up to $C_T = 0.09$, but then reached a maximum at $C_T = 0.123$ ($J = 0.7$). At this thrust setting, an increase in span efficiency of approximately 15% was computed compared to the propeller-off condition. At higher thrust coefficients, the span efficiency dropped again, reaching a level about 15% below

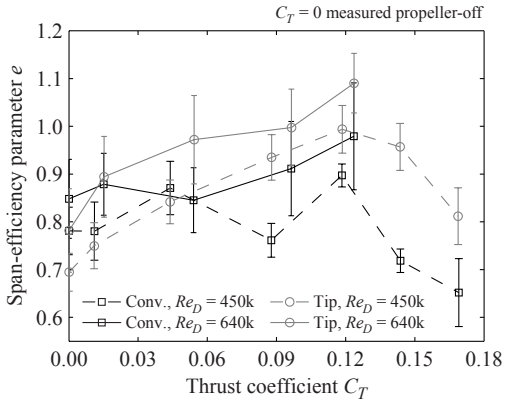

Figure 6.21: Effect of propeller thrust setting on the span-efficiency parameter of the wing with nacelle for the conventional and wingtip-mounted configurations.

the propeller-off result at a thrust coefficient of $C_T = 0.168$ ($J = 0.5$). Although an offset can be observed between the span-efficiency parameters measured at $Re_D = 450{,}000$ and $Re_D = 640{,}000$, the relative effects due to the propeller were comparable at both Reynolds numbers.

For the wingtip-mounted configuration, the swirl recovery and attenuation of the wingtip vortex led to significant induced-drag benefits. Combined with the smaller distortion of the wing lift distribution, the effect of the propeller was to increase the span-efficiency parameter with increasing thrust coefficient, except at the highest thrust setting considered. Relative to the propeller-off result, the changes in span efficiency due to the propeller were in the order of $20-40\%$ over the advance-ratio range $0.6 < J < 0.9$ ($0.05 < C_T < 0.15$). The decrease in span efficiency at $C_T = 0.168$ ($J = 0.5$) could be due to the increased distortion of the wing lift distribution caused by the high swirl and dynamic pressure in the propeller slipstream at this condition.

6.4. KEY FINDINGS

This chapter has presented an experimental analysis of the aerodynamic interaction effects for wingtip-mounted propellers installed in a tractor configuration. By positioning the propeller at the tip of the wing, the slipstream interacts with the flow around the wingtip, thus affecting the roll-up and downstream behavior of the wingtip vortex. PIV measurements downstream of a propeller–wing model showed that this leads to a reduction in overall swirl with inboard-up rotation, in which case the swirl in the slipstream is opposite to that associated with the wingtip vortex. At the same time, the system performance was found to improve due to a reduction of the wing induced drag, leading to the conclusion that the decrease in swirl causes a reduction in downwash experienced by the wing.

Apart from the change in drag, the interaction of the wing with the propeller slipstream also modifies the wing lift. The locally enhanced dynamic pressure increases the lift over the spanwise part of the wing washed by the slipstream. This is amplified by

the induced swirl for the case with inboard-up rotation. As a result, a strong spanwise variation in lift occurs with the propeller on. The induced velocities caused by this lift gradient lead to a spanwise shearing of the slipstream. With outboard-up rotation, the swirl in the slipstream acts to locally oppose the increase in wing lift due to the propeller-induced dynamic-pressure rise. Compared to the inboard-up rotation case, this leads to a reduction in wing lift at a given angle of attack, thus also a reduction in maximum lift coefficient. Furthermore, the direction of the spanwise shearing of the propeller slipstream is inverted on both sides of the wing.

To quantify the potential aerodynamic benefits of the wingtip-mounted propeller, a comparison was made with a conventional configuration, with the propeller mounted on the inboard part of the wing. The increase in wing lift due to the interaction with the propeller was $1-4\%$ smaller for the wingtip-mounted configuration than for the conventional configuration. For the latter, the enhanced dynamic pressure and swirl in the slipstream acts over double the spanwise extent, and on a part of the wing where the section lift is higher than for the wingtip-mounted configuration. At higher angles of attack, the lift advantage for the conventional configuration could be further enhanced by the local angle-of-attack increase in proximity to both sides of the nacelle.

In terms of drag performance, on the other hand, the wingtip-mounted configuration showed superior performance. At a wing lift coefficient of $C_L = 0.5$ and a thrust coefficient of $0.09 < C_T < 0.13$, the drag reduction amounted to about $15-40$ counts $(5-15\%)$ compared to the conventional configuration. The aerodynamic benefit of the wingtip-mounted configuration further increases with increasing wing lift coefficient and propeller thrust coefficient, leading to a drag reduction of $100-170$ counts $(25-50\%)$ at $C_L = 0.7$ and $0.14 < C_T < 0.17$. An analysis of the wing performance confirmed that this drag benefit is mostly due to a reduction of the wing induced drag. Compared to the conventional configuration, a relative increase in span efficiency of up to 40% was measured for the wingtip-mounted configuration. Although the exact drag benefit will be specific to vehicle design and operating conditions, it is concluded that the interaction between the propeller slipstream and the wingtip vortex leads to a clear drag reduction for the wingtip-mounted configuration. Multidisciplinary analyses are required to evaluate the resulting impact on the potential performance benefits at aircraft level.

7

PROPELLER-SLIPSTREAM IMPINGEMENT

Besides the effects on the time-averaged loading discussed in Chapter 6, the interaction between the propeller slipstream and a downstream surface such as a wing or pylon also introduces unsteady loads, which can lead to structure-borne noise. This chapter explains and quantifies the unsteady interaction effects caused by propeller-slipstream impingement for a typical pylon-mounted tractor-propeller configuration. The focus is on the aerodynamic forcing function of the structure-borne noise; the structural response of the pylon is not considered. The results provide novel information regarding the sensitivity of the unsteady loads to the operating conditions, and the spatial distribution of the fluctuating pressures that cause the unsteady loads. Section 7.1 characterizes the flowfield in the propeller slipstream, including a discussion of the distortion of the slipstream due to the interaction with the pylon. Subsequently, Section 7.2 provides detailed flow visualizations of the impingement of the propeller slipstream at the pylon leading edge. Section 7.3 then discusses unsteady pylon loading and its potential contribution to structure-borne noise, after which the key findings are stated in Section 7.4. The results were obtained with the PROWIM-US setup described in Chapter 4. All data were measured at the baseline operating conditions of $J = 0.8$, $\Delta X = 0.42D$, and $\alpha = 0$ deg, unless mentioned otherwise.

7.1. PROPELLER-SLIPSTREAM FLOWFIELD

7.1.1. ISOLATED PROPELLER

The fluctuating loads caused by the impingement of a propeller slipstream on a downstream surface are due to the unsteady nature of the slipstream, which contains the blade wakes, root vortices, and tip vortices. The time-accurate flowfield in the slipstream of the isolated propeller was measured using stereoscopic PIV (SSFOV setup, Fig. 4.7a), phase-locked with the propeller blade position. Figure 7.1 presents the resulting contours of the axial velocity. To highlight the velocities induced by the propeller, the velocity field

The contents of this chapter have been adapted from Ref. [46].

is presented as an offset from the freestream velocity ($\Delta V_X = V_X^{\text{P-on}} - V_\infty$). Contour lines of constant normalized vorticity, $\omega_Z^* = \omega_Z D / V_{\text{disk}}$, are included in Fig. 7.1, with ω_Z the Z-component of the vorticity and V_{disk} the equivalent velocity at the propeller disk estimated from actuator-disk theory [36].

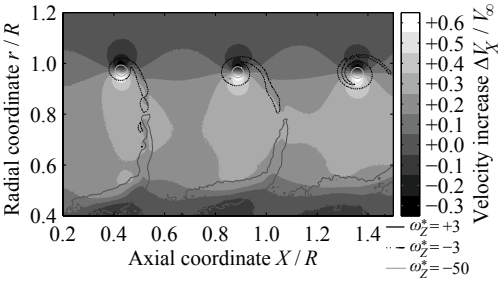

Figure 7.1: Phase-locked axial velocity variation in the slipstream of the isolated propeller, with contours of constant normalized vorticity superimposed ($C_T = 0.095$).

The axial velocity difference plot shown in Fig. 7.1 highlights several important characteristics of the propeller slipstream. The axial velocity is increased within the slipstream, consistent with the positive thrust generated by the propeller. Within the streamtube, three distinct flow structures are visible, associated with each blade passage. At the most inboard radial stations ($r/R < 0.5$), the propeller root vortex can be seen. Moving outboard ($0.5 < r/R < 1.0$), the blade wakes are present. In the initial part of the slipstream ($X/R < 0.5$), these wakes are practically straight. However, the nonuniform distribution of axial velocity in the propeller slipstream causes the shape of the blade wakes to become increasingly crescent when convecting downstream. A change in sign of normalized vorticity occurred in the blade wake around $r/R = 0.8$. This corresponds to the radial position of maximum loading on the propeller blades. Finally, the blade tip vortices cause strong velocity fluctuations around the edge of the slipstream ($r/R \approx 1.0$).

7.1.2. SLIPSTREAM DISTORTION BY THE PYLON

To assess the effect of installation of the pylon on the propeller slipstream, PIV measurements were taken in the wake of the models (WFOV setup, Fig. 4.7b). Figure 7.2 provides the velocity fields for the configurations with and without the pylon installed. Additionally, a reference case is included for which both the propeller blades and the pylon were removed (propeller-off, pylon-off), displaying the effect of the support structure on the measured velocity fields. The dashed lines indicate the projections of the nacelle, propeller disk, and pylon on the measurement plane; each subplot only shows those components that were present for that specific configuration.

Figure 7.2 displays the axial velocity increase due to the thrust-generating propeller, and the distortion of the propeller slipstream due to the installation of the pylon. For all configurations, the nacelle caused a strong velocity deficit around the propeller center. Moreover, a decrease in axial velocity can be seen in the middle of the upper half of the field of view ($Y/R = 0$, $Z/R < 0$). This was caused by the support sting to which the propeller was connected (Fig. 4.1). This sting was relatively thick, and its aerodynamic

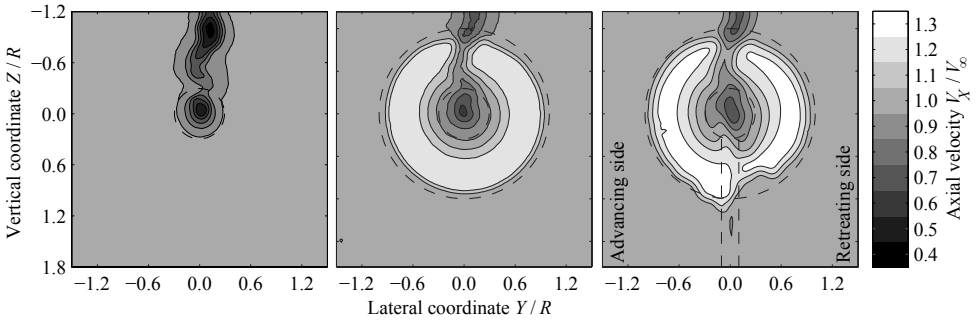

a) Propeller-off, pylon-off b) Propeller-on, pylon-off c) Propeller-on, pylon-on

Figure 7.2: Effect of propeller and pylon installation on the time-averaged slipstream flowfield, front view.

characteristics were deteriorated by wiring taped to its backside, resulting in a strong wake velocity deficit (Fig. 7.2a).

For the isolated propeller (Fig. 7.2b), the expected axisymmetric velocity distribution was obtained away from the region affected by the presence of the support sting. With the pylon present (Fig. 7.2c), the velocity deficit in the wake of the pylon is apparent below the propeller disk around $Y/R = 0$. At the location of the measurement plane, the velocity deficit was equal to around 5% of the freestream velocity. Moreover, the propeller slipstream was distorted considerably compared to the isolated propeller case, as discussed before in Chapter 6. On the advancing side of the pylon ($Y/R < 0$), the slipstream moved away from the propeller axis. On the retreating side ($Y/R > 0$), on the other hand, the slipstream was subjected to a displacement toward the propeller axis. This was confirmed by the surface-pressure measurements taken with the microphones, as described in Section 7.3.

In flight, the propeller–pylon combination might operate under asymmetric inflow conditions. This leads to a further distortion of the propeller slipstream. Figure 7.3 displays the flowfields in the wake of the setup for angles of attack of −6, 0, and +6 deg. The expected increased strength of the wakes of the pylon and the support sting at nonzero angle of attack is confirmed. Focusing on the slipstream geometries, it is concluded that the distortion of the slipstream is more pronounced at negative angle of attack than at positive angle of attack. This is due to a crossflow component originating over the nacelle, caused by the pressure difference across the pylon. At negative angle of attack, this crossflow is in the same direction as the induced velocity causing the radially inboard displacement of the slipstream on the retreating side (for an inboard-up rotating propeller). Therefore, the displacement was amplified on the retreating side. At positive angle of attack, on the other hand, the crossflow is oriented in the opposite direction, thereby counteracting the radially inboard displacement of the slipstream on the retreating side. This was confirmed by oil-flow visualizations, as shown in Fig. 7.4 for the cases at $\alpha = 0$ deg and $\alpha = +6$ deg, and the microphone data. Note that the oil-flow measurements were taken with a slightly modified pylon model, which featured the same dimensions but had a replaceable leading-edge insert mounted flush in the front part of the model. The resulting minor discontinuity in the pylon surface can be recognized in the oil-flow images, but is irrelevant for the phenomenon described here.

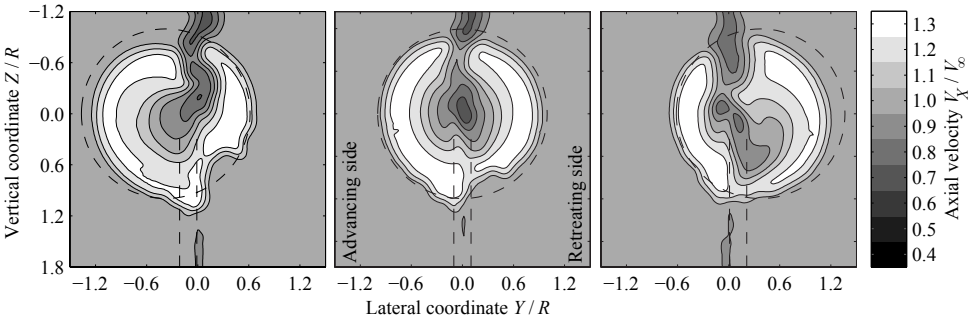

Figure 7.3: Effect of angle of attack on the time-averaged slipstream flowfield with pylon installed, front view.

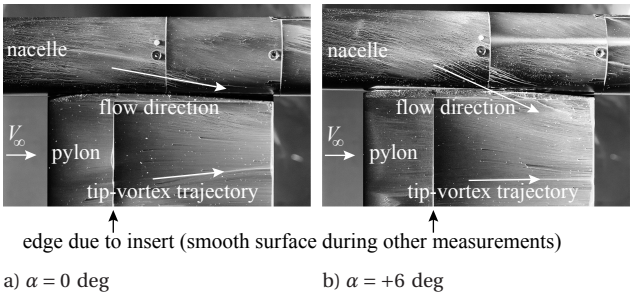

Figure 7.4: Oil-flow visualizations displaying the change in tip-vortex trajectory on the retreating side of the pylon caused by crossflow over the nacelle.

7.2. PROPELLER-SLIPSTREAM IMPINGEMENT AT THE PYLON LEADING EDGE

The impingement of the propeller blade wakes and tip vortices on the leading edge of the pylon was visualized using phase-locked planar PIV (LEFOV setup, Fig. 4.7d). To ease the interpretation of the results, Fig. 7.5 displays a schematic representation of the trajectory of a single tip vortex. For clarity, the associated bound and root vortices are omitted. The gray plane represents a measurement plane at an arbitrary position, while the double arrow heads indicate the sign of the circulation along the vortex filament. Finally, the gray dotted line on both sides of the pylon visualizes the path of the tip vortex along the pylon, displaying the spanwise displacement observed in Fig. 7.2 and Chapter 6. It can be seen from Fig. 7.5 how the velocities induced by the vortex are a function of its position relative to the measurement plane. An increase in axial velocity will be induced at the position of the measurement plane if the vortex impinges on the pylon leading edge below the measurement plane, and vice versa.

The blade-wake impingement process was measured at $Z/R = 0.74$ and is visualized in Fig. 7.6, while Fig. 7.7 shows the data obtained in the tip-vortex plane at $Z/R = 0.97$.

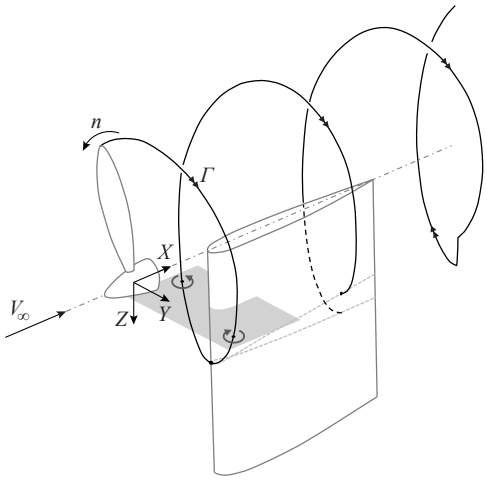

Figure 7.5: Illustration of the trajectory of a single tip vortex, and its relation to the measurements taken with the LEFOV PIV setup.

In both cases, measurements were taken with and without the propeller blades installed. The difference between the propeller-on and (time-averaged) propeller-off measurements ($|\Delta\mathbf{V}| = |\mathbf{V}^{\text{prop-on}}| - |\overline{\mathbf{V}^{\text{prop-off}}}|$) is considered here to isolate the effect of the propeller on the flowfield. For the results in the wake-impingement region (Fig. 7.6), contours of normalized vorticity are included to indicate the positions of the blade wakes and tip vortices. The blade position $\phi' = 0$ deg corresponds to the blade phase angle at the approximate time of vortex impingement on the leading edge of the pylon.

The flowfields presented in Fig. 7.6 clearly display the presence of the blade wakes and tip vortices. Since the measurement plane was positioned below the propeller axis, the lateral distance between the slipstream edges is smaller than the propeller diameter. The increase in velocity in the propeller slipstream can also be recognized, with the highest velocities occurring on the retreating side ($Y/R > 0$). This is due to the effective angle of attack perceived by the pylon due to the swirl in the slipstream, causing additional suction on the retreating side. The passage of the blade wake induces an increased suction peak at the leading edge of the pylon on the retreating side (Fig. 7.6f). This is the result of the modified inflow velocity vector during the wake encounter. The combination of a reduced axial velocity and increased tangential velocity causes a periodic unsteady upwash to the pylon.

Figure 7.7 displays how the tip vortex approaches the pylon at an oblique angle (Fig. 7.7a), caused by the helicoidal trajectory of the vortex. Directly before impinging on the leading edge (Fig. 7.7b), the vortex already bends around the pylon. During impingement (Fig. 7.7c), the axis of the vortex is nearly tangent to the measurement plane, as can be seen from the very small induced velocities close to the leading edge. On the advancing side ($Y/R < 0$), the pitch angle of the vortex remains similar to that observed before the impingement. The retreating side, on the other hand, displays bending of the vortex due to the acceleration caused by the angle of attack induced by the propwash.

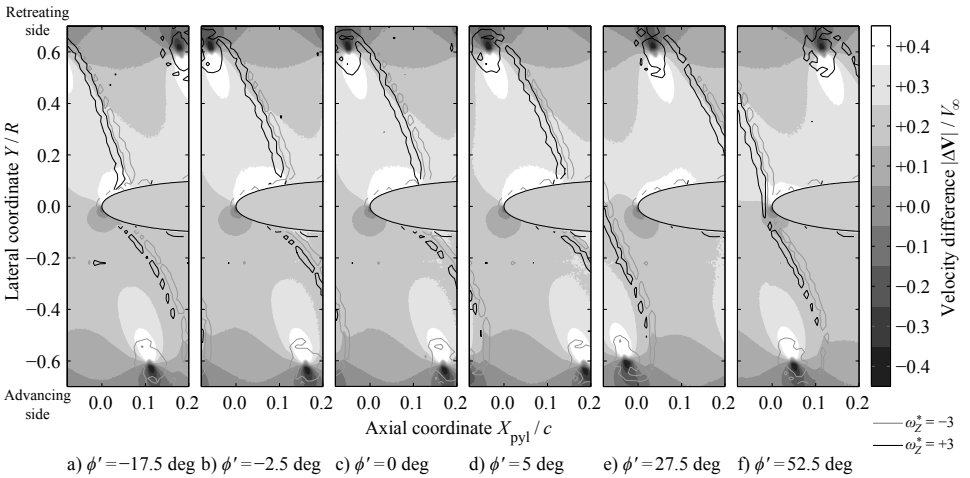

Figure 7.6: Wake-impingement process at the pylon leading edge (velocity difference propeller-on minus propeller-off); $Z/R = 0.74$.

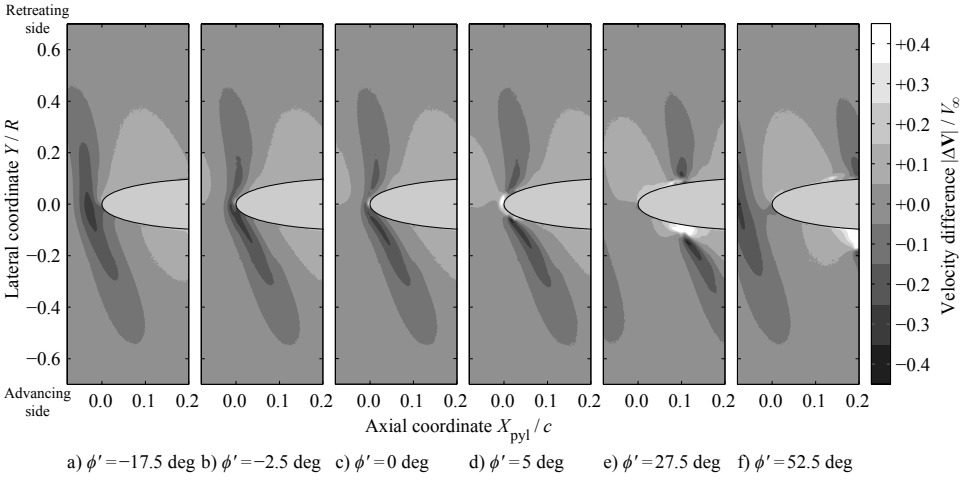

Figure 7.7: Vortex-impingement process at the pylon leading edge (velocity difference propeller-on minus propeller-off); $Z/R = 0.97$.

Directly after impingement (Fig. 7.7d), the axial velocity increased near the pylon leading edge, implying that part of the vortex had penetrated the measurement plane. This spanwise displacement of the vortex is due to an image-vortex effect [144, 145, 148]. Note that this local displacement near the leading edge is independent of the more gradual spanwise displacement of the tip-vortex trajectory along the chord of the pylon. The latter is caused by the spanwise lift variations on the pylon, as explained in Fig. 2.9.

As the vortex is convected downstream (Fig. 7.7e), it is split. On the retreating side, the vortex segment is almost parallel to the pylon. This can be seen from the fact that the region of influence of the vortex is aligned with the chordwise direction. The ve-

locities induced by the vortex segment on the advancing side are higher than on the retreating side. This is due to the gradual spanwise displacement of the vortex, which makes the vortex penetrate the plane farther on the advancing side than on the retreating side. This spanwise displacement further increases when the vortex continues to be convected downstream (Fig. 7.7f). At this phase angle, the next tip vortex can already be seen approaching the pylon, stressing the periodicity of the impingement phenomena.

When the propeller–pylon installation is operated at nonzero angle of attack, the impingement phenomena are modified due to the change of the flowfield surrounding the pylon. Figure 7.8 presents the velocity fields around the pylon leading edge as measured in the tip-vortex impingement plane ($Z/R = 0.97$) at an angle of attack of 6 deg. Again, the results are displayed as the difference between the velocity fields obtained for the propeller-on and propeller-off configurations.

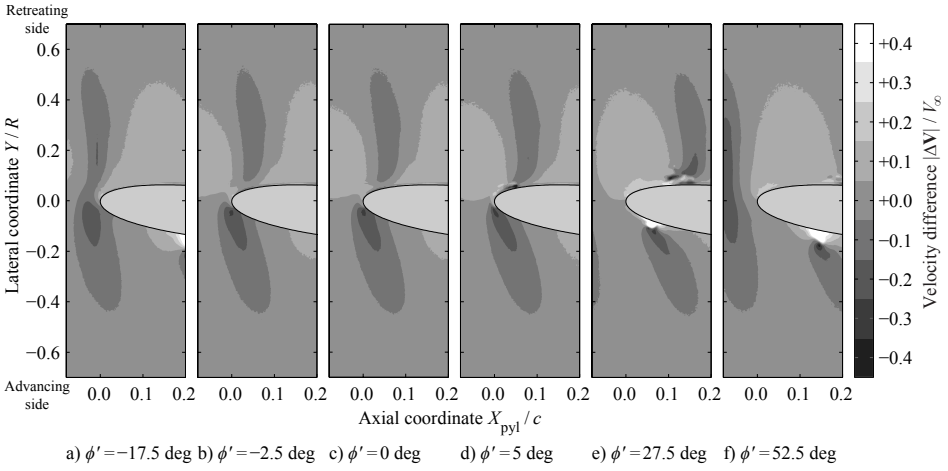

Figure 7.8: Vortex-impingement process at the pylon leading edge in asymmetric inflow conditions (velocity difference propeller-on minus propeller-off); $\alpha = 6$ deg, $Z/R = 0.97$.

The flowfields provided in Fig. 7.8 show that the introduction of a positive angle of attack causes increased bending of the vortex on the retreating side. This is due to the increase in velocity over the suction side of the pylon associated with the positive incidence angle. Compared to the symmetric inflow case (Fig. 7.7), at an angle of attack of 6 deg the vortex impinges closer to the propeller axis (smaller Z-coordinate). This can be seen from the negative velocity induced by the vortex near the pylon leading edge (Fig. 7.8c), and was expected considering the slipstream geometries plotted in Fig. 7.3. After impingement (Fig. 7.8d through 7.8f), the vortex is convected slower on the advancing side than for the case with symmetric inflow. This is due to the locally reduced pylon-induced velocity caused by the positive angle of attack. On the retreating side, the vortex remains closer to the measurement plane due to the decreased spanwise displacement. The increased shear of the vortex close to the surface leads to additional flow structures, which have been attributed before to the creation of secondary vortices in the chordwise vortex–pylon interaction process [148].

7.3. UNSTEADY PYLON LOADING

The impingement of the propeller slipstream on the pylon causes fluctuating pressures and associated unsteady loading. The unsteady pressure response on the pylon is discussed first. Subsequently, structure-borne-noise indicators are defined and the unsteady loading is assessed in terms of its possible contribution to structure-borne noise.

7.3.1. UNSTEADY PRESSURE RESPONSE ON THE PYLON SURFACE

The unsteady pressure response on the pylon surface was quantified using the microphones integrated into the sleeve installed around the pylon (Section 4.4.2). Figure 7.9 displays the distribution of the root mean square of the unsteady pressure over the pylon surface, both for the advancing side (Fig. 7.9a) and the retreating side (Fig. 7.9b). The black dots indicate the discrete positions at which microphone measurements were taken. The white markers along the dotted lines labeled A and B correspond to the positions for which the pressure waveforms are presented later in Figs. 7.10 and 7.11.

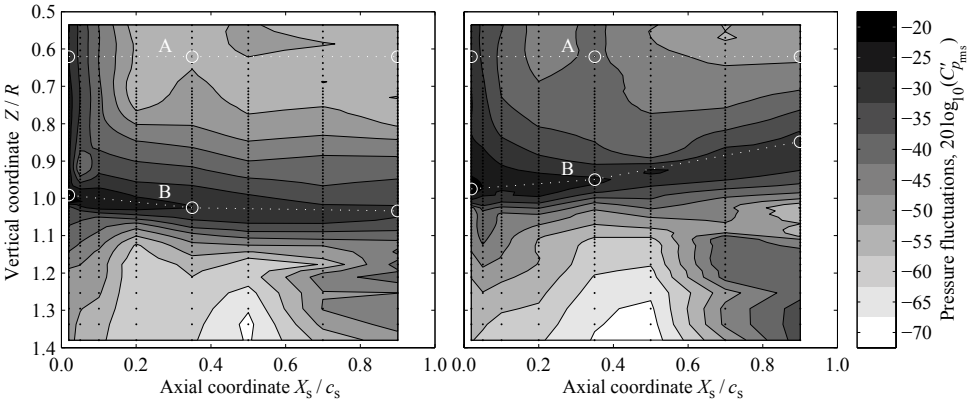

a) Advancing side b) Retreating side

Figure 7.9: Pressure fluctuations on both sides of the pylon.

Figure 7.9 shows that the propeller tip vortex is the dominant source of pressure fluctuations on the pylon. Impinging near a vertical coordinate of $Z/R = 1.0$, the tip vortex presents pressure fluctuations with relatively high amplitude over the entire pylon chord. These fluctuations are the result of the blade tip vortices passing over the microphones, leading to a periodic pressure perturbation due to the low pressure in the vortex core. The amplitude of the pressure fluctuations induced by the tip vortex is at a maximum near the pylon leading edge, and then slowly decreases along the pylon chord. This was attributed by Johnston and Sullivan [45] to the viscous interaction between the boundary layer and the vortex core, causing a reduction in strength of the part of the vortex immersed in the boundary layer of the pylon. Again, the spanwise displacement of the tip vortices can be seen, confirming the observations made from wake-rake and PIV data discussed before. Microphone measurements taken at advance ratios different from the baseline value showed that the spanwise displacement increases with decreasing advance ratio, consistent with Fig. 6.7. On the other hand, the spanwise displacement of the slipstream edge decreases with increasing angle of attack, as also shown in Fig. 7.3.

The pressure fluctuations due to the impingement of the blade wakes, inboard of the tip-vortex trajectory, peak at the leading edge of the pylon and then rapidly decrease in the downstream direction. This resembles the response to a gust normal to the airfoil section, caused by the periodic upwash when the blade wakes pass by the pylon. A small region of locally decreased pressure fluctuations can be observed directly inboard of the tip-vortex path near the leading edge on the advancing side (Fig. 7.9a, $X_s/c_s \approx 0.05$, $Z/R \approx 0.90$). Inspection of the time-accurate pressure data showed that this was due to destructive interference between the pressure perturbations caused by the blade wakes and the tip vortices, as treated in more detail in the discussion of Fig. 7.11. The opposite situation occurred on the retreating side, leading to a wider region of strong pressure fluctuations on this side of the pylon.

The contours plotted in Fig. 7.9 only provide information on the distribution of the pressure fluctuations on the pylon. To illustrate the associated waveforms, phase-averaged microphone signals and frequency spectra were extracted at the positions of the markers in Fig. 7.9. Figure 7.10 provides the waveforms obtained at a spanwise location of $Z/R = 0.62$, corresponding to the response associated with the impingement of the blade wakes (line A in Fig. 7.9). Both the advancing and retreating sides are included, while three chordwise locations are considered to show the development of the pressure fluctuations in the downstream direction. In a similar way, Fig. 7.11 provides the waveforms measured along the tip-vortex trajectory (line B in Fig. 7.9). In this case, the development in the chordwise direction was not considered at constant spanwise coordinate, but instead the path of the tip vortex was followed. The spanwise coordinates at which data were extracted equal $Z/R = 0.992, 1.025, 1.034$ on the advancing side and $Z/R = 0.975, 0.949, 0.848$ on the retreating side, for chordwise locations of $X_s/c_s = 0.02, 0.35, 0.90$, respectively. Spectral analysis was performed on the raw time series using Welch's method [140] with Hann windows, 100 blocks, and no overlap. The corresponding results are plotted for the advancing side in Fig. 7.12, for the same chordwise and spanwise locations as considered in Figs. 7.10 and 7.11. For reference, the spectra acquired outside of the slipstream at $Z/R = 1.38$ are also included. Markers are displayed at multiples of the blade-passage frequency for which the tonal content was at least 3 dB above the broadband noise floor.

The pressure response in the wake-impingement region given in Fig. 7.10 is periodic, with a dominant component at the blade-passage frequency. This indicates a relatively gradual loading change caused by the wake impingement, which is confirmed by inspection of the spectra shown in Fig. 7.12. The signals on the advancing and retreating sides have approximately equal amplitude, but opposite phase. A negative pressure is induced by the wakes on the retreating side, corresponding to the suction side of the pylon in the current setup. On both sides of the pylon, the pressure fluctuations decrease rapidly in chordwise direction, as expected from Fig. 7.9. On the front part of the pylon (Fig. 7.12a and 7.12b), the high turbulence level in the blade wakes causes increased broadband pressure fluctuations compared to the response outside of the slipstream. Toward the rear of the pylon (Fig. 7.12c), the broadband levels outside of the slipstream increased due to natural transition. Differences in local inflow angle, velocity, and upstream development of the boundary layer may explain the change in broadband response when compared to that obtained on the part of the pylon immersed in the slipstream.

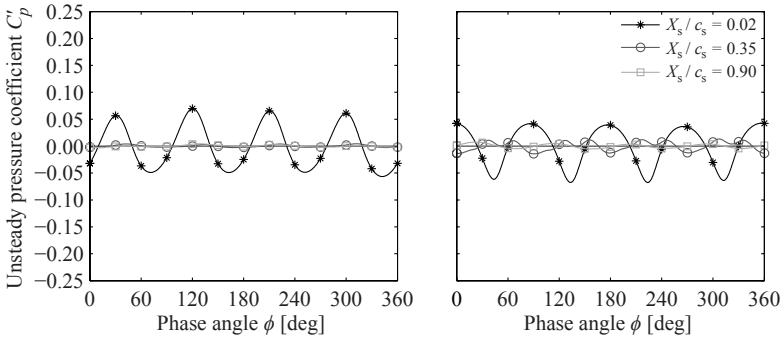

a) Advancing side b) Retreating side

Figure 7.10: Phase-averaged pressure waveforms in the blade-wake impingement region (line A in Fig. 7.9, $Z/R = 0.62$).

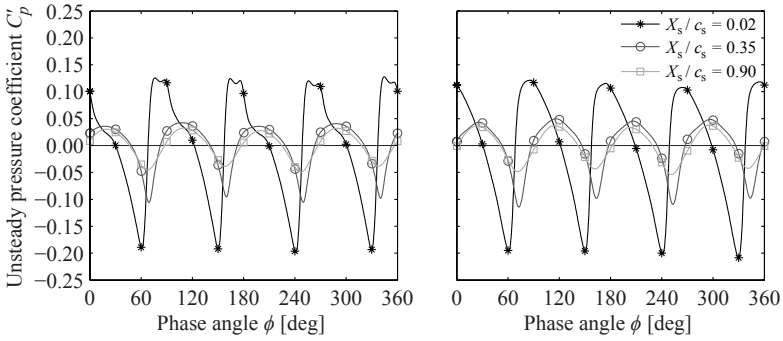

a) Advancing side b) Retreating side

Figure 7.11: Phase-averaged pressure waveforms along the tip-vortex trajectory (line B in Fig. 7.9).

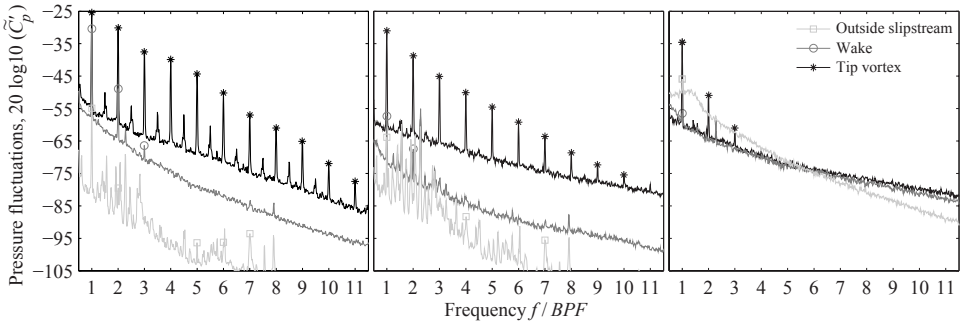

a) $X_s/c_s = 0.02$ b) $X_s/c_s = 0.35$ c) $X_s/c_s = 0.90$

Figure 7.12: Frequency spectra of the pressure fluctuations outside of the slipstream ($Z/R = 1.38$) and along the blade-wake and tip-vortex impingement trajectories (lines A and B in Fig. 7.9) on the advancing side.

Figures 7.11 and 7.12 show that the amplitude of the pressure fluctuations caused by the tip vortex is larger than that due to the wake impingement. This was also observed in Fig. 7.9. The passages of the tip-vortex cores are characterized by a strong drop in the pressure. Near the leading edge of the pylon ($X_s/c_s = 0.02$), sharp pressure peaks were obtained (Fig. 7.11), indicating a richer spectral content of the pressure signal when compared to that resulting from the wake impingement. This is confirmed by the spectra displayed in Fig. 7.12. The tonal content at the blade-passage frequency and associated multiples clearly dominates the broadband part of the signal, which also increased when compared to the blade-wake impingement region and the part of the pylon outside of the slipstream. The subharmonics, with relatively small amplitude, are most likely measurement artifacts related to slight differences between the propeller blades. Moving downstream, the pressure peaks caused by the impingement of the tip vortex become more sinusoidal-like and their amplitude decreases. As discussed in relation to Fig. 7.9, this is due to the viscous interaction between the tip vortex and the pylon boundary layer. Again, the amplitude of the pressure fluctuations is comparable on the advancing and retreating sides. However, the shape of the waveforms differs, with additional secondary oscillations occurring on the advancing side. This is attributed to effects due to the blade wakes, which roll up into the vortex (Fig. 7.1), and hence also affect the pressure fluctuations measured along the tip-vortex path. This effect was strongest slightly inboard of the trajectory of the tip vortex, explaining the local decrease of the root mean square of the pressure fluctuations in this region near the leading edge on the advancing side, as highlighted before in the discussion of Fig. 7.9.

7.3.2. STRUCTURE-BORNE-NOISE INDICATORS

To relate the unsteady pressures measured on the pylon to their potential impact on structure-borne-noise generation without considering the structural characteristics, two structure-borne-noise indicators were defined. These could then be used to compare the results measured at the different operating conditions in terms of their importance for structure-borne noise.

SPATIALLY AVERAGED ROOT MEAN SQUARE OF THE PRESSURE FLUCTUATIONS

The amplitude of the pressure fluctuations on the pylon surface is representative of the total energy available for generation of structure-borne noise. Therefore, the first structure-borne-noise indicator was defined as the spatial average of the root mean square of the pressure fluctuations over the pylon surface:

$$\overline{C'_{p_{\mathrm{rms}}}} = \frac{1}{2c(Z_{\max} - Z_{\min})} \int_{Z_{\min}}^{Z_{\max}} \int_{0}^{c} \left(\sqrt{\frac{1}{2\pi} \int_{0}^{2\pi} C'_{p_{\mathrm{adv}}} \left(X_{\mathrm{pyl}}, Z, \phi\right)^2 \mathrm{d}\phi} + \sqrt{\frac{1}{2\pi} \int_{0}^{2\pi} C'_{p_{\mathrm{retr}}} \left(X_{\mathrm{pyl}}, Z, \phi\right)^2 \mathrm{d}\phi} \right) \mathrm{d}X_{\mathrm{pyl}} \mathrm{d}Z. \tag{7.1}$$

The lower limit of integration $Z_{\min}$ was set to the first datapoint along the pylon span ($Z/R = 0.54$), while the upper limit $Z_{\max}$ was set as low as possible without excluding

part of the slipstream for any of the measurement cases ($Z/R = 1.25$). The pressure parameter defined by Eq. 7.1 is representative of the structure-borne-noise levels only if all vibrational energy is transmitted into the structure; i.e., the structural displacement at each location is assumed to be in phase with the aerodynamic loading acting on it.

ROOT MEAN SQUARE OF THE UNSTEADY LIFT COEFFICIENT

Although the average pressure-fluctuation level defined by Eq. 7.1 is representative of the total energy available for structure-borne-noise generation, it is not necessarily directly related to the actual structure-borne-noise levels because of the assumption that the structural displacement is in phase with the aerodynamic excitation at each location on the pylon. In a more realistic scenario, the relative phases of the pressure fluctuations at each location on the pylon affect the total unsteady loading. Assuming that the pylon is an elastic body with infinitely high speed of sound, all input loads are instantaneously transmitted to the fuselage. In such case, the root mean square of the unsteady lift coefficient, obtained from integration of the measured pressure fluctuations, is representative of the level of structure-borne noise:

$$C'_{L_{\text{rms}}} = \frac{1}{c(Z_{\max} - Z_{\min})} \sqrt{\frac{1}{2\pi} \int_0^{2\pi} \left(\int_{Z_{\min}}^{Z_{\max}} \int_0^{c} \Delta C'_p \left(X_{\text{pyl}}, Z, \phi \right) \mathrm{d}X_{\text{pyl}} \mathrm{d}Z \right)^2 \mathrm{d}\phi}, \tag{7.2}$$

with $\Delta C'_p = (C'_{p_{\text{retr}}} - C'_{p_{\text{adv}}})$ the difference between the unsteady pressure coefficient across the pylon. The same limits of integration were used as for Eq. 7.1.

To allow for the computation of the integral time-dependent loading on the pylon using Eq. 7.2, the spacing between adjacent measurement locations needs to be smaller than the characteristic wavelength of the periodic perturbation. If this is not the case, the relevant flow features that are convected downstream over the pylon chord will temporarily disappear from the data set when they are positioned between two adjacent microphones. This would lead to an incorrect measurement of the time-dependent loading. At the baseline operating condition, the axial separation between consecutive blade wakes in the propeller slipstream was around 47 mm. Therefore, the chordwise density of integration points was increased. This was done by interpolating the pressure waveforms between each pair of adjacent microphones (in chordwise direction) in both space and time. The procedure is illustrated in Fig. 7.13, in which two measurement locations are indicated by the subscripts 1 and 2, while an interpolated point is identified by the subscript i. Assuming a linear pressure evolution between the measurement locations and a constant phase velocity, the amplitude of the unsteady pressure at the interpolated point can be computed once the phase difference between measurement points 1 and 2 is known. This phase difference is directly related to the phase velocity, which was computed from the derivative of the cross-spectral density function of the raw pressure signals of the two microphones considered, following the approach introduced in Ref. [149]. On the spanwise part of the pylon not immersed in the slipstream, the prediction of the phase velocity was complicated by the absence of clearly defined flow structures. The resulting noise in the interpolated results was verified not to impact the computed unsteady loading, since that was dominated by the strong pressure fluctuations caused by the blade wakes and tip vortices.

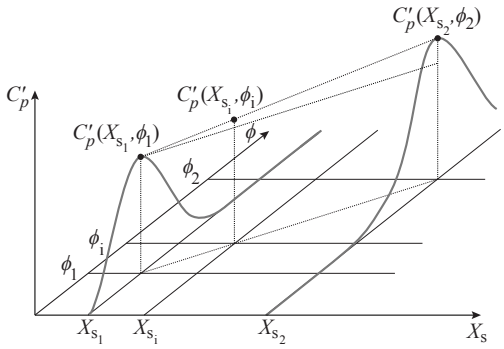

Figure 7.13: Illustration of the microphone interpolation procedure.

The sensitivity of the interpolation procedure to the number of chordwise grid points was investigated by computing the root mean square of the unsteady lift coefficient from Eq. 7.2 for different grid densities, as shown in Fig. 7.14. Note that the case with 8 chordwise points corresponds to the original microphone density, without interpolation. It can be seen that the interpolation procedure converged toward an asymptotic value for high grid densities. Based on these results, a total number of grid points of 76 was selected as a compromise between accuracy and processing time. At this grid density, the root mean square of the unsteady lift coefficient was within 0.2% of the value obtained at the finest grid spacing considered. The need for the interpolation scheme is confirmed by observing that the root mean square of the unsteady lift coefficient computed without interpolation (8 grid points) differs from the asymptotic value by about 30%.

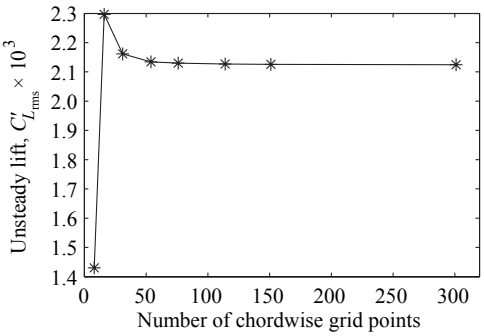

Figure 7.14: Sensitivity of root mean square of the unsteady lift coefficient to number of chordwise grid points used in the microphone interpolation procedure.

7.3.3. UNSTEADY LOADING AS POSSIBLE SOURCE OF STRUCTURE-BORNE NOISE

The structure-borne-noise indicators defined by Eqs. 7.1 and 7.2 were evaluated using the microphone data. Both indicators are discussed separately.

SPATIALLY AVERAGED ROOT MEAN SQUARE OF THE PRESSURE FLUCTUATIONS

The spatial average of the root mean square of the pressure fluctuations (Eq. 7.1) is presented in Fig. 7.15 as a function of advance ratio (Fig. 7.15a), propeller–pylon spacing (Fig. 7.15b), and angle of attack (Fig. 7.15c). In all subfigures, the operating parameters that were not varied were set equal to their baseline values.

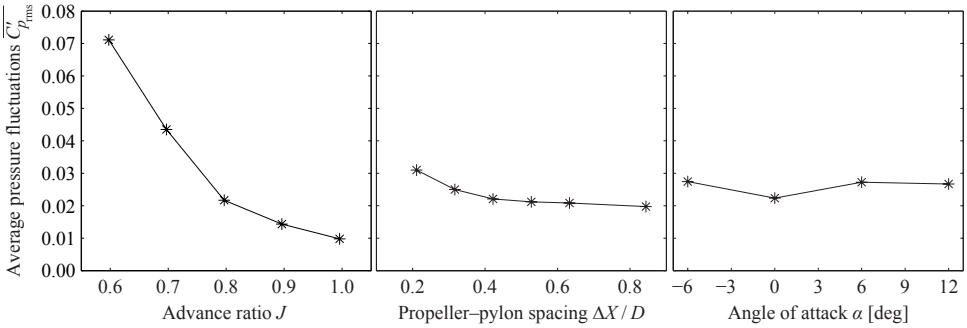

a) $\Delta X/D = 0.42$, $\alpha = 0$ deg b) $J = 0.8$, $\alpha = 0$ deg c) $J = 0.8$, $\Delta X/D = 0.42$

Figure 7.15: Spatial average of the root mean square of the unsteady pressure coefficient on the pylon versus advance ratio (a), propeller–pylon spacing (b), and angle of attack (c).

Figure 7.15a displays the expected decrease in pressure fluctuations with increasing advance ratio. This is due to the reduced strength of the blade wakes and tip vortices associated with the decreased blade loading at higher advance ratio. A nonlinear response is observed, with the pressure fluctuations approaching a nonzero minimum at high advance ratios. Whereas the tip-vortex strength tends to zero when the blades are unloaded, the blade wakes remain. Therefore, nonzero pressure fluctuations are obtained even for the case of an unloaded propeller. In such case, the blade wakes are the dominant source of unsteady pressure on the pylon.

Increasing the propeller–pylon spacing at constant advance ratio reduces the severity of the incoming flow perturbations due to diffusion of the flow structures in the slipstream. As a result, the pressure fluctuations decrease with increasing axial spacing between propeller and pylon (Fig. 7.15b). The decrease in pressure fluctuations with increasing propeller–pylon spacing is nonlinear because of the nonlinearity in axial development of the blade-wake and tip-vortex strength. Moreover, at the smallest propeller–pylon spacings an upstream interaction between the pylon and propeller might have occurred, locally increasing the blade loading, hence aggravating the impingement phenomena. However, this could not be verified with the measurement setup used.

Operating the propeller–pylon setup under asymmetric inflow conditions increases the pressure fluctuations compared to the symmetric case (Fig. 7.15c). At $\alpha = -6$ deg, the pressure fluctuations increased along the tip-vortex path. At $\alpha = +6$ deg, on the other hand, a separation bubble appeared near the leading edge of the pylon, introducing strong pressure fluctuations at the reattachment point. Finally, at $\alpha = +12$ deg the suction side of the pylon had stalled in the slipstream region because of the increase in angle of attack caused by the propeller swirl. As a result, the average amplitude of the tonal pressure fluctuations on the suction side of the pylon decreased in this condition compared to the results obtained at $\alpha = \pm 6$ deg.

ROOT MEAN SQUARE OF THE UNSTEADY LIFT COEFFICIENT

Figure 7.16 depicts the root mean square of the unsteady pylon lift coefficient (Eq. 7.2) versus advance ratio (Fig. 7.16a) and propeller–pylon spacing (Fig. 7.16b). No sensitivity to the angle of attack could be obtained, since the pressure interpolation procedure did not work if part of the flow on the pylon was separated.

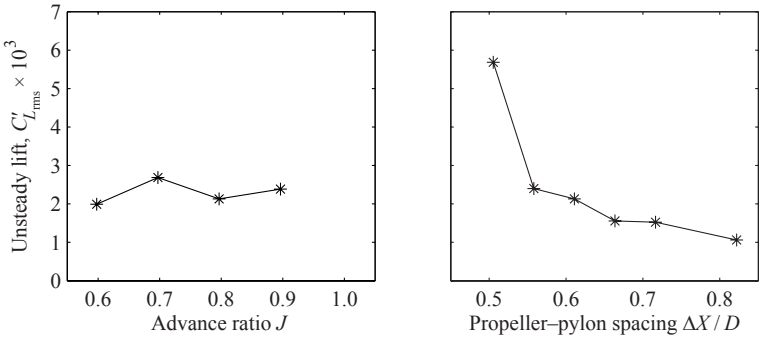

a) $\Delta X/D = 0.42$, $\alpha = 0$ deg b) $J = 0.8$, $\alpha = 0$ deg

Figure 7.16: Root mean square of the unsteady pylon lift coefficient versus advance ratio (a) and propeller–pylon spacing (b).

The root mean square of the unsteady lift coefficient of the pylon features a non-monotonic dependency on the propeller advance ratio (Fig. 7.16a). This differs from the spatially averaged amplitude of the pressure fluctuations, which showed a decreasing trend with increasing advance ratio (Fig. 7.15a). However, a change in advance ratio not only modifies the strength of the blade wakes and tip vortices, but also the pitch of the slipstream helix. As a result, the axial separation between the consecutive wakes and tip vortices, and hence the wavelength of the interaction problem, varies with advance ratio. For the four propeller operating conditions considered, the lowest unsteady loads were obtained for advance ratios at which the ratio between the wavelength of the perturbation associated with the propeller tip vortices and the pylon chord length was as close as possible to an integer number. This is explained in Fig. 7.17, which illustrates the resulting unsteady lift response for a simplified case with two different ratios of perturbation wavelength to pylon chord length. In this case, a perfectly sinusoidal pressure perturbation is assumed, which is constant in the spanwise direction.

From Eq. 7.2 it follows that the root mean square of the unsteady pylon lift coefficient would be zero for the case of a sinusoidal pressure waveform with wavelength equal to an integer multiple of the pylon chord length (Fig. 7.17a). For non-integer ratios between wavelength and chord length, on the other hand, a nonzero root mean square of the unsteady lift coefficient results (Fig. 7.17b). This implies that structure-borne noise may be reduced by matching the pylon chord length with an integer multiple of the axial separation between the propeller tip vortices. In reality, the pressure difference across the pylon will not be perfectly sinusoidal, for example due to the different response on the advancing and retreating sides (Fig. 7.11). Therefore, follow-up experiments involving additional test cases with varying ratios between perturbation wavelength and pylon chord length would be required to confirm the applicability of this theory.

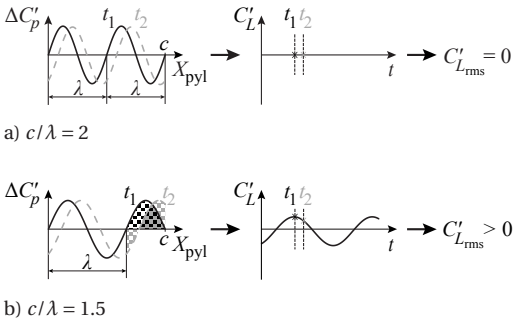

Figure 7.17: Illustration of lift coefficient fluctuations for integer (a) and non-integer (b) ratios of perturbation wavelength to pylon chord length.

In contrast to the sensitivity to the advance ratio, the root mean square of the unsteady lift coefficient monotonically decreases with propeller–pylon spacing (Fig. 7.16b). In this case, the advance ratio was fixed and thus the ratio between the wavelength of the pressure disturbance and the pylon chord length was constant. Therefore, the relative amplitude of the lift fluctuations was only affected by the relative amplitude of the pressure fluctuations, which feature a decreasing trend with increasing advance ratio, as shown in Fig. 7.15a.

7.4. KEY FINDINGS

This chapter has quantified the unsteady loading caused by the impingement of a propeller slipstream on a downstream pylon. A pylon-mounted tractor-propeller configuration was simulated by positioning a pylon downstream of a sting-mounted propeller in a low-speed wind tunnel.

Particle-image-velocimetry measurements confirmed the presence of the individual blade wakes and tip vortices in the propeller slipstream. The installation of the pylon leads to a spanwise shearing of the propeller slipstream, caused by the spanwise variations in lift on the pylon. The slipstream moves away from the propeller axis on the advancing side and toward the propeller axis on the retreating side. At nonzero angle of attack, the crossflow component over the nacelle modifies the distortion of the slipstream. For an inboard-up rotating propeller, the spanwise shearing of the slipstream is decreased at positive angle of attack and amplified at negative angle of attack.

Measurements of the pressure fluctuations on the pylon using microphones led to the conclusion that the blades' tip vortices dominate the unsteady pressure caused by the impingement of the propeller slipstream. The pressure fluctuations induced by the tip-vortex interaction are periodic with a rich spectral content, and persist up to the trailing edge of the pylon. The pressure fluctuations decrease with increasing advance ratio due to the associated reduction in strength of the blade wakes and tip vortices. At high advance ratios, the strength of the tip vortices tends to zero while the blade wakes remain, making the blade wakes the dominant source of unsteady loading in such conditions. Increasing the propeller–pylon spacing reduces the pressure fluctuations due to diffusion of the blade wakes and tip vortices before their interaction with the pylon.

From an assessment of the unsteady loading on the pylon, it is concluded that the unsteady pylon lift displays a nonmonotonic dependency on the propeller advance ratio. In this case, the ratio between the wavelength of the pressure perturbation and the pylon chord length is important. The unsteady loading was smallest for cases for which this ratio was closest to an integer value. In an idealized case, for integer ratios the integrated pressure differential across the pylon is zero. Based on this observation, it is concluded that structure-borne noise reductions might be obtained by proper tailoring of the pylon chord length.

8

PYLON-WAKE ENCOUNTER

Pusher propellers interact with the wake of their upstream support, leading to a periodic inflow disturbance experienced by the propeller blades. This chapter provides a comprehensive analysis of the resulting aerodynamic and aeroacoustic interaction effects for pylon-mounted pusher propellers. Although it is known that the pylon-wake encounter causes unsteady blade loads and a noise increase, the experimental study discussed in this chapter is the first that discusses both effects simultaneously. Following a characterization of the nonuniform inflow to the propeller due to the pylon wake in Section 8.1, the propeller's unsteady aerodynamic response is discussed in Section 8.2. Section 8.3 then highlights the impact of the pylon-wake encounter on the propeller's noise emissions, after which the key findings are reported in Section 8.4. Throughout the chapter, the sensitivity of the installation effects to the propeller operating conditions and incidence angle is considered. The results were obtained with the APIAN-INF setup described in Chapter 5.

8.1. PYLON-WAKE FLOWFIELD

The velocity deficit in the pylon wake governs the interaction between the pylon and the propeller. Therefore, the flowfield in the wake of the semi-installed pylon was measured using the stereoscopic PIV setup discussed in Section 5.4.1. Both symmetric ($\alpha = 0$ deg) and asymmetric ($\alpha = -6$ deg) inflow conditions were considered. The results measured for both conditions are discussed separately.

8.1.1. SYMMETRIC INFLOW

The axial velocity was extracted from the measurement planes at $0.075D$ upstream of the propeller, for the three propeller operating conditions considered. Linear interpolation was performed between the six measurement planes (Fig. 5.10a) to obtain the axial velocity at the vertical and lateral positions traced by a blade section at a given radial coordinate. The results are presented in Fig. 8.1 as the ratio of the velocity obtained for

The contents of this chapter have been adapted from Ref. [132].

the pylon-on and pylon-off configurations. A radial coordinate of $r/R = 0.65$ is considered, because the blade pressure distribution was measured at this position. Markers are indicated at 2-deg intervals for clarity; the actual resolution of the data was higher.

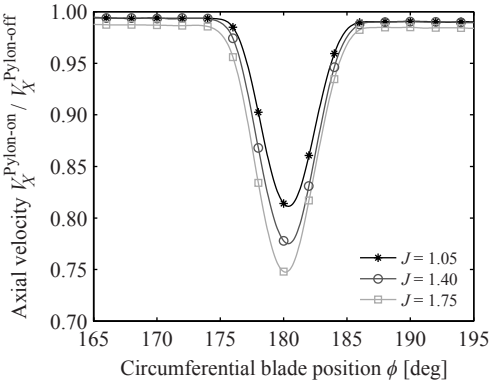

Figure 8.1: Effect of propeller thrust setting on the wake velocity deficit experienced by a blade section at $r/R = 0.65$, $0.075D$ upstream of the propeller; $\alpha = 0$ deg.

Figure 8.1 shows a net decrease in inflow velocity in the pylon wake, with a magnitude of 19 – 25% of the local velocity measured for the pylon-off configuration. The maximum deficit occurred in the center of the wake at a blade position of $\phi = 180$ deg, as expected. Both the wake width and maximum velocity deficit decreased with increasing propeller thrust. This is due to the favorable pressure gradient imposed by the propeller. Similar results have been presented in the literature for turbulent wakes in favorable pressure gradients (e.g. Ref. [150]). Outside of the wake region, an additional change in velocity is observed due to the installation of the pylon. This is due to the deceleration of the flowfield near the pylon trailing edge.

8.1.2. ASYMMETRIC INFLOW

Operation of the pylon-on configuration in asymmetric inflow leads to nonzero loading on the pylon. To assess whether this modified the pylon wake, Fig. 8.2 provides a comparison of the propeller inflow experienced under symmetric and asymmetric inflow conditions. The low thrust case is considered, while the PIV measurements in angular inflow were only taken at a negative angle of attack ($\alpha = -6$ deg), since that case offered the best optical access. For clarity, markers are again displayed at 2-deg intervals.

The velocity profiles plotted in Fig. 8.2 show that for the case with angular inflow, the location of the maximum velocity deficit shifted to a lower circumferential angle than for the symmetric configuration. Also, the flow deceleration outside of the pylon wake increased due to the operation at nonzero incidence angle. Both effects are due to the increased loading on the pylon, which intensified the impact of the pylon on the surrounding flowfield. Yet, the relative velocity deficit and wake width were comparable for both cases. Therefore, the impact of the wake encounter on the propeller blade loads is expected to be similar for the symmetric and asymmetric inflow cases. This is verified in the next section.

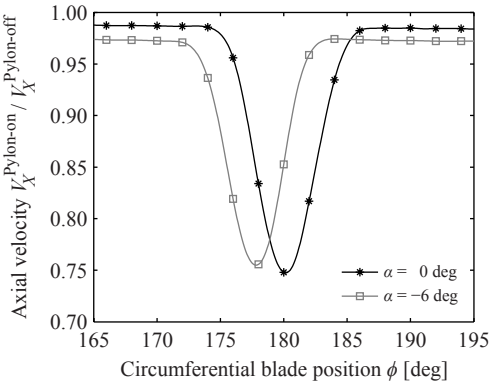

Figure 8.2: Effect of angular inflow on the wake velocity deficit experienced by a blade section at $r/R = 0.65$, $0.075D$ upstream of the propeller; $J = 1.75$.

8.2. PROPELLER LOADING

The velocity deficit in the pylon wake introduces a nonuniformity into the propeller inflow. To quantify the resulting impact on the propeller response, the surface-pressure transducers and rotating shaft balance were used (Section 5.4.2). Again, the results obtained under symmetric and asymmetric inflow conditions are discussed separately.

8.2.1. SYMMETRIC INFLOW

The unsteady blade loads were analyzed at a radial station of $r/R \approx 0.65$. Figure 8.3 presents the development of the normal-force coefficient throughout the rotation, while Table 8.1 summarizes the corresponding numerical values. Estimates of the uncertainty of the data were computed from the scatter of repeated measurements taken for the pylon-off configuration, and are indicated by the error bars plotted in the top left of the subplots of Fig. 8.3. Data markers are displayed at 15-deg intervals for clarity. The circumferential blade position is defined with respect to the leading edge of the blade at a radial station of $r/R \approx 0.65$, while the normal-force coefficient is defined with respect to the dynamic pressure in the rotational frame.

Table 8.1: Effect of pylon installation on the sectional blade-loading characteristics at $r/R \approx 0.65$, $\alpha = 0$ deg. The normal-force coefficient at the maximum impact of the wake encounter is indicated by $c_{n_{\text{wake}}}$.

J	$\overline{c_n}$		$\frac{(\overline{c_n})_{\text{Pylon-on}}}{(\overline{c_n})_{\text{Pylon-off}}}$	$\frac{c'_{n_{\text{rms}}}}{\overline{c_n}}$		$\frac{c_{n_{\text{wake}}}}{\overline{c_n}}$	$\phi(c_{n_{\text{wake}}})$
	Pylon-off	Pylon-on		Pylon-off	Pylon-on		
1.05	0.546	0.549	1.004	0.006	0.020	1.074	190 deg
1.40	0.320	0.334	1.042	0.016	0.049	1.263	183 deg
1.75	0.150	0.168	1.120	0.030	0.070	1.369	181 deg

Figure 8.3 shows an unexpected sinus-like variation of the section normal-force coefficient during the rotation for the pylon-off configuration. This is ascribed to a slight angular inflow to the measurement setup, caused by a flow perturbation due to the presence of the in-flow measurement infrastructure. The corresponding inflow angle was

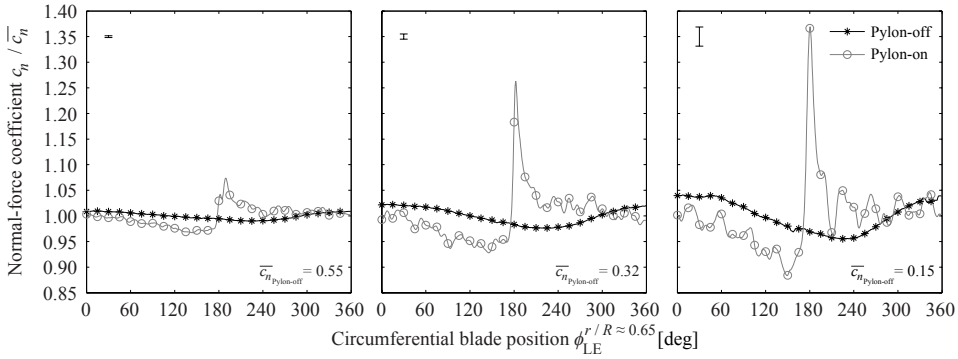

a) High thrust, $J = 1.05$ b) Intermediate thrust, $J = 1.40$ c) Low thrust, $J = 1.75$

Figure 8.3: Effect of pylon installation on the normalized section normal-force coefficient at $r/R \approx 0.65$, $\alpha = 0$ deg. Error bar displayed in the top left of each subplot.

estimated from the data to be approximately 0.2 deg. With the pylon installed, an impulsive increase in blade loading occurred during the wake encounter. Analysis of the pressure distributions showed that the normal-force increase was mainly due to a localized rise of the pressure jump across the leading-edge part of the blade, as illustrated in Fig. 8.4 for the intermediate thrust case ($J = 1.40$). The pressure distribution on the rear of the blades was hardly affected by the installation of the pylon.

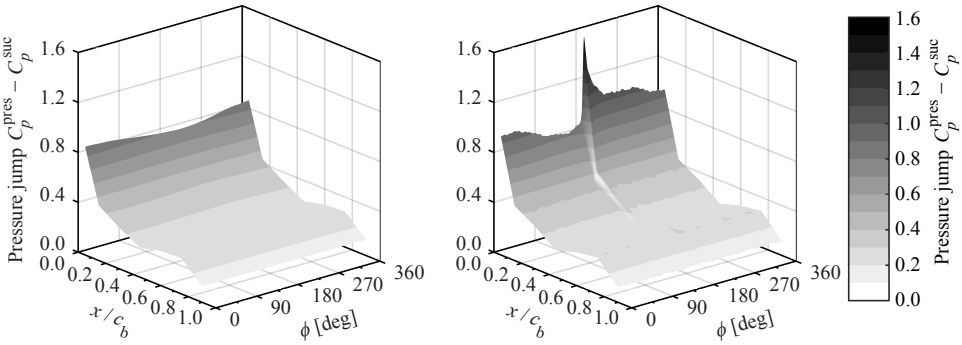

a) Pylon-off b) Pylon-on

Figure 8.4: Effect of pylon installation on the pressure jump throughout the rotation at $r/R \approx 0.65$; $J = 1.40$, $\alpha = 0$ deg. Pressure coefficient defined with respect to effective dynamic pressure in rotational frame.

The largest impact of the wake on the blade normal force occurred at the low thrust setting ($J = 1.75$). In this operating regime, the normal force increased by approximately 35% during the wake encounter when compared to the steady-state value. Considering the root mean square of the normal-force fluctuations, a similar conclusion can be drawn: with increasing thrust setting, the relative amplitude of the normal-force fluctuations decreased. The reduction in impact of the wake encounter with increasing thrust setting has three reasons. First, for a given velocity deficit in the propeller inflow, the ab-

solute change in angle of attack experienced by a blade section decreases with increasing rotational velocity, hence increasing rotational speed of the propeller. This effect is further enhanced by the reduction in wake deficit with increasing thrust coefficient, as shown in Fig. 8.1. Second, with increasing thrust setting the change in inflow angle due to the wake encounter loses importance relative to the unperturbed value, since the angle of attack of the blade sections increases with decreasing advance ratio. Finally, the reduced frequency of the wake-encounter phenomenon increases with increasing rotational speed, hence thrust setting. With increasing reduced frequency, the amplitude of the unsteady load perturbation decreases [114]. For the given blade geometry and operating parameters, the reduced frequency at $r/R \approx 0.65$ equaled 0.28, 0.26, and 0.24 at the fundamental frequency for the high, intermediate, and low thrust conditions, respectively. The unsteady response of the blades also leads to a phase lag between the peak normal-force response and the location of maximum velocity deficit in the wake (at $\phi = 180$ deg). This phase lag increased with the thrust setting due to the associated increase in reduced frequency of the perturbation problem.

Outside of the pylon-wake region, the blade responses for the pylon-off and pylon-on configurations also differed. Ahead of the wake encounter, the blades experienced a slight change in loading due to the local deceleration of the flowfield near the pylon trailing edge. After the wake encounter, the blade response slowly recovered toward the values recorded for the pylon-off configuration. The load oscillations occurring in this part of the rotation for the pylon-on configuration seem related to the excitation of the blades due to the wake passage. However, it is unknown whether they were the result of purely aerodynamic effects, or possibly a structural response of the blades.

The fluctuations of the suction-peak pressure coefficient were analyzed in the frequency domain to assess the tonal and broadband components of the unsteady blade loads resulting from the installation of the pylon. Repeated measurements provided 6 – 17 spectra for each operating condition. Ensemble averaging was performed to obtain the final results, as plotted in Fig. 8.5. Low-amplitude electronic noise was present in the pylon-off data at frequencies equal to integer multiples of 50 Hz, corresponding to mains interference.

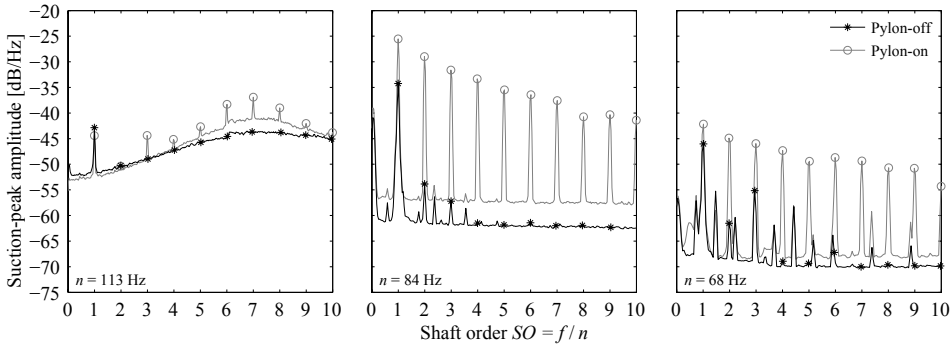

a) High thrust, $J = 1.05$ b) Intermediate thrust, $J = 1.40$ c) Low thrust, $J = 1.75$

Figure 8.5: Effect of pylon installation on the frequency spectra of the suction-peak pressure coefficient at $r/R \approx 0.65$; $x/c_b = 0.05$, $\alpha = 0$ deg.

The frequency spectra presented in Fig. 8.5 significantly differ between the three thrust settings. Comparing the pylon-off configurations, a strong increase in broadband component of the pressure fluctuations can be observed at the high thrust setting (Fig. 8.5a). This was due to the increased turbulence level induced by a leading-edge vortex, caused by the high blade sweep. The existence of this leading-edge vortex was confirmed by analysis of the data from the pressure sensors at the other locations on the blade, and numerical simulations of the isolated propeller discussed in Ref. [134]. For the lower thrust cases (Fig. 8.5b and 8.5c), the leading-edge vortex was less prominent ($J = 1.40$) or absent ($J = 1.75$). Therefore, the broadband response is lower for these thrust settings. Instead, at the intermediate and low thrust settings the spectra were dominated by the fundamental tone at the shaft frequency, while the levels of the harmonics were comparatively low. The observed tonal components in the pylon-off data were due to the slight inflow angularity discussed in conjunction with Fig. 8.3, and should be considered as an artifact rather than an expected feature of the investigated configuration.

For the pylon-on configurations, the periodic impulsive increase in suction-peak pressure during the wake encounter led to an increase of the power levels at the shaft order, and especially its harmonics. The largest tonal pressure oscillations occurred at the intermediate thrust setting (Fig. 8.5b). The increased turbulence intensity in the pylon wake amplified the broadband response of the blades at all thrust settings when compared to the pylon-off configuration.

So far, only results have been presented of the sectional blade loading. To assess whether the installation of the pylon also impacted the integrated propeller loads, the RSB data were evaluated. Figure 8.6 depicts the time-averaged propeller performance measured under symmetric inflow conditions, at the three thrust settings considered for the *APIAN-INF* setup throughout the thesis. The corresponding numerical values for the thrust coefficient are summarized in Table 8.2. The uncertainty of the data is indicated by error bars displayed at each datapoint for the pylon-off configuration, as computed by taking the standard deviation of all available repeated measurements.

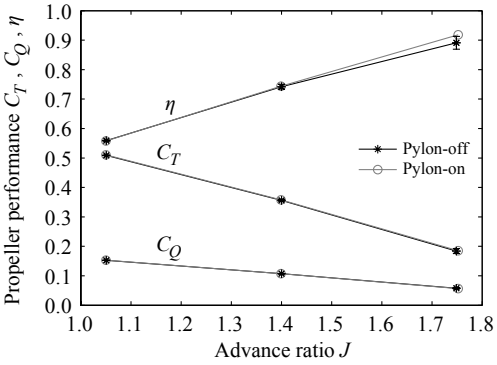

Figure 8.6: Effect of pylon installation on the time-averaged propeller performance; $\alpha = 0$ deg.

From Fig. 8.6 and Table 8.2 it is concluded that the pylon-wake encounter did not significantly alter the time-averaged propeller performance. At all operating points, the measured changes in propeller thrust were within the variability of the RSB data. Sim-

Table 8.2: Effect of pylon installation on the time-averaged propeller thrust coefficient at $\alpha = 0$ deg.

J	C_T		ΔC_T
	Pylon-off	Pylon-on	
1.05	0.509 ± 0.001	0.510 ± 0.001	+0.2%
1.40	0.356 ± 0.004	0.357 ± 0.004	+0.3%
1.75	0.183 ± 0.008	0.187 ± 0.008	+1.8%

ilarly small differences were measured for the torque coefficient. This agrees with the measurement data of Gentry et al. [69], who also concluded that the effect of the pylon wake on the time-averaged propeller performance was negligible. The favorable interference effect due to the nacelle that was observed in that study could not be reproduced here, since no nacelle was present upstream of the propeller. Note that the RSB results differ from the higher changes in section normal-force coefficient derived from the surface-pressure transducers (Table 8.1). However, integrated over the blade the overall increase in thrust could be smaller than predicted locally at $r/R \approx 0.65$ due to variations in unsteady response of the blade along the span.

8.2.2. ASYMMETRIC INFLOW

The results discussed in Section 8.1 showed that the characteristics of the pylon wake were comparable for the cases with symmetric and asymmetric inflow. To test the corresponding effect of the wake encounter on the propeller loading, Fig. 8.7 provides the phase-averaged sectional loading data for the pylon-off and pylon-on configurations, with and without angular inflow. The low thrust condition ($J = 1.75$) is considered, while markers are again plotted at 15-deg intervals. The associated numerical data are provided in Table 8.3.

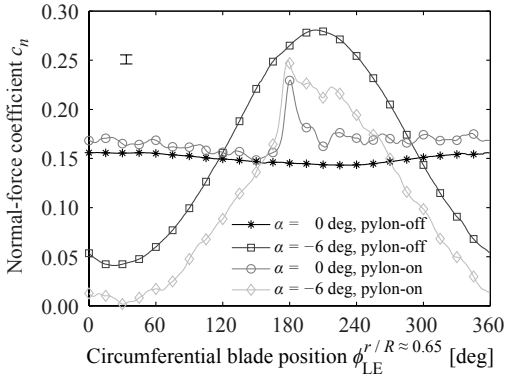

Figure 8.7: Effect of pylon installation and angular inflow on the sectional normal-force coefficient at $r/R \approx 0.65$; $J = 1.75$. Error bar displayed in the top left.

Figure 8.7 confirms that the loading of the isolated propeller becomes unsteady at nonzero angle of attack. The cyclic changes in the effective velocity experienced by the blade sections resulted in angle-of-attack perturbations during the rotation, leading to

Table 8.3: Effect of pylon installation and angular inflow on the sectional blade-loading characteristics at $r/R \approx 0.65$; $J = 1.75$.

Configuration	$\overline{c_n}$		$\frac{(\overline{c_n})_{\alpha=-6 \text{ deg}}}{(\overline{c_n})_{\alpha=0 \text{ deg}}}$	$\frac{c'_{n_{\text{rms}}}}{\overline{c_n}}$	
	$\alpha = 0$ deg	$\alpha = -6$ deg		$\alpha = 0$ deg	$\alpha = -6$ deg
Pylon-off	0.150	0.156	1.039	0.030	0.538
Pylon-on	0.168	0.103	0.614	0.070	0.749

the expected sinusoidal load variations [36, 62]. With the pylon present, a significant shift is observed in the sectional blade loading when comparing the cases at zero and negative incidence angle, as confirmed by Table 8.3. Since the blade normal force was affected throughout the entire rotation, this cannot be due to the more localized pylon-wake encounter. Instead, the offset is ascribed to an interaction with the tip vortex of the pylon. Depending on its direction of rotation relative to the propeller, the tip vortex either increases or decreases the rotational velocity experienced by the blade sections. Consequently, the effective advance ratio is modified due to the interaction with the tip vortex, thereby affecting the propeller blade loads. For the investigated case at $\alpha = -6$ deg, the rotation direction of the tip vortex was the same as that of the propeller, thus decreasing the effective rotational velocity experienced by the blades. Consequently, the blade loading decreased compared to the pylon-off configuration. This was discussed before by Patterson and Bartlett [26] (see also Section 2.2.2).

Apart from the offset in loading due to the tip-vortex interaction, the sinusoidal fluctuation of the normal force due to the angle of attack was similar for the pylon-off and pylon-on configurations. Therefore, it is concluded that the pylon did not appreciably modify the effective incidence angle experienced by the propeller. This opposes the conclusions drawn by Magliozzi [66], who attributed a drop in measured noise levels for the pylon-on configuration at angle of attack to a flow straightening effect due to the pylon.

Figure 8.7 also shows that the wake-encounter effects were comparable under symmetric and asymmetric inflow conditions, apart from a 4-deg phase offset between the blade positions corresponding to the peak normal-force perturbation. This was due to the asymmetry of the wake profile at nonzero angle of attack, which resulted in a shift of the maximum velocity deficit toward the blades entering the wake region (Fig. 8.2).

The shift in blade normal force due to the interaction with the pylon tip vortex strongly modified the propeller performance. Figure 8.8 presents the performance diagrams measured for the pylon-on configuration, at angles of attack of 0 deg and ±6 deg. The corresponding numerical data are provided in Table 8.4. Linear interpolation was applied to report the thrust-coefficient values at the three advance ratios considered in the rest of the chapter. The change in effective advance ratio due to the interaction with the pylon tip vortex is represented by the parameter ΔJ_α. The value of this parameter was approximated by comparing the advance ratios required to obtain the same thrust-coefficient values under symmetric and asymmetric inflow conditions.

The performance curves plotted in Fig. 8.8 show a critical change of the system's sensitivity to the pylon-installation effects due to the angular inflow, confirming the trends observed in the sectional loading data (Fig. 8.7). Operation at positive angle of attack sig-

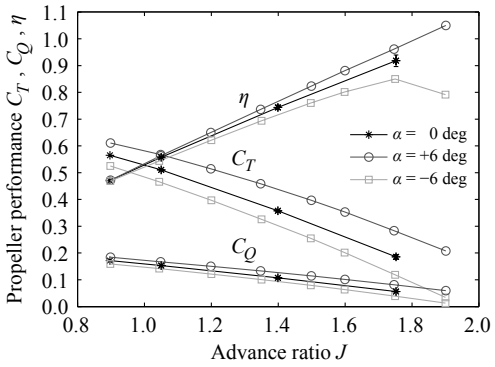

Figure 8.8: Effect of angular inflow on the time-averaged propeller performance; pylon-on.

Table 8.4: Effect of angular inflow on the time-averaged propeller thrust coefficient; pylon-on.

J	C_T			ΔJ_α	
	$\alpha = 0$ deg	$\alpha = +6$ deg	$\alpha = -6$ deg	$\alpha = +6$ deg	$\alpha = -6$ deg
1.05	0.510	0.567	0.464	−0.13	+0.10
1.40	0.357	0.438	0.302	−0.16	+0.10
1.75	0.187	0.281	0.119	−0.17	+0.11

nificantly increased the propeller thrust and torque at constant advance ratio. Table 8.4 shows that for this case, the effective advance ratio sensed by the blades was decreased by 0.13 to 0.17 when compared to the symmetric case. Considering the definition of the angle of attack (Fig. 5.2a), this implies that the effective advance ratio experienced by a tip-mounted pusher propeller decreases due to the tip-vortex interaction if the propeller rotation direction is inboard-up. In this way, a given thrust coefficient can be obtained at reduced rotational speed of the propeller, which is beneficial from both aerodynamic and acoustic points of view. It should be noted that the measured effects due to the pylon tip vortex might have been amplified due to the absence of a nacelle at the tip of the pylon in the test setup.

8.3. PROPELLER NOISE EMISSIONS

The unsteady blade loads resulting from the pylon-wake encounter introduce an additional noise-generating mechanism compared to the case without pylon. The periodic wake encounter phenomenon causes additional tonal noise emissions. The interaction of the blades with the increased turbulence intensity in the pylon wake constitutes a secondary effect, which might affect the broadband noise emissions.

8.3.1. SYMMETRIC INFLOW

Sound spectra were computed from the in-flow microphone data to compare the propeller noise emissions with and without the pylon. Figure 8.9 presents the spectra acquired at the high, intermediate, and low thrust settings. The data were obtained us-

ing the microphone corresponding to an axial emission angle in the propeller plane (θ_e = 90 deg), and a circumferential position perpendicular to the pylon (ϕ = 90 deg). For reference, measurements of the background noise were taken using a dummy spinner. The corresponding levels are indicated in Fig. 8.9 by the lines without markers. Note that noise from the wind-tunnel fan overpowered the propeller noise at frequencies below approximately 400 Hz.

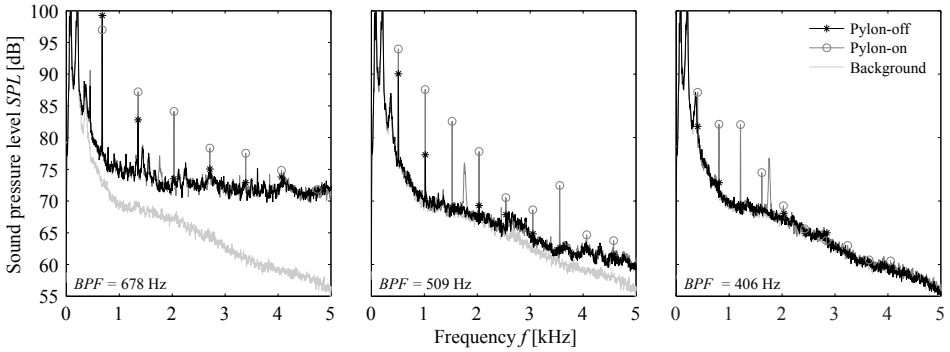

a) High thrust, J = 1.05 b) Intermediate thrust, J = 1.40 c) Low thrust, J = 1.75

Figure 8.9: Effect of pylon installation on the propeller noise spectra; θ_e = 90 deg, ϕ = 90 deg, α = 0 deg.

The spectra depicted in Fig. 8.9 display typical propeller noise signatures. For the pylon-off configuration, the noise emissions were dominated by the fundamental propeller tone (at $f = BPF$). With the pylon present, on the other hand, the noise levels increased and the harmonics contributed to the overall tonal noise level at all operating conditions considered. This is due to the impulsive blade-loading change during the pylon-wake encounter (Fig. 8.3), and was also observed before by other researchers [17]. The overall noise penalty was smallest in high thrust conditions (J = 1.05, Fig. 8.9a), because at this setting the thickness and steady-loading noise sources associated with the isolated propeller were dominant. At the selected microphone position, the level of the fundamental tone even decreased by 2 dB due to the installation of the pylon. At this frequency, the wavelength of the acoustic signal was of the order of the propeller diameter. Therefore, the observed reduction in tonal noise could have been due to local destructive interference between the various noise sources. This is treated in more detail in the discussion of Fig. 8.11. At the other two operating conditions (J = 1.40 and J = 1.75, Fig. 8.9b and 8.9c), the thickness and steady-loading sources were weaker, hence the noise penalty due to the installation of the pylon was larger. This trend of increasing installation impact with decreasing thrust condition agrees with the observations published before by Block and Gentry [14, 64].

The installation of the pylon did not significantly affect the measured broadband noise emissions. These only stood out of the background noise for the high and intermediate thrust cases (for f > 250 Hz and f > 2,500 Hz, respectively). At both thrust settings, the levels of the broadband noise emissions were the same for the pylon-off and pylon-on configurations. Apparently, the increase in random fluctuations of the suction-peak pressure caused by the installation of the pylon (Fig. 8.5) was insufficient to modify the

broadband component of the noise. The strong increase in broadband noise emissions at the highest thrust setting observed for the isolated propeller is as expected considering the spectra of the suction-peak pressure discussed before.

The spectra for the pylon-on configurations contained an additional tone at a frequency of around 1,770 Hz when compared to the pylon-off case. The propeller thrust setting did not affect the frequency and amplitude of this tone, which was ascribed to vortex shedding from the pylon trailing edge. This was concluded from analysis of the velocity fields downstream of the pylon acquired with the PIV setup, as shown in Fig. 8.10. A clear vortex street can be seen traveling downstream, with four shedding periods visible in the field of view. The shedding length was approximated at 26 mm, while the local axial velocity equaled around 45 m/s, leading to a shedding frequency of around 1,730 Hz. This is within 2% of the frequency of the tone observed in the sound spectra (Fig. 8.9), which confirms that the tone was indeed caused by vortex shedding.

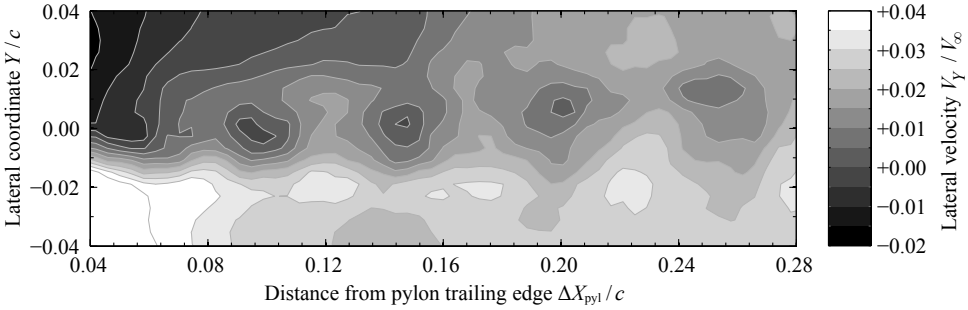

Figure 8.10: Contours of the lateral velocity downstream of the pylon trailing edge (bottom view) indicating vortex shedding; $J = 1.40$, $\alpha = 0$ deg.

Considering the negligible impact of the installation of the pylon on the broadband noise emissions, the remainder of this section focuses on the tonal noise levels. Figure 8.11 compares the pressure waveforms corresponding to the sum of the first ten propeller tones for the pylon-off and pylon-on configurations. It can be seen that the shapes of the pressure waveforms were similar among different thrust settings for the pylon-off configuration. A six-per-revolution cycle can be seen, corresponding to the individual blade passages. The installation of the pylon increased the complexity of the acoustic pressure signals, causing a modification of the noise emissions as discussed before under Fig. 8.9. The intermediate and low thrust cases displayed a comparable behavior. The amplitude of the positive pressure peaks increased due to the installation of the pylon, and the impulsive pressure changes on the blades during the wake encounter enriched the harmonic content of the acoustic signals. At the high thrust setting, a different pattern is observed. The interaction noise component effectively canceled part of the thickness and steady-loading noise generated by the isolated propeller. As a result, the installation of the pylon decreased the overall sound pressure level of the propeller tones at the considered observer position.

Besides the pronounced impact on the levels, the installation of the pylon also affects the directivity of the propeller noise emissions. In the circumferential direction, the noise penalty due to the pylon installation was relatively constant for the range of

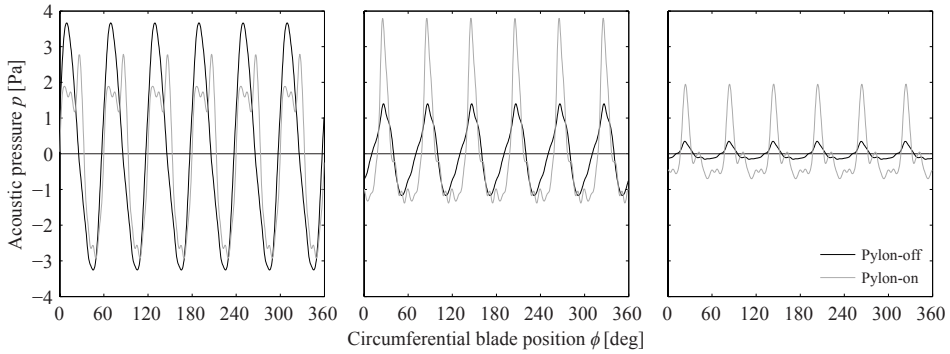

a) High thrust, $J = 1.05$ b) Intermediate thrust, $J = 1.40$ c) Low thrust, $J = 1.75$

Figure 8.11: Effect of pylon installation on the acoustic-pressure waveforms corresponding to the sum of the first ten propeller tones; $\theta_e = 90$ deg, $\phi = 90$ deg, $\alpha = 0$ deg.

angles covered by the in-flow microphones. Therefore, only the results measured with the microphone positioned perpendicular to the pylon ($\phi = 90$ deg) are discussed here. Figure 8.12 presents the corresponding total tonal noise levels as a function of the axial emission angle. An interaction noise metric (labeled 'Interaction') was defined as the sound pressure level corresponding to the difference between the pressure signals for the pylon-on and pylon-off configurations. The resulting values are indicative of the relative importance of the noise source associated with the pylon-wake encounter and the noise levels emitted by the isolated propeller.

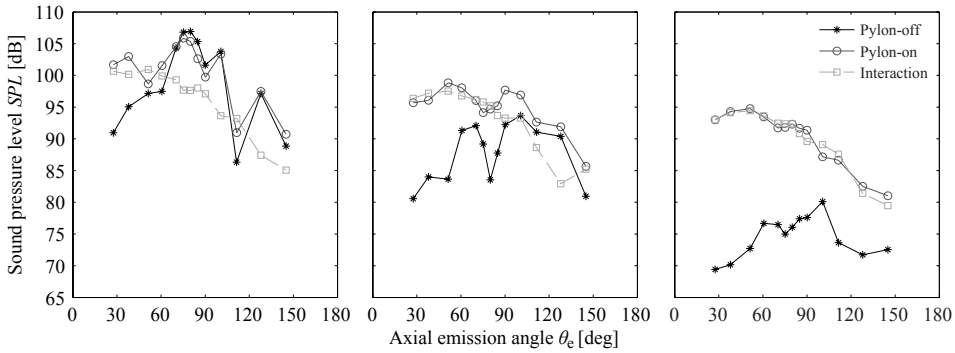

a) High thrust, $J = 1.05$ b) Intermediate thrust, $J = 1.40$ c) Low thrust, $J = 1.75$

Figure 8.12: Effect of pylon installation on the axial directivity of the propeller's tonal noise emissions; $\phi = 90$ deg, $\alpha = 0$ deg.

The data displayed in Fig. 8.12 present a clear directivity effect. The additional noise due to the installation of the pylon was especially pronounced in the upstream direction. Regardless of the propeller thrust setting, the interaction noise peaked at an axial emission angle of about 50 deg. The largest installation impact occurred at the low thrust setting, with a noise penalty of up to 24 dB. Consequently, the installation of the pylon

strongly reduced the sensitivity of the noise emissions to the propeller thrust setting. For the isolated propeller, a difference of 10 – 20 dB was present between the high and low thrust cases. With the pylon installed, this decreased to 5 – 10 dB. The measured directivity of the interaction noise due to the installation of the pylon matches with numerical results computed by Stürmer and Yin [71] for the front row of a contra-rotating open rotor with high blade sweep. Block and Gentry [14, 64], on the other hand, measured a strong noise penalty in both the forward direction and the aft direction. The exact reason for this difference is unknown, but it could be related to the significantly different blade shape used in the current experiment compared to the model used by Block and Gentry.

The directivity patterns measured for the isolated propeller showed unexpected local drops in the noise level at all three advance ratios. Analysis of the pressure waveforms showed that this was due to interference between the various noise sources, which might have locally reduced the measured sound pressure level. For the fundamental tone, with a wavelength in the order of the propeller diameter, the pressure signals at $\theta_e = 80$ deg and $\theta_e = 90$ deg were completely out of phase. No significant additional peaks were observed in the spectra apart from those corresponding to the individual blade passages. Therefore, the possibility of reflections influencing the data seems to be excluded.

8.3.2. ASYMMETRIC INFLOW

Operation of the propeller at angle of attack affects the propeller noise emissions in two different ways [151]. First, the oscillatory blade loading (Fig. 8.7) introduces a source of unsteady-loading noise. Second, the crossflow modifies the local Mach number of the blade sections when rotating toward the observer. The recorded noise levels are increased if the blades travel toward the microphones with increased Mach number, and vice versa. The relative impact of the two effects depends on the propeller operating condition. This is illustrated in Fig. 8.13, which presents the axial directivity patterns measured with the isolated propeller at the high and low thrust settings (Fig. 8.13a and 8.13b). For the low thrust setting, also the data acquired for the pylon-on configuration are provided (Fig. 8.13c). Results are presented for incidence angles of 0, +6, and −6 deg, except for the high thrust case for which only data were available at 0 and −6 deg.

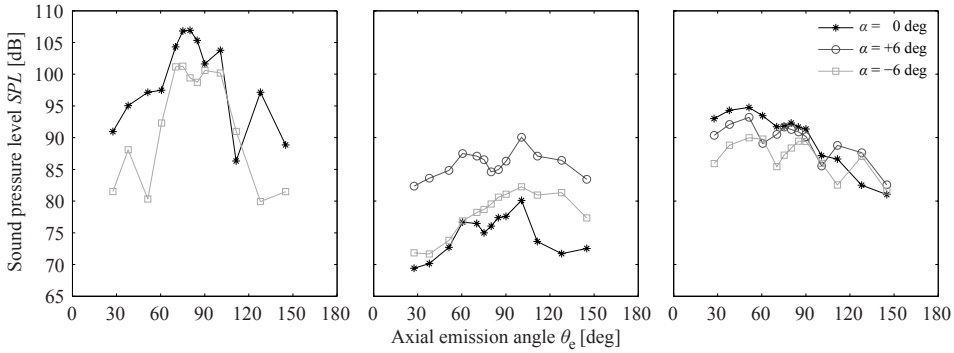

a) Pylon-off, $J = 1.05$ b) Pylon-off, $J = 1.75$ c) Pylon-on, $J = 1.75$

Figure 8.13: Effect of angular inflow on the axial directivity of the propeller's tonal noise emissions; $\phi = 90$ deg.

The directivity patterns shown in Fig. 8.13a and 8.13b highlight the shift in acoustic impact of the angle of attack with the propeller operating point. For the circumferential directivity angle considered here (ϕ = 90 deg), the blades traveled toward the microphones at increased Mach number for the positive incidence case. Therefore, at that condition the highest noise penalty was observed at all thrust settings, since both the unsteady blade loads and convective-amplification effects resulted in increased noise levels at the observer location. For the low thrust case at positive angle of attack, the resulting noise penalty was up to 12 dB when compared to the symmetric-flow case. At $\alpha = -6$ deg, on the other hand, the unsteady blade loads increased the noise levels, which was opposed by a noise decrease due to the reduced blade velocity in the direction of the microphones. Figure 8.13 shows that the effects due to the unsteady blade loads were dominant at the low thrust setting, while for the high thrust case the blade Mach number effects had the largest impact on the overall noise levels. This was confirmed by analysis of the pressure waveforms corresponding to the data depicted in Fig. 8.13.

As shown in Fig. 8.13c, the installation of the pylon also increased the noise emissions under angular inflow conditions. However, the noise levels were lower than for the symmetric case in most of the directivity range. Especially for the case at positive angle of attack, the noise penalty due to the installation of the pylon was significantly smaller than for the symmetric configuration. To investigate the angular-inflow effects in more detail, Fig. 8.14 presents the waveforms of the acoustic pressure for the three incidence angles at the low thrust condition (J = 1.75). Note that the results were obtained at constant advance ratio, which implies that the propeller loading differed considerably between the three cases (Fig. 8.8).

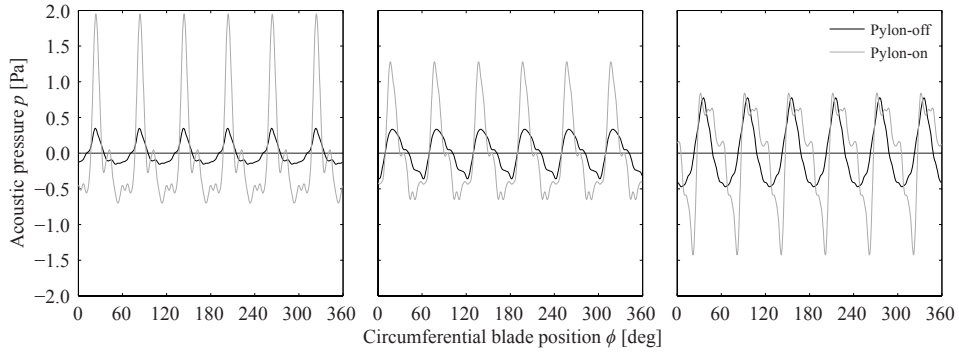

a) $\alpha = 0$ deg b) $\alpha = -6$ deg c) $\alpha = +6$ deg

Figure 8.14: Effect of pylon installation and angular inflow on the acoustic-pressure waveform corresponding to the sum of the first ten propeller tones; $J = 1.75$, $\theta_e = 90$ deg, $\phi = 90$ deg.

The pressure traces plotted in Fig. 8.14 confirm the complex changes to the sound-field due to the operation at nonzero incidence angle discussed before. At the negative angle of attack (Fig. 8.14b), the shape of the waveform corresponding to the isolated propeller (pylon-off) was modified due to the addition of the noise source caused by the unsteady blade loads. Operation at positive angle of attack (Fig. 8.14c) increased the amplitude of the isolated-propeller noise, due to both the unsteady blade loads and the blade Mach number effect.

The pylon-installation effects were strongly modified by operation at positive angle of attack. In this inflow regime, the amplitudes of the positive pressure peaks were hardly changed by the installation of the pylon, as opposed to the results at zero and negative angle of attack. Instead, the pylon-wake encounter led to strong negative peaks in the acoustic waveform. This is likely related to the concurrent effects of the angle-of-attack perturbations due to the operation at nonzero incidence angle and the installation of the pylon. At $\alpha = +6$ deg, the wake encounter occurred in the part of the rotation where the blade angle of attack decreased due to the angular inflow. Therefore, the velocity deficit in the pylon wake locally *reduced* the angle-of-attack disturbance experienced by the propeller blades. Consequently, the wake encounter resulted in an additional change of sign of the blade-loading gradient when compared to the cases at $\alpha = 0$ deg and $\alpha = -6$ deg. This explains the additional negative peak in the acoustic waveforms, and stresses the importance of proper consideration of the propeller rotation direction for optimal integration of the propellers with the airframe.

8.4. KEY FINDINGS

This chapter has presented a comprehensive analysis of the aerodynamic and aeroacoustic interaction effects for pylon-mounted pusher propellers. The unique evaluation of the flowfields between the pylon and the propeller showed that the suction of the propeller reduces the severity of the pylon-wake encounter. The wake width and velocity deficit decrease with increasing thrust setting due to the favorable pressure gradient imposed by the propeller.

Measurements of the propeller performance confirmed previously published results by showing that the passage of the blades through the pylon wake has a negligible effect on the time-averaged propeller forces. In contrast, the impact on the unsteady blade loads is significant, with a rapid increase in normal force during the wake encounter. The fluctuating blade pressures modify the amplitude, spectral content, and directivity of the propeller noise emissions, confirming results published in the literature. The sensitivity of the interaction noise to the propeller operating point is lower than for the noise sources associated with the isolated propeller. Therefore, the installation of the pylon reduces the sensitivity of the propeller noise emissions to the thrust setting. The additional noise due to the unsteady blade loads peaks in the upstream direction, independent of the propeller thrust setting. At the lowest thrust setting considered, a maximum tonal noise penalty of 24 dB was measured. The impulsive nature of the pylon-wake encounter enriches the spectral content of the noise emissions. As such, the harmonics significantly contribute to the overall noise levels for the pylon-on configuration. Only the tonal noise levels were affected by the pylon-installation effects, while the broadband levels remained unchanged.

When operating in asymmetric inflow, the pylon tip vortex interacts with the propeller to result in significant modifications of the mean propeller performance. The rotational velocity components induced by the tip vortex affect the effective advance ratio sensed by the propeller, thereby changing the propeller rotational speed required to achieve a given thrust. The propeller performance is enhanced when the direction of rotation of the pylon tip vortex is opposite to that of the propeller. The noise penalty due to the pylon-installation effect can significantly decrease in this condition if the wake

encounter occurs in the part of the rotation in which the effective rotational velocity is reduced by the angular inflow. This novel result emphasizes the importance of consideration of the propeller rotation direction for optimal integration of the propellers with the airframe.

IV

Performance-Enhancement Strategies

9

SWIRL-RECOVERY VANES

Chapter 6 showed that wingtip-mounted tractor propellers with inboard-up rotation provide aerodynamic benefits due to the interaction between the wing and the propeller slipstream. However, in the case of a vehicle configuration with co-rotating propellers, i.e. inboard-up propeller rotation on one side of the aircraft and outboard-up on the other, a strong asymmetry would arise in the aerodynamic loading. In such a case, swirl-recovery vanes (SRVs) can be applied to recover the propeller swirl before it interacts with the wing, thereby mitigating the potential performance penalties. Furthermore, the SRVs can provide an additional thrust force which enhances the efficiency of the propulsion system. This chapter first discusses the aerodynamic and aeroacoustic performance of an isolated propeller with SRVs in Section 9.1. For this case, the data were measured with the APIAN-INF setup (Chapter 5). Subsequently, a preliminary investigation of a pylon-installed configuration with SRVs is presented in Section 9.2; for this case, the PROWIM-T setup (Chapter 3) was used. Finally, the key findings are summarized in Section 9.3. The results provide unique insights into the effect of SRV installation on the flowfield, the resulting time-averaged and unsteady aerodynamic interactions, and the noise emissions.

9.1. ISOLATED PROPELLER CONFIGURATION

9.1.1. PROPELLER-SLIPSTREAM FLOWFIELD

The installation of SRVs downstream of the propeller modifies the slipstream flowfield. The PIV setup discussed in Section 5.4.1 was used to measure the velocity fields for the cases with and without SRVs. In Ref. [134], these results are compared to CFD data, which were in turn analyzed for a more detailed quantification of the swirl recovery achieved by the SRVs.

VELOCITY FIELDS

The goal of the SRVs is to convert the angular momentum of the swirl in the propeller slipstream into a force in the thrust direction. To compare the distribution of the swirl in

Parts of this chapter have been adapted from Ref. [134].

the slipstream with and without SRVs installed, Fig. 9.1 presents contours of the phase-locked tangential velocity at the position of the PIV measurement plane. The intermediate thrust condition ($J = 1.40$) is considered, since at this propeller setting the SRVs delivered the largest efficiency increase (see Section 9.1.2). No experimental data were available around $X/R = 0.6$ for the configuration with SRVs due to reflections from the nearby SRVs. It should be noted that with the SRVs installed the setup is no longer axisymmetric; hence, the single evaluation plane considered in Fig. 9.1 is not necessarily representative of the velocity distribution in the entire slipstream.

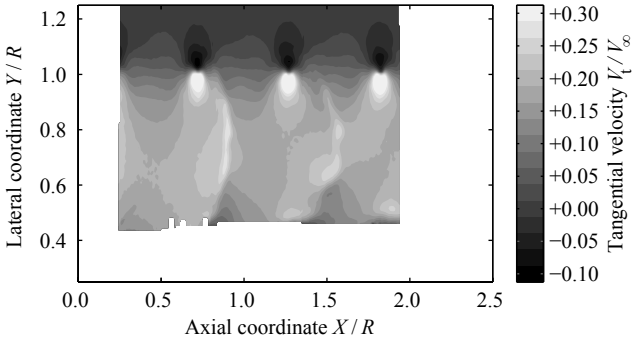

a) SRVs off

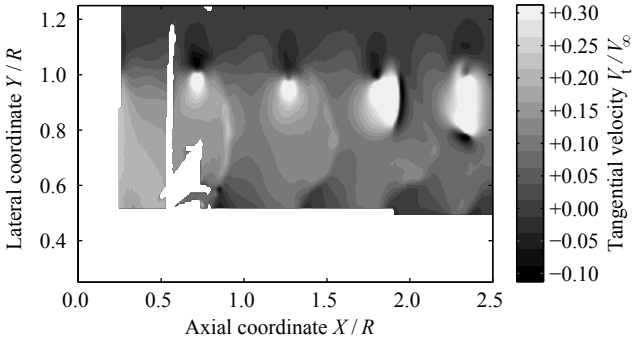

b) SRVs on

Figure 9.1: Effect of SRVs on the phase-locked tangential velocity in the propeller slipstream at $Z/R = 0.03$, $J = 1.40$.

The contours of the tangential velocity plotted in Fig. 9.1 indicate that the SRVs reduced the swirl in the propeller slipstream. Downstream of the SRVs ($X/R \geq 0.6$), the tangential velocity component was decreased over the radial extent of the slipstream covered by the SRVs ($Y/R < 0.9$) when compared to the result obtained for the isolated propeller. Because of the cropping of the SRVs relative to the propeller diameter, the swirl in the outboard region of the slipstream ($Y/R \geq 0.9$) could not be recovered. In fact, the swirl velocity was enhanced in this region due to the loading on the SRVs. Upstream of the SRVs, a small increase in the tangential velocity occurred. This is due to the upwash induced by the loaded SRVs. The wakes of the propeller blades can be seen in the

slipstream as vertical bands of increased tangential velocity (e.g. at $X/R = 0.9$), which become increasingly crescent when convecting downstream due to the nonuniform axial and tangential velocity distributions in the slipstream. The tip vortices of the propeller blades can be recognized by the pronounced velocity perturbations at the edge of the slipstream ($Y/R \approx 1.0$). At a streamwise coordinate of $X/R \approx 2.0$, the tip vortex from the nearest SRV entered the measurement plane at $Y/R \approx 0.9$ and started interacting with the tip vortex of the propeller blade [134]. This affected the trajectory of the tip vortex from the SRV, which as a result displayed an oscillating behavior.

To provide a quantitative comparison between the cases without and with SRVs, profiles of the time-averaged tangential and axial velocity were extracted from the evaluation plane, at $X/R = 1.5$ downstream of the propeller. The corresponding results are given in Fig. 9.2, which includes the data for all considered propeller thrust settings. Markers are plotted at every fifth datapoint for clarity, while the uncertainty of the data is indicated by the gray shading surrounding the measured average values.

The tangential-velocity profiles (Fig. 9.2a, 9.2c, 9.2e) confirm the conclusions drawn from Fig. 9.1. The largest reductions in swirl were obtained in the radial part of the slipstream covered by the SRVs ($Y/R < 0.9$), while for $Y/R \geq 0.9$ no benefits could be achieved because of the cropping of the SRVs. Near the root of the SRVs, a negative tangential velocity occurred, indicating that the velocity induced by the SRVs overcompensated the original swirl in the propeller slipstream. At the high thrust setting ($J = 1.05$, Fig. 9.2a), a tip vortex of one of the SRVs crossed near the considered evaluation location ($X/R = 1.5$). This caused the negative gradient in the tangential velocity around $0.7 < Y/R < 0.8$.

From the axial-velocity profiles (Fig. 9.2b, 9.2d, 9.2f) it is concluded that for the high thrust condition ($J = 1.05$, Fig. 9.2b), the installation of the SRVs decreased the axial velocity at the measurement location over most of the considered radial extent. At this operating point, relatively high tangential velocities occur in the slipstream (Fig. 9.2a), causing a large inflow angle to the SRVs. CFD simulations showed that this resulted in leading-edge separation over a large part of the span of the SRVs, reducing the axial velocity in the downstream part of the slipstream [134]. At the intermediate and low thrust settings, on the other hand, the installation of the SRVs increased the axial velocity in the part of the slipstream in which the swirl was recovered ($Y/R < 0.85$).

SWIRL RECOVERY

The results shown in Figs. 9.1 and 9.2 are only representative of a single horizontal plane in the slipstream of the propeller–SRV configuration. The swirl-recovery performance of the SRVs was quantified by analyzing the changes in rotational kinetic energy flow $\Delta\dot{E}_{k_{rot}}$ and total kinetic energy flow $\Delta\dot{E}_{k_{tot}}$ caused by the propulsion system over the entire propeller disk:

$$\Delta\dot{E}_{k_{rot}} = \iint_{\text{disk}} \frac{1}{2}\rho_\infty |V_a| V_t^2 \, \mathrm{d}A, \tag{9.1}$$

$$\Delta\dot{E}_{k_{tot}} = \iint_{\text{disk}} \frac{1}{2}\rho_\infty \left(|V_a| V^2 - V_\infty^3\right) \mathrm{d}A. \tag{9.2}$$

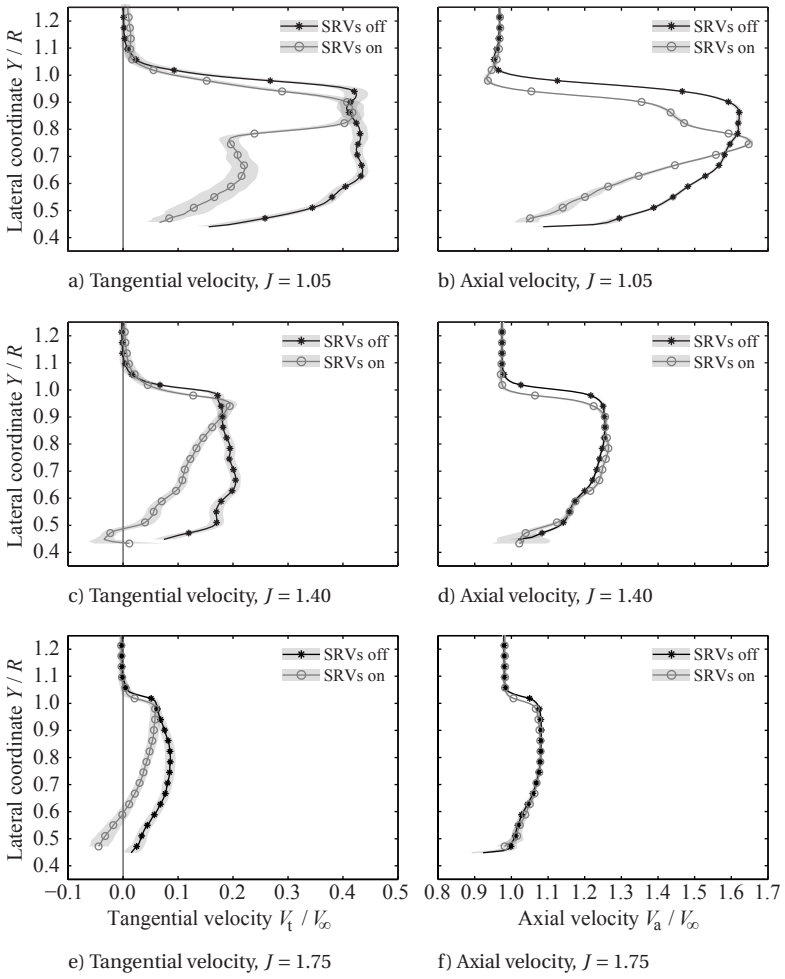

a) Tangential velocity, $J = 1.05$ b) Axial velocity, $J = 1.05$

c) Tangential velocity, $J = 1.40$ d) Axial velocity, $J = 1.40$

e) Tangential velocity, $J = 1.75$ f) Axial velocity, $J = 1.75$

Figure 9.2: Effect of SRVs on the time-averaged velocity in the propeller slipstream at $X/R = 1.5$, $Z/R = 0.03$.

The required data were extracted from the CFD simulations discussed in Ref. [134]. Integration was performed up to a radial coordinate of $r/R = 1.3$, which was sufficiently far away from the slipstream edge to make sure all tangential velocity components had vanished to zero. Table 9.1 reports the ratio of rotational kinetic energy flow to total kinetic energy flow for the cases with and without the SRVs, at all considered propeller thrust settings. It can be seen that the relative contribution of the swirl component to the total kinetic energy flow was decreased by the installation of the SRVs at all thrust settings. The swirl was reduced most effectively at the intermediate thrust condition ($J = 1.40$), with a decrease of 46% compared to the isolated propeller.

Table 9.1: Change in integral ratio of rotational to total kinetic energy flow due to installation of the SRVs.

J	$\Delta\dot{E}_{k_{rot}}/\Delta\dot{E}_{k_{tot}}$		
	SRVs off	SRVs on	Change due to SRVs
1.05	8.5%	5.5%	−35%
1.40	4.6%	2.5%	−46%
1.75	2.0%	1.3%	−35%

9.1.2. PROPULSIVE PERFORMANCE

The propulsive efficiency of the propeller–SRV configuration depends on the thrust of both components, and the propeller torque. The SRVs are designed to generate thrust by deflecting the flow in the propeller slipstream into the axial direction. In turn, the presence of the SRVs might affect the propeller performance due to upstream interference. Both effects are discussed separately.

PROPELLER PERFORMANCE

With the SRVs installed, the inflow to the propeller is modified when compared to the isolated propeller case. Similarly as for propeller–wing interactions (see Sections 2.2.1 and 6.2.4), the axial component of the inflow velocity vector decreases due to blockage, while the local tangential velocity component experienced by the blade sections decreases due to the upwash caused by the SRVs. Since these two effects oppose each other, the final modification of the propeller performance depends on the solidity of the SRVs, their loading, and the propeller–SRV spacing. Table 9.2 displays the measured time-averaged propeller thrust and torque for the configurations with the SRVs on and off. The RSB only measured the forces and moments generated by the rotating part of the setup, so the contribution of the SRVs to the total propulsive performance is not included in Table 9.2. A measure of the variability of the experimental data was obtained by taking the standard deviation of repeated acquisitions for the isolated propeller.

Table 9.2: Effect of SRVs on the time-averaged propeller performance.

J	C_T		C_Q	
	SRVs off	SRVs on	SRVs off	SRVs on
1.05	0.509 ± 0.001	0.510 ± 0.001	0.152 ± 0.001	0.152 ± 0.001
1.40	0.356 ± 0.003	0.357 ± 0.003	0.107 ± 0.001	0.106 ± 0.001
1.75	0.184 ± 0.008	0.187 ± 0.008	0.058 ± 0.003	0.055 ± 0.003

The performance data provided in Table 9.2 show that the overall upstream effect of the SRVs on the time-averaged propeller performance was limited. The differences between the propeller thrust and torque obtained with and without the SRVs were within the variability of the RSB measurements. The accompanying CFD analyses predicted a small but systematic increase in propeller thrust and torque of around 1% due to installation of the SRVs at all operating conditions [134]. This computed increase in loading with SRVs installed is in disagreement with previous experimental results published by Gazzaniga and Rose [79] and Dittmar and Hall [86], who showed an unloading of the

propeller due to the installation of SRVs. This is likely the result of differences in SRV solidity, loading, and propeller–SRV spacing, and not only affects the propulsive efficiency of the system but also the acoustic performance, as discussed in Section 9.1.3.

Whereas the change in time-averaged propeller performance due to the upstream effect of the SRVs was only around 1% of the performance of the isolated propeller, the flow perturbations introduced by the SRVs might still have induced nonnegligible unsteady loading on the propeller blades. Figure 9.3 presents the unsteady component of the blade normal-force coefficient as a function of the circumferential position of the leading edge of the instrumented propeller blade. The circumferential positions of the SRVs (Fig. 5.8) are indicated by the dotted lines. The unsteady normal force was extracted from the experimental data by integrating the pressures measured with the miniature pressure transducers installed in the propeller blades (Section 5.4.2). The influence of the viscous forces was thus neglected, while the results were nondimensionalized with the local effective dynamic pressure, including the rotational velocity of the blade. As discussed in Section 8.2.1, the measured unsteady blade-loading data displayed a dominant one-per-revolution sinusoidal perturbation due to a small flow angularity induced by the inflow measurement infrastructure. Since this effect was not related to the SRVs, it was removed from the data by subtracting the unsteady normal-force component measured for the isolated propeller. The error bars shown in Fig. 9.3 represent the standard deviation of the measured unsteady normal-force coefficient, as computed from repeated measurements at constant operating conditions.

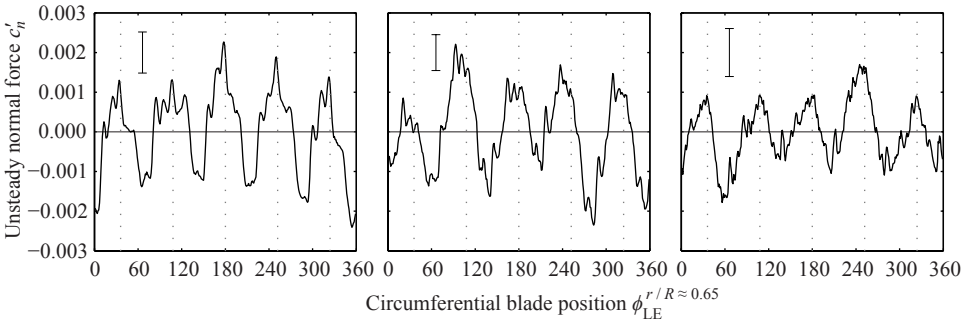

a) High thrust, $J = 1.05$ b) Intermediate thrust, $J = 1.40$ c) Low thrust, $J = 1.75$

Figure 9.3: Unsteady propeller blade loading at $r/R \approx 0.65$ caused by the upstream effect of the SRVs. SRV locations indicated by the dotted lines.

Figure 9.3 confirms the expected perturbation of the propeller blade loading due to the installation of the SRVs. A periodic loading cycle can be observed, at a frequency equal to the number of SRV passages in one revolution. During an SRV passage, the sectional propeller blade loading increased by a small but systematic amount at all propeller thrust settings. The peak-to-peak amplitude of the sectional normal-force coefficient equaled at most about 0.8% of the time-averaged result at the high thrust setting ($J = 1.05$), increasing up to 2.3% at the lowest thrust setting ($J = 1.75$). The low-frequency sinusoidal perturbation on the measured signal at the high-thrust condition ($J = 1.05$, Fig. 9.3a) is a remaining artifact related to the small inflow angularity in the experiment

discussed before. Comparison of the measured results with CFD data showed that the peak-to-peak amplitude of the unsteady loading may have been underpredicted by the experiment at the highest thrust setting. For this case, the finite frequency response of the pressure sensors resulted in a smoothing of the peaks in the pressure response [134].

SWIRL-RECOVERY-VANE PERFORMANCE

Since the SRVs used in the experiment were not instrumented, the CFD simulations discussed in Ref. [134] were considered to extract the contribution of the SRVs to the system thrust. Table 9.3 presents the results in terms of the thrust generated by the SRVs and the associated increase in propulsive efficiency ($\Delta\eta = \eta_{\text{SRVs-on}} - \eta_{\text{SRVs-off}}$). Even though the SRVs are stationary, the thrust coefficient of the SRVs was defined based on the rotational speed and diameter of the propeller to allow for a direct comparison with the propeller's thrust contribution.

Table 9.3: Contribution of the SRVs to the propulsive performance.

J	$C_{T_{\text{SRV}}}$	$\Delta\eta$
1.05	0.002	0.002
1.40	0.003	0.007
1.75	−0.002	−0.009

Table 9.3 shows that the SRVs generated a small amount of positive thrust at the high and intermediate thrust settings ($J = 1.05$ and $J = 1.40$), with a maximum associated efficiency gain of 0.7%. Analysis of the CFD data highlighted that under these conditions, the performance of the SRVs was limited by flow separation on the inboard part of the vanes, and an inefficient pitch-angle distribution near the tip of the vanes [134]. At the low thrust condition ($J = 1.75$), the thrust decreased due to the installation of the vanes. Although the SRVs generated a significant force in this condition, this force was not aligned with the thrust direction. As a result, despite of the achieved swirl recovery (Table 9.1), the overall thrust of the propeller–SRV configuration decreased.

Since the flowfield in the propeller slipstream is unsteady (Fig. 9.1), the SRVs experience an unsteady inflow with dominant perturbations caused by the propeller blade wakes and tip vortices. This leads to cyclic loading around the time-averaged result. Analysis of the numerical data [134] showed that especially at the high thrust condition ($J = 1.05$), a clear peak in the unsteady loading occurred near the tip of the SRVs, caused by the interaction with the tip vortices of the propeller blades. Upon decreasing the thrust setting, the strength of the propeller tip vortices decreases, while the reduced slipstream contraction leads to a larger separation between the vortices and the SRVs. As a result, the unsteady loading decreased significantly compared to the case at high thrust, and the peak caused by the vortex interaction practically disappeared.

Compared to the unsteady loading on the propeller blades (Fig. 9.3), the absolute amplitude of the load fluctuations on the SRVs was about one order of magnitude larger. This is in agreement with the results published by Li et al. [83] based on numerical simulations with a profile-transformation method. The absolute amplitude of the load oscillations increased with increasing propeller blade loading (decreasing advance ratio),

as expected. Relative to the time-averaged loading, on the other hand, the peak-to-peak amplitude of the unsteady loading amounted to approximately 20% at all thrust conditions considered (averaged over the span of the SRVs). Previous work for contra-rotating propellers and turbomachinery has suggested that the unsteady loads on the SRVs may be decreased by increasing the propeller–SRV spacing [84], or using the active technique of blowing from the propeller [152, 153].

9.1.3. ACOUSTIC PERFORMANCE

Although the installation of the SRVs increased the propulsive efficiency at the intermediate and high propeller thrust settings, it also introduced two additional noise sources. The upstream interaction of the SRVs with the propeller causes unsteady loading on the propeller blades (Fig. 9.3). Moreover, the time-dependent velocities induced by the propeller blade wakes and tip vortices lead to fluctuating loads on the SRVs [134].

To investigate the noise penalty caused by the installation of the SRVs, both the tonal and broadband components of the sound emissions were considered. Figure 9.4 displays waveforms of the (phase-averaged) harmonic content of the noise emissions for the configurations with and without the SRVs, for all considered thrust settings. In addition, Fig. 9.5 provides sound spectra obtained at the high thrust setting ($J = 1.05$), with the markers indicating the sound pressure levels at frequencies corresponding to integer multiples of the propeller blade-passage frequency. The spectrum of the background noise is included for reference. The sound spectra for the intermediate and low thrust settings are omitted, since for these cases the broadband noise emissions of the propeller–SRV configuration were mostly below the background noise floor. Moreover, at $J = 1.75$ the fundamental tone could only be extracted from the recorded data using the phase-averaging technique, since its level was below that of the wind-tunnel noise. The data presented in Figs. 9.4 and 9.5 were acquired using the microphone positioned at an axial emission angle in the propeller plane ($\theta_e = 90$ deg) and a circumferential directivity angle of $\phi = 90$ deg.

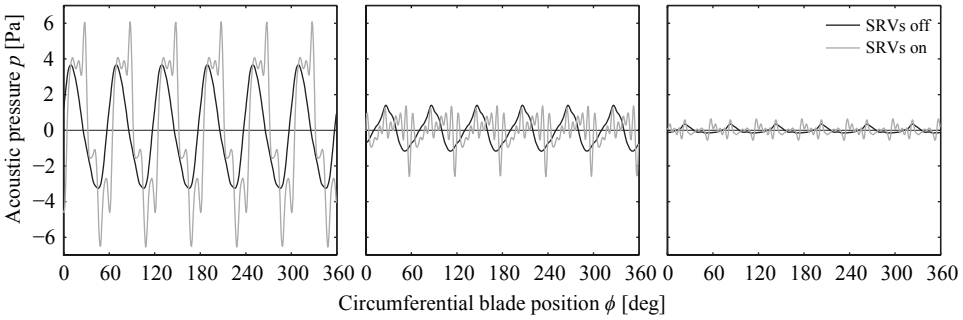

a) High thrust, $J = 1.05$ b) Intermediate thrust, $J = 1.40$ c) Low thrust, $J = 1.75$

Figure 9.4: Effect of SRVs on the acoustic-pressure waveforms at $\theta_e = 90$ deg, $\phi = 90$ deg.

Figures 9.4 and 9.5 highlight an increase in amplitude of the tones at the higher harmonics of the blade-passage frequency with SRVs installed. For the isolated propeller, the sound emissions are dominated by the fundamental propeller tone at $1 \cdot BPF$. With

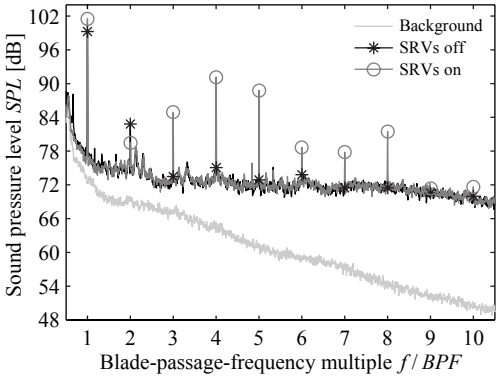

Figure 9.5: Effect of SRVs on the sound spectrum at $J = 1.05$, $\theta_e = 90$ deg, $\phi = 90$ deg.

the SRVs present, on the other hand, the noise emissions change significantly: additional high-frequency pressure oscillations are observed in the waveforms at all thrust settings (Fig. 9.4). At the high thrust setting ($J = 1.05$), the amplitude of several of the higher harmonics increased by up to 16 dB due to installation of the SRVs (Fig. 9.5).

The higher levels of the harmonics with SRVs installed impact the overall tonal noise levels of the propeller–SRV configuration. This is best illustrated by the development of the cumulative tonal noise level ΣSPL with increasing number of harmonics included in the summation. This quantity was defined as:

$$\Sigma SPL = 20\log_{10}\frac{\mathrm{rms}\left(\sum_{i=1}^{n_{BPF}} p_{i\cdot BPF}\right)}{20\cdot 10^{-6}}, \tag{9.3}$$

where n_{BPF} is the number of blade-passage-frequency multiples included in the summation and $p_{i\cdot BPF}$ is the acoustic pressure associated with the tone at the i^{th} multiple of the blade-passage frequency. Equation 9.3 was evaluated for the first ten multiples of the blade-passage frequency, considering the configurations with and without the SRVs installed. The results are plotted in Fig. 9.6. For the isolated propeller, the level of the fundamental tone was practically equal to the total tonal noise level based on a summation of the first 10 tones, for all propeller thrust settings. With the SRVs installed, the cumulative tonal noise level increased significantly upon including additional harmonics. The importance of the high-frequency content to the tonal sound pressure level was found to increase with increasing advance ratio due to the associated reduction of the time-averaged propeller blade loading. Note that at the intermediate and low thrust settings, the cumulative tonal noise level based on the first propeller tones was lower with SRVs installed than for the isolated propeller. This was due to destructive interference between the noise sources associated with the isolated propeller and the SRVs. This also explains the reduction in strength of the tone at $2\cdot BPF$ for the case at $J = 1.05$ (Fig. 9.5).

The increase in the tonal noise emissions with SRVs installed is in disagreement with the results published by Dittmar and Hall [86]. However, in their case the measured decrease of the noise emissions was attributed to unloading of the propeller with the SRVs

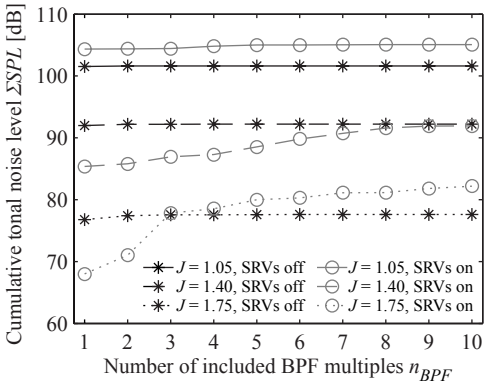

Figure 9.6: Cumulative tonal noise level (Eq. 9.3) with increasing number of included harmonics at $\theta_e = 90$ deg, $\phi = 90$ deg.

installed, which did not occur in the current study as discussed in relation to Table 9.2. In contrast to the tonal noise emissions, the broadband component was not affected by the installation of the SRVs at the hight thrust setting (Fig. 9.5). Therefore, it is concluded that for this propeller operating point the broadband noise generated by the isolated propeller dominated the broadband noise emitted from the SRVs. For the intermediate and low thrust settings, the broadband emissions from the propeller–SRV configuration were too low to be distinguished from the background noise, and hence no conclusions can be drawn regarding the impact of the installation of SRVs on the broadband noise levels for these propeller settings.

To study the directivity of the noise emissions with SRVs installed, the microphone measurements were taken over a range of axial directivity angles θ (defined in Fig. 5.12b). Figure 9.7 presents the resulting summed tonal noise levels (based on the first 10 tones) as a function of the axial emission angle. The sound pressure levels were scaled to a constant observer distance, equal to the distance between the propeller center and the microphone corresponding to $\theta_e = 90$ deg ($r_{mic} = 2.84$ m). The directivity patterns recorded for the isolated propeller feature a number of unexpected irregularities due to interference between the various noise sources, as discussed before in Section 8.3.1.

Figure 9.7 shows that the impact of the installation of the SRVs on the tonal noise emissions varies with the propeller thrust setting. Integrated over the considered axial emission range, noise penalties were measured of 3 dB, 5 dB, and 7 dB for the high, intermediate, and low thrust conditions, respectively. At the high thrust setting ($J = 1.05$, Fig. 9.7a), the noise sources associated with the isolated propeller were dominant in the forward direction ($\theta_e < 90$ deg). Since the steady-loading noise source decreases in amplitude with decreasing propeller thrust setting, the additional noise caused by the installation of the SRVs became significant over the entire directivity range at the lowest thrust setting ($J = 1.75$, Fig. 9.7c). In this condition, the noise penalty was mainly due to an increase in the sound pressure levels of the higher harmonics (Fig. 9.6).

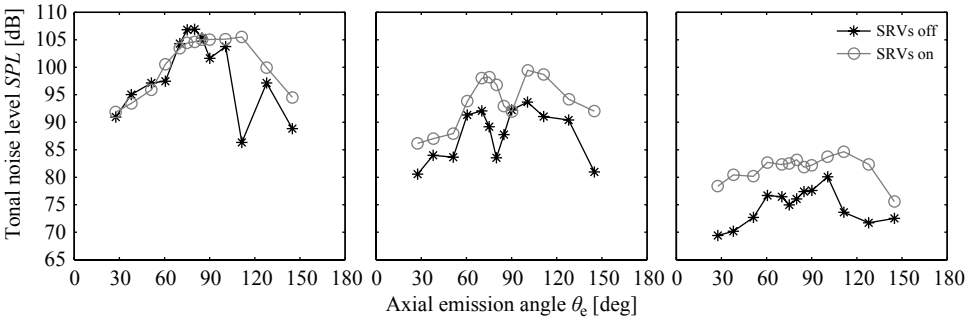

a) High thrust, $J = 1.05$ b) Intermediate thrust, $J = 1.40$ c) Low thrust, $J = 1.75$

Figure 9.7: Effect of SRVs on the axial directivity of the tonal noise emissions at $\phi = 90$ deg.

9.2. INSTALLED PROPELLER CONFIGURATION

In case of aircraft configurations with co-rotating propellers, asymmetric loading occurs due to the different interaction effects on the sides of the inboard-up and the outboard-up rotating propeller. This can be mitigated by reducing the swirl in the propeller slipstream before it interacts with the airframe. As shown in Section 9.1, the necessary swirl reduction can be achieved using swirl-recovery vanes. A preliminary investigation was performed with a propeller–SRV–pylon configuration to quantify the effects of the SRVs on the system's aerodynamic performance. A typical pylon-mounted configuration was considered, since for the wingtip-mounted configuration the beneficial aerodynamic interaction (Chapter 6) would always favor an aircraft layout with counter-rotating propellers (inboard-up on both sides). Note that the experimental setup used for this purpose (Section 3.3.3) was different from the one employed to study the effects of SRVs on the isolated propeller configuration. No detailed aeroacoustic measurements were performed with this setup. Preliminary investigations with wall-mounted microphones showed that the installation of the SRVs caused the same phenomena as discussed in Section 9.1.3: an increase in amplitude of the tonal noise which was especially pronounced for the higher harmonics, and an overall noise penalty which increased with decreasing propeller thrust setting.

9.2.1. PROPULSIVE PERFORMANCE

The propulsive performance of the propeller–SRV combination (without pylon) was measured using the sting-mounted variant of the *PROWIM-T* setup (Section 3.3.1), which was connected to the external balance. The SRVs were mounted on the nacelle through integrated 3-mm thick interfaces. To account for the additional drag of these interfaces, the reference measurements without the SRVs were taken with dummy interfaces installed on the nacelle at the same axial position as the SRVs. Figure 9.8 displays the effect of the SRVs on the system thrust coefficient at $\alpha = -0.2$ deg (due to a small misalignment). The absolute values of the thrust coefficient measured at $Re_D = 620{,}000$ are plotted in Fig. 9.8a for the configurations with and without the SRVs, together with corresponding third-order curve fits through the individual data points. Figure 9.8b plots the change in thrust coefficient due to installation of the SRVs, at Reynolds numbers of $Re_D = 470{,}000$, 620,000, and 780,000.

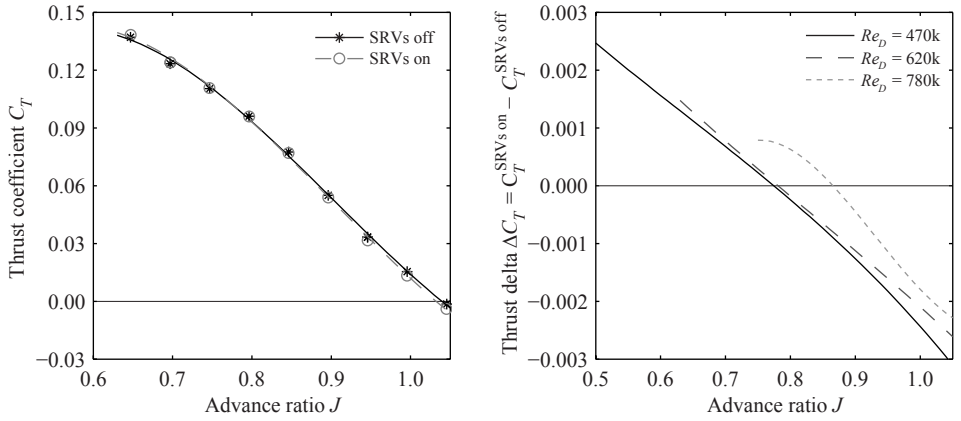

a) Absolute results at $Re_D = 620{,}000$

b) Change in thrust due to SRVs

Figure 9.8: Effect of SRVs on the thrust coefficient of the isolated propeller at $\alpha = -0.2$ deg.

Figure 9.8a shows that the impact of the SRVs on the system thrust was small at the reference Reynolds number of $Re_D = 620{,}000$. At the design advance ratio of $J = 0.7$, the thrust was increased by 0.7% due to the installation of the SRVs. This decreased upon decreasing the thrust setting due to the associated reduction of the swirl in the propeller slipstream. For $J > 0.8$ ($C_T < 0.095$), the installation of the SRVs decreased the system thrust because the additional friction drag could no longer be overcome by the positive thrust contribution due to swirl recovery.

To extend the range of attainable thrust coefficients and assess potential Reynolds-number effects, measurements were also taken at $Re_D = 470{,}000$ and $Re_D = 780{,}000$. From Fig. 9.8b it can be seen that the performance gain offered by the SRVs increased with increasing propeller thrust setting, and thus increasing swirl, reaching a level of 1.4% of the thrust of the isolated propeller at the highest thrust setting considered ($J = 0.5$, $C_T = 0.168$). The small size of the SRVs in the experiment led to low Reynolds numbers based on the SRV chord. For the range of Reynolds numbers considered, this made the SRV thrust relatively sensitive to the freestream conditions. At a given propeller setting, the SRV thrust increased with increasing Reynolds number. At higher Reynolds numbers, more representative of flight, the performance of the SRVs could therefore be better than measured in the experiment. The sudden drop in SRV performance around $J = 0.75$ at $Re_D = 780{,}000$ could be an artifact introduced by the curve-fitting process.

9.2.2. PYLON PERFORMANCE

Besides generating thrust, in the installed configuration the SRVs can minimize the asymmetric loading occurring in case of a co-rotating vehicle configuration. This is especially relevant for pylon-mounted or horizontal-tailplane-mounted configurations, for which the drag benefits due to tip-vortex attenuation and swirl recovery (Chapter 6) may not be sufficient to offset the increased complexity of a counter-rotating propeller layout. The external balance was used to measure the forces on the propeller–SRV–pylon con-

figuration depicted in Fig. 3.12 at Re_D = 640,000. The forces generated by the pylon with nacelle were then isolated by subtracting the propeller forces measured with the sting-mounted configuration, thus neglecting the upstream effect of the pylon on the propeller. Measurements were taken with the inboard-up configuration at $J = 0.7$ and $\delta_f = 0$ deg only. Considering the symmetry of the model, the results for the outboard-up rotation case could be obtained by flipping the inboard-up rotation data (Eq. 3.1). The resulting lift and drag polars are shown in Fig. 9.9.

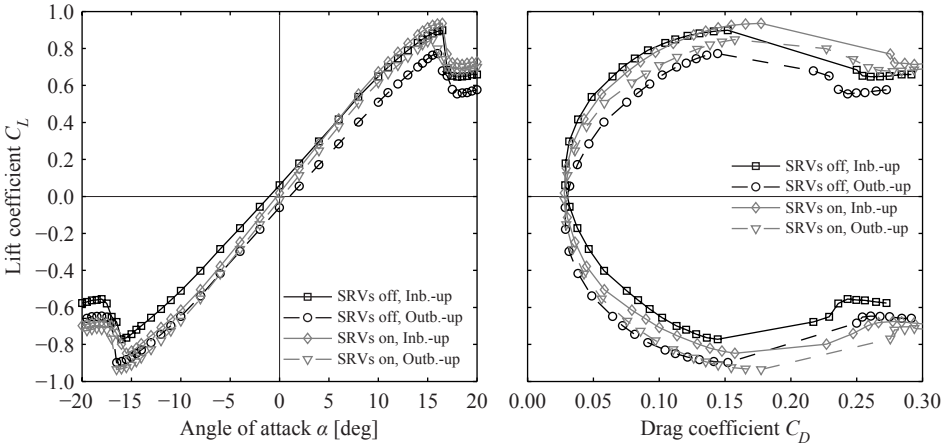

a) Lift polar b) Drag polar

Figure 9.9: Effect of SRVs on the pylon lift and drag polars (propeller forces subtracted) at $J = 0.7$; $\delta_f = 0$ deg.

For the configuration without SRVs, the lift and drag polars presented in Fig. 9.9 feature the phenomena discussed in Section 6.2. With the propeller on, the lift increases with inboard-up rotation and decreases with outboard-up rotation due to the opposite swirl angle induced by the propeller. This also leads to an asymmetry in the drag polar, due to the combined effects of tip-vortex attenuation and swirl recovery. In general, the inboard-up case displays better performance at positive lift coefficients and the outboard-up rotation case at negative lift coefficients. At a given angle of attack, the resulting asymmetric loading on a vehicle with a co-rotating propeller arrangement would lead to a combined rolling moment (due to the lift differences) and yawing moment (due to the drag differences).

By reducing the swirl in the propeller slipstream, the SRVs decrease the asymmetry in loading between the inboard-up and outboard-up rotation cases. This is confirmed by Fig. 9.9, which shows that both the lift and drag polars became more symmetric by installation of the SRVs. The reduction in swirl upstream of the pylon decreases the local change in angle of attack experienced by the pylon, thereby mitigating the asymmetry in loading due to the propeller–pylon interaction. This was confirmed by analysis of the sectional pylon lift at a spanwise location inside the propeller slipstream, as presented in Fig. 9.10. The reduced swirl in the slipstream directly translates into a shift of the sectional loading toward the propeller-off result, both with inboard-up and outboard-up rotation. Still, an offset remains due to the dynamic-pressure rise in the slipstream and because the SRVs most likely did not eliminate all swirl from the slipstream.

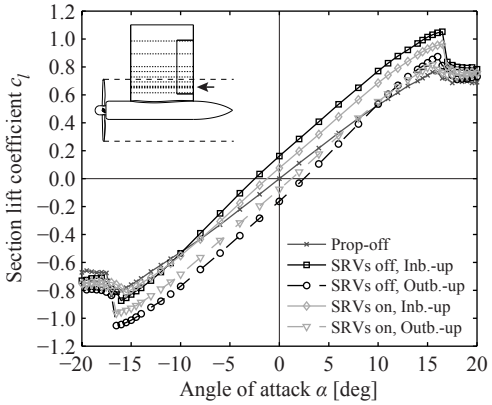

Figure 9.10: Effect of SRVs on the pylon section lift polars at a spanwise station inside the slipstream ($Y/s_S = 0.666$) at $J = 0.7$ (except propeller-off data); $\delta_f = 0$ deg.

Apart from the modification of the aerodynamic loading, the installation of the SRVs also increased the maximum lift coefficient (Fig. 9.9). Propeller-off measurements with the SRVs installed showed that this was not due to the loading on the wing, but instead due to the forces generated by the SRVs. This is consistent with Fig. 9.10, which indicates that the maximum local lift coefficient of the pylon did not increase due to the installation of the SRVs (compared to the propeller-on result without SRVs). This signifies the potential importance of the circumferential distribution of the SRVs, which could possibly be optimized to maximize the lifting potential of the SRVs.

9.3. KEY FINDINGS

This chapter has discussed the aerodynamic and aeroacoustic performance of a propeller with swirl-recovery vanes, both in isolated and (pylon-)installed configurations. The SRVs convert part of the swirl in the propeller slipstream into thrust, thereby lowering the thrust requirement for the propeller. In this way, the required power input to the propeller can be reduced and hence the efficiency of the propulsion system increased. Furthermore, the reduction of the swirl in the propeller slipstream can alleviate asymmetric aerodynamic loading in the case of vehicle configurations with co-rotating propellers (i.e. inboard-up on one side of the aircraft and outboard-up on the other).

9.3.1. ISOLATED CONFIGURATION

The measurements with the isolated propeller configuration showed that the tested SRVs decreased the time-averaged tangential velocity in the propeller slipstream, at all thrust settings considered. Computations showed that the relative rotational kinetic energy was decreased by approximately 46% due to application of the SRVs at an intermediate thrust setting. Consequently, the propulsive efficiency increased by 0.7% at this operating condition. The performance of the SRVs was limited by stall occurring on the inboard part of the vane, which could have been prevented by a local increase of the pitch angle.

The installation of SRVs introduces two aerodynamic interaction mechanisms. The upstream perturbation of the flowfield experienced by the propeller leads to fluctuating propeller loads. The peak-to-peak amplitude of the blade normal force at $r/R \approx 0.65$

was 1 – 2% of the local time-averaged loading, with the highest relative unsteady loads occurring at the lowest propeller thrust setting. The integral propeller loading, on the other hand, remained practically unaffected. In addition to the upstream interaction, the downstream impingement of the propeller blade wakes and tip vortices on the SRVs causes unsteady SRV loading. The amplitude of the unsteady loads increases toward the tip of the SRVs due to the strong interaction with the propeller tip vortices.

The unsteady interactions between the propeller and the SRVs introduce two additional noise sources. Far-field microphone measurements showed that the installation of the SRVs increased the tonal noise emissions, while the recorded broadband noise emissions were not affected. The increase in tonal noise was manifested mostly by a significant amplification of the levels of the higher harmonics. This especially affected the system noise emissions at low propeller thrust setting, for which the noise penalty was up to 7 dB. At higher thrust settings, the tonal noise penalty was lower at 3 – 5 dB. Multidisciplinary optimization of the SRV design could be employed to minimize the interaction-noise penalty while maximizing the aerodynamic benefits.

9.3.2. INSTALLED CONFIGURATION

Based on preliminary investigations with a pylon-mounted tractor propeller, it is concluded that SRVs can successfully be applied to reduce asymmetric loading on vehicles with a co-rotating propeller arrangement. By decreasing the swirl in the propeller slipstream, the interaction effects caused by the propeller slipstream are reduced, thereby decreasing the difference in aerodynamic response for the cases with inboard-up and outboard-up propeller rotation. For the case with inboard-up rotation, the installation of the SRVs increased the maximum lift coefficient due to the forces generated by the SRVs. This highlights the potential importance of the circumferential distribution of the SRVs, which could be optimized to maximize the SRVs' lifting potential.

10

FLOW-PERMEABILITY AT THE PYLON LEADING EDGE

Chapter 7 quantified the unsteady pylon loads caused by propeller-slipstream impingement for tractor configurations. These unsteady loads are a potential source of structure-borne noise. Previous work confirmed that a flow-permeable leading edge can alleviate comparable unsteady loads due to rotor–stator and blade–vortex interactions. The present chapter analyzes the time-averaged and unsteady performance of flow-permeable leading-edge inserts applied to alleviate unsteady pylon loading for a tip-mounted tractor-propeller configuration. The geometry of the inserts was not optimized; instead, it was based on previous work available in the literature. Section 10.1 first analyzes the effect of the flow-permeable leading edges on the time-averaged pylon performance without propeller. Subsequently, Section 10.2 visualizes the slipstream impingement phenomena at the flow-permeable leading edges and quantifies the effects on the far-field noise levels. Finally, Section 10.3 addresses the key findings. The data were obtained with the PROWIM-US setup described in Chapter 4, operated at J = 0.8 for the propeller-on measurements.

10.1. TIME-AVERAGED PYLON PERFORMANCE WITHOUT PROPELLER

The effect of the flow-permeable leading edges on the time-averaged aerodynamic performance of the pylon was initially considered without the propeller. The flowfield measurements were taken with the pylon–propeller setup (Fig. 4.3) with the blades removed, while the performance data were acquired with the extended pylon setup (Fig. 4.6).

10.1.1. FLOWFIELDS AROUND THE LEADING-EDGE INSERTS

The LEFOV PIV setup (Section 4.4.1, Fig. 4.7d) was used to characterize the flowfield around the leading-edge inserts at angles of attack of 0 and 6 deg. Figure 10.1 presents

The contents of this chapter have been adapted from Ref. [122].

contours of the velocity magnitude measured around the solid leading edge. These velocity fields served as baseline to which the flowfields measured with the flow-permeable inserts were compared. Figure 10.2 provides contours of the resulting difference in velocity magnitude with respect to the solid pylon for the four flow-permeable configurations.

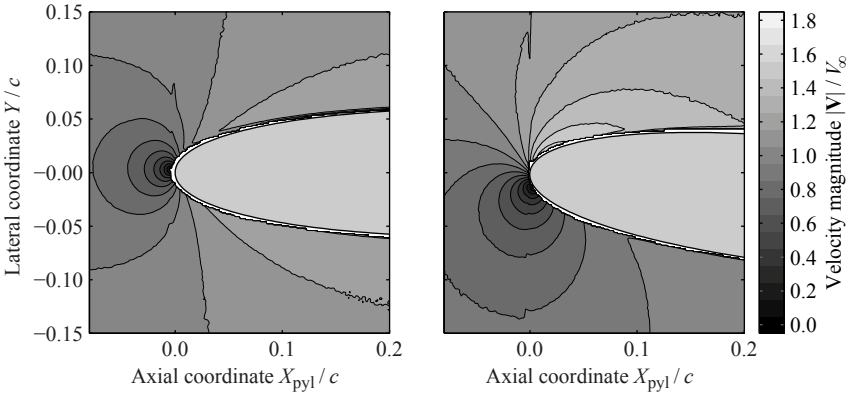

a) $\alpha = 0$ deg b) $\alpha = 6$ deg

Figure 10.1: Velocity magnitude around the solid leading-edge insert; propeller-off.

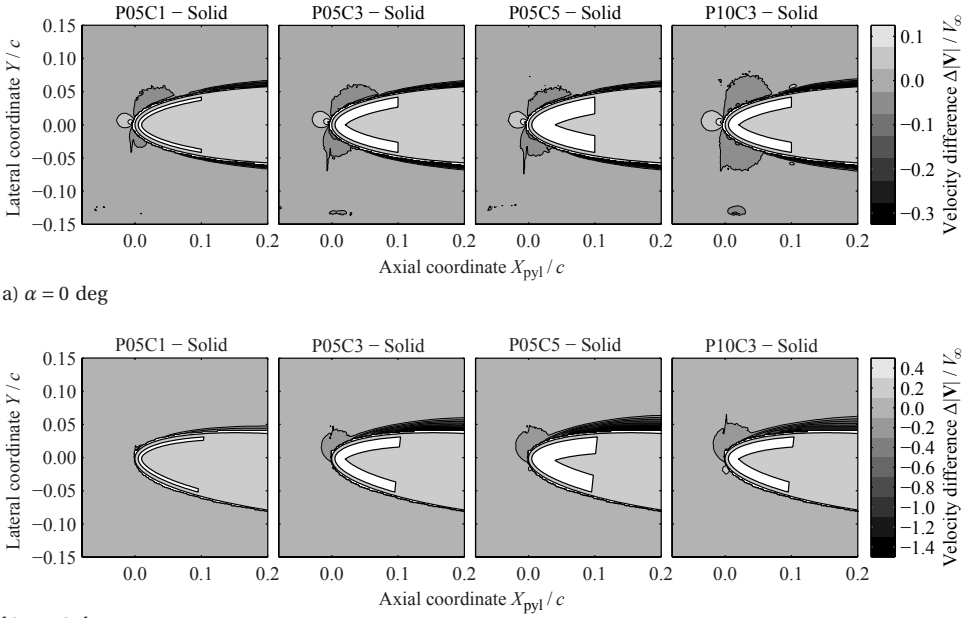

a) $\alpha = 0$ deg

b) $\alpha = 6$ deg

Figure 10.2: Difference in velocity magnitude with respect to the solid leading-edge insert; propeller-off.

The velocity fields shown in Fig. 10.1 for the solid pylon display the expected features for a symmetric airfoil. At an angle of attack of 0 deg (Fig. 10.1a), the flowfield is symmetric, with a stagnation point at the leading edge of the profile. Increasing the angle of attack to 6 deg (Fig. 10.1b) causes the velocity to rise on the suction side of the pylon ($Y/c > 0$), while the stagnation point moves toward the pressure side of the profile.

The velocity-difference fields provided in Fig. 10.2 highlight the significant impact of the flow-permeable inserts on the flowfield, especially at nonzero angle of attack. At an angle of attack of 0 deg (Fig. 10.2a), the velocity near the flow-permeable inserts increased around the stagnation point due to the local permeability of the pylon. Moreover, compared to the solid pylon, the boundary-layer thickness increased on both sides of the pylon. This is attributed to a combination of increased surface roughness, viscous losses in the holes and cavity of the flow-permeable inserts, and the change in effective outer shape due to flow passing through the flow-permeable inserts. Comparing the results for the different inserts, it can be concluded that the changes to the boundary-layer behavior become larger with increasing hole diameter and cavity depth.

When increasing the angle of attack to 6 deg (Fig. 10.2b), the pressure difference across the inserts increases. The effect of the P05C1 insert on the flowfield surrounding the pylon leading edge was relatively small. In contrast, a strong impact on the flowfield can be observed for the inserts with cavity depths of 3 and 5 mm. The thick boundary layer developing on the suction side of these inserts changed the effective thickness distribution of the airfoil, moving the suction peak downstream and decreasing its amplitude. The strong modification of the flowfield on the suction side of the pylon suggests that flow passed through the flow-permeable inserts from the pressure side to the suction side. To assess whether this throughflow was present, the lateral velocity component (in the Y-direction) was analyzed near the suction side of the P10C3 insert. Figure 10.3 displays contours of the time-averaged results and the root mean square of the instantaneous flowfields. The lateral velocity is defined positive in the positive Y-direction, hence outflow on this side of the insert would correspond to a positive lateral velocity.

The time-averaged data (Fig. 10.3a) show a pattern of narrow regions near the surface in which the amplitude of the lateral velocity was increased. The chordwise locations at which this occurred correspond to the locations of the holes in the P10C3 insert. This suggests that flow indeed passed through the holes of the insert, which then caused the changes to the flowfield displayed in Fig. 10.2. At the same locations, the fluctuations of the lateral velocity component (Fig. 10.3b) also peaked, with a root-mean-square level comparable to that of the time-averaged result. This could hint at a pulsating outflow from the flow-permeable inserts, as discussed previously by Tinetti et al. [87, 88] Following the experimental work detailed in the present thesis, also a computational study was performed with a similar geometry at the same operating conditions [154]. The numerical results obtained in that study support the outflow mechanism described above.

10.1.2. PYLON BOUNDARY LAYER

To quantify the changes to the boundary layer caused by the flow-permeable inserts, velocity profiles were extracted from the measured flowfields. Figure 10.4 presents the resulting velocity profiles on the suction side of the pylon as a function of the nondimensional wall-normal coordinate Y_n/c. The corresponding boundary-layer profiles on the

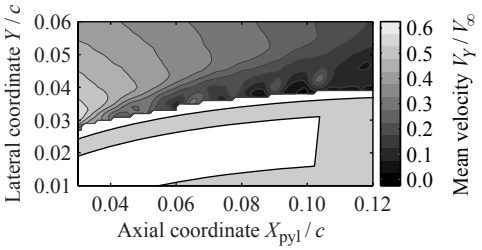

a) Mean velocity

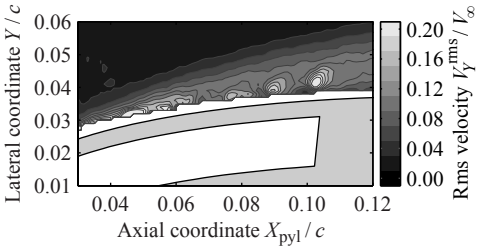

b) Velocity fluctuations (root mean square)

Figure 10.3: Lateral velocity component (Y-direction) on the suction side of the P10C3 insert at $\alpha = 6$ deg; propeller-off.

pressure side are shown in Fig. 10.5. Note that different ranges are used for the horizontal axis of both figures. Three chordwise positions are considered, corresponding to locations on top ($X_{pyl}/c = 0.08$), at the end ($X_{pyl}/c = 0.10$), and downstream ($X_{pyl}/c = 0.12$) of the flow-permeable part of the leading-edge inserts. Because of reflections, the boundary layers could not be resolved up to the surface of the pylon. Instead, the first data point is positioned at approximately $0.003c$ above the surface. The local boundary-layer thickness was approximated from the velocity profiles as the wall-normal coordinate of maximum velocity. Table 10.1 summarizes the data for both the suction side and the pressure side at $X_{pyl}/c = 0.12$, just downstream of the flow-permeable part of the inserts.

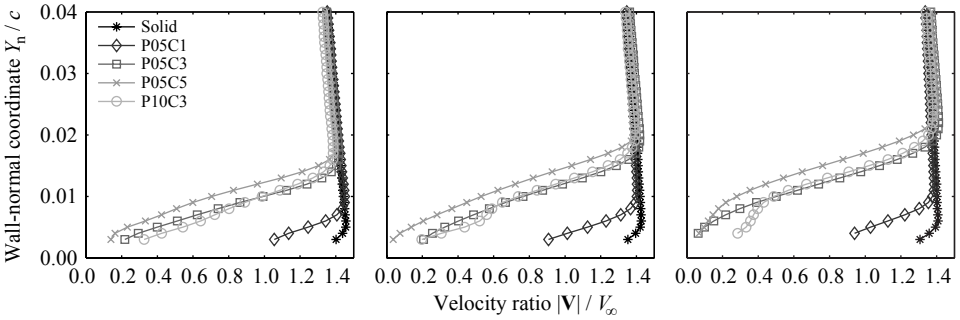

a) $X_{pyl}/c = 0.08$ b) $X_{pyl}/c = 0.10$ c) $X_{pyl}/c = 0.12$

Figure 10.4: Boundary-layer profiles on the suction side of the pylon at $\alpha = 6$ deg; propeller-off.

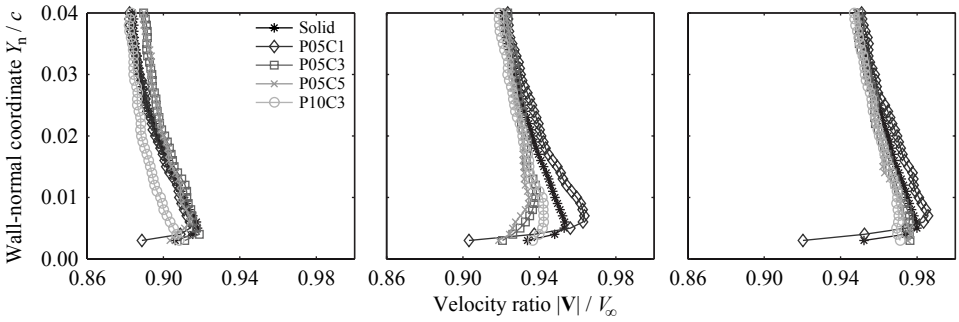

a) $X_{pyl}/c = 0.08$ b) $X_{pyl}/c = 0.10$ c) $X_{pyl}/c = 0.12$

Figure 10.5: Boundary-layer profiles on the pressure side of the pylon at $\alpha = 6$ deg; propeller-off.

Table 10.1: Effect of flow-permeable leading edges on the normalized boundary-layer thickness at $X_{pyl}/c = 0.12$; $\alpha = 6$ deg, propeller-off.

Configuration	$(\delta/c)_{suc}$	$(\delta/c)_{pres}$
Solid	0.006	0.005
P05C1	0.012	0.007
P05C3	0.022	< 0.003
P05C5	0.025	0.004
P10C3	0.023	< 0.003

The boundary-layer profiles plotted in Figs. 10.4 and 10.5 confirm the conclusions drawn from the flowfields shown in Figs. 10.1 and 10.2. Compared to the solid pylon configuration, the cases with flow-permeable leading-edge insert show a thickening of the boundary layer on the suction side. Moreover, the flow-permeable insert amplifies the growth of the boundary-layer thickness in the chordwise direction, as can be seen by comparison of Fig. 10.4a, 10.4b, and 10.4c. Both effects become stronger with increasing cavity depth, while the hole diameter has a smaller effect. On the pressure side, on the other hand, the boundary-layer thickness decreased compared to the solid baseline for the P05C3, P05C5, and P10C3 configurations. This is also shown by the data in Table 10.1, and confirms that flow passed through the flow-permeable inserts from the pressure side to the suction side of the pylon. This is further supported by the departure in shape from a regular turbulent boundary layer that can be seen in Fig. 10.4 for the flow-permeable configurations. For the P10C3 insert, a change in slope of the velocity profile occurred at a wall-normal coordinate of around $Y_n/c = 0.008$ at $X_{pyl}/c = 0.10$ (Fig. 10.4b) and $X_{pyl}/c = 0.12$ (Fig. 10.4c). A local increase in velocity can be seen, which is attributed to the additional momentum coming through the distinct holes in the leading-edge insert. The local velocity maxima could not be identified in the boundary-layer profiles for the configurations with the smaller hole diameter ($D_{hole} = 0.5$ mm). For these inserts, the throughflow is divided over a larger number of holes, hence the viscous losses are higher and the local velocity perturbation through each hole is smaller than for the P10C3 insert.

10.1.3. LIFT AND DRAG PERFORMANCE

The changes to the flowfield resulting from the installation of the flow-permeable inserts affect the aerodynamic performance of the pylon. The lift and drag of the flow-permeable inserts was determined using the test setup with the extended pylon configuration (Fig. 4.6). The average sectional lift at the spanwise position of the leading-edge inserts was determined from the wall-pressure-tap data following Eq. 4.1, as discussed in Section 4.4.2. The sectional drag was obtained from the wake-rake measurements, as also explained in Section 4.4.2. Figure 10.6 presents the resulting sectional lift and drag as a function of angle of attack for the five pylon configurations. The lift data were obtained over an angle-of-attack range spanning from −6 up to +12 deg, while the drag measurements were taken at six angles of attack in the range of −6 up to +9 deg.

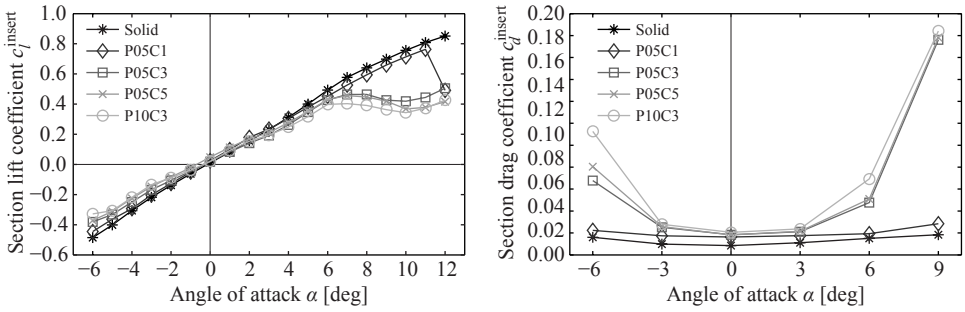

a) Lift b) Drag

Figure 10.6: Aerodynamic performance of the leading-edge inserts.

The lift polars depicted in Fig. 10.6a highlight the strong dependence of the lift performance at higher angle of attack on the design of the flow-permeable insert. For angles of attack between approximately −6 and +6 deg, the lift increased linearly with angle of attack for all inserts, with a lift gradient lower than the theoretical value of 2π expected from thin-airfoil theory. This was due to nonnegligible induced effects caused by the 2-mm gaps on both ends of the pylon (Fig. 4.6), which were implemented in the setup to allow for external balance measurements. Compared to the solid pylon, the configurations with flow-permeable insert displayed a reduction of the lift slope. The performance decreased nonlinearly with increasing hole diameter and increasing cavity depth. Considering that the results for the P05C3 and P05C5 inserts were equivalent, it is concluded that increasing the cavity depth beyond a limit value no longer has a significant effect on the generated lift. The reduced performance of the flow-permeable inserts was due to the flow through the permeable surface, mitigating the pressure difference at the leading edge of the pylon. As shown in Figs. 10.1 and 10.2, the inflow and outflow mechanism changed the effective outer shape of the insert. This resulted in a decrease in amplitude of the suction peak, hence a reduction of the lift. Note that the PIV evaluations were performed on the propeller–pylon setup (Fig. 4.3), and thus the effective angle of attack at the measurement plane might have been different from the one experienced in the performance measurements taken with the extended pylon setup.

At higher angle of attack, the lift decreased significantly compared to the solid baseline for the P05C3, P05C5, and P10C3 inserts. The strongest effect was observed for the insert with the largest hole diameter, for which the throughflow will have been the most severe. The insert with the smallest cavity depth (P05C1), on the other hand, displayed better performance. For this insert, the significant drop in lift at higher angle of attack only occurred at $\alpha = 12$ deg, while at lower angle of attack the reduction in section lift coefficient was within ± 0.05 compared to the solid pylon.

Figure 10.6b displays increased drag due to installation of the flow-permeable inserts. This was as expected considering the associated increase in boundary-layer thickness shown in the previous sections. The insert with smallest hole diameter and cavity depth (P05C1) displayed the smallest drag penalty. Compared to the solid insert, the development of drag coefficient with angle of attack was similar for this configuration, albeit at levels up to approximately two times higher. For the flow-permeable inserts with larger cavity depth, on the other hand, the drag coefficient started to increase rapidly at angles of attack of 6 deg and above. This matches with the flowfields presented in Figs. 10.1 and 10.2, and the lift response observed in Fig. 10.6a.

The results provided in Fig. 10.6 show reduced lift and significantly increased drag for the flow-permeable inserts. However, the largest unsteady loading due to the interaction with the slipstream occurs at the spanwise location of tip-vortex impingement (Chapter 7). Therefore, in a realistic application possibly only a small spanwise part of the pylon needs to be covered with porosity to achieve reductions of the unsteady loads. Consequently, the absolute lift and drag penalties for a pylon treated with a flow-permeable insert would be smaller than the change measured over the spanwise extent of the insert. Therefore, a projection was made of the aerodynamic performance of a realistic pylon with flow-permeable treatment along 10% of the span, hence only covering the spanwise part around the tip-vortex impingement location. The corresponding effective aerodynamic span of the flow-permeable inserts was scaled based on the approach described in the discussion of Eq. 4.1. Figure 10.7a presents the resulting pylon lift as a function of angle of attack. In terms of the pylon drag, a drag penalty was computed relative to the results obtained for the solid baseline configuration, as shown in Fig. 10.7b.

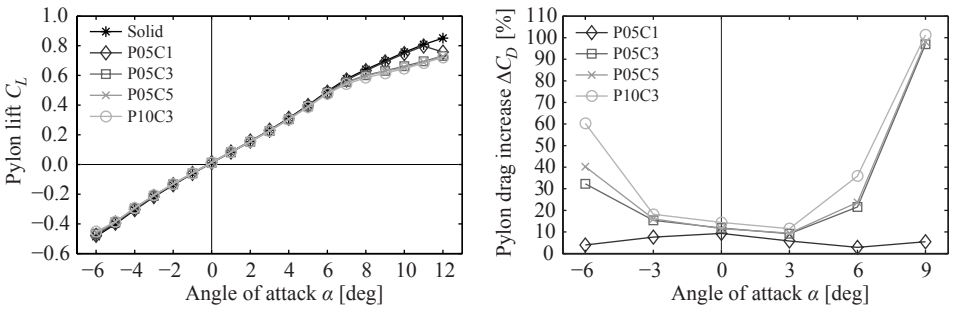

a) Lift

b) Drag penalty w.r.t. solid configuration

Figure 10.7: Projected aerodynamic performance for a pylon with 10% of the span treated with a flow-permeable leading edge.

Figure 10.7a highlights that application of a 10%-span flow-permeable insert hardly affects the lift performance of the pylon. This is particularly relevant for wing-mounted or tailplane-mounted configurations, for which the lifting performance of the aerodynamic surface is more important than for the pylon-mounted case. For the P05C1 configuration, only a slight reduction in lift can be observed at the highest angle of attack considered ($\alpha = 12$ deg). The other flow-permeable configurations would decrease the lift performance for angles of attack beyond 6 deg. The maximum drop in lift coefficient was approximately 15% at the highest angle of attack considered.

From Fig. 10.7b it can be seen that the projected drag increase for the complete pylon would be 5 – 100%, depending on the configuration and angle of attack. For the P05C1 configuration, the drag penalty remained within 10% at all studied angles of attack. The reduced drag penalty observed for this configuration at higher angle of attack is due to transition on the solid baseline configuration. At low angle of attack, the natural transition point on the solid pylon will have been more downstream than for the P05C1 configuration because of the lower surface roughness of the solid model. This corresponds to lower skin-friction drag for the solid pylon, hence a drag penalty for the P05C1 configuration. At higher angle of attack, on the other hand, the natural transition point on the solid pylon will have also moved toward the leading edge. As a result, the relative drag penalty of the P05C1 insert decreased at higher angle of attack. The P05C3, P05C5, and P10C3 inserts displayed larger drag penalties, especially at high angle of attack. This is as expected considering the sectional drag performance of these inserts displayed in Fig. 10.6b. The largest increase in drag occurred for the P10C3 configuration, with a projected drag penalty of approximately 35% at an angle of attack of 6 deg.

At higher Reynolds numbers, more representative of flight, the extent of laminar flow on the solid pylon would decrease when compared to the situation in the experiment. The associated increased drag on the solid pylon would lead to a reduction of the relative drag penalty caused by the flow-permeable inserts, analogously to the above discussion of the impact of transition on the drag penalty of the P05C1 insert.

10.2. PROPELLER-SLIPSTREAM IMPINGEMENT AT THE PYLON LEADING EDGE

The interaction between the propeller slipstream and the pylon leading edge was visualized using the LEFOV PIV setup (Section 4.4.1, Fig. 4.7d). Phase-uncorrelated and phase-locked measurements were taken to assess the effects of the flow-permeable inserts on the time-averaged and unsteady flowfields around the pylon leading edge. Moreover, stereoscopic PIV measurements with the CWFOV setup (Section 4.4.1, Fig. 4.7c) were used to compare velocity fluctuations near the leading edge of the pylon. These data were complemented by far-field acoustic data obtained with a microphone array, which are related to the pressure fluctuations on the pylon surface.

10.2.1. TIME-AVERAGED PYLON RESPONSE

The phase-uncorrelated velocity fields measured with the propeller on were used to compute the time-averaged pressure field around the pylon leading edge. Pressure distributions were then extracted as close as possible to the pylon, which corresponded to

an offset of $0.0075c$ from the surface. Figure 10.8 presents the pressure distributions at vertical locations in the wake impingement region ($Z/R = 0.74$, Fig. 10.8a) and tip-vortex impingement region ($Z/R = 0.97$, Fig. 10.8b), for an angle of attack of $\alpha = 0$ deg. The error bars shown in the top left of both subplots indicate the 95% confidence interval of the pressure data. Markers are displayed for clarity at chordwise intervals of $0.03c$; the actual spatial resolution of the data was about 20 times higher (see Table 4.3).

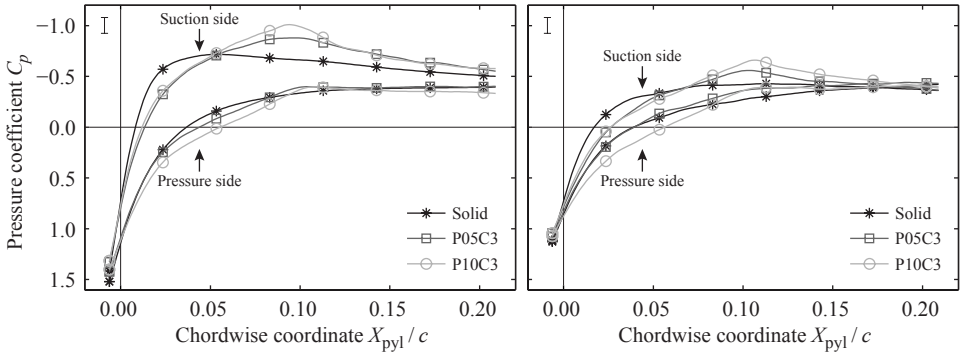

a) Wake impingement region ($Z/R = 0.74$) b) Tip-vortex impingement region ($Z/R = 0.97$)

Figure 10.8: Pressure distributions around the leading-edge inserts at $0.0075c$ from the surface; $\alpha = 0$ deg.

Compared to the solid pylon, the effect of the flow-permeable inserts on the pressure distribution was comparable in the wake impingement region (Fig. 10.8a) and the tip-vortex impingement region (Fig. 10.8b). For the flow-permeable configurations, the suction peak displaced downstream toward the end of the flow-permeable part of the inserts, and increased in magnitude compared to the solid pylon. Similar modifications to the pressure distribution occur for a clean airfoil by increasing the profile thickness and/or moving the location of maximum thickness aft [155]. This matches with the change in effective aerodynamic shape of the pylon observed before in Figs. 10.1 and 10.2 for the case without the propeller, which was attributed to crossflow through the flow-permeable inserts. Similar conclusions were drawn by Tinetti et al. [87–89] and Mineck and Hartwich [156]. The downstream displacement of the suction peak was also found in the numerical research of Lee [90], although in that case the amplitude of the suction peak decreased due to the application of porosity. This was also observed in the present study (Fig. 10.2), but only at a higher effective angle of attack than for the data shown in Fig. 10.8.

For a given configuration, significant differences can be observed between the pressure distributions measured in the wake impingement region ($Z/R = 0.74$, Fig. 10.8a) and the tip-vortex impingement region ($Z/R = 0.97$, Fig. 10.8b). This is due to the radial gradients of axial and tangential velocity in the propeller slipstream. At $Z/R = 0.74$, the effect of the propeller is to increase the axial velocity. As a result, the local dynamic pressure was higher than the freestream dynamic pressure, hence the pressure coefficient at the stagnation point increased beyond unity. Near the edge of the slipstream, on the other hand, the axial velocity increment is approximately zero, hence the dynamic pressure was about equal to the freestream value. The distribution of the tangential velocity

in the propeller slipstream causes an increased effective angle of attack at $Z/R = 0.74$. This leads to a stronger suction peak and larger pressure differential across the suction and pressure sides of the pylon than at the edge of the slipstream.

10.2.2. FLOWFIELDS AROUND THE LEADING-EDGE INSERTS

The time-dependent interaction between the propeller slipstream and the pylon leading edge was visualized using the phase-locked measurements taken with the LEFOV PIV setup. Figure 10.9 presents the corresponding velocity fields at time instants before, during, and after impingement of the tip vortex on the pylon leading edge. These time instants correspond to relative propeller blade phase angles of $\phi' = -17.5$ deg, $\phi' = 0$ deg, and $\phi' = +27.5$ deg, respectively, with $\phi' = 0$ deg taken as the phase angle corresponding to the blade location at the approximate time of tip-vortex impingement. The measurements were taken at the tip-vortex impingement location ($Z/R = 0.97$). An in-depth analysis of the tip-vortex impingement process for the solid pylon configuration was presented in Chapter 7. The below discussion focuses on the changes to the flowfield induced by the flow-permeable leading edges.

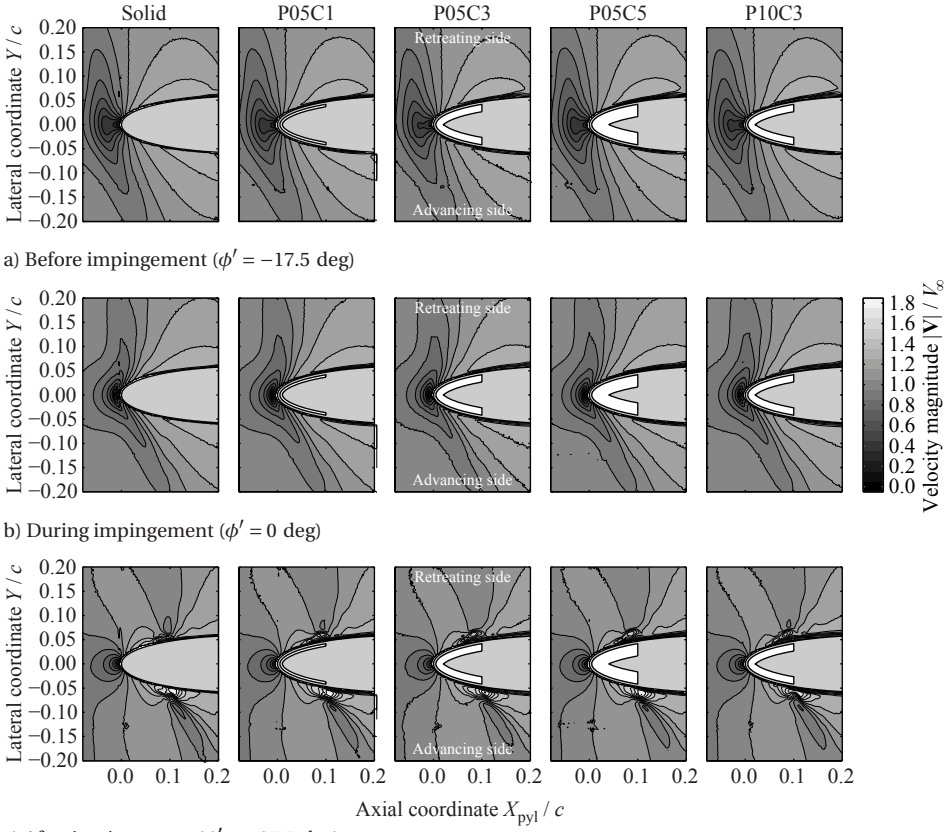

a) Before impingement ($\phi' = -17.5$ deg)

b) During impingement ($\phi' = 0$ deg)

c) After impingement ($\phi' = +27.5$ deg)

Figure 10.9: Velocity fields before, during, and after impingement of the tip vortex on the pylon leading edge at $Z/R = 0.97$; $\alpha = 0$ deg.

Before impingement of the vortex on the pylon leading edge (Fig. 10.9a), the dominant effect of the flow-permeable inserts is to increase the boundary-layer thickness on the pylon, consistent with the propeller-off data presented in Section 10.1. A small angle of attack is induced by the slipstream, changing the flowfields compared to the propeller-off case shown in Figs. 10.1 and 10.2.

When the tip vortex impinges (Fig. 10.9b), it has already started bending around the pylon leading edge. Initially, the flowfield remains practically unaffected by the leading-edge configuration. However, once the vortex has traveled downstream (Fig. 10.9c), the effect of the flow-permeable insert becomes more pronounced. The viscous interaction of the vortex with the pylon boundary layer leads to dissipation, reducing the strength of the vortex near the pylon surface [45]. This process is amplified when the boundary-layer thickness is increased. Moreover, the increased boundary-layer thickness also causes the vortex core to move away from the pylon surface, which is further enhanced by the outflow from the flow-permeable surface on the suction side of the model (Fig. 10.3).

Both the reduction in strength of the vortex and the displacement of the core away from the surface should reduce the pressure fluctuations on the pylon surface. In principle, these two effects could also be achieved using a rough surface, assuming the same boundary-layer growth could be achieved as displayed here for the cases with flow-permeable insert. However, a flow-permeable insert enables two additional mechanisms: the flow through the holes and cavity leads to additional dissipation, while the communication between regions of high and low pressure alleviates local pressure gradients and thus unsteady loading. These effects are smallest for the insert with the smallest cavity depth (P05C1), which is as expected considering the flowfields measured for the propeller-off case (Figs. 10.1 and 10.2).

10.2.3. FLOWFIELDS AROUND THE ENTIRE PYLON

In addition to the local measurements near the leading edge provided by the LEFOV setup, the CWFOV PIV setup was used to obtain phase-locked velocity fields around the pylon at the vertical position of tip-vortex impingement ($Z/R = 0.97$). For this setup, data are only available for the solid and P10C3 configurations. To illustrate the results obtained with the CWFOV setup, Fig. 10.10 presents an example phase-locked flowfield for the solid pylon configuration, displaying contours of the axial velocity. In addition to the velocity field, isolines of normalized vorticity $\omega_Z^* = \omega_Z D/V_{\text{disk}}$ are superimposed, with V_{disk} the effective velocity at the propeller disk estimated from actuator-disk theory [36]. The two crosses indicate the positions at which velocity fluctuations were extracted, as presented in Fig. 10.11.

Figure 10.10 shows the tip vortices being convected downstream along the pylon chord. The spanwise shearing of the propeller slipstream (discussed in Chapters 6 and 7) caused the vortex cores to gradually move away from the measurement plane on both sides of the pylon. On the advancing side, the slipstream displaces in the direction away from the propeller axis. As a result, the vortices crossed the measurement plane, as can be seen from the vorticity contours. This led to strong induced velocities in the field of view. On the retreating side, the slipstream displaces toward the propeller axis. Therefore, the vortices were above the measurement plane and thus their effect on the measured velocity field was smaller.

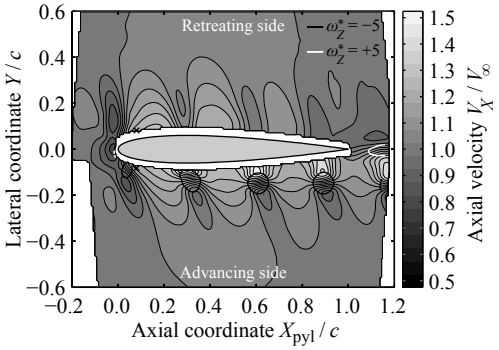

Figure 10.10: Flowfield around the solid pylon at $Z/R = 0.97$ and $\phi = 0$ deg; $\alpha = 0$ deg.

To analyze the local unsteadiness near the pylon, time histories of the fluctuating velocity magnitude were extracted at $0.0375c$ from the surface at $X_{pyl}/c = 0.08$. Figure 10.11 presents the results for the solid and P10C3 configurations. The measurement data were acquired for a single blade passage only; these data were repeated for the remaining three blade passages to describe the response over a complete revolution. The error bar plotted in the top left of the subplots represents the 95% confidence interval of the respective velocity component from PIV.

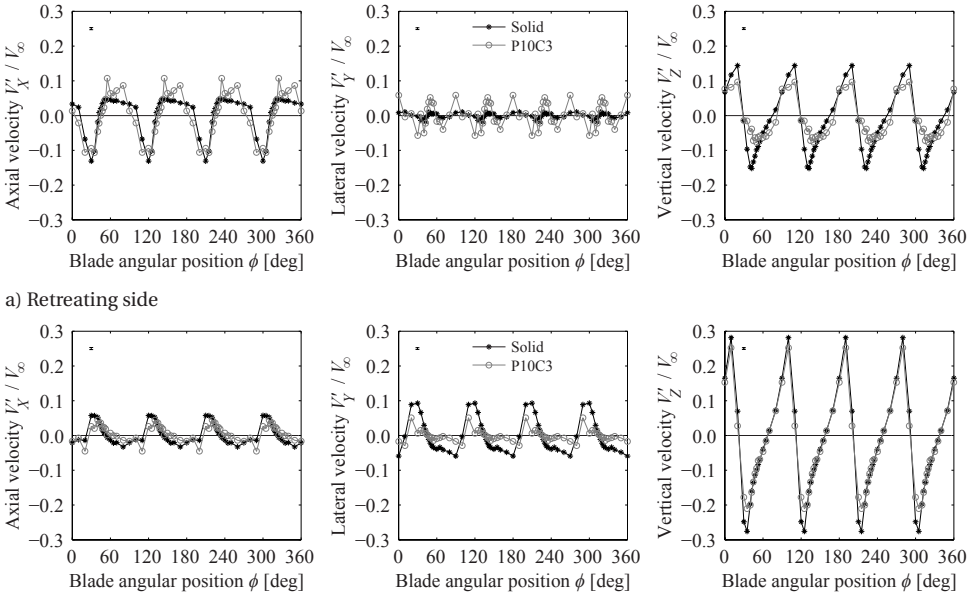

Figure 10.11: Velocity fluctuations at $0.0375c$ from the pylon surface at $X_{pyl}/c = 0.08$ (i.e. at the markers indicated in Fig. 10.10) at $Z/R = 0.97$; $\alpha = 0$ deg. Error bar shown in top left of subplots.

The waveforms displayed in Fig. 10.11 highlight the strong effect of the tip-vortex passage on the velocity field around the pylon. Since locally the axis of the vortex was mostly aligned with the X,Y-plane, the tangential velocities induced by the vortex led to strong fluctuations of the vertical velocity component (in the Z-direction). The rotation direction of the vortex was such that the vertical velocity increased, i.e. a velocity component away from the propeller axis, when the vortex approached the sampling location (see Fig. 7.5). The measured velocity fluctuations were largest on the advancing blade side, as expected from Fig. 10.10. This is due to the spanwise shearing of the slipstream, as discussed above. Because of the tilting of the vortex path relative to the measurement plane, the velocities induced by the vortices also modified the other components of the velocity vector at the sampling location. The spanwise shearing in the direction away from the propeller axis on the advancing side led to an increase in axial velocity there, while the opposite occurred on the retreating side.

The flow through the holes and cavity of the flow-permeable insert at least partially mitigated the local velocity fluctuations caused by the periodic impingement of the tip vortices on the pylon. On the retreating side, the thicker boundary layer (Fig. 10.9) caused increased dissipation of the vortex compared to the solid configuration, which is reflected by the reduced velocity fluctuations in the Z-direction. Compared to the solid baseline, the root mean square of the fluctuations decreased by about 35% by application of the flow-permeable insert. The throughflow mechanism increased the fluctuations in the Y-direction, albeit with small amplitude compared to the other velocity components. On the advancing side, on the other hand, the velocity fluctuations in the Y-direction decreased by the flow through the flow-permeable insert. This also seems to apply to the Z-component, although in that case the peak amplitudes could be affected by the relatively coarse sampling. The reduced velocity fluctuations near the surface are promising in view of the desired reduction of the unsteady pylon loads.

10.2.4. FAR-FIELD ACOUSTIC DATA

The flowfield information provided by the PIV measurements was complemented by far-field acoustic data acquired with the microphone array discussed in Section 4.4.4. The impingement of the propeller slipstream on the pylon causes periodic velocity and pressure fluctuations on the pylon surface, as discussed in the previous sections. The pressure fluctuations lead to tonal noise radiated from the pylon. Although it will be shown that the sound pressure level of these tones is negligible compared to the noise emitted by the propeller, the levels can still serve as an indirect measure of the unsteady pressure fluctuations on the pylon. Therefore, the far-field acoustic data measured with the microphone array can be used to assess the potential mitigation of structure-borne noise offered by the flow-permeable inserts.

Figure 10.12 presents example sound-source maps for the solid pylon at frequencies of 2 and 5 times the blade-passage frequency. The source maps confirm that the airborne noise associated with the pressure fluctuations on the pylon is negligible compared to the steady-loading noise emitted by the propeller. However, the nonzero pressure fluctuations on the pylon can still be experienced as an additional noise source inside the cabin via the structure-borne noise path. Therefore, a reduction of these pressure fluctuations can increase passenger comfort.

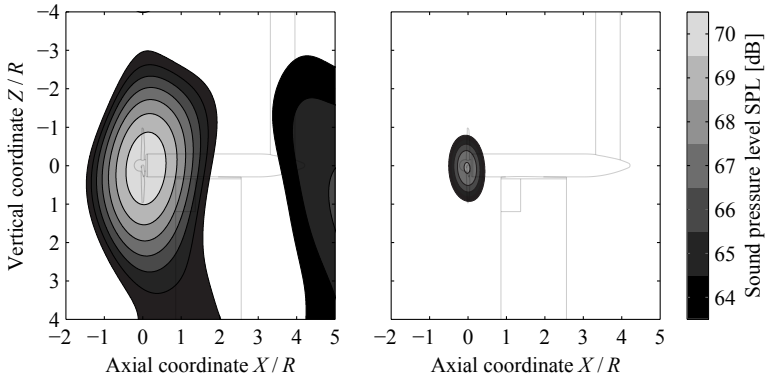

a) $f = 2BPF$ (resolution $2.0R$) b) $f = 5BPF$ (resolution $0.8R$)

Figure 10.12: Sound-source maps for the solid pylon configuration.

To separate the sound emitted from the propeller and the pylon, source power integration was performed over the two sectors defined in Fig. 4.10. Figure 10.13 compares the resulting sound pressure levels for the different pylon configurations over a range of 1/3-octave bands. It can be seen that the propeller noise was hardly affected by the pylon configuration, while the pylon noise decreased compared to the solid baseline for two of the flow-permeable inserts (P05C3 and P10C3). Furthermore, a noise increase from the pylon can be observed at high frequency for the P10C3 insert, albeit at levels significantly below the dominant noise at low frequency. These results are discussed in detail in the paragraphs below.

Note that at low frequency, the resolution of the microphone-array data was insufficient to distinguish the propeller and pylon noise sources (Eq. 4.2). As a result, the levels obtained in sector II (Fig. 10.13b) also contained a contribution due to the propeller. Although this effect gradually decreased with increasing frequency, it means that the data from sector II could only be used to study relative differences in sound emissions from the pylon with respect to the solid baseline configuration.

Propeller Noise The upstream effect of the different leading-edge inserts on the propeller was investigated in more detail by analysis of narrowband spectra of the propeller noise emissions, as determined by integration of the sound sources in the area surrounding the propeller (sector I in Fig. 4.10). Figure 10.14 presents the resulting spectra for a frequency range including the first 4 propeller tones. To illustrate the difference in upstream effect for the various pylon configurations, the standard deviation was computed from the tonal levels measured at each multiple of the blade-passage frequency. Small values of the resulting standard deviations indicate a limited upstream effect of the different inserts on the propeller noise.

Figure 10.14 shows that the propeller noise emissions were practically independent of the installed leading-edge insert. Tones were recorded at the first 4 multiples of the blade-passage frequency, while broadband noise was dominant at higher frequency. The variation in tonal levels for the different pylon configurations was lowest at the funda-

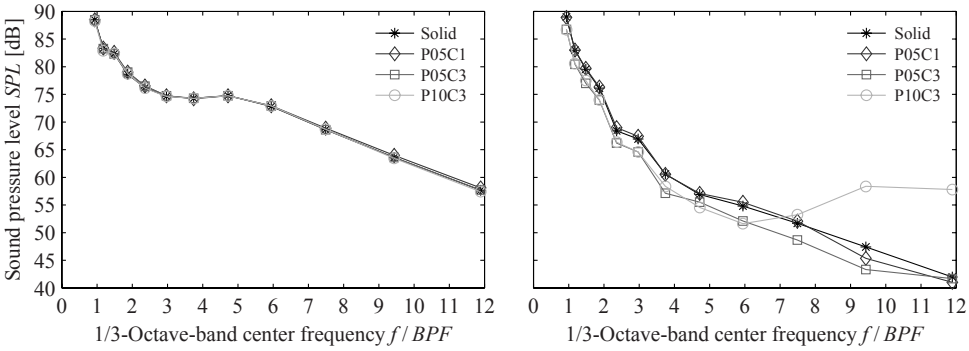

a) Sector I: propeller

b) Sector II: pylon

Figure 10.13: 1/3-Octave-band sound pressure levels obtained from source power integration in sectors I (propeller) and II (pylon) of Fig. 4.10.

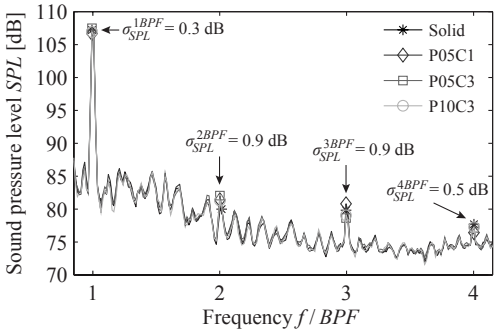

Figure 10.14: Narrowband propeller noise spectra for the different leading-edge configurations, obtained from source power integration in sector I of Fig. 4.10.

mental frequency ($1 \cdot BPF$), for which the standard deviation of the sound pressure level was 0.3 dB. The tonal amplitudes at the higher blade-passage-frequency multiples were lower, leading to an increased variation of at most ±1 dB. For the 1/3-octave-band levels (Fig. 10.13a), the standard deviation of the measurements for the different leading-edge inserts decreased to a maximum of 0.3 dB over the entire frequency range.

Pylon Noise The small difference between the propeller noise spectra shown in Fig. 10.14 confirms that the upstream effect of the pylon on the propeller did not depend on the installed leading-edge insert. Therefore, any difference between the measured noise signatures in the pylon integration area (sector II in Fig. 4.10) should have been due to a change in response at the pylon itself. The far-field tonal noise extracted from the pylon sector could therefore be used as an indirect measure of the pressure fluctuations on the leading-edge inserts.

The results presented in Fig. 10.13b already indicated a change in noise emissions from the pylon for the different leading-edge configurations. Figure 10.15 presents the

data as difference in sound pressure level with respect to the results recorded for the solid baseline configuration (ΔSPL). Positive values of ΔSPL indicate reductions of the measured sound pressure level by application of the flow-permeable inserts. Both the 1/3-octave-band levels (Fig. 10.15a) and the tonal levels (Fig. 10.15b) are considered. The data uncertainty is indicated by the dashed lines in Fig. 10.15a and by the error bars in Fig. 10.15b. The associated values correspond to the standard deviation of the repeated propeller noise measurements, evaluated as the maximum over each of the 1/3-octave bands in Fig. 10.15a and separately at each multiple of the blade-passage frequency in Fig. 10.15b.

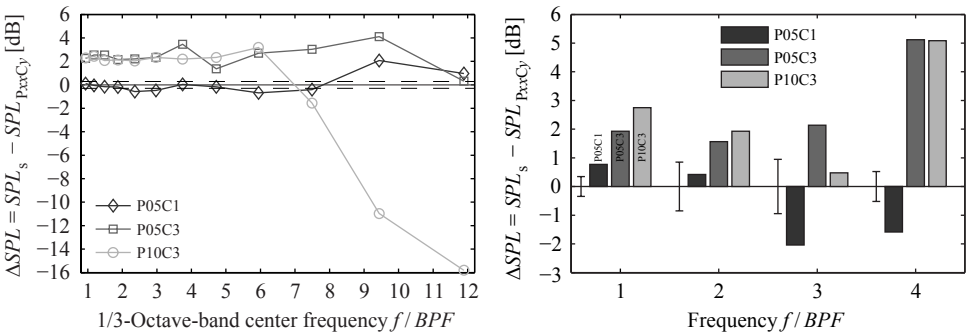

a) 1/3-Octave-band levels

b) Tonal levels

Figure 10.15: Reduction in far-field acoustic pressure emitted by the flow-permeable inserts with respect to the solid pylon, obtained from source power integration in sector II of Fig. 4.10.

The 1/3-octave-band data presented in Fig. 10.15a indicate that the P05C1 insert did not have a significant effect on the noise emissions from the pylon for frequencies up to about 8 times the blade-passage frequency. The P05C3 and P10C3 inserts, on the other hand, provided a far-field noise reduction of 2 to 3 dB in this frequency range. This indicates that the pressure fluctuations at the surface were reduced by application of these flow-permeable inserts, hence the interaction mechanism caused by the impingement of the propeller slipstream was at least partially mitigated. The observed differences between the P05C3 and P10C3 inserts were approximately within the measurement uncertainty for frequencies up to 6 times the blade-passage frequency.

At high frequency ($f/BPF > 7$), the P10C3 configuration displayed a strong noise *increase* compared to the solid pylon. As shown in Fig. 10.16, the associated broadband noise source was found near the leading edge of the pylon and did not occur with the solid leading edge. The mechanism causing the noise penalty at high frequency for the P10C3 insert is as of yet unknown. However, it was also observed in numerical simulations of a similar geometry at the same operating conditions [154]. A previous study [96] focusing on porous treatments applied at the trailing edge of airfoils showed similar results, which were attributed to increased surface roughness due to the flow-permeable material. It should be noted that the absolute sound pressure level in this frequency range was well below that at low frequency, and thus the additional noise-generating mechanism did not noticeably affect the overall sound pressure level.

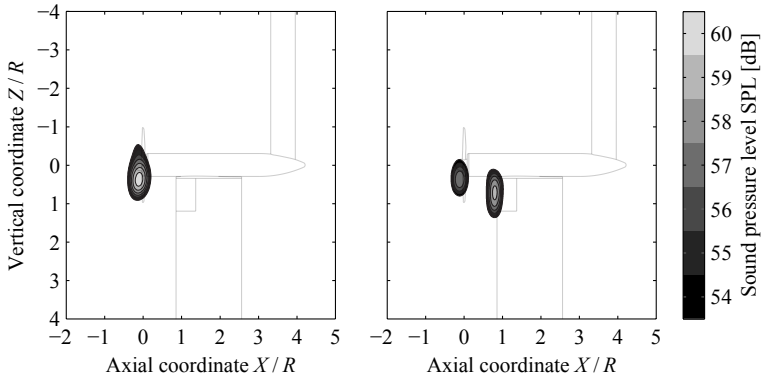

Figure 10.16: High-frequency broadband noise generation at the leading edge of the P10C3 insert; $6.7 \leq f/BPF \leq 13.4$ (resolution $< 0.6R$).

The tonal levels shown in Fig. 10.15b confirm the observations made based on the 1/3-octave-band levels. At the dominant fundamental frequency ($1 \cdot BPF$), the P05C1 configuration returned a decrease in sound pressure level of only 0.8 dB, whereas the P05C3 and P10C3 configurations displayed reductions of 1.9 dB and 2.8 dB, respectively. For these two inserts, significant reductions of the far-field sound emissions also occurred at the higher harmonics. Therefore, it is concluded that the P05C3 and P10C3 inserts offered more effective unsteady-load alleviation than the P05C1 insert. This highlights the sensitivity of the unsteady-load alleviation to the cavity depth. Comparing the trends in unsteady-load alleviation with the time-averaged aerodynamic-performance data (Fig. 10.6), which indicated increased throughflow for the P05C3 and P10C3 inserts, it is concluded that the throughflow mechanism has a key impact on the unsteady-load alleviation obtained by installation of the flow-permeable inserts. However, the throughflow also reduces the time-averaged performance of the inserts at nonzero angle of attack. Therefore, when designing flow-permeable inserts a careful trade-off is required between time-averaged aerodynamic performance and unsteady-load alleviation.

10.3. KEY FINDINGS

This chapter has focused on quantifying the potential of a flow-permeable leading edge to alleviate the unsteady loading caused by propeller-slipstream impingement. A propeller was positioned upstream of a pylon featuring replaceable leading-edge inserts. A solid insert was used as baseline to which the results obtained with four different flow-permeable inserts were compared.

From the velocity fields acquired with particle-image velocimetry, it is concluded that the application of a flow-permeable leading edge strongly modifies the flowfield around the pylon, especially at nonzero angle of attack. The flow through the holes and cavity of the flow-permeable insert causes an increase in boundary-layer thickness, thereby modifying the effective outer shape of the pylon. This was particularly pronounced for the inserts with larger cavity depths. The resulting lift performance was

shown to be reduced, especially at angles of attack above 6 deg. Also, the drag increased, which was concluded to be the result of viscous dissipation and increased surface roughness compared to the solid pylon model.

The increase in boundary-layer thickness resulted in a local reduction in strength of the propeller blades' tip vortices due to increased viscous interaction, while the vortices also displaced away from the surface. Furthermore, the flow through the holes and cavity caused additional dissipation. Consequently, the velocity fluctuations induced by the blade tip vortices decreased by up to 35% near the pylon surface in the tip-vortex impingement region. Microphone-array measurements showed that this led to reduced far-field noise, suggesting a reduction in pressure fluctuations at the pylon surface. Larger reductions in far-field noise and thus pressure fluctuations were obtained from the inserts with larger cavity depth. Therefore, it is concluded that a careful trade-off is required between time-averaged aerodynamic performance and unsteady-load alleviation when designing the flow-permeable inserts.

11

PYLON TRAILING-EDGE BLOWING

The wake-encounter phenomenon for pusher propellers discussed in Chapter 8 causes a significant noise penalty. Pylon blowing can eliminate the momentum deficit in the wake, thereby removing the physical mechanism driving the adverse interaction. This chapter assesses the working principles of pylon trailing-edge blowing by quantifying the reduction in installation penalty at the source: the fluctuating propeller blade loads. The resulting benefits to the far-field noise levels, confirmed previously in the literature, are also discussed. The presented comprehensive study provides unique evidence of the efficacy of trailing-edge blowing for the suppression of interaction noise due to the wake encounter, a potentially significant noise source for pusher propellers. Following a characterization of the pylon-wake flowfields with and without blowing in Section 11.1, the suppression of the unsteady propeller blade loads is first discussed in Section 11.2. Subsequently, Section 11.3 evaluates the corresponding changes in propeller noise emissions, and relates these to the changes in the flowfield due to pylon blowing. Finally, the key findings are summarized in Section 11.4. The results were measured with the APIAN-INF setup described in Chapter 5. The chapter focuses on propeller operating conditions for which the additional noise due to the pylon-installation effects was relevant and identifiable. Therefore, the data were obtained at an intermediate thrust setting ($J = 1.4$, $C_T = 0.36$), unless otherwise stated.

11.1. PYLON-WAKE FLOWFIELD

The goal of the trailing-edge blowing system is to cancel the momentum deficit in the pylon wake, thereby alleviating the unsteady propeller blade loads and eliminating the associated noise penalty caused by the wake encounter. To assess whether the wake was indeed filled successfully, PIV measurements of the pylon-wake flowfield (Section 5.4.1) were performed for the cases with and without blowing. Similarly to the results presented in Section 8.1, all measurements were taken with the thrusting propeller present. For reference, the inflow to the isolated propeller (pylon-off) was also evaluated.

Parts of this chapter have been adapted from Refs. [133] and [157].

Figure 11.1 provides an overview of the measurement results, displaying contours of the axial velocity for the cases with and without blowing under symmetric inflow conditions. The blowing coefficient $c_{\dot{m}}$ was defined as $c_{\dot{m}} = \dot{m}/\rho_\infty V_\infty A_{\text{out}}$ (Eq. 5.1). The results obtained in the PIV plane located at 69% of the propeller radius below the propeller axis ($Z/R = 0.69$) are discussed in detail in Sections 11.1.1 and 11.1.2 for symmetric and asymmetric inflow conditions, respectively. This measurement plane was chosen because it was closest to the position of the pressure sensors on the instrumented propeller blade when it passed through the center of the pylon wake. The outflow from the blowing system was reasonably constant upstream of the outboard part of the propeller blades ($0.6 \leq Z/R \leq 1.0$, see Fig. 5.7). Therefore, similar results were obtained from the lowest 4 measurement planes, except for the one at $Z/R = 0.79$ since this plane was located downstream of one of the struts in the blowing system (Fig. 5.7).

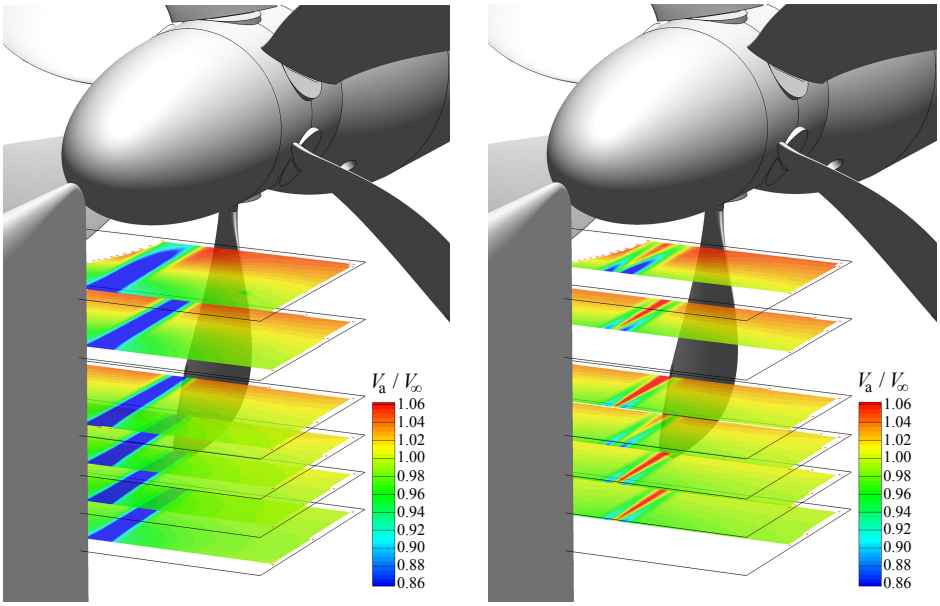

a) Blowing off ($c_{\dot{m}} = 0.0$)

b) Blowing on ($c_{\dot{m}} = 1.6$)

Figure 11.1: Effect of trailing-edge blowing on the velocity deficit in the pylon wake in symmetric inflow.

11.1.1. SYMMETRIC INFLOW

Figure 11.2 presents the mean velocity fields for the pylon-off and pylon-on (unblown and blown) configurations, in terms of the magnitude of the total velocity vector at $Z/R = 0.69$. Additionally, contours of the total turbulence intensity are depicted in Fig. 11.3 to quantify the unsteadiness of the flow in the wake region. The mean velocity field governs the harmonic features of the wake encounter, while the turbulence intensity affects the broadband response (Chapter 8). The blown results shown in Figs. 11.2 and 11.3 were obtained at a blowing coefficient of $c_{\dot{m}} = 1.6$.

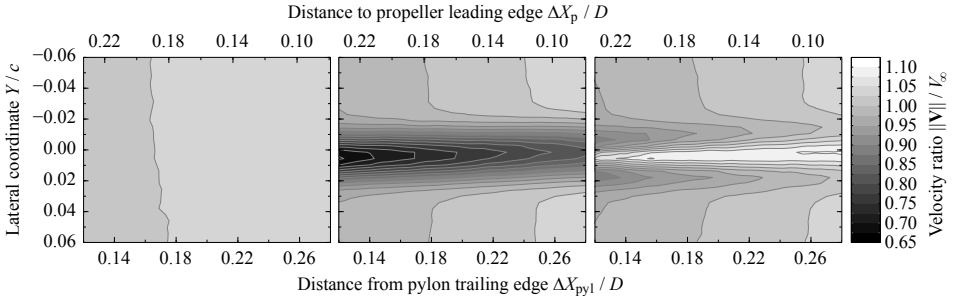

a) Pylon-off b) Pylon-on, $c_{\dot{m}} = 0.0$ c) Pylon-on, $c_{\dot{m}} = 1.6$

Figure 11.2: Effect of pylon installation with and without blowing on the time-averaged velocity magnitude upstream of the propeller; $Z/R = 0.69$.

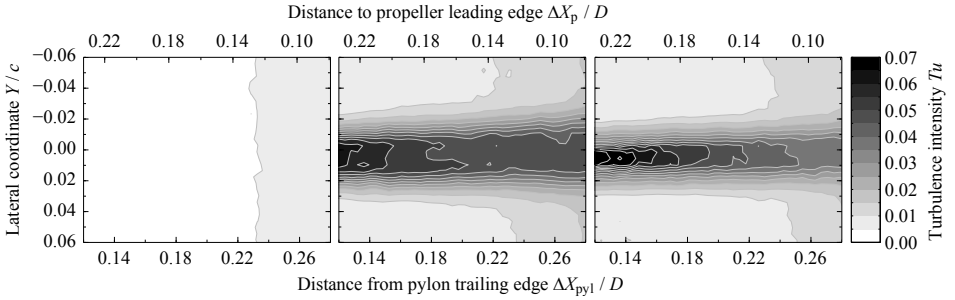

a) Pylon-off b) Pylon-on, $c_{\dot{m}} = 0.0$ c) Pylon-on, $c_{\dot{m}} = 1.6$

Figure 11.3: Effect of pylon installation with and without blowing on the turbulence intensity upstream of the propeller; $Z/R = 0.69$.

Figure 11.2 confirms that the blowing system reduced the velocity deficit in the pylon wake. Outside of the wake region, the velocity was lower for all pylon-on configurations than for the pylon-off case. This was caused by the local deceleration of the flow due to the presence of the pylon, as discussed before in Section 8.1. For all cases, the suction of the propeller induced a positive velocity gradient toward the propeller. From Fig. 11.3 it can be seen that the turbulence intensity was small for the pylon-off configuration. The velocity fluctuations increased toward the propeller, because the turbulence intensity was computed using the complete data set, involving all phase angles. Since the dependency of the flowfield on the blade position becomes stronger toward the propeller, an increase in turbulence intensity is observed in this direction. When considering the velocity fields per individual phase angle, the turbulence intensity was constant in the entire field of view. For the pylon-on configurations, the increased turbulence in the pylon-wake region is readily apparent. The application of blowing initially intensified the turbulence level near the wake centerline. Because of an increased decay rate, however, the maximum turbulence intensity for the blown configuration decreased below that of the unblown case for $\Delta X_{pyl}/c > 0.19$. Integrated in the lateral direction, the turbulence intensity was reduced by blowing at all axial positions considered.

To analyze the flowfield in the blown pylon wake in more detail, velocity data were extracted from the measurement planes at $0.075D$ upstream of the leading edge of the propeller blade. The same interpolation procedure was performed as explained in Section 8.1.1, resulting in the velocity components at the lateral and vertical coordinates traced by a blade section at a radial coordinate of $r/R = 0.65$. The results are presented in Fig. 8.1 as the ratio of the velocity data obtained for the pylon-on and pylon-off configurations. A radial coordinate of $r/R = 0.65$ is considered, because the blade pressure distribution was measured at this position. Figure 11.4 provides the distributions of the mean axial velocity component in the pylon-wake region for the different configurations considered, while Fig. 11.5 presents profiles of the three components of the turbulence-intensity vector. Markers are indicated at 2-deg intervals for clarity; the actual resolution of the data was higher. The data for the averaged lateral and vertical velocity components are omitted, since these only amounted to less than 2% of the axial velocity component at the selected evaluation location. The key numerical values corresponding to the data presented in Figs. 11.4 and 11.5 are provided in Table 11.1, in which the quantities related to the mean axial velocity are nondimensionalized with the axial velocity at the edge of the wake (V_X^e).

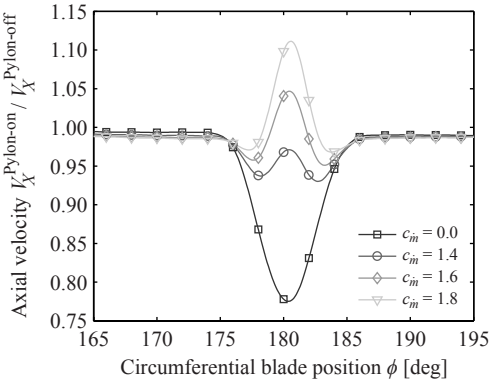

Figure 11.4: Effect of blowing coefficient on the axial velocity deficit experienced by a blade section at $r/R = 0.65$, $0.075D$ upstream of the propeller; $\alpha = 0$ deg.

Table 11.1: Pylon-wake characteristics experienced by a blade section at $r/R = 0.65$, $0.075D$ upstream of the propeller; $\alpha = 0$ deg. CL = wake centerline, L = left wake edge ($\phi_L = 170$ deg), R = right wake edge ($\phi_R = 190$ deg).

Configuration	$\left(1 - \frac{V_X}{V_X^e}\right)_{CL}$	$\frac{1}{\phi_R - \phi_L} \int_{\phi_L}^{\phi_R} \left\lvert 1 - \frac{V_X}{V_X^e} \right\rvert d\phi$	$(Tu)_{max}$	$\frac{1}{\phi_R - \phi_L} \int_{\phi_L}^{\phi_R} (Tu) d\phi$
Pylon-off	+0.00	$7.0 \cdot 10^{-4}$	$1.7 \cdot 10^{-2}$	$1.6 \cdot 10^{-2}$
$c_{\dot{m}} = 0.0$	+0.22	$5.8 \cdot 10^{-2}$	$7.0 \cdot 10^{-2}$	$4.3 \cdot 10^{-2}$
$c_{\dot{m}} = 1.4$	+0.02	$1.8 \cdot 10^{-2}$	$5.4 \cdot 10^{-2}$	$3.3 \cdot 10^{-2}$
$c_{\dot{m}} = 1.6$	−0.06	$1.4 \cdot 10^{-2}$	$7.2 \cdot 10^{-2}$	$3.6 \cdot 10^{-2}$
$c_{\dot{m}} = 1.8$	−0.12	$2.1 \cdot 10^{-2}$	$8.6 \cdot 10^{-2}$	$4.0 \cdot 10^{-2}$

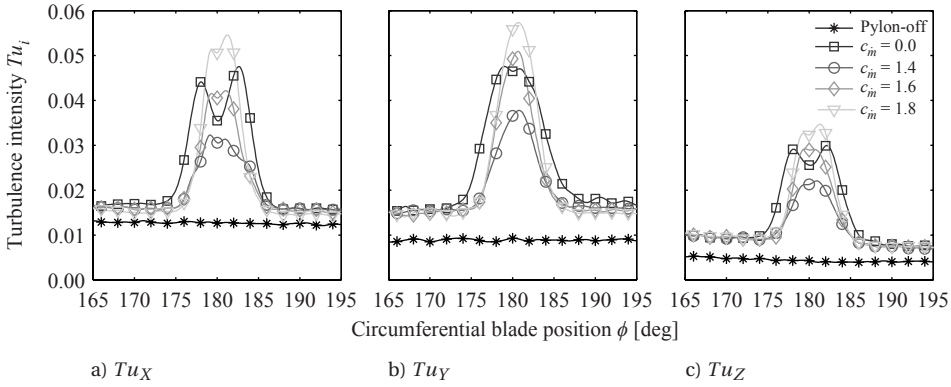

Figure 11.5: Effect of blowing coefficient on the turbulence intensity experienced by a blade section at $r/R = 0.65, 0.075D$ upstream of the propeller; $\alpha = 0$ deg.

Figure 11.4 displays the expected velocity deficit in the wake of the unblown pylon. For this configuration, a maximum velocity deficit of 22% was measured relative to the velocity outside of the wake region. The lateral position of maximum velocity deficit in the wake was slightly offset from the centerline. This was due to an inflow angularity of approximately 0.2 deg, induced by the in-flow measurement equipment. The wake profiles for the blown configurations confirm the efficacy of the blowing system in reducing the nonuniformity of the propeller inflow. At a blowing rate of $c_{\dot{m}} = 1.6$, the integral velocity deficit in the pylon wake was decreased by 76% compared to the unblown pylon-on configuration. The blown velocity profiles did not become completely uniform because of the small width of the blowing slit and the limited length from the pylon trailing edge to the measurement location available for mixing of the blown jet with the external flow. Instead, a velocity overshoot can be noted on the wake centerline that rises with increasing blowing coefficient. This overshoot can be reduced by integrating a blowing outlet along the chord on each side of the pylon, instead of using a single blowing slit in the trailing edge of the pylon. This is discussed in Appendix A. Outside of the wake region, the average velocity for the pylon-on configurations was about 1% of the freestream velocity lower than without pylon. This is due to the deceleration of the flowfield in the vicinity of the pylon trailing edge.

The unsteadiness of the pylon wake is highlighted in Fig. 11.5. With pylon present, the maximum turbulence intensity increased to almost four times the value measured for the pylon-off configuration. The introduction of the blown jet reduced the shear forces in the wake region, thereby decreasing the fluctuations of all three velocity components. At $c_{\dot{m}} = 1.4$, the integral total turbulence level was 24% lower than for the unblown pylon-on configuration. At the higher blowing rates, the increased strength of the jet intensified the unsteadiness around the wake centerline. For these cases, the reduction in turbulence level compared to the case without blowing was decreased to 16% at $c_{\dot{m}} = 1.6$ and 8% at $c_{\dot{m}} = 1.8$. To fully describe the temporal character of the fluctuations, a more advanced analysis would be needed with a time-resolved system.

11.1.2. ASYMMETRIC INFLOW

As shown in Section 8.1.2, operation of the pylon at nonzero angle of attack results in an asymmetric wake. To investigate the effects of trailing-edge blowing under asymmetric inflow conditions, Fig. 11.6 provides the velocity profiles in the wake as measured at an incidence angle of $\alpha = -6$ deg, at the low thrust setting ($J = 1.75$). The results for the unblown configuration were shown before in Fig. 8.2.

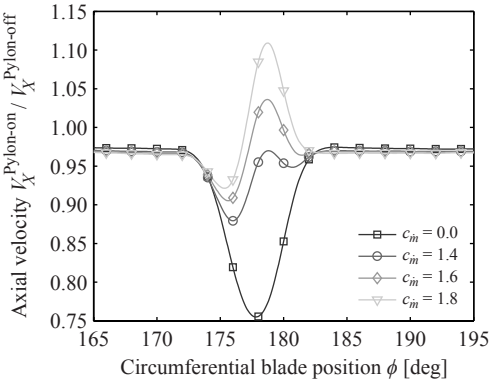

Figure 11.6: Effect of blowing coefficient on the axial velocity deficit experienced by a blade section at $r/R = 0.65$, $0.075D$ upstream of the propeller; $\alpha = -6$ deg, $J = 1.75$.

Figure 11.6 shows that the wake filling was worse under asymmetric inflow conditions than for the case with symmetric inflow (Fig. 11.4). Due to the asymmetry in the boundary layers on both sides of the pylon, a velocity overshoot occurred in one half of the wake, while in the other half a velocity deficit remained. Nonetheless, application of the blowing system still reduced the integral magnitude of the velocity deficit in the wake region by around 70% at the optimal blowing rate ($c_{\dot{m}} = 1.6$). To achieve better performance in angular inflow conditions, a blowing system would be required with an outlet integrated along the chord on each side of the pylon. This approach is discussed in Appendix A.

11.2. PROPELLER LOADING

11.2.1. SYMMETRIC INFLOW

BLADE LOADING

The local impact of the pylon-wake encounter on the propeller blade loads was quantified using the miniature surface-pressure transducers integrated into the blades (Section 5.4.2). Figure 11.7 compares the pressure distributions measured at $r/R \approx 0.65$ for the pylon-off and pylon-on configurations. Five circumferential blade positions are considered, corresponding to time instances before, during, and after the wake encounter. The circumferential angle is defined with respect to the leading edge of the blade at $r/R \approx 0.65$, while the pressure coefficient is referenced to the effective dynamic pressure in the rotational frame. The 95% confidence interval of the measurement data is indicated in Fig. 11.7 by the error bar plotted in the top left of each subplot. The standard

deviation was determined from the time-averaged pressure coefficients acquired at constant operating conditions for the unblown pylon-on configuration. The procedure was performed per individual phase angle, after which the maximum of the resulting values was taken as a conservative measure of the repeatability of the pressure measurements.

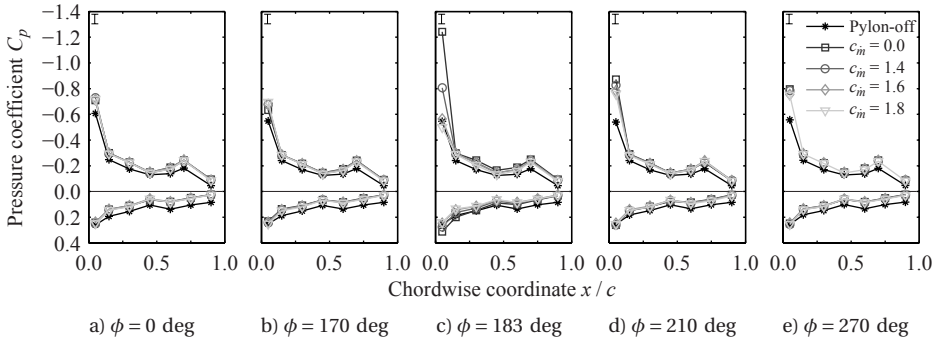

Figure 11.7: Effect of pylon installation on the phase-locked blade-pressure distributions at $r/R \approx 0.65$.

Figure 11.7 demonstrates the strong local impact of the wake encounter on the propeller blade loads. Opposite to the pylon (Fig. 11.7a), the pressure distributions for all five cases were comparable. A shift in the zero-loading outputs of the pressure transducers caused a slight offset between the results obtained with and without the pylon. This offset was approximately constant in the chordwise direction and was observed at all circumferential blade positions. Closer to the pylon wake region (Fig. 11.7b), the change in blade response due to the pylon was still negligible. During the wake encounter, the locally reduced inflow velocity causes a rapid increase in angle of attack experienced by the blade. This resulted in increased suction on the leading-edge region of the blade. For the unblown pylon-on configuration, this can be seen at $\phi = 183$ deg (Fig. 11.7c). A slight lag occurred between the circumferential position of maximum velocity deficit in the wake and that of the unsteady suction peak, as discussed in Section 8.2.1. Following the interaction with the pylon wake, the pressure distribution slowly recovered toward that characteristic of the undisturbed situation (Fig. 11.7d and 11.7e).

The application of pylon blowing reduced the nonuniformity of the propeller inflow (Fig. 11.4). Consequently, the wake encounter was less severe with blowing enabled, and the resulting pressure distributions more similar to those measured for the isolated propeller. At a blowing rate of $c_{\dot{m}} = 1.6$, the surge in the suction peak at $\phi = 183$ deg was practically eliminated, leading to a pressure distribution comparable to that acquired for the pylon-off configuration. At the other blowing settings, fluctuations of the pressure coefficient remained. An increase in magnitude of the suction peak was still obtained at $c_{\dot{m}} = 1.4$, albeit at a lower level than measured for the unblown case. This is due to the remaining velocity deficit in the pylon wake at this blowing setting, as shown in Fig. 11.4. At the highest blowing coefficient of $c_{\dot{m}} = 1.8$, on the other hand, the velocity overshoot in the pylon wake led to a decrease in magnitude of the suction peak during the wake interaction. This is a direct result of the reduced effective angle of attack of the propeller blade sections in the wake region at this blowing setting.

At $\phi = 210$ deg (Fig. 11.7d), the suction-peak pressures for the pylon-on configurations were comparable, but significantly offset from the value measured for the pylon-off case. For this part of the rotation, it can therefore be concluded that the change in loading due to pylon installation was not the result of the momentum deficit in the pylon wake. Instead, it was due to the deceleration of the flow near the pylon trailing edge. Even if optimal wake filling had been achieved, the blade response would still have changed at these circumferential angles compared to the pylon-off case.

The changes in the pressure distributions due to the installation of the pylon directly translate into fluctuating blade loads. Figure 11.8 presents the development of the blade normal-force coefficient over the rotation, as computed by integration of the recorded pressure distributions at each of the phase angles considered. Table 11.2 provides the corresponding numerical values characterizing the blade response. For clarity, markers are displayed in Fig. 11.8 at fifteen-degree intervals, while the 95% confidence interval is indicated by the error bar in the top left. The standard deviation of the normal-force-coefficient values was obtained from repeated unblown pylon-installed measurements. The blade response for the pylon-off configuration displayed a sinusoidal pattern due to the inflow angularity discussed before.

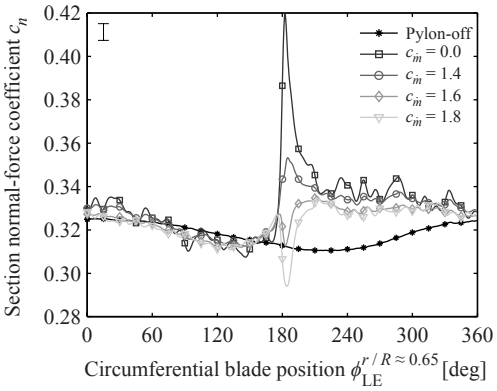

Figure 11.8: Effect of pylon installation on the phase-locked blade normal-force coefficient at $r/R \approx 0.65$.

Table 11.2: Effect of pylon installation on the unsteady blade-loading characteristics at $r/R \approx 0.65$.

Configuration	$\overline{c_n}$	$c_{n_{\text{wake}}}^{\partial c_n/\partial\phi=0}$	$(c_n - \overline{c_n})_{\text{rms}}$	$\frac{1}{360}\int_0^{360} \left\lvert \frac{c_n}{\overline{c_n}} - 1 \right\rvert \mathrm{d}\phi$
Pylon-off	0.318	0.312	$5.1 \cdot 10^{-3}$	$1.4 \cdot 10^{-2}$
$c_{\dot{m}} = 0.0$	0.331	0.420	$1.6 \cdot 10^{-2}$	$3.3 \cdot 10^{-2}$
$c_{\dot{m}} = 1.4$	0.329	0.353	$8.9 \cdot 10^{-3}$	$2.2 \cdot 10^{-2}$
$c_{\dot{m}} = 1.6$	0.324	0.313	$6.6 \cdot 10^{-3}$	$1.8 \cdot 10^{-2}$
$c_{\dot{m}} = 1.8$	0.323	0.294	$7.5 \cdot 10^{-3}$	$1.9 \cdot 10^{-2}$

Concurrent inspection of Figs. 11.4 and 11.8 reveals a direct link between the unsteady blade loads and the nonuniformity of the propeller inflow. The installation of the unblown pylon caused a sudden rise in normal-force coefficient during the wake en-

counter. As shown in Table 11.2, a peak increase of around 34% was observed compared to the pylon-off configuration. Averaged over the entire rotation, the section normal-force coefficient was increased by about 4% due to the installation of the pylon. This corresponds to an increase of the local thrust contribution by 4% as well.

The application of blowing reduced the unsteady loading peak, leading to a response closer to that measured for the isolated propeller. The smallest fluctuations were obtained at the blowing rate resulting in the most uniform propeller inflow ($c_{\dot{m}} = 1.6$). At this blowing setting, the normal force was reduced compared to the pylon-off configuration by a small but systematic amount around the center of the blown jet, where the compensating momentum overshoot occurred. Compared to the unblown pylon-on configuration, the reduction in integral normal-force variations equaled approximately 50%. At the same time, the root mean square of the normal-force fluctuations was decreased by about 60%. The time histories of the normal-force coefficient matched the expected trends at the other two blowing rates. At $c_{\dot{m}} = 1.4$, the injected mass flow was insufficient to fill the momentum deficit in the pylon wake, hence a normal-force increase remained during the wake encounter. At this blowing setting, the root-mean-square variation in normal force was the highest of the three blown cases, although still a 45% reduction was achieved compared to the unblown case. At the highest blowing coefficient considered, $c_{\dot{m}} = 1.8$, the opposite situation occurred. For this configuration, the strong velocity overshoot on the wake centerline introduced a reduction in blade normal force during the wake passage.

Away from the wake encounter, a series of wiggles can be observed in Fig. 11.8 for the unblown pylon-on configuration. At a blowing coefficient of $c_{\dot{m}} = 1.4$ these normal-force fluctuations were decreased, while at the two highest blowing rates they were eliminated completely. This indicates that the measured normal-force oscillations in this part of the rotation were indeed related to the pylon-wake interaction. The wake encounter caused a periodic forcing function, leading to variations of the blade normal force. It is unknown whether these fluctuations resulted from aerodynamic or structural effects.

Apart from the impact of the pylon-wake encounter on the blade loading, the response for the pylon-on configurations was also affected by the change of the potential flowfield induced by the pylon. Consequently, the results for the pylon-on configurations differed from those recorded for the pylon-off case throughout the entire rotation. This change in loading was unaffected by the blowing setting, since it was not related to the momentum deficit in the pylon wake.

The sensitivity of the unsteady-load reduction by blowing to the propeller operating point was studied by also taking measurements at high and low thrust settings, corresponding to $J = 1.05$ and $J = 1.75$. The associated thrust coefficients equaled $C_T = 0.51$ and $C_T = 0.18$, respectively. Figure 11.9 plots the root-mean-square amplitude of the normal-force fluctuations over a full rotation as a function of blowing rate and propeller thrust setting. The data were normalized by the mean normal-force coefficients obtained at the respective operating conditions.

Figure 11.9 confirms the impact of the propeller thrust setting on the relative importance of the normal-force fluctuations due to the pylon-wake encounter. Compared to the steady blade loads, the relative amplitude of the normal-force fluctuations increased with decreasing thrust setting. Moreover, it can be seen that the application

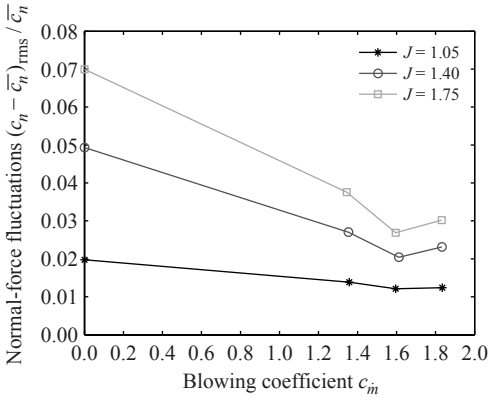

Figure 11.9: Effect of propeller thrust setting and blowing coefficient on unsteady blade loading at $r/R \approx 0.65$.

of pylon trailing-edge blowing effectively decreased the root-mean-square amplitude of the normal-force oscillations at all thrust settings. The load fluctuations were not fully eliminated because of the remaining unsteady loading caused by the non-ideal wake filling, and the angle-of-incidence effect discussed previously. The blowing coefficient leading to the smallest unsteady loads was the same regardless of the propeller operating point, and equal to $c_{\dot{m}} = 1.6$. This was also the blowing rate leading to the smallest integral velocity deficit in the pylon wake.

INTEGRATED LOADING

The fluctuating blade loads resulting from the installation of the pylon induce a time-dependent thrust coefficient on each of the blades. To quantify the magnitude of the variations in total blade thrust, measurements of the integrated propeller performance were taken using a rotating shaft balance (Section 5.4.2). It was known that such balances have a limited capability to capture high-frequency unsteady loads. As a result, the response time of the balance will most likely have been insufficient to follow the rapid load oscillations introduced by the wake encounter, resulting in a smoothing of the recorded signals. Furthermore, the time-dependent signals can be masked by vibrations introduced into the measurement signal due to eigenmodes of the balance. However, at the selected operating point the rotating shaft balance could be used to assess the change in response between the cases with and without blowing. Figure 11.10 displays the development of the phase-locked thrust coefficient over one revolution, as acquired for the pylon-off and pylon-on configurations. Two blowing coefficients are considered, corresponding to the unblown case ($c_{\dot{m}} = 0.0$) and the optimal blowing setting ($c_{\dot{m}} = 1.6$). Markers are depicted at 15-deg intervals for clarity. The 95% confidence interval is indicated by the error bar plotted in the top left of Fig. 11.10. The standard deviation was computed from the mean installed thrust coefficients obtained from all available data points at the considered propeller operating point.

Considering the symmetric inflow, a constant thrust coefficient would be expected throughout the rotation for the pylon-off case. In contrast, significant fluctuations can be seen for this configuration in the time history of the thrust shown in Fig. 11.10. These were due to shaft vibrations and the small inflow angularity mentioned earlier.

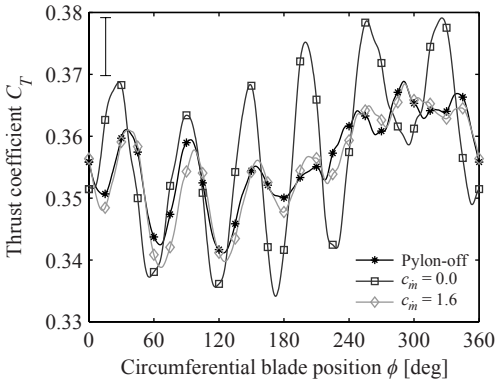

Figure 11.10: Effect of pylon installation on the phase-locked propeller thrust coefficient.

Focusing on the pylon-on configuration without blowing ($c_{\dot{m}} = 0.0$), a six-per-revolution loading cycle can be seen in Fig. 11.10. The rotation frequency of the propeller equaled 84.7 Hz at the considered operating point, hence the frequency of the observed phenomenon amounted to 508 Hz. This periodicity at the blade-passage frequency matches the frequency of the wake encounters experienced by the blades. These wake encounters introduced a forcing function acting periodically on the propeller–balance combination, resulting in blade-loading oscillations. However, the gradual nature of these oscillations does not match the expected impulsive increase in thrust during the wake passages. This can partially be attributed to phase-lag effects introduced by the swept blade planform. As a result, the different blade sections experienced the wake encounter at different times, smoothing the measured load fluctuations. Additionally, a lag in the blade response is observed in Fig. 11.10. Whereas the center of the first blade encountered the maximum velocity deficit in the pylon wake at a phase angle of $\phi \approx 0$ deg, the corresponding maximum load fluctuation only occurred around $\phi = 15$ deg. At this position, the trailing edge of the blade had just passed the wake region, hence the shift cannot be explained by effects due to sweep only. Also, the delay is significantly larger than the 3-deg phase lag observed in the sectional blade-loading data (Fig. 11.8). Therefore, it is concluded that the response time of the balance was insufficient to follow the rapid load oscillations, as expected.

The responses measured for the pylon-off and blown pylon-on configurations were approximately equal. Both did not display the strong cyclic behavior characteristic of the case with the unblown pylon. Therefore, it is concluded that the wake filling achieved by blowing reduced the magnitude of the forcing function experienced by the blades when passing behind the pylon. This confirms the observation that the unsteadiness of the propeller response was indeed reduced by the application of blowing, as deduced earlier from the surface-pressure data. Considering the good agreement between the signals recorded for the pylon-off and blown pylon-on configurations, the remaining fluctuations observed for the blown case were not related to a pylon-installation effect.

11.2.2. ASYMMETRIC INFLOW

Section 8.2.2 showed that the wake encounter also strongly affects the propeller blade loading at nonzero angle of attack. The unsteady blade-loading data were analyzed to verify the efficacy of trailing-edge blowing under asymmetric inflow conditions. Data were only available at $\alpha = -6$ deg and the low thrust setting ($J = 1.75$, $C_T = 0.18$). Figure 11.11 plots the circumferential variation of the section normal-force coefficient at $r/R \approx 0.65$ for the different blowing coefficients, with the isolated-propeller (pylon-off) data included as reference. The error bar indicates the 95% confidence level, which was estimated in the same way as discussed above Fig. 11.8.

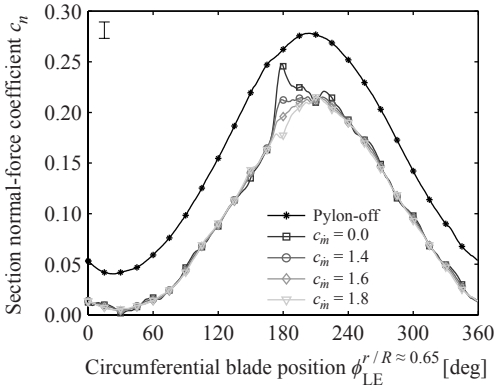

Figure 11.11: Effect of pylon installation on the phase-locked blade normal-force coefficient at $r/R \approx 0.65$; $\alpha = -6$ deg, $J = 1.75$.

For the case at negative incidence angle, the installation of the unblown pylon causes a combination of two interaction effects. The mean blade loading is decreased due to the interaction with the tip vortex (which rotates in the same direction as the propeller), while the wake encounter causes a sudden loading peak. Both effects were discussed in Section 8.2.2. The effect of blowing is to decrease the amplitude of the loading peak, similarly as for the case in symmetric inflow (Fig. 11.8). Again, the intermediate blowing rate of $c_{\dot{m}} = 1.6$ provided the largest reduction in load fluctuations, as expected considering the velocity profiles in the wake (Fig. 11.6).

11.3. PROPELLER NOISE EMISSIONS

The analyses provided in Section 8.3 showed that the unsteady loading caused by the wake encounter leads to a strong noise penalty, especially at a low propeller thrust setting. The unsteady-load reductions achieved with the trailing-edge blowing system should suppress at least part of this noise penalty.

11.3.1. SYMMETRIC INFLOW

Figure 11.12 displays the sound spectra measured with and without the pylon installed. All data were obtained for an axial emission angle in the propeller plane ($\theta_e = 90$ deg) and a circumferential angle perpendicular to the pylon ($\phi = 90$ deg). The results for the

blown case were acquired at the blowing rate leading to the largest reduction of the unsteady blade loads ($c_{\dot{m}} = 1.6$). To allow for a comparison of the tonal levels, markers are displayed at the sound pressure levels measured at frequencies corresponding to integer multiples of the blade-passage frequency. To quantify the difference between the recorded noise levels and the background noise in the test section, measurements were also taken using a dummy spinner, without the pneumatic motor running. The corresponding levels are indicated by the unmarked light gray line in Fig. 11.12. The initial parts of the spectra are omitted because they were dominated by background noise. The tonal noise component observed at a frequency between three and four times the blade-passage frequency was due to vortex shedding from the pylon trailing edge, as discussed in Section 8.3.1.

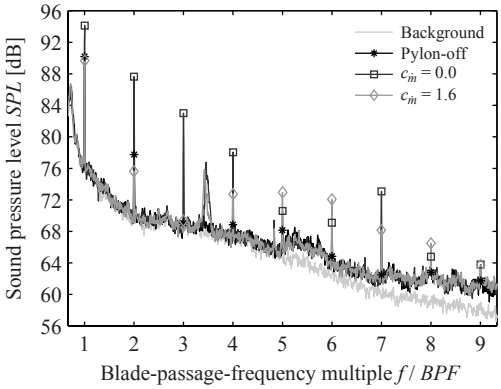

Figure 11.12: Effect of trailing-edge blowing on the propeller sound spectrum at $\theta_e = 90$ deg, $\phi = 90$ deg.

The spectra plotted in Fig. 11.12 highlight the significant noise penalty associated with the installation of the unblown pylon. Compared to the isolated propeller, the sound pressure level of the fundamental tone ($1 \cdot BPF$) increased by around 4 dB due to the presence of the pylon. The noise penalty for the harmonics was up to 14 dB, albeit at levels at least 7 dB below that of the fundamental. The recorded broadband levels were dominated by background noise up to a frequency of about five times the blade-passage frequency, corresponding to approximately 2,500 Hz. At higher frequency, no significant change was observed between the broadband emissions obtained for the pylon-off and the pylon-on configurations.

The reduction of the unsteady blade loads achieved by blowing (Fig. 11.8) directly led to a reduction of the noise penalty due to the installation of the pylon. For the first two propeller tones, the application of blowing resulted in a full recovery of the noise levels to the values measured for the isolated propeller. Moreover, at three times the blade-passage frequency the tonal amplitude was brought back to the background noise level, similarly as for the isolated propeller. At the higher harmonics, part of the noise penalty remained. This is attributed to the residual blade-loading fluctuations for the blown configuration observed in Fig. 11.8, that can be traced back to the remaining nonuniformities in the blown pylon wake shown in Fig. 11.4. The same trends are observed in the waveforms of the acoustic pressure, plotted in Fig. 11.13 for the same microphone

location as considered for the spectra in Fig. 11.12 ($\theta_e = 90$ deg, $\phi = 90$ deg). The reduction of the velocity perturbations in the propeller inflow by blowing is directly reflected in the acoustic response of the propeller. The amplitude of the acoustic-pressure perturbations decreases with decreasing inflow perturbations, as expected. At the lowest thrust condition considered (Fig. 11.13c), the performance of the blowing system was insufficient to fully eliminate the noise penalty caused by the installation of the pylon. At this thrust setting, the amplitude of the steady-loading noise was lower, and thus the relative contribution of the remaining unsteady-loading noise was larger.

The influence of the pylon-wake encounter on the directivity of the propeller's tonal noise emissions was assessed by performing the in-flow acoustic measurements at thirteen distinct axial positions. To extract the harmonic components from the recorded signals, the microphone data were first phase-averaged. Subsequently, bandpass filtering was performed around the frequencies corresponding to the first ten multiples of the blade-passage frequency. A total tonal noise level was then computed from the root mean square of the resulting pressure signatures. The levels recorded at the different axial positions were scaled toward a constant observer range using the inverse-distance law ($p_2/p_1 = r_1/r_2$). The selected distance equaled that from the propeller to the microphone position corresponding to an emission angle of 90 deg ($r_{mic} = 2.84$ m). The resulting directivity patterns are plotted in Fig. 11.14. As discussed in Section 8.3.1, the noise levels obtained for the isolated propeller featured an unexpected trough around an emission angle of $\theta_e = 80$ deg due to interference between the various noise sources.

Figure 11.14 shows that the installation of the unblown pylon increased the propeller noise emissions over the entire directivity range considered. Compared to the pylon-off configuration, a tonal-noise increase of up to 15 dB was measured. The noise penalty was especially large in the upstream direction, as discussed before in Section 8.3.1. The application of pylon trailing-edge blowing decreased the noise emissions to approximately the levels recorded for the isolated propeller at all emission angles. This once more confirms the direct relation between the unsteady propeller blade loads and the propeller noise emissions. The reduction of the unsteady blade loads obtained by blowing effectively eliminated the noise-generating mechanism related to the installation of the pylon.

To compare the performance of the trailing-edge blowing system at the three operating conditions considered, an integral noise penalty was defined as the difference between the sound pressure levels for the pylon-on and pylon-off configurations:

$$\Delta SPL = SPL_{\text{Pylon-on}} - SPL_{\text{Pylon-off}} = 20\log_{10}\left(\frac{p_{\text{rms}}^{\text{Pylon-on}}}{p_{\text{rms}}^{\text{Pylon-off}}}\right). \tag{11.1}$$

The sound pressure levels were integrated over the full range of considered axial emission angles to obtain a single value representative of the sound emissions of each configuration. Figure 11.15 displays the results as a function of propeller thrust setting and pylon-blowing coefficient.

The data presented in Fig. 11.15 emphasize the sensitivity of the pylon-installation effects to the propeller operating point. With increasing thrust setting, the steady blade loading became more dominant (Fig. 11.9), hence the noise penalty due to the installation of the pylon decreased. At the highest thrust setting considered, $J = 1.05$, the integral

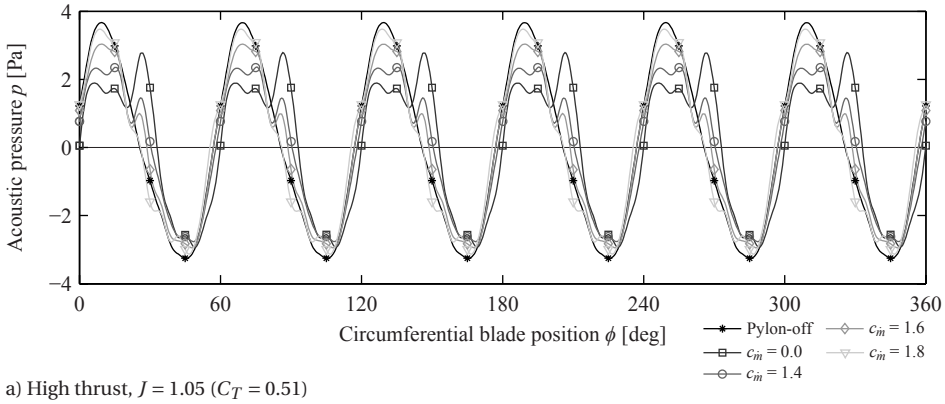

a) High thrust, $J = 1.05$ ($C_T = 0.51$)

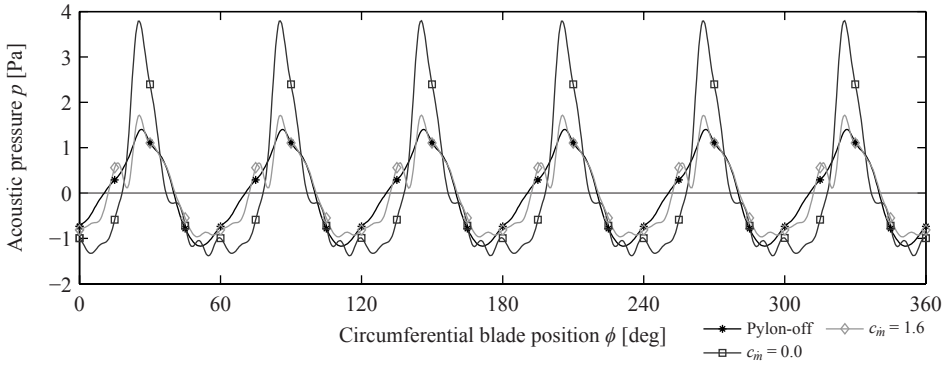

b) Intermediate thrust, $J = 1.40$ ($C_T = 0.36$)

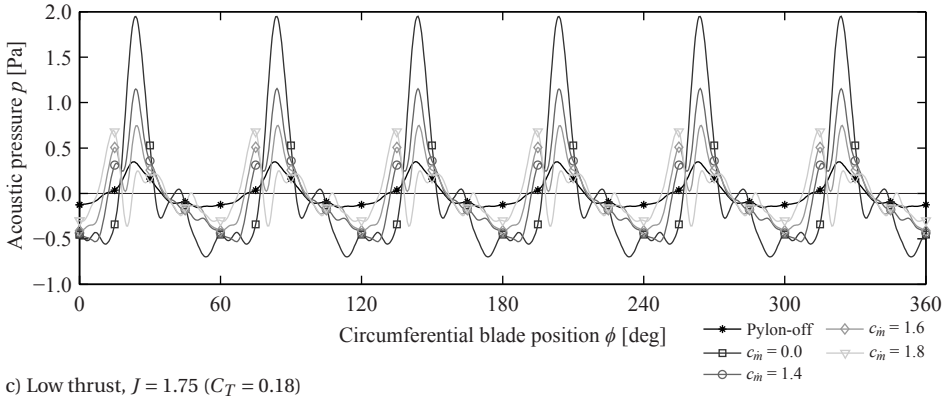

c) Low thrust, $J = 1.75$ ($C_T = 0.18$)

Figure 11.13: Effect of trailing-edge blowing on the waveforms of the acoustic pressure at $\theta_e = 90$ deg, $\phi = 90$ deg.

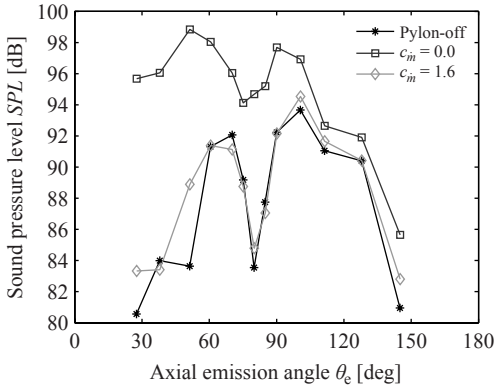

Figure 11.14: Effect of trailing-edge blowing on the directivity of the tonal noise emissions of the propeller at $\phi = 90$ deg, $J = 1.40$.

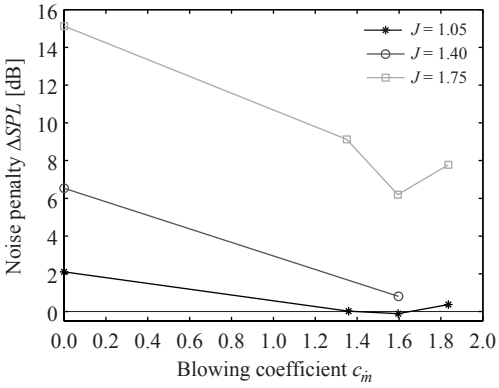

Figure 11.15: Effect of propeller thrust setting and blowing coefficient on the noise penalty due to pylon installation, integrated over the axial emission angle range at $\phi = 90$ deg.

sound pressure level only increased by 2 dB, while at the low thrust condition ($J = 1.75$) the installation of the pylon amplified the propeller noise emissions by 15 dB. The application of pylon blowing decreased the pylon-installation noise penalty at all operating conditions considered. At the high and intermediate thrust settings, the tonal noise levels were practically recovered toward those observed for the pylon-off configuration. Under these conditions, the remaining unsteady-loading noise caused by the non-ideal filling of the pylon wake was irrelevant compared to the noise sources corresponding to the isolated propeller. At the low thrust setting, on the other hand, the relative contribution of the unsteady-loading noise was larger, and a noise penalty of 6 dB remained even with blowing enabled. It is anticipated that the noise penalty at the low thrust setting could be further reduced by optimizing the uniformity of the blown pylon wake.

11.3.2. ASYMMETRIC INFLOW

When operating under asymmetric inflow conditions, the propeller noise is modified due to the sinusoidal loading fluctuations experienced by the blades, and due to convective-amplification effects. As shown in Section 8.3.2, this can either increase or decrease the noise emissions, depending on the observer location and propeller thrust condition. Compared to the isolated configuration, the installation of the pylon still introduces a noise penalty when the setup is set to nonzero angle of incidence, thus leaving room for potential noise reductions by blowing. However, Section 11.1.2 showed that the uniformity of the blown wake was worse at nonzero incidence angle when compared to the symmetric case. Therefore, measurements were taken to investigate the potential of the trailing-edge blowing system for noise reductions at nonzero incidence angle. The measurements were taken at incidence angles of ±6 deg, while only the low thrust setting of $J = 1.75$ ($C_T = 0.18$) was considered. Figure 11.16 presents the noise penalty due to the installation of the pylon as a function of the blowing coefficient and incidence angle. The noise penalty was again obtained by integration over the considered axial directivity range, in the same way as done for Fig. 11.15.

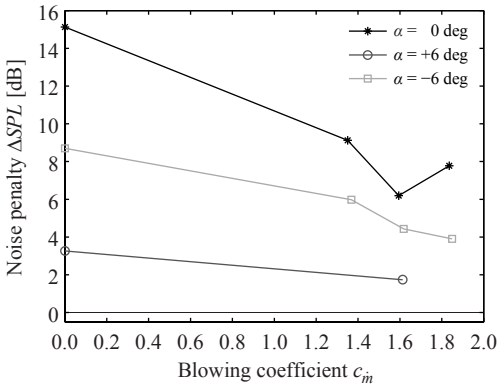

Figure 11.16: Effect of trailing-edge blowing on the installation noise penalty under asymmetric inflow conditions; $J = 1.75$, $\theta_e = 90$ deg, $\phi = 90$ deg.

Figure 11.16 shows that the noise penalty for the unblown configuration was the largest at $\alpha = 0$ deg, as discussed before in Section 8.3.2. At nonzero incidence angle, the noise emissions of the isolated propeller were higher than for the symmetric case. As a result, the relative impact of the noise source caused by the wake encounter was smaller for the cases at nonzero incidence than at zero incidence.

Application of the blowing system reduced the noise penalty due to the installation of the pylon at all inflow angles. The symmetric case displayed best performance at $c_{\dot{m}} = 1.6$, as already shown in Fig. 11.15. For the cases at nonzero angle of incidence, the remaining noise penalties with blowing enabled were smaller than at $\alpha = 0$ deg. This was as expected considering the higher noise level associated with the isolated propeller at nonzero incidence angle (Fig. 8.13b), which partially masked the noise due to the pylon-installation effects. At $\alpha = +6$ deg, the angular-inflow effects were relatively strong for the isolated propeller, as discussed before. Consequently, the reduction of the unsteady

blade loads by blowing was sufficient to reduce the noise penalty due to the installation of the pylon to about 2 dB. The negative-incidence case featured a larger remaining noise penalty. For this case, the smallest noise penalty was observed at the blowing rate which introduced a clear velocity overshoot near the wake centerline ($c_{\dot{m}} = 1.8$), leading to local unloading of the blades.

11.4. KEY FINDINGS

This chapter has provided an overview of the physical working principles of pylon trailing-edge blowing for the mitigation of pusher-propeller installation effects. Based on the measurements of the pylon-wake flowfields, it is concluded that the application of pylon trailing-edge blowing successfully decreases the velocity deficit in the pylon wake. For a typical pylon–propeller spacing, however, the wake profiles do not become completely uniform. A velocity overshoot remains on the wake centerline due to the small thickness of the blowing slit and the limited length from the pylon trailing edge to the propeller plane available for mixing of the blown jet with the external flow. At nonzero incidence angle, an asymmetric velocity distribution was obtained in the pylon wake due to the different boundary-layer development on both sides of the pylon.

The reduction of the velocity deficit in the pylon wake by blowing resulted in the practical elimination of the unsteady lift peak during the wake encounter. Compared to the unblown case, the root mean square of the blade normal-force fluctuations was decreased by up to 60% at an intermediate thrust setting. The corresponding propeller noise levels with blowing enabled were found comparable to those emitted by the isolated propeller, at all axial directivity angles. Consequently, it is concluded that the elimination of the unsteady blade loads by blowing is responsible for the successful mitigation of the noise penalty due to the installation of the pylon.

The noise penalty due to pylon installation was not fully eliminated by blowing at the lowest thrust condition considered. At this operating point, the unsteady-loading noise which remained because of the non-ideal pylon-wake filling was still relevant compared to the low levels of the steady-loading noise. Further improvements could be obtained by optimizing the uniformity of the blown pylon wake, for example by using a chordwise-blowing system with a blowing outlet integrated along the chord on each side of the pylon, as discussed in Appendix A. This could also enhance the performance of the blowing system under asymmetric inflow conditions.

V

Conclusion

12

CONCLUSIONS AND RECOMMENDATIONS

This thesis has discussed an experimental study of the key aerodynamic and aeroacoustic interaction effects for tip-mounted propellers, including consideration of three performance-enhancement strategies aimed at mitigating the adverse interactions and exploiting the beneficial interactions. Throughout the thesis, the discussion was centered around the research question:

> *What are the key aerodynamic and aeroacoustic interaction effects for tip-mounted propeller configurations, and how can the performance of such configurations be enhanced?*

Section 12.1 first discusses the conclusions drawn from the analyses presented in the previous chapters. Then, Section 12.2 provides recommendations for future work.

12.1. CONCLUSIONS

Parts III and IV of this thesis have provided the results of comprehensive wind-tunnel experiments that investigated the physical mechanisms of the aerodynamic and aeroacoustic interaction effects for tip-mounted propellers. Furthermore, potential performance-enhancement strategies were assessed which could be valuable in optimizing the performance of such propellers. In this way, crucial information on propeller–wing interactions for tip-mounted configurations has been contributed to the literature, while the detailed experimental data can be used for validation of both low-order and high-order computational tools. Although the experiments were performed at low Mach and Reynolds numbers, the results are representative of interactions at full scale. In most cases, the change in propeller or airframe response due to the interactions can be considered primarily as a potential-flow effect, induced by the changes in velocity and pressure in the vortical regions which cause the interaction effects. Therefore, the dominant physical phenomena caused by the interactions will be present also at the lower Mach

and Reynolds numbers typical of the experiments. The vortical regions themselves naturally are the result of viscous processes and, therefore, subject to the Reynolds and Mach number scaling.

The conclusions drawn from the results described in Parts III and IV of this thesis are summarized below, separately for each of the subquestions defined in Section 1.1. The discussion mostly echoes the key findings sections provided at the end of Chapters 6 through 11.

12.1.1. INTERACTION-EFFECTS ANALYSIS

Three key aerodynamic and aeroacoustic interaction effects for tip-mounted propellers were studied:

1. Wingtip-vortex attenuation and swirl recovery
2. Propeller-slipstream impingement (on a pylon)
3. Pylon-wake encounter (by a propeller)

In order to answer the first part of the research question, the physical mechanisms of the interaction effects were investigated based on three subquestions, discussed separately below.

1. *What is the physical mechanism driving the efficiency increase observed for wingtip-mounted propellers in tractor configuration, and how does it relate to the propeller and wing operating conditions?*

Chapter 6 assessed the key aerodynamic interaction effects for wingtip-mounted propellers installed in a tractor configuration. For such a layout, the propeller slipstream interacts with the flow around the wingtip, thus affecting the roll-up and downstream behavior of the wingtip vortex. This modifies the aerodynamic performance of the wing. Measurements with the propeller installed on a symmetric wing model with flap led to the following conclusions:

- The rotational velocity in the wake of a wingtip-mounted propeller decreases when the swirl in the slipstream is opposite to that associated with the wingtip vortex. Assuming positive wing lift, this occurs with inboard-up rotation, and improves system performance due to a reduction of the wing induced drag.
- The increased dynamic pressure in the propeller slipstream increases the lift on the part of the wing washed by the slipstream. This is amplified by the induced swirl for the case with inboard-up rotation. As a result, a strong spanwise variation occurs in the wing lift.
- The vorticity introduced into the flowfield by the spanwise lift gradient at the slipstream edge causes a spanwise shearing of the slipstream. The slipstream edge moves away from the propeller axis on the advancing blade side, and toward the propeller axis on the retreating blade side. With inboard-up rotation, the crossflow component over the nacelle induced by the wingtip vortex decreases the slipstream distortion at positive angle of attack and increases the distortion at negative angle of attack.

- The interaction amplifies with increasing thrust setting, owing to the accompanied increase in dynamic pressure and swirl in the slipstream. With outboard-up rotation, the interaction effects due to swirl are opposite to those observed with inboard-up rotation, while the dynamic-pressure effect is the same.

To quantify the potential aerodynamic benefits of the wingtip-mounted tractor-propeller configuration, a direct comparison was made with a conventional configuration, with the propeller mounted on the inboard part of the wing (at 44% of the span from the root). This comparison led to the following conclusions:

- The increase in wing lift due to the interaction with the slipstream was smaller for the wingtip-mounted configuration than for the conventional configuration. This is due to the smaller spanwise extent of the wing washed by the slipstream for the wingtip-mounted configuration, and the relatively low loading near the wingtip.
- The interaction between the propeller slipstream and the wingtip vortex leads to a clear drag reduction for the wingtip-mounted configuration. This is mostly due to a reduction of the wing induced drag. At a wing lift coefficient of $C_L = 0.5$ and a thrust coefficient of $C_T = 0.12$, the drag reduction amounted to about 15% when compared to the conventional configuration with the propeller mounted on the inboard part of the wing.
- The exact drag benefit of the wingtip-mounted configuration is specific to vehicle design and operating conditions. Compared to the propeller-off case, the benefit increases with increasing wing lift coefficient and propeller thrust coefficient, until a maximum is reached. After that point, the interaction with the slipstream leads to such a strong distortion of the wing lift distribution that the associated increase in induced drag is no longer offset by the wingtip-vortex-attenuation and swirl-recovery mechanisms.

The analyses have shown that the efficiency increase offered by wingtip-mounted propellers is due to wingtip-vortex attenuation and swirl recovery, and thus depends on the wing loading and the swirl in the propeller slipstream. Besides this time-averaged effect, the interaction between the propeller slipstream and the wing also causes unsteady effects. These are addressed by the next subquestion.

2. *What is the physical mechanism driving the unsteady loading on a surface immersed in the slipstream of a tractor propeller, and how does it relate to the propeller operating conditions and the spacing between propeller and downstream surface?*

Chapter 7 quantified the unsteady loading caused by the impingement of a propeller slipstream on a downstream pylon. Such unsteady loading may lead to vibrations responsible for structure-borne noise, thereby potentially reducing passenger comfort. The same effects would occur for a wing-mounted propeller configuration. Microphone measurements on the surface of the pylon model led to the following conclusions:

- The pressure fluctuations caused by the impingement of a propeller slipstream on a downstream wing or pylon are dominated by the passages of the blades' tip vortices. The unsteady pressure is periodic with a rich spectral content, and persists up to the trailing edge of the wing or pylon.

- The pressure fluctuations decrease with decreasing blade loading due to the associated reduction in strength of the blade wakes and tip vortices. At conditions with very low blade loading, the strength of the tip vortices tends to zero while the blade wakes remain, making the blade wakes the dominant source of unsteady loading in such case.
- Increasing the spacing between the propeller and the wing or pylon reduces the pressure fluctuations due to diffusion of the blade wakes and tip vortices before their interaction with the wing or pylon.

The measured pressure data were integrated to obtain the unsteady loading on the pylon caused by the interaction with the incoming propeller slipstream. From these data, the following conclusion was drawn:

- The unsteady pylon lift displays a nonmonotonic dependency on the propeller advance ratio. The unsteady loading was smallest for cases for which the ratio between the wavelength of the pressure perturbation and the pylon chord length was closest to an integer value. In an idealized case, for integer ratios the integrated pressure differential across the pylon is zero. Structure-borne noise reductions might thus be obtained by proper tailoring of the pylon chord length.

The results have identified the tip vortex as the main source of unsteady loading on a surface immersed in the slipstream of a tractor propeller. For pusher propellers, a different interaction phenomenon occurs. This was addressed by the last subquestion used to answer the first part of the research question.

3. *What is the physical mechanism driving the noise penalty for propellers in pusher configuration, and how does it relate to the propeller operating conditions?*

Chapter 8 presented a comprehensive analysis of the aerodynamic and aeroacoustic interaction effects for pylon-mounted pusher propellers. Such a configuration is especially interesting to minimize interior noise, by placing the propellers as far away as possible from the cabin. From the unique evaluation of the flowfields between the pylon and the running propeller, it was concluded that:

- The suction of the propeller reduces the severity of the pylon-wake encounter. The wake width and velocity deficit decrease with increasing thrust setting due to the favorable pressure gradient imposed by the propeller.

Measurements of the propeller performance confirmed previously published results by showing that:

- The passage of the blades through the pylon wake has a negligible effect on the time-averaged propeller thrust and torque.
- The impact on the unsteady blade loads, on the other hand, is significant, with a rapid increase in normal force during the wake encounter. The relative amplitude of the unsteady loads increases with decreasing thrust setting because of the associated increase in absolute and relative angle-of-attack variation and the decrease in reduced frequency of the perturbation.

In terms of acoustic performance, the following conclusions were drawn:

- The fluctuating blade pressures modify the amplitude, spectral content, and directivity of the propeller noise emissions. At the lowest thrust setting considered ($C_T = 0.18$), a maximum tonal noise penalty of 24 dB was measured.
- The impulsive nature of the pylon-wake encounter enriches the spectral content of the noise emissions. As such, the harmonics significantly contribute to the overall noise levels for the pylon-installed configuration.
- The additional noise due to the unsteady blade loads peaks in the upstream direction, independent of the propeller thrust setting.
- The installation of the pylon reduces the sensitivity of the propeller noise emissions to the thrust setting. This is because the interaction noise is less sensitive to the propeller operating point than the noise sources associated with the isolated propeller.
- Only the tonal noise was affected by the pylon-installation effects, while the broadband levels remained unchanged.

When operating in asymmetric inflow, the wing or pylon tip vortex interacts with the propeller to result in significant modifications of the propeller performance and noise emissions:

- The rotational velocity components induced by the tip vortex affect the effective advance ratio sensed by the propeller, thereby changing the propeller rotational speed required to achieve a given thrust. The propeller performance is enhanced when the direction of rotation of the tip vortex is opposite to that of the propeller.
- The noise penalty due to the pylon-installation effect can significantly decrease in this condition if the wake encounter occurs in the part of the rotation where the effective rotational velocity is reduced by the angular inflow.

These conclusions emphasize the importance of the consideration of the propeller rotation direction for optimal integration of tip-mounted propellers with the airframe.

12.1.2. PERFORMANCE-ENHANCEMENT STRATEGIES

For each of the interaction effects discussed in Part III of this thesis, a suitable performance-enhancement strategy was investigated through the application of:

1. Swirl-recovery vanes
2. Flow-permeability at the pylon leading edge
3. Pylon trailing-edge blowing

The potential of these performance-enhancement strategies was examined by addressing three subquestions, treated separately below.

4. *To what extent can swirl-recovery vanes increase the efficiency of an isolated propeller without prohibitive noise penalty, and can these vanes be used to eliminate the asymmetry in aerodynamic loading for a vehicle configuration with co-rotating propellers in tractor configuration?*

Chapter 9 discussed the aerodynamic and aeroacoustic performance of a propeller with swirl-recovery vanes, both in isolated and pylon-installed configurations. The vanes convert part of the swirl in the propeller slipstream into thrust, thereby lowering the thrust requirement for the propeller. In this way, the required power input to the propeller can be reduced and hence the efficiency of the propulsion system increased. Furthermore, the reduction in swirl can alleviate asymmetric aerodynamic loading in the case of vehicle configurations with co-rotating propellers (i.e. inboard-up on one side of the aircraft and outboard-up on the other).

Measurements of the aerodynamic performance of an isolated propeller with SRVs highlighted that:

- The SRVs can decrease the time-averaged rotational velocity in the propeller slipstream over a wide range of thrust settings. Computations performed to complement the experiments showed that application of the SRVs at an intermediate thrust setting ($C_T = 0.36$) decreased the relative rotational kinetic energy in the slipstream by approximately 46%.

- The propulsive efficiency increased by 0.7% at $C_T = 0.36$ due to the swirl recovery. The performance of the tested SRVs was limited by stall occurring on the inboard part of the vane, which could have been prevented by a local increase of the pitch angle.

- The upstream perturbation of the flowfield experienced by the propeller due to the presence of the SRVs leads to fluctuating propeller loading. The peak-to-peak amplitude of the blade normal-force at $r/R \approx 0.65$ was $1-2\%$ of the local time-averaged loading, with the highest relative unsteady loads occurring at the lowest propeller thrust setting considered ($C_T = 0.18$).

- The integrated propeller loading remained practically unaffected by the installation of the SRVs.

- In addition to the upstream interaction, the downstream impingement of the propeller blade wakes and tip vortices on the SRVs causes unsteady SRV loading. Computations complementary to the experimental assessment showed that the amplitude of the unsteady loads increases toward the tip of the SRV due to the strong interaction with the propeller tip vortices.

Far-field microphone measurements were used to assess the aeroacoustic effects of SRV installation:

- The unsteady interactions between the propeller and the SRVs introduce two additional noise sources: unsteady loading on the propeller blades and on the SRVs. The installation of the SRVs increased the tonal noise, while the recorded broadband noise emissions were not affected.

- The increase in tonal noise was manifested mostly by a significant amplification of the levels of the higher harmonics. This especially affected the system noise emissions at a low propeller thrust setting ($C_T = 0.18$), for which the noise penalty was up to 7 dB. At higher thrust settings, the tonal noise penalty was lower at $3-5$ dB.

Preliminary investigations with a pylon-mounted tractor propeller confirmed that SRVs can successfully reduce asymmetric loading on vehicles with a co-rotating propeller arrangement:

- By minimizing the swirl in the propeller slipstream, the interaction effects on the downstream pylon were reduced, thereby decreasing the difference in aerodynamic response for the cases with inboard-up and outboard-up propeller rotation.
- For the case with inboard-up rotation, the installation of the SRVs increased the maximum lift coefficient due to the forces generated by the SRVs. This highlights the potential importance of the circumferential distribution of the SRVs, which could be optimized to maximize the SRVs' lifting potential.

The results have confirmed the aerodynamic benefits of SRVs. Multidisciplinary optimization of the SRV design could be employed to minimize the interaction-noise penalty while maximizing the aerodynamic benefits.

5. *To what extent can a flow-permeable leading edge alleviate the unsteady loading caused by slipstream impingement for propellers in tractor configuration, and what is the associated impact on the lift and drag performance?*

Chapter 10 quantified the potential of a flow-permeable leading edge to alleviate the unsteady loading caused by propeller-slipstream impingement. The possible interior noise penalty caused by this unsteady loading, through the structure-borne noise path, can be mitigated in two different ways: by modifying the transmission path of the vibrations through the aircraft structure or by decreasing the amplitude of the unsteady aerodynamic loads. The application of a flow-permeable leading edge falls into the latter category. The geometry of the considered flow-permeable leading edges was not optimized; instead, it was based on previous work available in the literature.

From velocity fields acquired with particle-image velocimetry, it is concluded that the application of a flow-permeable insert introduces the following effects:

- The flow through the holes and cavity of the flow-permeable insert causes an increase in boundary-layer thickness, thereby modifying the effective outer shape of the pylon. This was especially pronounced for the inserts with relatively large cavity depth.
- The lift performance was reduced by application of the flow-permeable insert, especially at angles of attack above 6 deg.
- The drag was increased due to viscous dissipation and increased surface roughness compared to the solid pylon model.

The modifications to the flowfield affect the generation of pressure fluctuations on the surface:

- The increase in boundary-layer thickness and flow through the holes and cavity of the flow-permeable insert amplifies the viscous dissipation of the blade tip vortices. Consequently, the velocity fluctuations near the pylon surface induced by the blade tip vortices decreased by up to 35% in the tip-vortex impingement region.
- Microphone-array measurements showed that this led to reduced far-field noise, suggesting a reduction in pressure fluctuations on the pylon surface. Larger reductions in far-field noise and thus pressure fluctuations were obtained from the inserts with larger cavity depth.

The results highlight that the application of a flow-permeable leading edge can reduce the pressure fluctuations due to the impingement of a propeller slipstream, but also decreases the time-averaged performance of the pylon or wing. Therefore, it is concluded that a careful trade-off is required between time-averaged aerodynamic performance and unsteady-load alleviation when designing a flow-permeable insert.

6. *To what extent can pylon trailing-edge blowing alleviate the noise penalty due to the wake encounter for propellers in pusher configuration?*

Chapter 11 provided an overview of the physical working principles of pylon trailing-edge blowing for the mitigation of pusher-propeller installation effects. By reducing the velocity deficit in the wake, the perturbation of the propeller inflow can be decreased, thereby alleviating the unsteady blade loading and associated noise penalty.

From measurements of the pylon-wake flowfields, it is concluded that:

- The application of pylon trailing-edge blowing successfully decreases the velocity deficit in the pylon wake.
- For a typical pylon–propeller spacing, the wake profiles do not become completely uniform at the location of the propeller plane. A velocity overshoot remains on the wake centerline due to the small thickness of the blowing slit and the limited length available for mixing between the pylon trailing edge and the propeller.

The increased wake uniformity achieved by blowing alleviates the unsteady effects due to the pylon-wake encounter:

- The reduction of the velocity deficit in the pylon wake practically eliminates the unsteady lift peak during the wake encounter. Compared to the unblown case, reductions of up to 60% were measured in root mean square of the blade normal-force fluctuations at an intermediate thrust setting of $C_T = 0.36$.
- The elimination of the unsteady blade loads by blowing successfully mitigates the noise penalty due to the installation of the pylon. At an intermediate thrust setting ($C_T = 0.36$), the pylon-installed propeller noise levels with blowing enabled were comparable to those emitted by the isolated propeller, at all axial directivity angles.

- The noise penalty due to pylon installation was not fully eliminated by blowing at the lowest thrust condition considered ($C_T = 0.18$). At this operating point, the unsteady-loading noise which remained because of the non-ideal pylon-wake filling was still relevant compared to the low levels of the steady-loading noise.

The analyses have shown that pylon blowing is an effective strategy to alleviate the noise penalty due to the pylon-wake encounter. Further improvements could be obtained by optimizing the uniformity of the blown pylon wake, for example by using a chordwise-blowing strategy with a blowing outlet integrated along the chord on each side of the pylon. This is confirmed by the numerical analyses provided in Appendix A, which additionally show that with a chordwise blowing approach the wake can also be made uniform at nonzero angle of attack.

12.2. RECOMMENDATIONS

The thorough analyses of interaction effects and performance-enhancement strategies for tip-mounted propellers discussed in this thesis could be further expanded by performing additional research. This section provides various suggestions for future work, which could be useful to further enhance understanding of the interaction effects for tip-mounted propellers, and aid in the analysis and design of future vehicles with tip-mounted propellers. Recommendations are provided separately for the assessment of interaction effects and performance-enhancement strategies.

12.2.1. INTERACTION-EFFECTS ANALYSIS

The key interaction effects for tip-mounted propellers were studied in Part III of this thesis, based on experimental work at model scale in low-speed wind tunnels. Despite the inherent advantages of this approach, it also leaves room for additional work using alternative means:

- The effects of the low Mach and Reynolds numbers characteristic of model-scale experiments in low-speed wind tunnels were discussed at various points in this thesis. A trivial suggestion for future work is to also perform experiments at higher Mach and Reynolds numbers. Although this most likely will not lead to new insights in terms of the physical background of the interaction effects, the relative amplitude of various sources of the interaction may still be different. Also, relevant compressibility effects may be encountered at higher Mach numbers.

- Numerical simulations with CFD tools (RANS, URANS, LBM) could provide additional insight into the interaction effects studied experimentally in this thesis. Whereas the experimental approach is particularly suited to study the sensitivity of the interaction effects to various quantities (propeller loading, wing loading, angle of attack, etc.), the computational approach will always lead to a more complete data set. If the numerical result can be sufficiently validated, then it may be useful in explaining additional aspects of the interactions, mostly by overcoming the limitations of experimental setups in terms of the amount of instrumentation. This applies especially to the propeller. Numerical simulations could also identify

unexpected aspects of the interaction, which could be overlooked in an experiment, since the experimental setup is typically optimized to measure the anticipated effects. Other potential advantages of the numerical approach include the avoidance of wall effects and scaling effects, and more straightforward bookkeeping of the various contributions to the lift and drag forces.

The use of experimental models is often constrained by either financial or planning aspects. Although the experimental setups employed in this thesis (see Part II) were selected such that they allowed for an adequate study of the parameters of interest, improvements could be made for future work:

- The results for the tractor-propeller configuration (*PROWIM-T* and *PROWIM-US* setups) were obtained with an old-fashioned propeller design, with an inefficient blade geometry at the inboard radial stations (see Section 3.3.1). The resulting flow separation at the root of the blade may complicate potential comparisons with numerical tools. This is further amplified by the discontinuity in geometry at the interface between the nacelle and the propeller hub. These concerns could be addressed by modifying the propeller, hub, and spinner geometry for future experiments. The blade cross-sections should feature airfoil shapes up to the root of the blade, while the outer shape of the hub and nacelle should be such that there is no discontinuity in the geometry. Furthermore, the thrust coefficients reached with this propeller setup were relatively low. Investigations of the interaction effects for the tractor configuration should also be performed at higher thrust coefficients to study the resulting impact on aerodynamics and aeroacoustics.

- To quantify the aerodynamic benefits of the wingtip-mounted propeller, a bookkeeping procedure is required to separate the forces generated by the wing and the propeller. To properly isolate the contributions by both components, the propeller forces should be measured separately. This could be achieved by either using a rotating shaft balance or an internal balance which isolates the motor and propeller from the rest of the nacelle. This approach would avoid the assumption made in Chapter 6 that the propeller performance is unaffected by the installation effects, and thus the isolated propeller data can be used for the drag bookkeeping procedure. For the tractor configuration, this assumption is reasonably valid, considering that the upstream effect of the wing on the propeller loading is typically small (see Section 6.2.4). For a pusher configuration, on the other hand, this approach would not suffice since the propeller loading will be affected significantly by the interaction with the wingtip vortex (see Section 8.2.2).

Besides potential improvements in terms of approach and tools, also additional areas of research remain which were not addressed in this thesis, or in previous literature:

- The experiments discussed in this thesis have focused on configurations with a propeller and a nearby wing or pylon. On a real airplane, additional interaction effects will occur due to the presence of the rest of the airframe. Analyses at airplane level would be important to quantify these additional interaction effects, and also to provide insight into the impact of the interaction effects on the overall airplane performance.

- This thesis has assessed the aerodynamic and aeroacoustic interactions separately for tractor propellers and pusher propellers. This approach was chosen to avoid the need for dedicated optimizations of both configurations. However, despite the challenges involved in a direct comparison between tractor and pusher propellers, it could be valuable to provide the aircraft designer with additional insight into the advantages and disadvantages of both configurations.

- The wingtip-mounted propeller seems particularly attractive for a vehicle with distributed propulsion. Therefore, it is recommended to also investigate the interaction effects for tip-mounted propellers in such a configuration. The combination of several slipstreams will modify the interaction with the wing, thus changing the wing loading. In order to arrive at an optimal configuration, all propellers should be considered simultaneously.

- The comprehensive experimental analysis of the wingtip-mounted propeller in tractor configuration discussed in Chapter 6 highlighted potential aerodynamic benefits for this configuration. A similarly detailed study of the pusher configuration would be interesting in light of the potential efficiency benefits that could be obtained in such case. Obviously, the acoustic performance should then also be considered, since the wake-encounter phenomenon would be even stronger than for the pylon-mounted case discussed in Chapter 8.

- The assessment of structure-borne noise provided in this thesis focused on the forcing function of the potential noise generation: the unsteady loads generated on the pylon or wing by the interaction with the blade wakes and tip vortices. Insufficient evidence is available in the literature of the importance of the structure-borne noise generated by these unsteady loads compared to the airborne noise from the propeller. The relative contribution of the structure-borne noise source can most conveniently be studied by numerical tools. This would most likely require a high-fidelity model capable of simultaneously considering the aerodynamic, aeroacoustic, and structural response of the system.

By addressing the recommendations given above, additional understanding will be obtained of the interaction effects, which may be useful in the definition of more effective performance-enhancement strategies.

12.2.2. PERFORMANCE-ENHANCEMENT STRATEGIES

Following the discussion of the interaction effects, Part IV of this thesis evaluated the potential of three performance-enhancement strategies to optimize the aerodynamic and aeroacoustic performance of the installed tip-mounted propeller. Increased understanding of the potential of these performance-enhancement strategies could be obtained by performing additional in-depth studies:

- As shown in Chapter 9, swirl-recovery vanes can be used for multiple purposes. The vanes are mostly interesting to improve propulsive performance for propellers with a high disk loading, while for installed configurations asymmetric loading on downstream surfaces can be minimized. However, the swirl-recovery vanes used

during the experiments discussed in this thesis were not fully optimized. Simultaneous optimization for aerodynamic and aeroacoustic performance would be required to exploit the full potential of swirl-recovery vanes.

- The unsteady loading on a surface immersed in a propeller slipstream can be decreased using a flow-permeable leading edge, as shown in Chapter 10. However, the design of the flow-permeable leading edge considered for that research was taken from the literature, without further optimization. The benefits of the flow-permeable insert could be maximized by optimizing it for maximum unsteady-load alleviation while minimizing the loss in time-averaged aerodynamic performance. Furthermore, additional instrumentation could be used to quantify the reduction of the unsteady surface pressures, while CFD evaluations might be valuable to study the flow in the cavity in more detail.

- The efficacy of pylon trailing-edge blowing for the minimization of interaction noise due to the wake encounter for pusher propellers was confirmed by Chapter 11, agreeing with and complementing the results published in the literature. However, application of an active control technique such as blowing requires energy, with a consequent impact on vehicle efficiency. More detailed analyses of the blowing system design combined with an analysis of energy use at airplane level would be needed to trade off the potential aeroacoustic benefits against the inherent efficiency loss. Furthermore, a study of the sensitivity of the propeller noise to the remaining nonuniformity in the blown wake would be helpful in assessing the quality of wake filling required to achieve acceptable acoustic performance.

Chapter 2 identified additional performance-enhancement strategies which could not be studied within the time frame of the research project discussed in this thesis. Therefore, unexplored areas of research remain:

- This thesis has not investigated the potential of propeller and wing design modifications to enhance aerodynamic and aeroacoustic performance. For the tractor configuration, the swirl-recovery mechanism can be maximized by simultaneous optimization of the propeller and wing designs. For the pusher configuration, propeller design optimization could be performed to maximize tip-vortex recovery and minimize unsteady loading due to nonuniform inflow caused by the wing or pylon wake. The latter approach could potentially provide an alternative to pylon blowing for alleviating the noise penalty due to the wake encounter, eliminating the need for an active control system and its associated efficiency penalty.

- An alternative means of reducing the unsteady loading due to slipstream impingement is to modify the strength of the tip vortices shed by the blades. This could be achieved by propeller tip blowing; the potential of such an approach for unsteady-load alleviation needs to be verified by dedicated experiments.

This thesis has provided detailed studies of the aerodynamic and aeroacoustic interaction effects and performance-enhancement strategies for tip-mounted propellers. Analyses of the effects at airplane level are indispensable to advance the technology readiness level of the tip-mounted configuration, and prepare for the successful application of tip-mounted propellers on future aircraft.

REFERENCES

[1] Hager, R. D., and Vrabel, D., "Advanced Turboprop Project," NASA SP-495, Jan. 1988.

[2] Rohrbach, C., and Metzger, F. B., "The Prop-Fan: A New Look in Propulsors," *11th Propulsion Conference*, AIAA Paper 1975-1208, Sept. 1975. doi:10.2514/6.1975-1208.

[3] Van Zante, D. E., "Progress in Open Rotor Research," *Encyclopedia of Aerospace Engineering*, American Cancer Society, 2015, pp. 1–17. doi:10.1002/9780470686652.eae1019.

[4] Harris, R. W., and Cuthbertson, R. D., "UDF/727 Flight Test Program," *23rd Joint Propulsion Conference*, AIAA Paper 1987-1733, June 1987. doi:10.2514/6.1987-1733.

[5] Bowles, M. D., and Dawson, V. P., "The Advanced Turboprop Project: Radical Innovation in a Conservative Environment," *From Engineering Science to Big Science: The NACA and NASA Collier Trophy Research Project Winners*, edited by P. E. Mack, NASA History Series, SP-4219, National Aeronautics and Space Administration, Washington, D.C., U.S.A., 1998, pp. 321–343.

[6] Mann, S. A. E., and Stuart, C. A., "Advanced Propulsion Through the 1990s - An Airframer's View," *21st Joint Propulsion Conference*, AIAA Paper 1985-1192, July 1985. doi:10.2514/6.1985-1192.

[7] Blythe, A. A., and Smith, P., "Prospects and Problems of Advanced Open Rotors for Commercial Aircraft," *21st Joint Propulsion Conference*, AIAA Paper 1985-1191, July 1985. doi:10.2514/6.1985-1191.

[8] Van Zante, D. E., Collier, F., Orton, A., Arif Khalid, S., Wojno, J. P., and Wood, T. H., "Progress in Open Rotor Propulsors: The FAA/GE/NASA Open Rotor Test Campaign," *The Aeronautical Journal*, Vol. 118, No. 1208, 2014, pp. 1181–1213. doi:10.1017/S0001924000009842.

[9] Arif Khalid, S., Wojno, J. P., Breeze-Stringfellow, A., Lurie, D. P., Wood, T. H., Ramakrishnan, K., and Paliath, U., "Open Rotor Designs for Low Noise and High Efficiency," *ASME Turbo Expo 2013: Turbine Technical Conference and Exposition*, ASME Paper GT2013-94736, June 2013. doi:10.1115/GT2013-94736.

[10] Negulescu, C., "Airbus AI-PX7 CROR Design Features and Aerodynamics," *SAE International Journal of Aerospace*, Vol. 6, No. 2, 2013, pp. 626–642. doi:10.4271/2013-01-2245.

[11] Stürmer, A., and Akkermans, R. A. D., "Multidisciplinary Analysis of CROR Propulsion Systems: DLR Activities in the JTI SFWA Project," *CEAS Aeronautical Journal*, Vol. 5, No. 3, 2014, pp. 265–277. doi:10.1007/s13272-014-0105-4.

[12] Guynn, M. D., Berton, J. J., Haller, W. J., Hendricks, E. S., and Tong, M. T., "Performance and Environmental Assessment of an Advanced Aircraft with Open Rotor Propulsion," NASA TM-2012-217772, Oct. 2012.

[13] Hendricks, E. S., Berton, J. J., Haller, W. J., Tong, M. T., and Guynn, M. D., "Updated Assessments of an Open Rotor Airplane Using Advanced Blade Designs," *49th Joint Propulsion Conference*, AIAA Paper 2013-3628, July 2013. doi:10.2514/6.2013-3628.

[14] Block, P. J. W., "Experimental Study of the Effects of Installation on Single- and Counter-Rotation Propeller Noise," NASA TP-2541, Apr. 1986.

[15] Magliozzi, B., Brown, P., and Parzych, D., "Acoustic Test and Analysis of a Counter-rotating Prop-Fan Model," NASA CR-179590, Oct. 1987.

[16] Shivashankara, B. N., Johnson, D. P., and Cuthbertson, R. D., "Installation Effects on Counter Rotating Propeller Noise," *13th Aeroacoustics Conference*, AIAA Paper 1990-4023, Oct. 1990. doi:10.2514/6.1990-4023.

[17] Ricouard, J., Julliard, E., Omaïs, M., Regnier, V., Parry, A. B., and Baralon, S., "Installation Effects on Contra-Rotating Open Rotor Noise," *16th AIAA/CEAS Aeroacoustics Conference*, AIAA Paper 2010-3795, June 2010. doi:10.2514/6.2010-3795.

[18] Paquet, C., Julliard, E., Genoulaz, N., Ricouard, J., and Spiegel, P., "Z08: Low-Speed Aero-Acoustic Experimental Characterization of Open Rotor Installation on Aircraft," *20th AIAA/CEAS Aeroacoustics Conference*, AIAA Paper 2014-2747, June 2014. doi:10.2514/6.2014-2747.

[19] Eret, P., Kennedy, J., Amoroso, F., Castellini, P., and Bennett, G. J., "Experimental Observations of an Installed-on-Pylon Contra-Rotating Open Rotor With Equal Blade Number in Pusher and Tractor Configuration," *International Journal of Aeroacoustics*, Vol. 15, No. 1-2, 2016, pp. 228–249. doi:10.1177/1475472X16642063.

[20] Page, M. A., Ivey, D. M., and Welge, H. R., "Ultra High Bypass Engine Applications to Commercial and Military Aircraft," *SAE Aerospace Technology Conference and Exposition*, SAE International TP-861720, Oct. 1986. doi:10.4271/861720.

[21] Goldsmith, I. M., and Bowles, J. V., "Potential Benefits for Propfan Technology on Derivatives of Future Short- to Medium-Range Transport Aircraft," *16th Joint Propulsion Conference*, AIAA Paper 1980-1090, June 1980. doi:10.2514/6.1980-1090.

[22] Friedrich, C., and Robertson, P. A., "Hybrid-Electric Propulsion for Aircraft," *Journal of Aircraft*, Vol. 52, No. 1, 2015, pp. 176–189. doi:10.2514/1.C032660.

[23] Moore, M. D., and Fredericks, B., "Misconceptions of Electric Propulsion Aircraft and their Emergent Aviation Markets," *52nd Aerospace Sciences Meeting*, AIAA Paper 2014-0535, Jan. 2014. doi:10.2514/6.2014-0535.

[24] Snyder, M. H., Jr., and Zumwalt, G. W., "Effects of Wingtip-Mounted Propellers on Wing Lift and Induced Drag," *Journal of Aircraft*, Vol. 6, No. 5, 1969, pp. 392–397. doi:10.2514/3.44076.

[25] Miranda, L. R., and Brennan, J. E., "Aerodynamic Effects of Wingtip-Mounted Propellers and Turbines," *4th Applied Aerodynamics Conference*, AIAA Paper 1986-1802, June 1986. doi:10.2514/6.1986-1802.

[26] Patterson, J. C., Jr., and Bartlett, G. R., "Evaluation of Installed Performance of a Wing-Tip-Mounted Pusher Turboprop on a Semispan Wing," NASA TP-2739, Aug. 1987.

[27] McVeigh, M. A., Grauer, W. K., and Paisley, D. J., "Rotor/Airframe Interactions on Tiltrotor Aircraft," *Journal of the American Helicopter Society*, Vol. 35, No. 3, 1990, pp. 43–51. doi:10.4050/JAHS.35.43.

[28] Stoll, A. M., Bevirt, J., Moore, M. D., Fredericks, W. J., and Borer, N. K., "Drag Reduction Through Distributed Electric Propulsion," *14th AIAA Aviation Technology, Integration, and Operations Conference*, AIAA Paper 2014-2851, June 2014. doi:10.2514/6.2014-2851.

[29] Borer, N. K., Patterson, M. D., Viken, J. K., Moore, M. D., Clarke, S., Redifer, M. E., Christie, R. J., Stoll, A. M., Dubois, A., Bevirt, J., Gibson, A. R., Foster, T. J., and Osterkamp, P. G., "Design and Performance of the NASA SCEPTOR Distributed Electric Propulsion Flight Demonstrator," *16th AIAA Aviation Technology, Integration, and Operations Conference*, AIAA Paper 2016-3920, June 2016. doi:10.2514/6.2016-3920.

[30] Wald, Q. R., "The Aerodynamics of Propellers," *Progress in Aerospace Sciences*, Vol. 42, No. 2, 2006, pp. 85–128. doi:10.1016/j.paerosci.2006.04.001.

[31] Magliozzi, B., Hanson, D. B., and Amiet, R. K., "Propeller and Propfan Noise," *Aeroacoustics of Flight Vehicles: Theory and Practice. Volume 1: Noise Sources*, edited by H. H. Hubbard, NASA Langley Research Center, Hampton, VA, U.S.A., 1991, pp. 1–64.

[32] Li, Q., Öztürk, K., Sinnige, T., Ragni, D., Wang, Y., Eitelberg, G., and Veldhuis, L. L. M., "Design and Experimental Validation of Swirl Recovery Vanes for Propeller Propulsion Systems," *AIAA Journal*, advance online publication, 2018. doi:10.2514/1.J057113.

[33] Nahuis, R., and Sinnige, T., "Design, manufacture and commissioning of a new NLR 6-component rotating shaft balance for Delft University of Technology," *10th International Symposium on Strain-Gauge Balances*, Mianyang, China, May 2016.

[34] Bass, R. M., "Small Scale Wind Tunnel Testing of Model Propellers," *24th Aerospace Sciences Meeting*, AIAA Paper 1986-0392, Jan. 1986. doi:10.2514/6.1986-392.

[35] Bass, R. M., "Techniques of Model Propeller Testing," *Business Aircraft Meeting & Exposition*, SAE International TP-830750, Apr. 1983. doi:10.4271/830750.

[36] Veldhuis, L. L. M., "Propeller Wing Aerodynamic Interference," Ph.D. thesis, Faculty of Aerospace Engineering, Delft University of Technology, Delft, The Netherlands, 2005.

[37] Ortun, B., Boisard, R., and Gonzalez-Martino, I., "Assessment of Propeller 1P Loads Predictions," *International Journal of Engineering Systems Modelling and Simulation*, Vol. 4, No. 1-2, 2012, pp. 36–46. doi:10.1504/IJESMS.2012.044842.

[38] Strack, W. C., Knip, G., Weisbrich, A. L., Godston, J., and Bradley, E., "Technology and Benefits of Aircraft Counter Rotation Propellers," NASA TM-82983, Oct. 1982.

[39] Parry, A. B., Kingan, M., and Tester, B. J., "Relative Importance of Open Rotor Tone and Broadband Noise Sources," *17th AIAA/CEAS Aeroacoustics Conference*, AIAA Paper 2011-2763, June 2011. doi:10.2514/6.2011-2763.

[40] Trebble, W. J. G., Williams, J., and Donnelly, R. P., "Comparative Acoustic Wind-Tunnel Measurements and Theoretical Correlations on Subsonic Aircraft Propellers at Full-Scale and Model-Scale," *7th Aeroacoustics Conference*, AIAA Paper 1981-2004, Oct. 1981. doi:10.2514/6.1981-2004.

[41] Prandtl, L., "Mutual Influence of Wings and Propeller," NACA TN-74, Dec. 1921.

[42] Witkowski, D. P., Lee, A. K. H., and Sullivan, J. P., "Aerodynamic Interaction Between Propellers and Wings," *Journal of Aircraft*, Vol. 26, No. 9, 1989, pp. 829–836. doi:10.2514/3.45848.

[43] Fratello, G., Favier, D., and Maresca, C., "Experimental and Numerical Study of the Propeller/Fixed Wing Interaction," *Journal of Aircraft*, Vol. 28, No. 6, 1991, pp. 365–373. doi:10.2514/3.46036.

[44] Chiaramonte, J. Y., Favier, D., Maresca, C., and Agnes, A., "Unsteady Interactional Effects Between a Propeller and a Fixed Wing," *9th Applied Aerodynamics Conference*, AIAA Paper 1991-3231, Sept. 1991. doi:10.2514/6.1991-3231.

[45] Johnston, R. T., and Sullivan, J. P., "Unsteady Wing Surface Pressures in the Wake of a Propeller," *Journal of Aircraft*, Vol. 30, No. 5, 1993, pp. 644–651. doi:10.2514/3.46393.

[46] Sinnige, T., de Vries, R., Della Corte, B., Avallone, F., Ragni, D., Eitelberg, G., and Veldhuis, L. L. M., "Unsteady Pylon Loading Caused by Propeller-Slipstream Impingement for Tip-Mounted Propellers," *Journal of Aircraft*, Vol. 55, No. 4, 2018, pp. 1605–1618. doi:10.2514/1.C034696.

[47] Ljunggren, S., Samuelsson, I., and Widing, K., "Slipstream-Induced Pressure Fluctuations on a Wing Panel," *Journal of Aircraft*, Vol. 26, No. 10, 1989, pp. 914–919. doi:10.2514/3.45861.

[48] Mukund, R., and Kumar, A. C., "Velocity Field Measurements in the Wake of a Propeller Model," *Experiments in Fluids*, Vol. 57, No. 10, 2016. doi:10.1007/s00348-016-2237-2.

[49] Miley, S. J., Howard, R. M., and Holmes, B. J., "Wing Laminar Boundary Layer in the Presence of a Propeller Slipstream," *Journal of Aircraft*, Vol. 25, No. 7, 1988, pp. 606–611. doi:10.2514/3.45630.

[50] Howard, R. M., and Miley, S. J., "Time-Dependent Boundary-Layer Response in a Propeller Slipstream," *Journal of Aircraft*, Vol. 26, No. 9, 1989, pp. 863–869. doi:10.2514/3.45852.

[51] Jonhston, J. F., and Donham, R. E., "Attenuation of Propeller-Related Vibration and Noise," *Journal of Aircraft*, Vol. 19, No. 10, 1982, pp. 858–867. doi:10.2514/3.61568.

[52] Miller, B. A., Dittmar, J. H., and Jeracki, R. J., "Propeller Tip Vortex: A Possible Contributor to Aircraft Cabin Noise," *Journal of Aircraft*, Vol. 19, No. 1, 1982, pp. 84–86. doi:10.2514/3.44747.

[53] Metcalf, V. L., and Mayes, W. H., "Structureborne Contribution to Interior Noise of Propeller Aircraft," *Business Aircraft Meeting & Exposition*, SAE International TP-830735, Apr. 1983. doi:10.4271/830735.

[54] Loeffler, I. J., "Structureborne Noise Control in Advanced Turboprop Aircraft," *25th AIAA Aerospace Sciences Meeting*, AIAA Paper 1987-0530, Mar. 1987. doi:10.2514/6.1987-530.

[55] Unruh, J. F., "Aircraft Propeller Induced Structure-Borne Noise," NASA CR-4255, Oct. 1989.

[56] Cole, J. E., III, and Martini, K. F., "Structureborne Noise Measurements on a Small Twin-Engine Aircraft," NASA CR-4137, June 1988.

[57] Junger, M. C., Garrelick, J. M., Martinez, R., and Cole III, J. E., "Analytical Model of the Structureborne Interior Noise Induced by a Propeller Wake," NASA CR-172381, May 1984.

[58] Martinez, R., "Predictions of Unsteady Wing and Pylon Forces Caused by Propeller Installation," NASA CR-178298, May 1987.

[59] Martinez, R., Cole, J. E., III, Martini, K., and Westagard, A., "All-Theoretical Prediction of Cabin Noise due to Impingement of Propeller Vortices on a Wing Structure," *11th Aeroacoustics Conference*, AIAA Paper 1987-2681, Oct. 1987. doi:10.2514/6.1987-2681.

[60] Unruh, J. F., "Prediction of Aircraft-Propeller-Induced, Structure-Borne Interior Noise," *Journal of Aircraft*, Vol. 25, No. 8, 1988, pp. 758–764. doi:10.2514/3.45655.

[61] Cole, J. E., III, Westagard Stokes, A., Garrelick, J. M., and Martini, K. F., "Analytical Modeling of the Structureborne Noise Path on a Small Twin-Engine Aircraft," NASA CR-4136, June 1988.

[62] Heidelberg, L. J., and Woodward, R. P., "Advanced Turboprop Wing Installation Effects Measured by Unsteady Blade Pressure and Noise," *11th Aeroacoustics Conference*, AIAA Paper 1987-2719, Oct. 1987. doi:10.2514/6.1987-2719.

[63] Farokhi, S., "Pressure-Time History of Pylon Wake on a Pusher Propeller in Flight," *Journal of Propulsion and Power*, Vol. 6, No. 6, 1990, pp. 758–768. doi:10.2514/3.23282.

[64] Block, P. J. W., and Gentry, G. L., Jr., "Directivity and Trends of Noise Generated by a Propeller in a Wake," NASA TP-2609, Sept. 1986.

[65] Woodward, R. P., and Hughes, C. E., "Noise of a Model Counterrotation Propeller With Simulated Fuselage and Support Pylon at Takeoff/Approach Conditions," NASA TM-101996, Apr. 1989.

[66] Magliozzi, B., "Noise Characteristics of Model Counter-Rotating Prop-Fans," *11th Aeroacoustics Conference*, AIAA Paper 1987-2656, Oct. 1987. doi:10.2514/6.1987-2656.

[67] Elliott, D. M., "Initial Investigation of the Acoustics of a Counter-Rotating Open Rotor Model With Historical Baseline Blades in a Low-Speed Wind Tunnel," NASA TM-2012-217258, Mar. 2012.

[68] Czech, M. J., and Thomas, R. H., "Open Rotor Aeroacoustic Installation Effects for Conventional and Unconventional Airframes," *19th AIAA/CEAS Aeroacoustics Conference*, AIAA Paper 2013-2185, May 2013. doi:10.2514/6.2013-2185.

[69] Gentry, G. L., Jr., Booth, E. R., Jr., and Takallu, M. A., "Effect of Pylon Wake With and Without Pylon Blowing on Propeller Thrust," NASA TM-4162, Feb. 1990.

[70] Farokhi, S., Taghavi, R., and Wetzel, K. K., "Frequency-Domain Analysis of Fluctuating Pressure on a Pusher Propeller Blade Surface," *Journal of Aircraft*, Vol. 31, No. 1, 1994, pp. 42–48. doi:10.2514/3.46453.

[71] Stürmer, A., and Yin, J., "Installation Impact on Pusher CROR Engine Low Speed Performance and Noise Emission Characteristics," *International Journal of Engineering Systems Modelling and Simulation*, Vol. 4, No. 1-2, 2012, pp. 59–68. doi:10.1504/IJESMS.2012.044844.

[72] Mauk, C. S., and Farokhi, S., "The Effect of Unsteady Blade Loading on the Aeroacoustics of a Pusher Propeller," *29th Joint Propulsion Conference & Exhibit*, AIAA Paper 1993-1805, June 1993. doi:10.2514/6.1993-1805.

[73] Patterson, J. C., Jr., and Bartlett, G. R., "Effect of a Wing-Tip Mounted Pusher Turboprop on the Aerodynamic Characteristics of a Semi-Span Wing," *21st Joint Propulsion Conference*, AIAA Paper 1985-1286, July 1985. doi:10.2514/6.1985-1286.

[74] Catalano, F. M., "On the Effects of an Installed Propeller Slipstream on Wing Aerodynamic Characteristics," *Acta Polytechnica*, Vol. 44, No. 3, 2004, pp. 8–14.

[75] Kroo, I., "Propeller-Wing Integration for Minimum Induced Loss," *Journal of Aircraft*, Vol. 23, No. 7, 1986, pp. 561–565. doi:10.2514/3.45344.

[76] Rakshith, B. R., Deshpande, S. M., Narasimha, R., and Praveen, C., "Optimal Low-Drag Wing Planforms for Tractor-Configuration Propeller-Driven Aircraft," *Journal of Aircraft*, Vol. 52, No. 6, 2015, pp. 1791–1801. doi:10.2514/1.C032997.

[77] Hoff, G. E., "Experimental Performance and Acoustic Investigation of Modern, Counterrotating Blade Concepts," NASA CR-185158, Jan. 1990.

[78] Stürmer, A., Marquez Gutierrez, C. O., Roosenboom, E. W. M., Schröder, A., Geisler, R., Pallek, D., Agocs, J., and Neitzke, K.-P., "Experimental and Numerical Investigation of a Contra Rotating Open-Rotor Flowfield," *Journal of Aircraft*, Vol. 49, No. 6, 2012, pp. 1868–1877. doi:10.2514/1.C031698.

[79] Gazzaniga, J. A., and Rose, G. E., "Wind Tunnel Performance Results of Swirl Recovery Vanes as Tested With an Advanced High Speed Propeller," *28th Joint Propulsion Conference and Exhibit*, AIAA Paper 1992-3770, July 1992. doi:10.2514/6.1992-3770.

[80] Yamamoto, O., "Numerical Calculations of Propfan/Swirl Recovery Vane Flow Field," *28th Joint Propulsion Conference and Exhibit*, AIAA Paper 1992-3771, July 1992. doi:10.2514/6.1992-3771.

[81] Wang, Y., Li, Q., Eitelberg, G., Veldhuis, L. L. M., and Kotsonis, M., "Design and Numerical Investigation of Swirl Recovery Vanes for the Fokker 29 Propeller," *Chinese Journal of Aeronautics*, Vol. 27, No. 5, 2014, pp. 1128–1136. doi:10.1016/j.cja.2014.03.009.

[82] Stokkermans, T. C. A., van Arnhem, N., and Veldhuis, L. L. M., "Mitigation of Propeller Kinetic Energy Losses With Boundary Layer Ingestion and Swirl Recovery Vanes," *Proceedings of the 2016 Applied Aerodynamics Research Conference*, Royal Aeronautical Society, London, U. K., 2016, pp. 56–69.

[83] Li, Q., Wang, Y., and Eitelberg, G., "An Investigation of Tip Vortices Unsteady Interaction for Fokker 29 Propeller With Swirl Recovery Vane," *Chinese Journal of Aeronautics*, Vol. 29, No. 1, 2016, pp. 117–128. doi:10.1016/j.cja.2015.12.004.

[84] Dring, R. P., Joslyn, H. D., Hardin, L. W., and Wagner, J. H., "Turbine Rotor-Stator Interaction," *Journal of Engineering for Power*, Vol. 104, No. 4, 1982, pp. 729–742. doi:10.1115/1.3227339.

[85] Rai, M. M., "Navier-Stokes Simulations of Rotor/Stator Interaction Using Patched and Overlaid Grids," *Journal of Propulsion and Power*, Vol. 3, No. 5, 1987, pp. 387–396. doi:10.2514/3.23003.

[86] Dittmar, J. H., and Hall, D. G., "Cruise Noise of an Advanced Propeller with Swirl Recovery Vanes," *Journal of Aircraft*, Vol. 30, No. 2, 1993, pp. 221–226. doi:10.2514/3.56885.

[87] Tinetti, A. F., "On the Use of Surface Porosity to Reduce Wake-Stator Interaction Noise," Ph.D. thesis, College of Engineering, Virginia Polytechnic Institute and State University, Blacksburg, VA, U.S.A., 2001.

[88] Tinetti, A. F., Kelly, J. J., Bauer, S. X. S., and Thomas, R. H., "On the Use of Surface Porosity to Reduce Unsteady Lift," *15th AIAA Computational Fluid Dynamics Conference*, AIAA Paper 2001-2921, June 2001. doi:10.2514/6.2001-2921.

[89] Tinetti, A. F., Kelly, J., J, Thomas, R. H., and Bauer, S. X. S., "Reduction of Wake-Stator Interaction Noise Using Passive Porosity," *40th AIAA Aerospace Sciences Meeting & Exhibit*, AIAA Paper 2002-1036, Jan. 2002. doi:10.2514/6.2002-1036.

[90] Lee, S., "Reduction of Blade-Vortex Interaction Noise Through Porous Leading Edge," *AIAA Journal*, Vol. 32, No. 3, 1994, pp. 480–488. doi:10.2514/3.12011.

[91] Vergara Torralba, C., Bilka, M., and Schram, C., "Experimental and Analytical Study of Tonal Source Attenuation in Wake-Stator Interaction with Porous Material," *14th International Symposium on Transport Phenomena and Dynamics of Rotating Machinery (ISROMAC-14)*, Feb. 2012.

[92] Raghunathan, S., "Passive Control of Shock-Boundary Layer Interaction," *Progress in Aerospace Sciences*, Vol. 25, No. 3, 1988, pp. 271–296. doi:10.1016/0376-0421(88)90002-4.

[93] Roger, M., Schram, C., and De Santana, L., "Reduction of Airfoil Turbulence-Impingement Noise by Means of Leading-Edge Serrations and/or Porous Material," *19th AIAA/CEAS Aeroacoustics Conference*, AIAA Paper 2013-2108, May 2013. doi:10.2514/6.2013-2108.

[94] Angland, D., Zhang, X., and Molin, N., "Measurements of Flow Around a Flap Side Edge with Porous Edge Treatment," *AIAA Journal*, Vol. 47, No. 7, 2009, pp. 1660–1671. doi:10.2514/1.39311.

[95] Bae, Y., and Moon, Y. J., "Effect of Passive Porous Surface on the Trailing-Edge Noise," *Physics of Fluids*, Vol. 23, No. 12, 2011. doi:10.1063/1.3662447.

[96] Geyer, T., Sarradj, E., and Fritzsche, C., "Measurement of the Noise Generation at the Trailing Edge of Porous Airfoils," *Experiments in Fluids*, Vol. 48, No. 2, 2010, pp. 291–308. doi:10.1007/s00348-009-0739-x.

[97] McAlister, K. W., Tung, C., and Heineck, J. T., "Devices that Alter the Tip Vortex of a Rotor," NASA TM-2001-209625, Feb. 2001.

[98] Mineck, R. E., "Study of Potential Aerodynamic Benefits from Spanwise Blowing at Wingtip," NASA TP-3515, June 1995.

[99] Lee, C. S., Tavella, D., Wood, N. J., and Roberts, L., "Flow Structure and Scaling Laws in Lateral Wing-Tip Blowing," *AIAA Journal*, Vol. 27, No. 8, 1989, pp. 1002–1007. doi:10.2514/3.10211.

[100] Han, Y. O., and Gordon Leishman, J., "Investigation of Helicopter Rotor-Blade-Tip-Vortex Alleviation Using a Slotted Tip," *AIAA Journal*, Vol. 42, No. 3, 2004, pp. 524–535. doi:10.2514/1.3254.

[101] Heyes, A. L., and Smith, D. A. R., "Spatial Perturbation of a Wing-Tip Vortex Using Pulsed Span-Wise Jets," *Experiments in Fluids*, Vol. 37, No. 1, 2004, pp. 120–127. doi:10.1007/s00348-004-0791-5.

[102] Duraisamy, K., and Baeder, J. D., "Numerical Simulation of the Effects of Spanwise Blowing on Tip Vortex Formation," *Journal of Aircraft*, Vol. 43, No. 4, 2006, pp. 996–1006. doi:10.2514/1.19746.

[103] Vedamanickam, S., Ragni, D., de Oliveira, G., and Veldhuis, L. L. M., "Aerodynamics of an Aircraft Propeller Model with Passive Tip Jet," *Journal of Aircraft*, Vol. 55, No. 3, 2018, pp. 1276–1286. doi:10.2514/1.C034588.

[104] Jindal, A., Sinnige, T., Hulshoff, S. J., and Veldhuis, L. L. M., "Numerical Analysis of Pylon-Blowing Systems for Pusher-Propeller Applications," *35th AIAA Applied Aerodynamics Conference*, AIAA Paper 2017-3908, June 2017. doi:10.2514/6.2017-3908.

[105] Stürmer, A., and Yin, J., "Pylon Trailing Edge Blowing for the Control of CROR Unsteady Blade Loads," *New Results in Numerical and Experimental Fluid Mechanics VIII*, Notes on Numerical Fluid Mechanics and Multidisciplinary Design, Vol. 121, edited by A. Dillmann, G. Heller, H.-P. Kreplin, W. Nitsche, and I. Peltzer, Springer-Verlag, Berlin Heidelberg, Germany, 2013, pp. 715–722. doi:10.1007/978-3-642-35680-3.

[106] Fernando, R., and Leroux, M., "Open-Rotor Low Speed Aero-Acoustics: Wind Tunnel Characterization of an Advanced Blade Design in Isolated and Installed Configurations," *20th AIAA/CEAS Aeroacoustics Conference*, AIAA Paper 2014-2749, June 2014. doi:10.2514/6.2014-2749.

[107] Ben Nasr, N., Rodriguez, B., Chelius, A., and Canard-Caruana, S., "Blowing Strategies of Pylon-Propeller Configuration for Noise Reduction using Numerical Approach," *6th AIAA Flow Control Conference*, AIAA Paper 2012-2658, June 2012. doi:10.2514/6.2012-2658.

[108] Bury, Y., Bordron, A., Belloc, H., and Prat, D., "CROR-Powerplant Pylon Wake Mitigation for Noise Reduction Through Innovative Blowing/Suction-Based Active Flow Control System," *34th AIAA Applied Aerodynamics Conference*, AIAA Paper 2016-3116, June 2016. doi:10.2514/6.2016-3116.

[109] Colin, Y., Carazo, A., Caruelle, B., Nodé-Langlois, T., and Parry, A. B., "Computational Strategy for Predicting CROR Noise at Low-Speed Part I: Review of the Numerical Methods," *18th AIAA/CEAS Aeroacoustics Conference*, AIAA Paper 2012-2221, June 2012. doi:10.2514/6.2012-2221.

[110] Dunn, M. H., and Tinetti, A. F., "Advanced Time Domain Noise Prediction Methods for Open Rotors and Installation Effects," *18th AIAA/CEAS Aeroacoustics Conference*, AIAA Paper 2012-2217, June 2012. doi:10.2514/6.2012-2217.

[111] Gérard, A., Berry, A., Masson, P., and Gervais, Y., "Evaluation of Tonal Aeroacoustic Sources in Subsonic Fans Using Inverse Models," *AIAA Journal*, Vol. 45, No. 1, 2007, pp. 98–109. doi:10.2514/1.21957.

[112] Sears, W. R., "Some Aspects of Non-Stationary Airfoil Theory and Its Practical Application," *Journal of the Aeronautical Sciences*, Vol. 8, No. 3, 1941, pp. 104–108. doi:10.2514/8.10655.

[113] Sears, W. R., "A Systematic Presentation of the Theory of Thin Airfoils in Non-Uniform Motion," Ph.D. thesis, California Institute of Technology, Pasadena, CA, U.S.A., 1938.

[114] Amiet, R. K., "Compressibility Effects in Unsteady Thin-Airfoil Theory," *AIAA Journal*, Vol. 12, No. 2, 1974, pp. 252–255. doi:10.2514/3.49212.

[115] Sinnige, T., van Arnhem, N., Stokkermans, T. C. A., Eitelberg, G., and Veldhuis, L. L. M., "Wingtip-Mounted Propellers: Aerodynamic Analysis of Interaction Effects and Comparison with Conventional Layout," *Journal of Aircraft*, in press, 2018.

[116] Ragni, D., "PIV-Based Load Determination in Aircraft Propellers," Ph.D. thesis, Faculty of Aerospace Engineering, Delft University of Technology, Delft, The Netherlands, 2012.

[117] Yang, Y., Sciacchitano, A., Veldhuis, L. L. M., and Eitelberg, G., "Analysis of Propeller-Induced Ground Vortices by Particle Image Velocimetry," *Journal of Visualization*, Vol. 21, No. 1, 2018, pp. 39–55. doi:10.1007/s12650-017-0439-1.

[118] Scarano, F., and Riethmuller, M. L., "Iterative Multigrid Approach in PIV Image Processing with Discrete Window Offset," *Experiments in Fluids*, Vol. 26, No. 6, 1999, pp. 513–523. doi:10.1007/s003480050318.

[119] Wieneke, B., "PIV Uncertainty Quantification From Correlation Statistics," *Measurement Science and Technology*, Vol. 26, No. 7, 2015. doi:10.1088/0957-0233/26/7/074002.

[120] Chue, S. H., "Pressure Probes for Fluid Measurement," *Progress in Aerospace Sciences*, Vol. 16, No. 2, 1975, pp. 147–223. doi:10.1016/0376-0421(75)90014-7.

[121] Loving, D. L., and Katzoff, S., "The Fluorescent-Oil Film Method and Other Techniques for Boundary-Layer Flow Visualization," NASA MEMO-3-17-59L, Mar. 1959.

[122] Sinnige, T., Della Corte, B., de Vries, R., Avallone, F., Merino-Martínez, R., Ragni, D., Eitelberg, G., and Veldhuis, L. L. M., "Alleviation of Propeller-Slipstream-Induced Unsteady Pylon Loading by a Flow-Permeable Leading Edge," *manuscript submitted*, 2018.

[123] Ragni, D., Simão Ferreira, C., and Correale, G., "Experimental Investigation of an Optimized Airfoil for Vertical-Axis Wind Turbines," *Wind Energy*, Vol. 18, No. 9, 2015, pp. 1629–1643. doi:10.1002/we.1780.

[124] van Oudheusden, B. W., "PIV-based pressure measurement," *Measurement Science and Technology*, Vol. 24, No. 3, 2013. doi:10.1088/0957-0233/24/3/032001.

[125] Ragni, D., van Oudheusden, B. W., and Scarano, F., "3D Pressure Imaging of an Aircraft Propeller Blade-Tip Flow by Phase-Locked Stereoscopic PIV," *Experiments in Fluids*, Vol. 52, No. 2, 2012, pp. 463–477. doi:10.1007/s00348-011-1236-6.

[126] Abbott, I. H., Von Doenhoff, A. E., and Stivers, L., Jr., "Summary of Airfoil Data," NACA TR-824, Jan. 1945.

[127] Brandt, A., *Statistics and Random Processes*, 2nd ed., Noise and Vibration Analysis: Signal Analysis and Experimental Procedures, Wiley, New York, NY, U.S.A., 2011, pp. 65–71.

[128] Dougherty, R. P., "Beamforming In Acoustic Testing," *Aeroacoustic Measurements*, edited by T. Mueller, Springer-Verlag, Berlin Heidelberg, Germany, 2002, pp. 62–97.

[129] Sijtsma, P., "Phased Array Beamforming Applied to Wind Tunnel and Flyover Tests," NLR TP-2010-549, Dec. 2010.

[130] Arce León, C., Merino-Martínez, R., Ragni, D., Avallone, F., and Snellen, M., "Boundary Layer Characterization and Acoustic Measurements of Flow-Aligned Trailing Edge Serrations," *Experiments in Fluids*, Vol. 57, No. 12, 2010. doi:10.1007/s00348-016-2272-z.

[131] Lord Rayleigh, F. R. S., "XXXI. Investigations in Optics with Special Reference to the Spectroscope," *The London, Edinburgh and Dublin Philosophical Magazine and Journal of Science*, Vol. 8, No. 49, 1879, pp. 261–274. doi:10.1080/14786447908639684.

[132] Sinnige, T., Ragni, D., Malgoezar, A. M. N., Eitelberg, G., and Veldhuis, L. L. M., "APIAN-INF: An Aerodynamic and Aeroacoustic Investigation of Pylon-Interaction Effects for Pusher Propellers," *CEAS Aeronautical Journal*, Vol. 9, No. 2, 2018, pp. 291–306. doi:10.1007/s13272-017-0247-2.

[133] Sinnige, T., Ragni, D., Eitelberg, G., and Veldhuis, L. L. M., "Mitigation of Pusher-Propeller Installation Effects by Pylon Trailing-Edge Blowing," *Journal of Aircraft*, Vol. 54, No. 1, 2017, pp. 292–300. doi:10.2514/1.C034000.

[134] Sinnige, T., Stokkermans, T. C. A., Ragni, D., Eitelberg, G., and Veldhuis, L. L. M., "Aerodynamic and Aeroacoustic Performance of a Propeller Propulsion System with Swirl-Recovery Vanes," *Journal of Propulsion and Power*, advance online publication, 2018. doi:10.2514/1.B36877.

[135] Crozier, P., "APIAN Installed Tests in the ONERA S1MA Wind Tunnel," *39th Aerospace Sciences Meeting & Exhibit*, AIAA Paper 2001-0580, 2001. doi:10.2514/6.2001-580.

[136] Frota, J., and Maury, E., "Analysis of APIAN High Speed Isolated Test Results – Acoustics and Aerodynamics," *Air & Space Europe*, Vol. 3, No. 3–4, 2001, pp. 87–92. doi:10.1016/S1290-0958(01)90064-4.

[137] Philipsen, I., Hoeijmakers, H., and Hegen, S., "An Overview of Advanced Propeller Simulation Tests in the German Dutch Wind Tunnels (DNW)," *22nd AIAA Aerodynamic Measurement Technology and Ground Testing Conference*, AIAA Paper 2002-2920, June 2002. doi:10.2514/6.2002-2920.

[138] Drela, M., and Youngren, H., "XROTOR Download Page," online, 2011. URL `http://web.mit.edu/drela/Public/web/xrotor/`, retrieved 28 November 2013.

[139] Bret, J. F., Leconte, P., Vieira, J. P., Fetet, T., and Séchaud, J. F., "Rotating Shaft Balances for CRORs and Propellers," *53rd AIAA Aerospace Sciences Meeting*, AIAA Paper 2015-1790, Jan. 2015. doi:10.2514/6.2015-1790.

[140] Welch, P. D., "The Use of Fast Fourier Transform for the Estimation of Power Spectra: A Method Based on Time Averaging Over Short, Modified Periodograms," *IEEE Transactions on Audio and Electroacoustics*, Vol. 15, No. 2, 1967, pp. 70–73. doi:10.1109/TAU.1967.1161901.

[141] Stokkermans, T. C. A., van Arnhem, N., Sinnige, T., and Veldhuis, L. L. M., "Validation and Comparison of RANS Propeller Modeling Methods for Tip-Mounted Applications," *2018 AIAA Aerospace Sciences Meeting*, AIAA Paper 2018-0542, Jan. 2018. doi:10.2514/6.2018-0542.

[142] van Arnhem, N., Sinnige, T., Stokkermans, T. C. A., Eitelberg, G., and Veldhuis, L. L. M., "Aerodynamic Interaction Effects of Tip-Mounted Propellers Installed on the Horizontal Tailplane," *2018 AIAA Aerospace Sciences Meeting*, AIAA Paper 2018-2052, Jan. 2018. doi:10.2514/6.2018-2052.

[143] Samuelsson, I., "Experimental Investigation of Low Speed Model Propeller Slipstream Aerodynamic Characteristics Including Flow Field Surveys and Nacelle/Wing Static Pressure Measurements," *Proceedings of the 17th International Congress of the Aeronautical Sciences*, Stockholm, Sweden, Sept. 1990, pp. 71–84.

[144] Thom, A. D., "Analysis of Vortex-Lifting Surface Interactions," Ph.D. thesis, College of Science and Engineering, University of Glasgow, Glasgow, United Kingdom, 2011.

[145] Felli, M., Roberto, C., and Guj, G., "Experimental Analysis of the Flow Field Around a Propeller–Rudder Configuration," *Experiments in Fluids*, Vol. 46, No. 1, 2009, pp. 147–164. doi:10.1007/s00348-008-0550-0.

[146] Fleming, J. L., Simpson, R. L., Cowling, J. E., and Devenport, W. J., "An Experimental Study of a Turbulent Wing-Body Junction and Wake Flow," *Experiments in Fluids*, Vol. 14, No. 5, 1993, pp. 366–378. doi:10.1007/BF00189496.

[147] Gand, F., Deck, S., Brunet, V., and Sagaut, P., "Flow Dynamics Past a Simplified Wing Body Junction," *Physics of Fluids*, Vol. 22, No. 11, 2010. doi:10.1063/1.3500697.

[148] Bodstein, G. C. R., George, A. R., and Hui, C.-Y., "The Three-Dimensional Interaction of a Streamwise Vortex With a Large-Chord Lifting Surface: Theory and Experiment," *Journal of Fluid Mechanics*, Vol. 322, 1996, pp. 51–79. doi:10.1017/S0022112096002704.

[149] Romano, G. P., "Analysis of Two-Point Velocity Measurements in Near-Wall Flows," *Experiments in Fluids*, Vol. 20, No. 2, 1995, pp. 68–83. doi:10.1007/BF00189296.

[150] Liu, X., Thomas, F. O., and Nelson, R. C., "An Experimental Investigation of the Planar Turbulent Wake in Constant Pressure Gradient," *Physics of Fluids*, Vol. 14, No. 8, 2002, pp. 2817–2838. doi:10.1063/1.1490349.

[151] Hanson, D. B., "Sound From a Propeller at Angle of Attack: A New Theoretical Viewpoint," *Proceedings of the Royal Society A: Mathematical, Physical and Engineering Sciences*, Vol. 449, No. 1936, 1995, pp. 315–328. doi:10.1098/rspa.1995.0046.

[152] Akkermans, R. A. D., Stürmer, A., and Delfs, J. W., "Active Flow Control for Interaction Noise Reduction of Contra-Rotating Open Rotors," *AIAA Journal*, Vol. 54, No. 4, 2016, pp. 1413–1423. doi:10.2514/1.J053756.

[153] Wo, A. M., Lo, A. C., and Chang, W. C., "Flow Control via Rotor Trailing Edge Blowing in Rotor/Stator Axial Compressor," *Journal of Propulsion and Power*, Vol. 18, No. 1, 2002, pp. 93–99. doi:10.2514/2.5902.

[154] Avallone, F., Casalino, D., and Ragni, D., "Impingement of a Propeller Slipstream on a Leading Edge With a Flow-Permeable Insert: A Computational Aeroacoustic Study," *International Journal of Aeroacoustics*, advance online publication, 2018. doi:10.1177/1475472X18788961.

[155] Abbott, I. H., and von Doenhoff, A. E., *Theory of Wing Sections: Including a Summary of Airfoil Data*, Dover Publications Inc., New York, NY, U.S.A., 1959.

[156] Mineck, R. E., and Hartwich, P. M., "Effect of Full-Chord Porosity on Aerodynamic Characteristics of the NACA 0012 Airfoil," NASA TP-3591, Apr. 1996.

[157] Sinnige, T., Ragni, D., Eitelberg, G., and Veldhuis, L. L. M., "Pusher-Propeller Installation Effects in Angular Inflow," *22nd AIAA/CEAS Aeroacoustics Conference*, AIAA Paper 2016-2875, May 2016. doi:10.2514/6.2016-2875.

[158] ANSYS, Inc., "Help System ANSYS® Academic Research Release 15.0, Fluent," software, 2014.

[159] Nakayama, A., "Characteristics of the Flow Around Conventional and Supercritical Airfoils," *Journal of Fluid Mechanics*, Vol. 160, 1985, pp. 155–179. doi:10.1017/S0022112085003433.

VI

Appendices

A

PYLON CHORDWISE BLOWING

The trailing-edge blowing technique discussed in Chapter 11 proved successful in alleviating the noise penalty due to the wake encounter that occurs for pusher propellers. However, the chapter also showed that a further improvement of the wake uniformity is needed to eliminate the noise penalty at low propeller thrust setting and at nonzero angle of attack. Both these issues can be solved by using a chordwise blowing system, which features a blowing slot positioned along the chord on both the upper and lower side of the pylon. This chapter discusses the sensitivity of the wake uniformity obtained with such a chordwise blowing system to the slot position, the slot height, and the blowing coefficient, and compares the resulting wake characteristics to those obtained with trailing-edge blowing. Also, the performance at nonzero angle of attack is evaluated. In contrast to the work presented in the body of this thesis, a numerical approach was taken, since this allowed for a faster parameter study in which the geometry of the blowing system was varied systematically. The propeller response was not considered in the analyses. The results provide novel insight into the working principles of chordwise blowing, complementing previous work which confirmed that chordwise blowing leads to a more uniform wake than trailing-edge blowing. The setup of the CFD simulations is introduced in Section A.1. By comparing the downstream wake uniformity for a range of blowing slot parameters, Section A.2 then illustrates the sensitivity of the wake flowfield to the layout of the blowing system. Thereafter, Section A.3 discusses the robustness of the chordwise blowing system under asymmetric inflow conditions. Finally, the key findings are stated in Section A.4.

A.1. COMPUTATIONAL SETUP

The flow around a two-dimensional pylon profile with a chordwise blowing system was investigated numerically, with the goal of finding the optimal design for mitigating the velocity deficit in the downstream wake. In this case, the choice was made for computations instead of experiments since this allowed for various geometry modifications (slot location, slot height) without the need for a large number of wind-tunnel models.

The contents of this chapter have been adapted from Ref. [104].

A.1.1. GEOMETRY

A symmetric NACA 0010 airfoil was modified to incorporate chordwise blowing slots on both upper and lower surfaces, as shown in Fig. A.1. The blowing slots were introduced by an inward displacement of the profile downstream of the blowing slot. The magnitude of the vertical shift was based on the selected blowing-slot height. The combination of chord length and operating conditions was chosen such that the chordwise Reynolds number was $Re_c = 1.9 \cdot 10^6$. The numerical results were validated using different geometries and operating conditions, imposed by those considered in the experiments from which data were available. The details are discussed in Ref. [104] for the chordwise and trailing-edge blowing configurations separately.

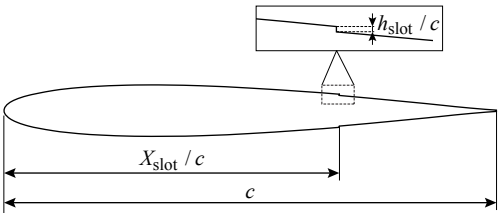

Figure A.1: Considered layout of airfoil with chordwise blowing system.

A.1.2. MODELING

The flowfield around the pylon was simulated by solving the Reynolds-averaged Navier–Stokes equations using ANSYS® Fluent release 15.0 [158]. Steady-state simulations were performed, in which the pylon boundary layer was considered as fully turbulent. A number of turbulence models were tested for their predictive capability of the pylon-wake flow, using experimental data measured by Nakayama [159]. The numerical data computed using the different turbulence models were compared to the experimental results in terms of the wake width, wake area, and maximum deficit in the wake at $X/c = 1.01$. The Spalart–Allmaras turbulence model resulted in the smallest offset from the experimental data by Nakayama, and was therefore selected for all subsequent computations.

The solutions were obtained using a pressure-based solver with a segregated algorithm. The interpolation procedures for momentum and eddy viscosity were carried out with a second-order upwind scheme, while a least-squares cell-based approach was used to calculate the gradients of scalar variables. The coupling of pressure and velocity was done with the SIMPLEC (Semi-Implicit Method for Pressure-Linked Equations-Consistent) algorithm, while the pressure interpolation was performed with a second-order scheme. The solution was initialized from the inlet boundary condition to start the iterative process used to reach a converged solution. Convergence of the numerical solution was monitored using the integral of the velocity magnitude in the pylon wake.

The flow domain and the respective boundary conditions used for the simulations are shown in Fig. A.2. Velocity inlet and pressure outlet ($p = p_{atm}$) boundary conditions were prescribed on the inlet and outlet boundaries. For symmetric inflow conditions ($\alpha = 0$ deg), the upper and lower walls were treated as slip walls. As discussed below, it was verified that the walls were sufficiently far away from the airfoil to model the velocity perturbations on them as zero. In case of asymmetric inflow ($\alpha \neq 0$ deg), the upper

and lower boundaries were treated as velocity inlets. The airfoil model was defined as solid wall, while the outflow from the blowing slots was specified using velocity-inlet boundary conditions, defined in the direction normal to the slot outlet. This means that the flow from the slots was uniform, whereas in practice the boundary layer inside the blowing system will play a role with respect to the occurrence of vorticity and the mixing process. Such effects are ignored in the present study.

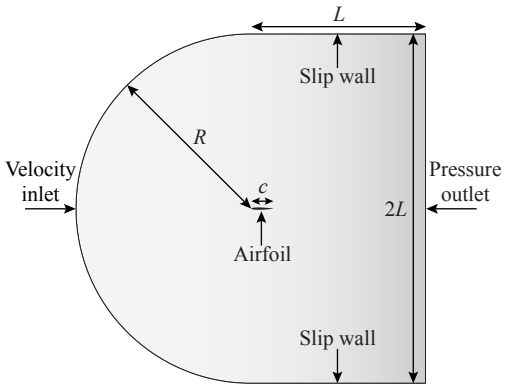

Figure A.2: Flow domain and boundary conditions for the simulations with symmetric inflow conditions.

Five domains of increasing size ($R/c = L/c = 20, 40, 100, 200, 500$) were tested on a baseline airfoil case without blowing to select the smallest domain for which the solution was found to be independent of the domain size. This was assessed by extracting velocity profiles in the pylon wake at $X/c = 1.01$, and investigating the wake width, area, and maximum deficit for the five domain sizes. The corresponding results are depicted in Fig. A.3, in which the data are normalized with the values obtained for the largest domain. It can be seen that from a domain size of $R/c = L/c = 40$ onward, the results were within approximately 1% of the data computed with the largest domain. Therefore, this domain size was considered adequate and was selected for all subsequent simulations.

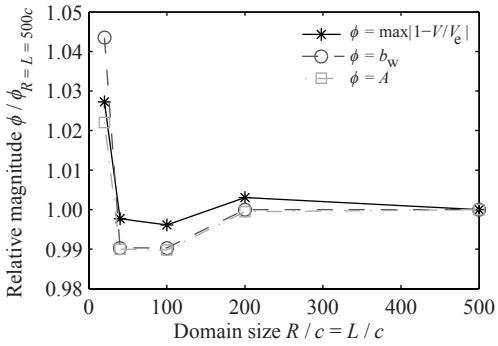

Figure A.3: Domain dependence of the maximum velocity deficit, wake width, and integral deficit in the wake.

A structured multiblock C-mesh was generated for the domain around the airfoil. Refinements were applied to capture the flow physics downstream of the blowing slots and in the wake region. The normal spacing at the first cell adjacent to the airfoil surface was chosen to lie at $y^+ \leq 1$, inside the viscous sublayer of the developed boundary layer. Appropriate regions of refinement were determined from the results of the mesh-convergence study described in Ref. [104]. The final mesh used for the chordwise blowing layout featured a y^+ value of 0.25 and consisted of about $3.5 \cdot 10^5$ quadrilateral elements. It is shown in Fig. A.4.

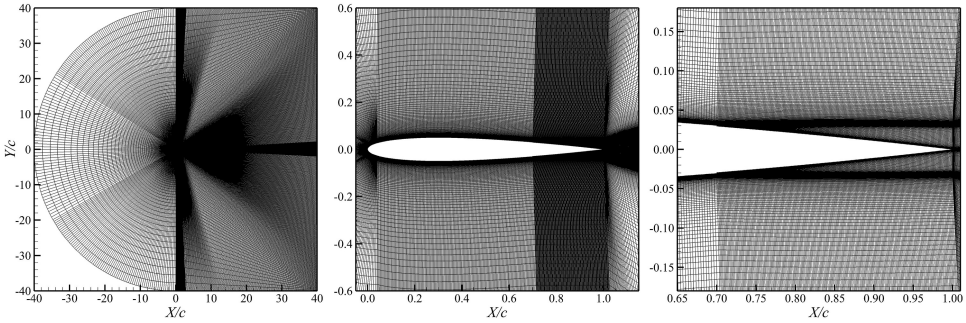

Figure A.4: Visualization of the final mesh used for the simulations of the chordwise blowing layout.

A.1.3. TEST CASES

The objective of the blowing-system design was to minimize the nonuniformity of the pylon wake. The optimization was performed following an exhaustive-search approach, involving three design variables:

1. **Chordwise location of blowing slots:** the chordwise location of the slots X_{slot}/c drives the uniformity of the blown wake. By moving the slots upstream, the distance available for the blown jets to mix with the external flow can be increased, at the cost of additional momentum deficit generated downstream of the slots.

2. **Slot height:** the slot height h_{slot}/c was considered as the most important geometrical characteristic of the blowing slot itself. For a given outflow momentum, the slot height affects the velocity of the blown jet.

3. **Slot blowing coefficient:** the slot blowing coefficient C_μ is a measure of the momentum of the air blown into the pylon wake. For an incompressible flow with equal densities of the freestream and blown air, C_μ is defined as:

$$C_\mu = 2\frac{h_{\text{slot}}}{c}\frac{V_{\text{j}}^2}{V_\infty^2}. \tag{A.1}$$

   Note that the blowing coefficient defined by Eq. A.1 is different from the one used in the study of trailing-edge blowing discussed in Chapter 11 (see Eq. 5.1). In that case, the jet velocity at the slot outlet was unknown, and thus an alternative definition was used.

The distinct levels considered for the design variables are listed in Table A.1. A relatively large number of different blowing coefficients was analyzed to account for the sensitivity of the blown wake profiles to the blowing rate. Note that the values of the blowing coefficient are defined per slot. The wake uniformity was evaluated along lines at three different axial positions in the pylon wake, as illustrated in Fig. A.5. These positions were selected to span the typical range of pylon–propeller spacings observed for pusher-propeller configurations. Table A.2 provides a complete overview of the flow conditions considered in the design study. The optimization was performed for symmetric inflow only. The optimized configuration was then used to perform analyses with asymmetric inflow conditions, as discussed in Section A.3.

Table A.1: Considered values of the design variables.

X_{slot}/c	h_{slot}/c	C_μ		
0.6	$5.0\cdot10^{-4}$	0.0000	0.0087	0.0128
0.7	$7.5\cdot10^{-4}$	0.0009	0.0094	0.0130
0.8	$1.0\cdot10^{-3}$	0.0020	0.0102	0.0132
0.9		0.0036	0.0109	0.0134
		0.0056	0.0117	0.0138
		0.0068	0.0121	0.0142
		0.0080	0.0126	

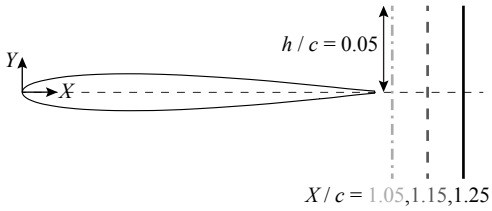

Figure A.5: Locations of the wake survey planes used in the design study.

Table A.2: Flow conditions considered in the optimization study.

Parameter	**Symbol**	**Value**
Angle of attack	α	0 deg
Freestream velocity	V_∞	30 m/s
Atmospheric pressure	p_{atm}	101,325 Pa
Density	ρ_∞	1.1835 kg/m^3
Dynamic viscosity	μ_∞	$1.848\cdot10^{-5}$ kg/(m·s)
Reynolds number	Re_c	$1.9\cdot10^6$

A

A.1.4. QUANTIFICATION OF WAKE UNIFORMITY

The response of the propeller with the pylon installed is a function of both the integral velocity deficit and the maximum velocity perturbation in the wake. To quantify the uniformity of the blown pylon wake, an integral criterion was therefore defined that includes both the total area of the velocity deficit as well as the maximum relative velocity deficit or overshoot in the wake. The resulting parameter is referred to as the W-criterion, and was defined as:

$$W = A \cdot \max\left|1 - \frac{V}{V_e}\right|, \tag{A.2}$$

with an integral wake velocity deficit A defined as:

$$A = \int_{-b_w/c}^{+b_w/c} \left|1 - \frac{V}{V_e}\right| \mathrm{d}\frac{Y}{c}. \tag{A.3}$$

The semiwidth of the wake b_w/c was taken as the distance between the wake center and the vertical position Y/c at which the nondimensional velocity gradient was larger than 0.1 for the first time, starting from outside of the wake. This is illustrated in Fig. A.6.

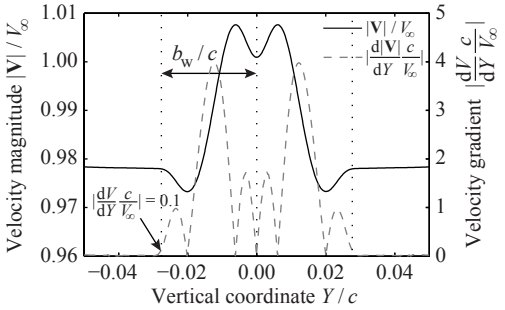

Figure A.6: Determination of the wake semiwidth for an example blown wake profile.

A.2. WAKE UNIFORMITY IN SYMMETRIC INFLOW

A.2.1. EFFECT OF CHORDWISE SLOT LOCATION

Simulations were performed for each combination of the values of the design variables given in Table A.1. Initially, the effect of the chordwise slot location and blowing coefficient were determined with the slot height fixed at $h_{slot}/c = 1.0 \cdot 10^{-3}$. Figure A.7 shows the response surface of the W-criterion (Eq. A.2) as extracted from the wake plane at $X/c = 1.25$ as a function of chordwise slot location and blowing momentum coefficient.

It can be seen in Fig. A.7 that optimal wake filling (minimum value of W) occurred for a slot located at $X_{slot}/c = 0.7$ and a blowing momentum coefficient of around $C_\mu = 0.0130$. At lower blowing coefficients ($C_\mu \leq 0.010$), the blown jets were not sufficiently strong to overcome the momentum deficit of the boundary layer upstream and downstream of the slots, resulting in a type-A velocity profile (Fig. 2.18). For these cases, the wake uniformity improved by moving the slot toward the pylon trailing edge. At higher

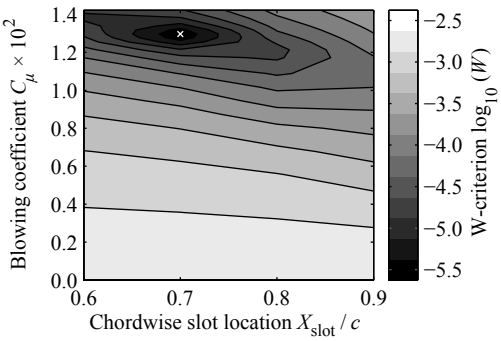

Figure A.7: Wake uniformity versus chordwise slot location and blowing coefficient; $X/c = 1.25$, $h_{slot}/c = 1.0 \cdot 10^{-3}$.

blowing settings, on the other hand, a downstream slot location provided insufficient distance for the blown jets to mix with the external flow and the wake profile to become uniform, leading to a type-C velocity profile (Fig. 2.18). Therefore, the most favorable chordwise slot location was shifted upstream, until the optimum was reached at $X_{slot}/c = 0.7$ with a blowing momentum coefficient of $C_\mu = 0.0130$.

The development of the pylon wake in the streamwise direction is important for the selection of the optimal pylon–propeller spacing for pusher-propeller configurations. Therefore, the wake characteristics were also extracted at $X/c = 1.05$ and $X/c = 1.15$. Figure A.8 presents the sensitivity of the wake uniformity to the axial position in the pylon wake. The best performing slot parameters and the resulting minimum value of the W-criterion at the three axial positions are summarized in Table A.3. Further optimization work with more sophisticated methods could refine the optima obtained with the exhaustive-search approach taken in this chapter.

Table A.3: Maximum wake uniformity versus axial distance from the pylon trailing edge; $h_{slot}/c = 1.0 \cdot 10^{-3}$.

X/c	X^*_{slot}/c	C^*_μ	$\log_{10}(W^*)$	$\frac{W^* - W_{C_\mu=0}}{W_{C_\mu=0}}$
1.05	0.8	0.0121	−4.12	−97.7%
1.15	0.7	0.0130	−5.04	−99.5%
1.25	0.7	0.0130	−5.57	−99.8%

Figure A.8 and Table A.3 show that the wake uniformity improves with increasing distance from the trailing edge of the pylon. This is as expected considering the associated increase in length available for the blowing jets to mix with the freestream flow. Close to the pylon trailing edge, the sensitivity of the wake uniformity to the axial position X/c is stronger than further downstream. This can be seen in Fig. A.8 and Table A.3 by noting that the decrease of the value of the W-criterion upon moving from location $X/c = 1.05$ to $X/c = 1.15$ is larger than when going from $X/c = 1.15$ to $X/c = 1.25$. At the most downstream wake plane considered ($X/c = 1.25$), a maximum improvement of the wake uniformity of 99.8% was achieved compared to the unblown result.

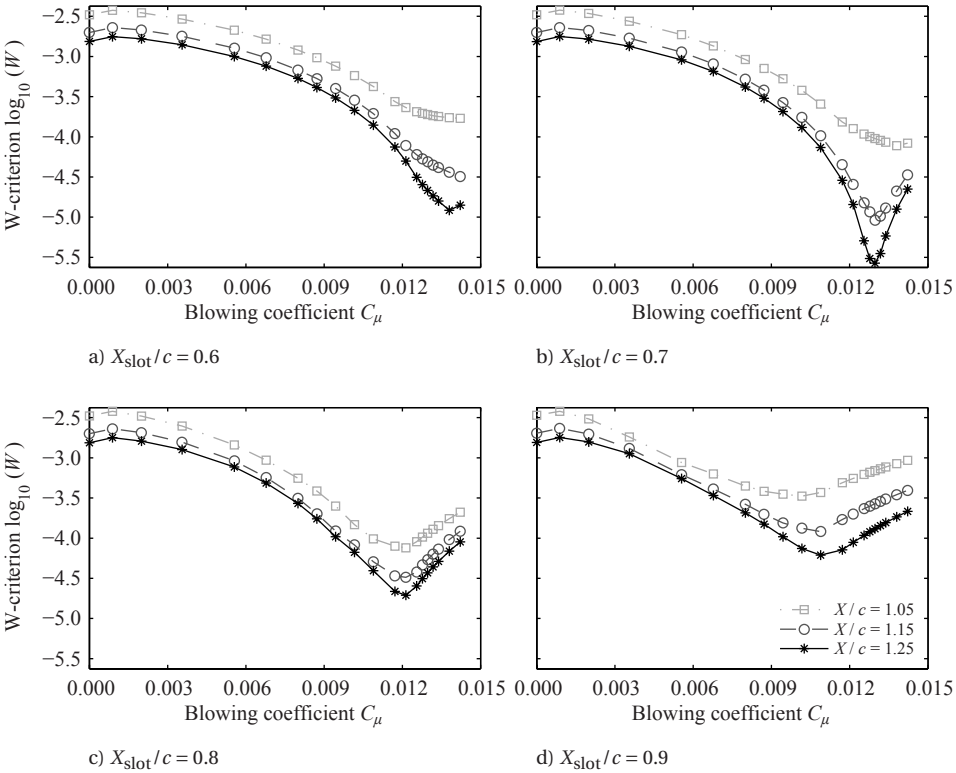

a) $X_{\text{slot}}/c = 0.6$ b) $X_{\text{slot}}/c = 0.7$

c) $X_{\text{slot}}/c = 0.8$ d) $X_{\text{slot}}/c = 0.9$

Figure A.8: Sensitivity of wake uniformity to axial position in the pylon wake; $h_{\text{slot}}/c = 1.0 \cdot 10^{-3}$.

From Fig. A.8 it can be concluded that the optimal blowing coefficient decreases upon moving the slot closer to the trailing edge of the pylon, at all axial evaluation planes considered. For slots located close to the trailing edge, the distance available for the blown jets to mix with the external flow is relatively short, resulting in a type-C velocity profile (Fig. 2.18) with a pronounced overshoot in the velocity profile caused by the blowing jets. By reducing the blowing coefficient, this overshoot is minimized and thereby the wake uniformity improved. However, because of the reduced blowing rate the momentum deficit associated with the boundary layer upstream of the blowing slots is compensated less effectively. Therefore, the resulting wake is less uniform than for a configuration with the blowing slots positioned more upstream.

The sensitivity of the wake uniformity to the blowing coefficient, shown in Fig. A.8, confirms the previous conclusions drawn based on Fig. A.7. The wake uniformity initially improves with increasing blowing coefficient, until an optimum is reached after which the uniformity decreases again upon further increasing the blowing rate. This is clearly visible in the velocity distributions in the pylon wake, which are plotted in Fig. A.9 for a blowing slot location of $X_{\text{slot}}/c = 0.7$. At the best of the considered blowing coefficients ($C_\mu = 0.0130$), the velocity throughout the entire pylon wake is within 1% of the local velocity outside of the wake. For this case, the shape of the velocity profile

corresponds to the type-B profile shown in Fig. 2.18. The change in wake uniformity around the optimum value of the blowing coefficient is relatively steep, highlighting the sensitivity of the wake uniformity to the blowing coefficient.

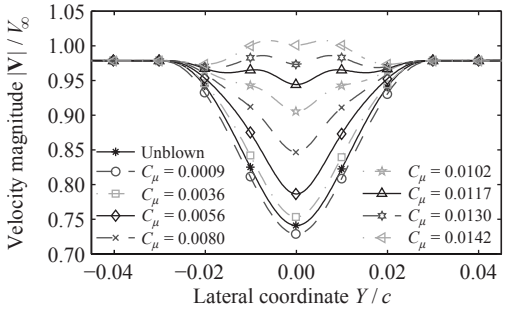

Figure A.9: Velocity profiles in the pylon wake; $X/c = 1.25$, $X_{\text{slot}}/c = 0.7$, $h_{\text{slot}}/c = 1.0 \cdot 10^{-3}$.

To investigate the relation between the velocity distribution in the wake and the boundary layer of the pylon, the velocity profiles along vertical lines normal to the airfoil are plotted in Fig. A.10. Three different chordwise positions are considered, all on the aft part of the pylon. For comparison reasons, the results obtained at blowing coefficients below ($C_\mu = 0.0109$) and above ($C_\mu = 0.0142$) the optimal value are also included.

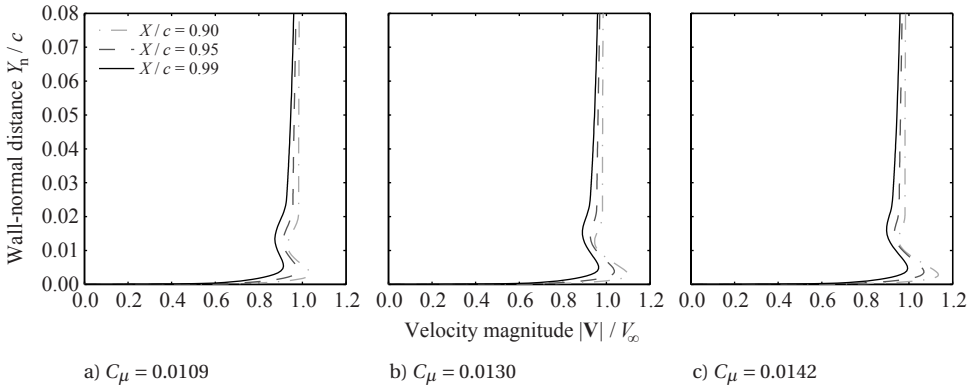

a) $C_\mu = 0.0109$ b) $C_\mu = 0.0130$ c) $C_\mu = 0.0142$

Figure A.10: Velocity profiles in the blown pylon boundary layer; $X_{\text{slot}}/c = 0.7$, $h_{\text{slot}}/c = 1.0 \cdot 10^{-3}$.

The boundary-layer profiles given in Fig. A.10 show that the blowing jet accelerates the flow near the wall, leading to a local velocity overshoot. Away from the surface, the momentum deficit of the boundary layer formed upstream of the blowing slot is visible, causing a velocity deficit. The velocity deficit and overshoot should mix to end up with a uniform wake profile. This is illustrated in Fig. A.11, which displays the boundary-layer profiles and resulting wake-velocity distribution at the lowest and highest blowing coefficients considered in Fig. A.10. The unblown case is also included. It can be seen that the central minimum in the wake profile is the result of the velocity deficit caused by the development of the boundary layers downstream of the blowing slot. The two maxima,

on the other hand, are the result of the extra momentum blown from the slots on both surfaces of the pylon. Finally, the two velocity minima near the wake edges are due to the remainder of the thick boundary layer that develops on the pylon surface upstream of the blowing slots. This part of the boundary layer is accelerated by the blown jets, resulting in an almost uniform wake profile at the considered axial location downstream of the pylon trailing edge.

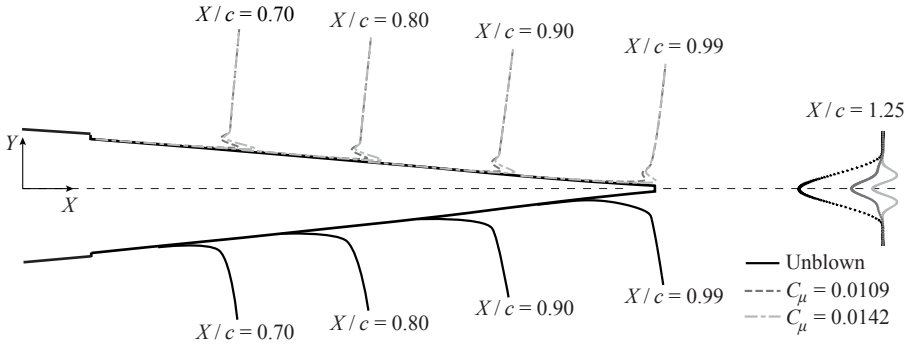

Figure A.11: Typical boundary-layer development and wake velocity profiles for different blowing coefficients.

Comparing the boundary-layer profiles and the resulting velocity distributions in the wake, it is clear that the uniformity of the pylon wake depends on the magnitude of the velocity overshoot in the boundary layer. A certain overshoot is required to compensate for the momentum loss downstream of the blowing slot. However, if the overshoot is too large then the wake profile will be characterized by a velocity overshoot, reducing the uniformity of the propeller inflow. This confirms the conclusion that a trade-off needs to be made between the chordwise position of the slot and the blowing momentum coefficient to achieve the most uniform velocity distribution in the pylon wake.

A.2.2. EFFECT OF SLOT HEIGHT

So far, the slot height was ignored in the process of determining the optimal blowing configuration. To illustrate its effect on the wake uniformity, Fig. A.12 plots the trend of the W-criterion versus blowing coefficient for the three different slot heights considered in the design study. The chordwise slot location was set to the optimal value identified before ($X_{\text{slot}}/c = 0.7$), while additional blowing rates were considered to increase the resolution around the blowing coefficients leading to optimal wake uniformity. It can be seen that the slot height has a small impact on the uniformity of the pylon wake. The blowing coefficient required to achieve optimum wake filling decreases slightly with decreasing slot height. This is due to the different shapes of the velocity profile exiting from the blowing slots. By decreasing the slot height, the velocity profile of the blown jet becomes more parabolic. Moreover, at a given blowing coefficient the velocity of the blowing jet is increased. This affects the mixing with the external flow, thereby modifying the velocity profile in the downstream wake. This implies that considering the blowing coefficient alone is not sufficient to accurately compare the wake filling potential of configurations with different slot heights.

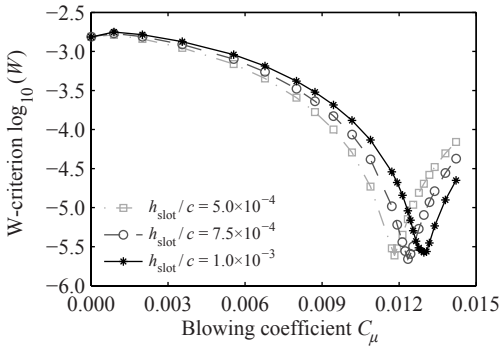

Figure A.12: Effect of slot height on the wake uniformity; $X_{slot}/c = 0.7$.

For the considered chordwise slot location and blowing coefficients, the slot height of $h_{slot}/c = 7.5 \cdot 10^{-4}$ provided the most uniform wake. For this case, the higher velocity of the blowing jets resulted in a better filling of the velocity deficit near the edges of the wake than for the configuration with $h_{slot}/c = 1.0 \cdot 10^{-3}$. The velocity overshoots around the centerline of the wake, on the other hand, were hardly affected. For the configuration with the smallest slot height ($h_{slot}/c = 5.0 \cdot 10^{-4}$), the higher velocity of the blowing jets caused this velocity overshoot to increase, leading to a reduced optimal wake uniformity.

Even though optimal wake uniformity was achieved for a slot height of $h_{slot}/c = 7.5 \cdot 10^{-4}$, the results discussed in the remainder of this chapter were obtained using a slot height of $h_{slot}/c = 1.0 \cdot 10^{-3}$. This allows for a better comparison with the results presented so far. Also, it prevents issues for the cases at nonzero angle of attack, for which the velocity of the blowing jets would have become too high for the cases with smaller slot heights for the incompressible-flow assumption to hold.

A.2.3. EFFECT OF REYNOLDS NUMBER

To assess the sensitivity of the performance of the blowing system to the Reynolds number, simulations were also performed at a Reynolds number representative of a full-scale pylon design. This was achieved by decreasing the viscosity by a factor of ten, while keeping the velocity constant. As a result, the Reynolds number was ten times higher than the default Reynolds number (see Table A.2). Figure A.13 shows the resulting contours of the W-criterion as a function of chordwise slot location and blowing coefficient.

Compared to the results obtained at the reference Reynolds number (Fig. A.7), Fig. A.13 shows that an increase in Reynolds number leads to an increase of the maximum wake uniformity, which is reached at a lower blowing coefficient. This is as expected, considering that the boundary-layer thickness decreases with increasing Reynolds number. As a result, less momentum deficit needs to be compensated for by the blowing system, and hence a lower value of the blowing coefficient is required to optimize the wake uniformity. The optimal chordwise slot location remained unchanged compared to the results obtained at the reference Reynolds number. Apparently, the trade-off between boundary-layer thickness upstream of the slot and boundary-layer growth downstream of the slot remained unchanged despite the increase of the Reynolds number. This was

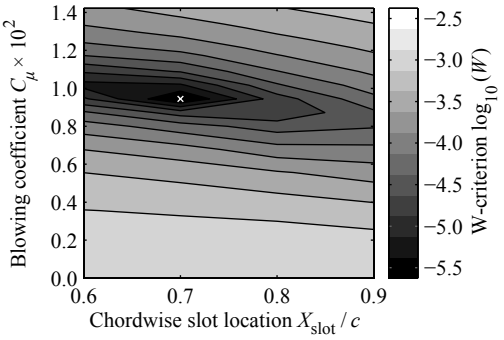

Figure A.13: Wake uniformity versus chordwise slot location and blowing coefficient; $X/c = 1.25$, $h_{slot}/c = 1.0 \cdot 10^{-3}$, $Re_c = 1.9 \cdot 10^7$.

confirmed by analysis of the development of the wake uniformity with blowing coefficient at each of the slot locations considered, which was similar to that shown in Fig. A.8 for the reference Reynolds number.

A.2.4. COMPARISON WITH TRAILING-EDGE BLOWING

The goal of positioning the blowing slots along the pylon chord is to increase the uniformity of the blown wake with respect to a trailing-edge blowing layout. Figure A.14 compares the best available velocity profiles at $X/c = 1.25$ obtained using the two types of blowing system. The geometry used for the trailing-edge blowing case was the same as for the validation study discussed in Ref. [104]. Therefore, the slot height was larger than for the chordwise blowing system.

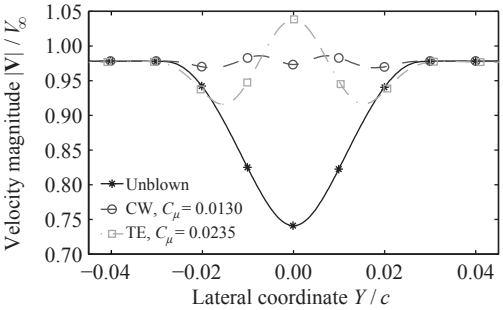

Figure A.14: Best available velocity profiles with chordwise (CW) and trailing-edge (TE) blowing; $X/c = 1.25$.

Figure A.14 illustrates the superior performance of the chordwise blowing layout, which provides a much higher wake uniformity than achieved with the trailing-edge blowing system, at a lower mass flow. The boundary layer at the pylon trailing edge is thicker than upstream of the chordwise blowing slot. Therefore, the wake thickness is larger with trailing-edge blowing than for the chordwise blowing case. Moreover, with trailing-edge blowing the available distance for mixing of the blown jets with the external

flow is reduced when compared to chordwise blowing. Consequently, the velocity overshoot in the wake due to the high-momentum blowing jets is much more pronounced with trailing-edge blowing. Also, the deficit due to the pylon boundary layer is filled less effectively, leading to a type-C velocity profile (Fig. 2.18) with relatively strong remaining velocity fluctuations. The experimental analysis of Chapter 11 identified a wake profile with similar characteristics to result in the lowest unsteady propeller blade loading and associated noise penalty for a semi-installed pusher propeller. This confirms that the W-criterion (Eq. A.2) is a relevant measure for the uniformity of the blown pylon wake.

A.3. WAKE UNIFORMITY IN ASYMMETRIC INFLOW

In case of operation in asymmetric inflow, the wake filling is more challenging. Since the boundary-layer characteristics are now different on both sides of the pylon, the resulting wake will be asymmetric. As a result, the efficacy of the symmetric trailing-edge blowing approach is reduced significantly. This was discussed in Chapter 11. With chordwise blowing, on the other hand, the blowing coefficient can be optimized on each surface individually. Moreover, since the mixing between the high- and low-momentum flows already starts at the pylon surface, the asymmetry of the wake presents a smaller challenge for optimal wake filling.

It was shown before in Fig. A.11 that the wake uniformity depends on the velocity overshoot and deficit in the boundary-layer profile leaving the pylon surface. The boundary-layer characteristics in turn are a function of the combination of slot location and blowing coefficient. Therefore, for a fixed slot location, the blowing coefficient can be controlled to arrive at an optimally filled wake. To find the blowing coefficients required when operating at nonzero angle of attack, it is assumed here that a linear relation exists between the optimal blowing coefficient and the boundary-layer thickness at the slot location $\delta_{X_{\text{slot}}}/c$:

$$C_\mu^* = \lambda \frac{\delta_{X_{\text{slot}}}}{c}, \tag{A.4}$$

with λ a sensitivity parameter. Based on the simulations performed for the symmetric case, the value of λ was found to equal 0.99 for the configuration studied in this chapter. To successfully apply Eq. A.4, first the boundary-layer thickness at the location of the blowing slots needed to be found for each of the considered angles of attack. This was done by performing a simulation for the unblown configuration at each of the desired angles of attack. Subsequently, Eq. A.4 was applied to determine the required blowing rates on both sides of the pylon. The corresponding results are given in Table A.4 for angles of attack of 3, 6, 9, and 12 degrees. For reference, the data for the symmetric inflow case are also included.

The blowing coefficients provided in Table A.4 were used to simulate the flowfield around the blown pylon at nonzero angle of attack. For each angle of attack, also a simulation was performed using the optimal blowing coefficient obtained for the symmetric case. In this way, the improvement in wake uniformity achieved by applying the asymmetric blowing approach could be quantified. Figure A.15 compares the computed wake uniformity as a function of angle of attack for the symmetric and asymmetric blowing approaches. For reference, the unblown results are also included.

Table A.4: Boundary-layer thickness and required blowing rate versus angle of attack for upper (u) and lower (l) sides of the pylon.

α [deg]	δ_u/c	δ_l/c	$\left(C_\mu^u\right)^*$	$\left(C_\mu^l\right)^*$
0	0.0131	0.0131	0.0130	0.0130
3	0.0155	0.0114	0.0153	0.0112
6	0.0189	0.0099	0.0187	0.0098
9	0.0240	0.0088	0.0237	0.0087
12	0.0317	0.0078	0.0313	0.0077

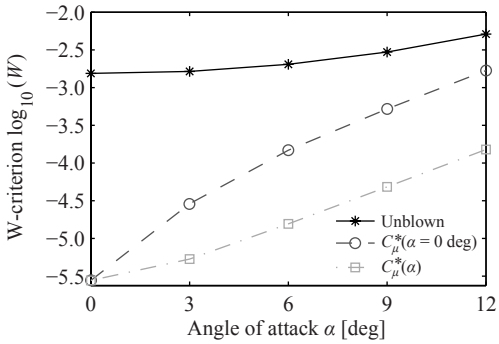

Figure A.15: Effect of angle of attack on the wake uniformity; $X/c = 1.25$.

Figure A.15 confirms that, even under asymmetric flow conditions, chordwise blowing still leads to significant filling of the downstream wake. The asymmetric blowing approach, following Eq. A.4, leads to better results than blowing at the optimal coefficient determined for the symmetric inflow case. This confirms that the blowing rate needs to be matched with the local boundary-layer characteristics. Compared to the unblown case at the same angle of attack, a reduction in W-criterion of 98.4% was achieved at $\alpha = 9$ deg. The corresponding velocity profile is depicted in Fig. A.16. When operated at a nonzero angle of attack, the distance required for the blown jet to mix with the external flow is longer on the upper surface of the pylon on which the boundary layer is thicker than on the lower surface. In fact, the thickness of the boundary layer on the suction side was too large to be filled completely, causing a remaining velocity deficit around $Y/c = 0.035$ in the velocity profile obtained using asymmetric blowing. As a result, the uniformity of the blown wakes decreased slowly with increasing angle of attack.

The successful wake filling illustrated in Fig. A.16 confirms the applicability of Eq. A.4. Despite the complex flow physics involved, the use of a linear relation between required blowing coefficient and boundary-layer height resulted in effective wake filling at nonzero angle of attack. Further improvements of the wake uniformity in asymmetric inflow could be achieved by taking the values obtained from the simplified relation of Eq. A.4 as the starting point of a more in-depth optimization study.

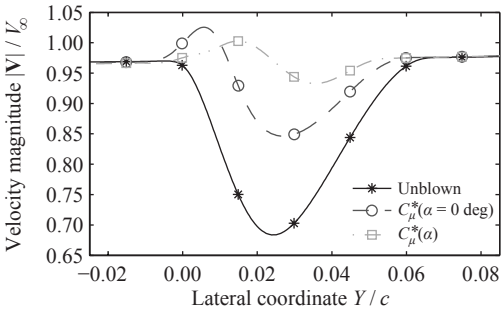

Figure A.16: Wake velocity profiles at $\alpha = 9$ deg; $X/c = 1.25$.

A.4. KEY FINDINGS

This chapter has discussed a numerical analysis of a chordwise blowing system, targeted at minimizing the nonuniformity of a pylon wake. Such a blowing system is relevant for pusher-propeller configurations, for which the propellers operate in the wake of the upstream support pylon. It was concluded that the optimal chordwise location of the blowing slot is determined by a compromise between the boundary-layer thickness at the blowing slot, the boundary-layer development downstream of the blowing slot, and the distance available for the blown jets to mix with the external flow. For the considered configuration and design options, a chordwise slot location around $X/c = 0.7$ was found to provide the best performance. The blowing coefficient should be selected such that a velocity overshoot occurs in the boundary layer directly downstream of the blowing slot. In this way, the low-momentum flow associated with the boundary layer downstream of the blowing slot can be compensated by mixing, resulting in the most uniform wake possible. With the optimal slot location and momentum coefficient defined, the impact of the slot height was found to be comparatively small.

Using the optimal slot parameters, the chordwise blowing system provided almost full elimination of the wake under symmetric inflow conditions, with a reduction in nonuniformity of 99.8% compared to the unblown case. Increasing the Reynolds number to values representative of a full-scale design further improved the wake uniformity, while lowering the required blowing coefficient. For comparison reasons, a trailing-edge blowing case was also evaluated. The optimal wake uniformity achieved with trailing-edge blowing was significantly less than that obtained using chordwise blowing, and required a higher blowing rate. This was the result of both the thicker boundary layer at the location of the blowing slot at the trailing edge and the reduced distance from the blowing slot to the evaluation plane in the downstream wake.

At nonzero angle of attack, the boundary layer develops differently on the pylon's upper and lower sides. As a result, different blowing rates are required from the two slots to achieve a uniform wake. An empirical relation was defined between the blowing coefficient required for optimal wake filling and the boundary-layer thickness at the blowing slot, based on the data obtained for the case with symmetric inflow. The relation was successfully applied to find the required asymmetric blowing rates for cases with nonzero angle of attack. This confirms the potential of chordwise blowing in realistic flight scenarios, in which the pylon–propeller combination can operate at an angle of incidence to the incoming flow.

Acknowledgments

This section is only included in the printed version of the thesis.

CURRICULUM VITAE

Tomas SINNIGE

19-08-1989 Born in Amsterdam, the Netherlands

RESEARCH

2014–2018 **PhD in Propeller Integration Aerodynamics and Aeroacoustics**
Delft University of Technology, Delft, the Netherlands
Thesis Aerodynamic and Aeroacoustic Interaction Effects for Tip-Mounted Propellers: An Experimental Study
Promotors prof. dr. ir. L. L. M. Veldhuis
prof. Dr.-Ing. G. Eitelberg
Teaching Supervised 9 MSc thesis students and 2 BSc project groups
Misc. 2-year appointment in faculty PhD council

EDUCATION

2014–2018 **Doctoral Education Program**
Delft University of Technology, Delft, the Netherlands

2010–2013 **MSc in Aerospace Engineering (with distinction)**
Delft University of Technology, Delft, the Netherlands
Thesis The Effects of Pylon Blowing on Pusher Propeller Performance and Noise Emissions: An Experimental and Numerical Study
Supervisor prof. dr. ir. L. L. M. Veldhuis

2010–2013 **Honors Track in Aircraft Design and Operation**
Delft University of Technology, Delft, the Netherlands

2007–2010 **BSc in Aerospace Engineering (with distinction)**
Delft University of Technology, Delft, the Netherlands
Minor Aerospace System Design and Technology

2001–2007 **Pre-University Education**
Stedelijk Gymnasium, Leiden, the Netherlands

List of Publications

Journal Papers

9. Sinnige, T., van Arnhem, N., Jindal, A., Hulshoff, S. J., and Veldhuis, L. L. M., "Numerical Analysis of a Chordwise Pylon-Blowing System for Pusher-Propeller Applications," *manuscript in preparation*, 2018.

8. Sinnige, T., Della Corte, B., de Vries, R., Avallone, F., Merino-Martínez, R., Ragni, D., Eitelberg, G., and Veldhuis, L. L. M., "Alleviation of Propeller-Slipstream-Induced Unsteady Pylon Loading by a Flow-Permeable Leading Edge," *manuscript submitted*, 2018.

7. Stokkermans, T. C. A., van Arnhem, N., Sinnige, T., and Veldhuis, L. L. M., "Validation and Comparison of RANS Propeller Modeling Methods for Tip-Mounted Applications," *manuscript submitted*, 2018.

6. Sinnige, T., van Arnhem, N., Stokkermans, T. C. A., Eitelberg, G., and Veldhuis, L. L. M., "Wingtip-Mounted Propellers: Aerodynamic Analysis of Interaction Effects and Comparison with Conventional Layout," *Journal of Aircraft*, in press, 2018.

5. Li, Q., Öztürk, K., Sinnige, T., Ragni, D., Wang, Y., Eitelberg, G., and Veldhuis, L. L. M., "Design and Experimental Validation of Swirl-Recovery Vanes for Propeller Propulsion Systems," *AIAA Journal*, advance online publication, 2018. doi: 10.2514/1.J057113

4. Sinnige, T., Stokkermans, T. C. A., Ragni, D., Eitelberg, G., and Veldhuis, L. L. M., "Aerodynamic and Aeroacoustic Performance of a Propeller Propulsion System with Swirl-Recovery Vanes," *Journal of Propulsion and Power*, advance online publication, 2018. doi: 10.2514/1.B36877

3. Sinnige, T., de Vries, R., Della Corte, B., Avallone, F., Ragni, D., Eitelberg, G., and Veldhuis, L. L. M., "Unsteady Pylon Loading Caused by Propeller-Slipstream Impingement for Tip-Mounted Propellers," *Journal of Aircraft*, Vol. 55, No. 4, 2018, pp. 1605-1618. doi: 10.2514/1.C034696

2. Sinnige, T., Ragni, D., Malgoezar, A. M. N., Eitelberg, G., and Veldhuis, L. L. M., "APIAN-INF: An Aerodynamic and Aeroacoustic Investigation of Pylon-Interaction Effects for Pusher Propellers," *CEAS Aeronautical Journal*, Vol. 9, No. 2, 2018, pp. 291-306. doi: 10.1007/s13272-017-0247-2

1. Sinnige, T., Ragni, D., Eitelberg, G., and Veldhuis, L. L. M., "Mitigation of Pusher-Propeller Installation Effects by Pylon Trailing-Edge Blowing," *Journal of Aircraft*, Vol. 54, No. 1, pp. 292-300, 2017. doi: 10.2514/1.C034000

Conference Papers

13. van Arnhem, N., Sinnige, T., Stokkermans, T. C. A., Eitelberg, G., and Veldhuis, L. L. M., "Aerodynamic Interaction Effects of Tip-Mounted Propellers Installed on the Horizontal Tailplane," *2018 AIAA Aerospace Sciences Meeting*, AIAA Paper 2018-2052, Jan. 2018. doi: 10.2514/6.2018-2052

12. Stokkermans, T. C. A., van Arnhem, N., Sinnige, T., and Veldhuis, L. L. M., "Validation and Comparison of RANS Propeller Modeling for Tip-Mounted Applications," *2018 AIAA Aerospace Sciences Meeting*, AIAA Paper 2018-0542, Jan. 2018. doi: 10.2514/6.2018-0542

11. Li, Q., Öztürk, K., Sinnige, T., Ragni, D., Eitelberg, G., Veldhuis, L. L. M., and Wang, Y., "Design and Experimental Validation of Swirl Recovery Vanes for Propeller Propulsion Systems," *35th AIAA Applied Aerodynamics Conference*, AIAA Paper 2017-3571, June 2017. doi: 10.2514/6.2017-3571

10. Jindal, A., Sinnige, T., Hulshoff, S. J., and Veldhuis, L. L. M., "Numerical Analysis of Pylon-Blowing Systems for Pusher-Propeller Applications," *35th AIAA Applied Aerodynamics Conference*, AIAA Paper 2017-3908, June 2017. doi: 10.2514/6.2017-3908

9. Della Corte, B., Sinnige, T., de Vries, R., Avallone, F., Ragni, D., Eitelberg, G., and Veldhuis, L. L. M., "Tractor Propeller–Pylon Interaction, Part II: Mitigation of Unsteady Pylon Loads by Application of Passive Porosity," *55th AIAA Aerospace Sciences Meeting*, AIAA Paper 2017-1176, Jan. 2017. doi: 10.2514/6.2017-1176

8. de Vries, R., Sinnige, T., Della Corte, B., Avallone, F., Ragni, D., Eitelberg, G., and Veldhuis, L. L. M., "Tractor Propeller–Pylon Interaction, Part I: Characterization of Unsteady Pylon Loading," *55th AIAA Aerospace Sciences Meeting*, AIAA Paper 2017-1175, Jan. 2017. doi: 10.2514/6.2017-1175

7. Veldhuis, L. L. M., Stokkermans, T. C. A., Sinnige, T., and Eitelberg, G., "Analysis of Swirl Recovery Vanes for Increased Propulsive Efficiency in Tractor Propeller Aircraft," *30th Congress of the International Council of the Aeronautical Sciences*, ICAS Paper 2016-0060, Sept. 2016.

6. Sinnige, T., Ragni, D., Eitelberg, G., and Veldhuis, L. L. M., "Pusher-Propeller Aerodynamics With and Without Pylon Trailing-Edge Blowing," *34th AIAA Applied Aerodynamics Conference*, AIAA Paper 2016-3421, June 2016. doi: 10.2514/6.2016-3421

5. Sinnige, T., Ragni, D., Eitelberg, G., and Veldhuis, L. L. M., "Pusher-Propeller Installation Effects in Angular Inflow," *22nd AIAA/CEAS Aeroacoustics Conference*, AIAA Paper 2016-2875, May 2016. doi: 10.2514/6.2016-2875

4. Nahuis, R., and Sinnige, T., "Design, Manufacture and Commissioning of a New NLR Six-Component Rotating Shaft Balance for Delft University of Technology," *10th International Symposium on Strain-Gauge Balances*, May 2016.

3. Sinnige, T., Malgoezar, A. M. N., Ragni, D., Scheper, K. Y. W., Snellen, M., Eitelberg, G., and Veldhuis, L. L. M., "APIAN-INF: A Low-Speed Aerodynamic and Aeroacoustic Investigation of Pylon–Pusher Propeller Interaction Effects," *CEAS 5th Air and Space Conference*, CEAS Paper 2015-152, Sept. 2015.

2. Sinnige, T., van Kuijk, J. J. A., Lynch, K. P., Ragni, D., Eitelberg, G., and Veldhuis, L. L. M., "The Effects of Swirl Recovery Vanes on Single-Rotation Propeller Aerodynamics and Aeroacoustics," *21st AIAA/CEAS Aeroacoustics Conference*, AIAA Paper 2015-2358, June 2015. doi: 10.2514/6.2015-2358

1. Sinnige, T., Lynch, K. P., Ragni, D., Eitelberg, G., and Veldhuis, L. L. M., "Aerodynamic and Aeroacoustic Effects of Pylon Trailing Edge Blowing on Pusher Propeller Installation," *21st AIAA/CEAS Aeroacoustics Conference*, AIAA Paper 2015-2356, June 2015. doi: 10.2514/6.2015-2356